Doctoral Dissertation

博士論文

Heteroepitaxial metal-organic vapor phase epitaxy of III-V semiconductors on Si for high efficiency and low-cost solar cells

(高効率・低コスト太陽電池の作製に向けたSi上III-V族半導体の有機金属気相成長)

平成30年11月30日提出

指導教員： 杉山　正和　教授

Department of Electrical Engineering and Information Systems, School of Engineering,

The University of Tokyo

東京大学大学院工学系研究科電気系工学専攻

学籍番号： 37-167088

Boram Kim

金　ボラム

Abstract

III-V top absorber integrated on active Si substrate is a promising structure for realizing high energy conversion efficiency solar cells with low production cost. However, there are still remaining challenges to integrate III-V material on Si substrate by epitaxial growth due to its property mismatches between III-V material and Si such as lattice constant, thermal expansion coefficient and polarization.

In the III-V on Si structures, GaAs/Si(1 0 0) is the most widely targeted for optical devices and CMOS uses as well as two-terminal multi-junction solar cell. Heteroepitaxy by metal-organic vapor phase epitaxy (MOVPE) is regarded as the most suitable method for industrial fabrication because the epitaxy process is simple comparing to mechanical bonding, and it has large scale epitaxial chamber than molecular beam epitaxy. For these backgrounds, in this research aims at fabrication of GaAs(P)/Si by MOVPE for solar cell application.

The major challenge for GaAs(P) heteroepitaxy on Si(1 0 0) is reducing the threading dislocation density (TDD) on the epitaxial layer. The threading dislocations in the grown epitaxial layer causes the degradation of open circuit voltage of the cell, so that degrades the energy conversion efficiency. To suppress performance degradation of the cell due to TDD, it should be 10^6 cm^{-2} or less in the epitaxial layer. However, to obtain high quality of GaAs(P) heteroepitaxial layer on Si is very difficult due to the material property differences between GaAs(P) and Si.

In this study, a new concept for reducing the burden for GaAsP heteroepitaxy on Si(1 0 0) by introducing the multi-quantum wells to the top absorber is proposed. In order to realize a band gap of 1.73 eV, which is the current matching with the Si bottom cell, with a GaAsP compound semiconductor, an As content of 75% is required. As the content of As increases, the lattice mismatch becomes larger and the burden on crystal growth becomes greater. Here, we propose a new structure for a two terminal III-V/Si tandem solar cell which bases on strain-balanced multi-quantum wells (MQWs) embedded in a GaAsP top cell. Strain-balanced MQWs extend the absorption edge to a longer wavelength and enable a reduction of the arsenic contents in the GaAsP metamorphic top cell matrix. The accumulation of carriers in MQWs favors radiative recombination, which is beneficial for high efficiency while deep quantum well lowering the carrier collection efficiency. In chapter 4, efficiency of the MQWs-GaAsP/Si tandem cell is predicted with considering about carrier dynamics in low-dimensional quantum well. The solar energy conversion efficiencies over 42.6% with an entire MQW as thin as 500 nm is predicted by theoretical calculation. The applied model takes into account the drawbacks of MQWs, such as limited light absorption and the bottleneck of carrier collection from the confinement in the wells.

Chapter 5 introduces a series of studies for heteroepitaxy by MOVPE. In the heteroepitaxy of III-V materials on a Si substrate, antiphase domains, which induces threading dislocations and degrade the device performances, need to be suppressed in order to obtain high quality epitaxial layers. For reducing the antiphase domains, Si surfaces should be prepared to have double-layer steps. In contrast to the initial achievements of double-layer step formation by high-temperature annealing (>1000°C) under H_2 ambience, exposure of Si surface to an As precursor can reduce the annealing temperature and make the process relatively robust. In this study, the relationship between surface reconstruction parameters and surface state under arsenic ambience is verified with in-situ measurement by reflectance anisotropy spectroscopy (RAS) in the MOVPE reactor. In the succeeding growth of thin GaP film on double-layer stepped Si(1 0 0) surface, the clear RA peak for the P-rich (2×2)/c(4×2) surface was observed and XRD measurement suggested non-relaxed single-crystalline GaP.

This work was specifically aimed at generalizing the manufacturing process, that is, making conditions applicable to any reactor. The later part of chapter 5 introduce the results tested on two types of reactors, regrowth of Ga(As)P layer subsequent to GaP growth.

Table of contents

Chapter 1 Introduction

1.1 Photovoltaics: sustainable energy resource for future

Global energy consumption has become increasing since 1800s, industrial revolution. As shown in fig. 1-1, in the 20th century, its energy consumption was sharply increased due to expansion of global economy scale (1400%) and population (400%). The energy consumption still has been increasing continuously, and the primary energy consumption reached to 150,000TWh at 2017 [1]-[2]. Furthermore, it is expected to reach 205,000TWh, increased 30% from 2017, at 2040 [3]-[5].

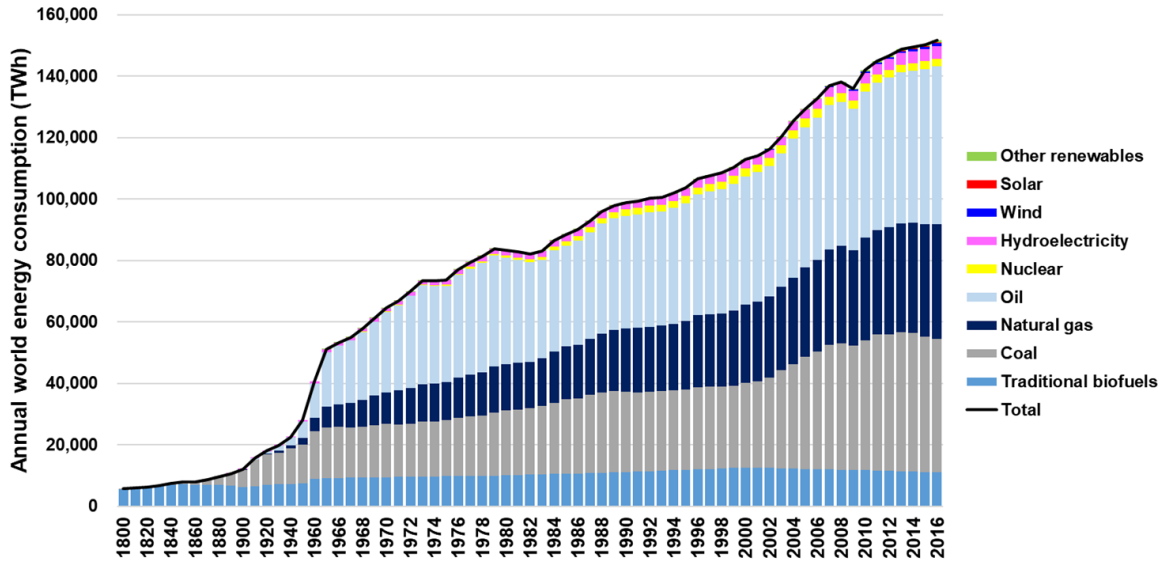

Fig. 1-1 Primary energy consumption trend: energy demands has increasing continuously, and the energy supply is relying on the fossil fuels over 85%.

The main reason for the increase in energy consumption is analyzed as the expansion of economies of non-OECD countries and the increase of population [1]-[5]. As shown in fig. 1-2, the energy consumption in non-OECD countries has been increasing rapidly since 2007, while it is quite stable in OECD countries. About the energy resources, both of non-OECD countries and OECD countries use mainly fossil fuels, and it is 81% and 88% respectively (fig. 1-3). It means that the pollution of the air as well as the exhaustion of fossil fuels is considered as a serious problem in coming decades. From these backgrounds, the sustainable energy resources are getting focus of recent international attention.

Sustainable energy is a form of energy that meets today's energy demands without being expired or

exhausted and can be used over and again. Sustainable energy should be widely recommended because it is environmentally friendly and free of cost to get the resources. All renewable energy sources, such as solar, wind, geothermal, hydro and marine energy are stable, well secured and sustainable. Photovoltaic (PV), among these energy resources, has large potential in many countries as alternative energy source for future. There are three main advantages of using solar power.

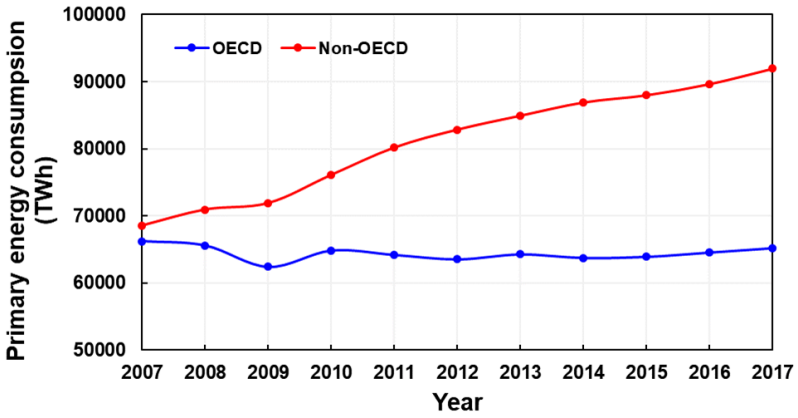

Fig. 1-2 Primary energy consumption trend: energy consumption in non-OECD countries have been increasing rapidly, while energy consumption in OECD countries are stable.

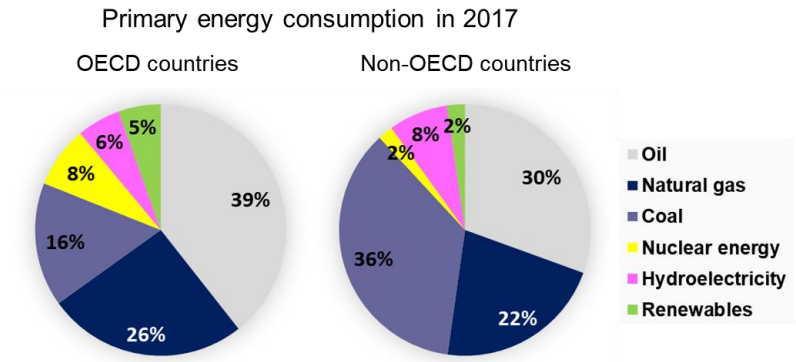

Fig. 1-3 Primary energy consumption in 2017: global energy consumption is relying on fossil fuels, especially in non-OECD countries, it is reached 89%.

1) Clean energy

The primary energy consumption will be increase 30% from 2017, and it is expected to increase 60% in non-OECD countries due to its economic growth and population increase [1]. As the consumption of fossil fuels is largely increased, emission of carbon dioxide (CO_2) and other greenhouse gases (GHGs) are expected to increase significantly. The most primary cause of emitting the CO_2 is combustion of fossil fuels [6], and

CO2 affect to the global warming. In the case of photovoltaics power generation, it can be a clean energy resource, since it does not emit CO2 and any harmful substances when the power generation.

2) Safe energy

Safety problem of power generation system has become important issue in last decades from several experiences such as Chernobyl disaster and Fukushima accident in nuclear power plants, and the accident from Sayano–Shushenskaya hydroelectric power station. From a safety point of view, PV systems do not include any elements that could cause unexpected accidents. Solar cells do not emit any hazardous materials during the power generation, and there is no risk of explosion.

3) Energy security

Energy is an indispensable part of supporting the national economy and is deeply associated with the security of the nation, which means that it is important to provide a stable and rational supply of energy. However, many countries depending on energy import. Japan highly depends on imports for most of the essential energy of the national economy, and the energy supply rate in 2017 is only 7%. Sustainable energies, including solar cells, are regarded as an important alternative from the viewpoint of energy security, because they use nature resources wherever they are, regardless of region, such as the sun light, the wind.

1.2 Levelized cost of electricity (LCOE) of solar photovoltaics

Levelized cost of electricity (LCOE) is index of electricity production costs. The LCOE, also known as levelized energy cost (LEC), is the net present value of the unit-cost of electricity over the lifetime of a energy generator. LCOE is the first-order economical index of an electricity generating system that includes all costs over its lifetime: initial investment, operations and maintenance, cost of fuel, cost of capital.

This can be roughly calculated as the net present value of all costs over the lifetime of the asset divided by the total electrical energy output of the asset as given in eq. (1.1).

$$LCOE = \frac{Sum\ of\ costs\ over\ lifetime}{Sum\ of\ produced\ electricity\ over\ lifetime} \tag{1.1}$$

Some caution must be taken when using formulas for the levelized cost, as they often embody unseen assumptions, neglect effects like taxes, and may be specified in real or nominal levelized cost. For example, other versions of the above formula do not discount the electricity stream. Here, LCOE modeling by IRENA [7]-[8] is used for all LCOE values in this section as shown in eq. (1.2).

$$LCOE = \frac{\sum_{t=1}^{n}(I_t + M_t + F_t) \times (1+r)^{-t}}{\sum_{t=1}^{n} E_t (1+r)^{-t}} \tag{1.2}$$

Where, I_t, M_t, F_t, and E_t is investment expenditures, operations and maintenance expenditures, fuel expenditures, and electricity generation in the year t. r represents discount rate and n is life of the system.

Typically, the unit of LCOE is given in the form of currency / mega- or kilo-watt-hour. Care should be taken when comparing LCOE in different study, since it is highly dependent on the assumptions, and financing terms.

Almost all solar cell research aims to reduce this LCOE as following approaches.

- ✓ Enhance energy conversion efficiency: By enhancing the energy conversion efficiency of solar cells, amount of generated electricity over the life time can be increased.
- ✓ Reduce the cell fabrication cost: Strategies to reduce the manufacturing cost of solar cells include 1) mass production of large size cells, 2) increase in manufacturing speed, and 3) cost reduction of materials such as substrate.

1.3 Photovoltaics and solar cells

Solar cell is a device which generates electrical energy from light energy of sun. In this section, the characteristics of solar irradiation and basic operating principles of semiconductor based solar cells is discussed.

1.3.1 Solar spectrum and photon flux

Blackbody radiation and air mass

All light sources, such as sun and light bulb, are work as a blackbody emitter. Blackbody absorbs all the radiation incident on its surface and emits radiation according to the temperature. Its spectral irradiance, *F(λ,T)* per unit wavelength, from the blackbody can be written as eq. (3.1) by Planck's law [12].

$$F(\lambda, T) = \frac{2hc^2}{\lambda^5(e^{hc/k_B\lambda T} - 1)} \tag{1.3}$$

Where, λ and T are the wavelength of the radiation and temperature of the blackbody respectively, and other parameters h, c and k_B are the constants (Planck's constant, speed of light in vacuum and Boltzmann's constant). Spectral intensity irradiated from blackbody by its temperature is shown in fig. 1-4 (a). The sun also works as a blackbody. The temperature at the core of the sun is very high, over 20,000,000K and even at the surface, its temperature is reach to 5760K. The energy density of solar irradiation at 5760K is 6.2×10^7

W/m^2 and the peak wavelength is 503 nm.

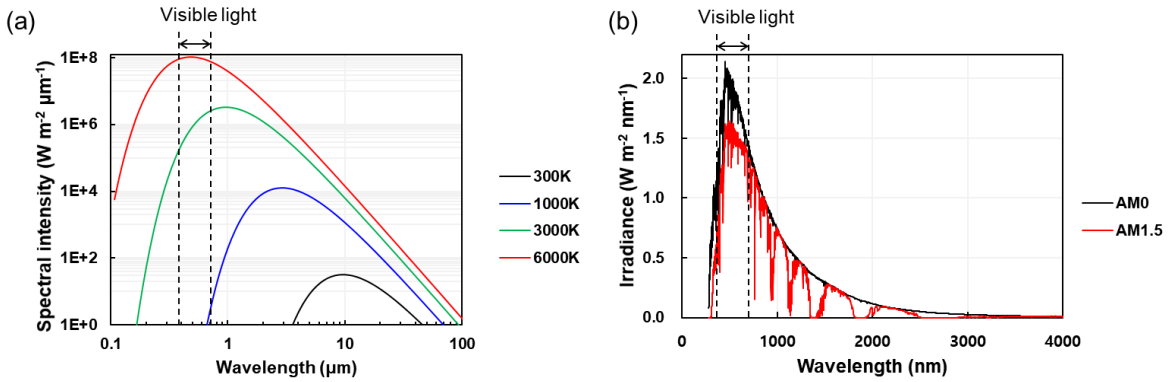

Fig. 1-4 (a) Spectral intensity emitted from blackbody: log-log scale. (b) Solar irradiance from sun: extra-terrestrial (AM0), standard terrestrial (AM1.5).

Calculating from the radius of sun and earth, and the distance between the sun and earth, solar irradiance at the outside of the earth's atmosphere is 1.35 kW/m^2 so called air mass 0 (AM0) [13]. The air mass is defined as eq. (1.4).

$$n_{air\ mass} = \frac{optical\ path\ length\ to\ sun}{optical\ path\ length\ if\ sun\ directly\ overhead} = \frac{1}{\sin\theta_s} \tag{1.4}$$

Where, θ_s is the angle of elevation of the sun. The standard spectrum on the earth is AM1.5 which the angle of elevation of the sun is 42° and the mean irradiance is ~970 W/m^2. For the convenience, however, the standard terrestrial solar spectrum is normalized, so that the integrated irradiance is 1000 W/m^2 [14]. The solar irradiance of AM0 and standard terrestrial AM1.5 is shown in fig. 1-4 (spectral data for the graphs is taken from ref. [15], and modified in this paper).

Photon flux

The photon flux, defined as the number of photons per unit time and unit area, is important in determining the number of electrons which are generated, and hence the current produced from a solar cell. The irradiance of the light can be converted to photon flux as below. The radiation irradiance from the blackbody $F(\lambda,T)$ in wavelength range of $\lambda \sim \Delta\lambda$, can be written as the function of photon energy E as eq. (1.5).

$$F(\lambda,T)d\lambda = F(E,T)\frac{\lambda^2}{hc}dE = \frac{2}{h^3c^2}\left(\frac{E^3}{e^{E/k_BT}-1}\right)dE \tag{1.5}$$

From the eq. (1.5), the spectral photon flux $\beta(E,\boldsymbol{s},\theta,\phi)$, at a point $\boldsymbol{s}$ on the surface of the black body the

number of photons with energy in the range of $E \sim E + dE$ emitted through per unit area per unit solid angle per unit time, can be converted as eq. (1.6).

$$\beta(E, \boldsymbol{s}, \theta, \phi) d\Omega d\boldsymbol{s} dE = \frac{2}{h^3 c^2}\left(\frac{E^2}{e^{E/k_B T} - 1}\right) d\Omega d\boldsymbol{s} dE \tag{1.6}$$

The photon flux *b(E)* issued normal to the surface is given by integrating β over solid angle and surface area, is given by eq. (1.7).

$$b(E) = \frac{2F}{h^3 c^2}\left(\frac{E^2}{e^{E/k_B T} - 1}\right) \tag{1.7}$$

Where, F is a geometrical factor which arises from integrating over the relevant angular range is given by $\pi sin^2\theta$. The θ is the half angle subtended by the radiating body to the flux measurement point. For the sun as seen from the earth θ is 0.26°.

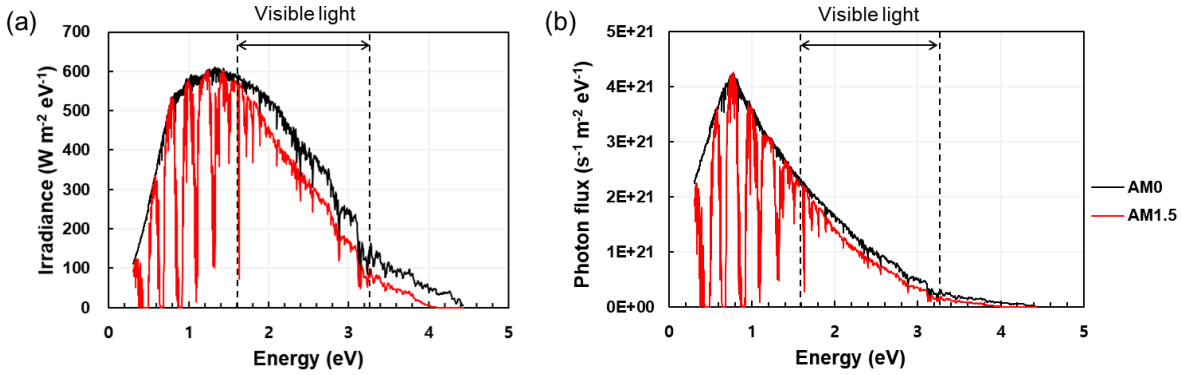

Fig. 1-5 (a) Spectral intensity and (b) photon flux emitted from the sun with describing as function of photon energy.

The visible light range (380~770 nm) occupies the largest part of sunlight reaching to the earth's surface. Therefore, it is an important point that use visible light efficiently in the use of sunlight as energy.

1.3.2 Principles of solar cells

p-n junction

The semiconductor-based p-n junction structure, which is formed by joining n-type and p-type semiconductor materials, is the most common model of solar cell. The absorbed photons with energy above the band gap E_g in the p-n junction area generate electron-hole pairs. The photo-exited electrons (holes)

transport from the p-type (n-type) to n-type by the electric field, and those carriers are extracted to the external circuit as the photocurrent. A schematic of p-n junction and equivalent circuit of ideal solar cell is shown in fig. 1-6.

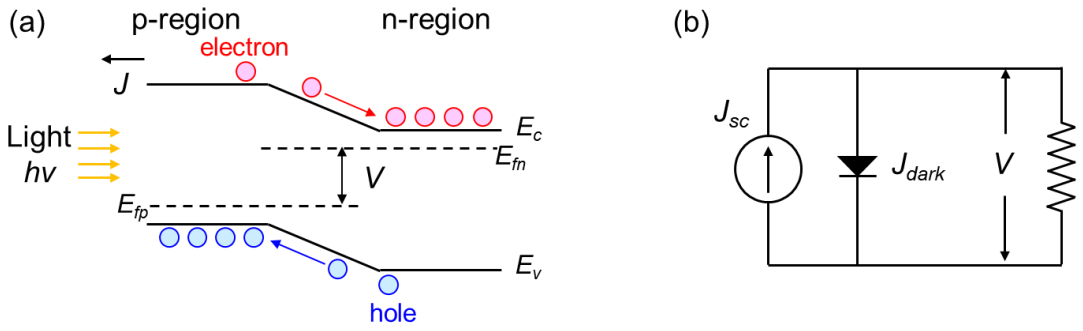

Fig. 1-6 (a) Band diagram of a p-n junction solar cell, and (b) equivalent circuit of ideal solar cells.

Where, the applied voltage V is the potential difference between the quasi-Fermi levels of the holes in the p-type region (E_{fp}) and that of the electrons in the n-type region (E_{fn}).

Photocurrent and quantum efficiency

The photocurrent generated by a solar cell under solar irradiation at short circuit is dependent on the incident light intensity. The photocurrent density at short circuit (J_{sc}) can be described as eq. (1.8).

$$J_{sc} = q \int b_s(E) QE(E) dE \tag{1.8}$$

Where, q is the electronic charge, $b_s(E)$ and $QE(E)$ are the photon flux and quantum efficiency (QE) of the incident photon energy in the range of $E \sim E+dE$.

The quantum efficiency (QE) is the ratio of the number of carriers collected by the solar cell to the number of incident photons on the solar cell and it is also called as external quantum efficiency (EQE). QE depends on the absorption coefficient of the cell materials, the efficiency of charge separation and the efficiency of charge collection in the solar cell but does not depend on the incident light spectrum.

When a load is present, a potential difference is generated between the terminals of the cell because the structure of solar cell is identical with a diode in principle. This generates the reverse current to the photocurrent which usually called the dark current. Therefore, the net current $J(V)$ by light absorption for an ideal diode can be written as eq. (1.9).

$$J(V) = J_{sc} - J_0\left(e^{qV/k_BT} - 1\right) \tag{1.9}$$

Where, $J(V)$, V, J_{sc} and J_0 are density of output photocurrent, applied bias, density of photogenerated current and saturation current of the diode. Other parameters, q, k, and T are the electronic charge, Boltzmann constant, and temperature.

When the terminals are isolated (when $J(V) = 0$), the potential difference has its maximum value which is called open circuit voltage V_{oc}.

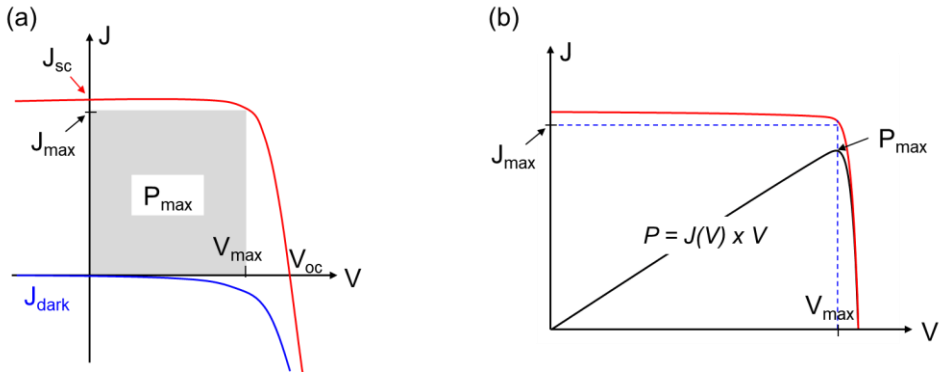

Fig. 1-7 (a) Voltage-current characteristics of solar cell, and (b) the maximum power point P_{max} and J_{max}, V_{max}.

Energy conversion efficiency

The efficiency (η) of solar cell is the probability of energy conversion from the sunlight to electrical energy via photovoltaic cells. The energy conversion efficiency is the most commonly used parameter to compare the performance of solar cells. Efficiency is defined as the ratio of output power density from the solar cell to input power density from the sun. The output power density P reaches a maximum at the operating point (or maximum power point). This occurs at the voltage V_{max} and with a corresponding current density J_{max} as shown in fig. 1-7. The efficiency of a solar cell η is determined as the fraction of incident power which is converted to electricity and is defined as eq. (1.9).

$$\eta = \frac{J_{max}V_{max}}{P_{in}} = \frac{J_{sc}V_{oc}FF}{P_{in}} \tag{1.9}$$

Where, P_{in} is total input power density, and J_{max} and V_{max} are the current and voltage at maximum power point (fig. 1-7). The J_{sc} and V_{oc} are the short circuit current and open circuit voltage respectively. The FF is the fill factor. In addition to reflecting the performance of the solar cell, the efficiency depends on the spectrum and intensity of the incident sunlight and the temperature of the solar cell. Therefore, conditions

under which efficiency is measured must be carefully controlled in order to compare the performance of one device to another. Terrestrial solar cells are measured under AM1.5 conditions and at a temperature of 25°C. Solar cells intended for space use are measured under AM0 conditions.

The fill factor is a parameter which determines the maximum power from a solar cell in conjunction with V_{oc} and J_{sc}. The *FF* is defined as the ratio of the maximum power density from the solar cell to the product of V_{oc} and J_{sc}, and the *FF* describes the "squareness" of the J-V curve.

The four quantities introduced in this section, J_{sc}, V_{oc}, *FF* and η, are the key parameters characteristics of solar cells.

1.4 Multi-junction solar cell for high efficiency

The solar spectrum has a wide range of photon energy from 0 eV to 4 eV. When the light, which has energy E, is incident to the tow band photoconverter shown in fig. 1-8, photon is act as below by its photon energy.

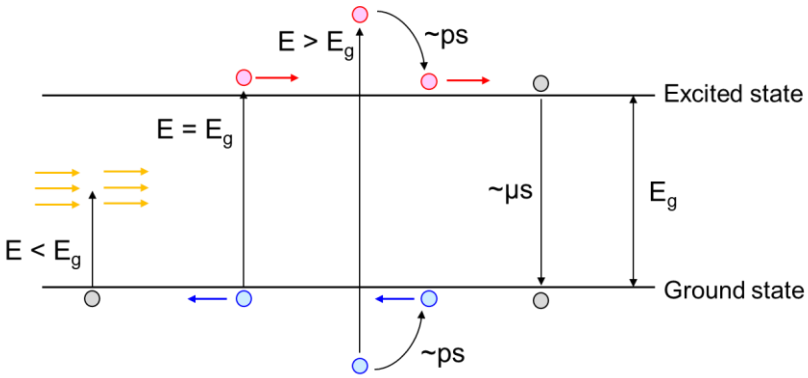

Fig. 1-8 A schematic of carrier excitation, loss and collection by the light radiation.

1) $E < E_g$: Transmission loss

Photons with energy less than the band gap E_g can not promote the electron from the ground state, so the light is not absorbed.

2) $E = E_g$: Ideal photon energy for solar cell

Photons with energy same as band gap E_g are absorbed and extracted as photocurrent.

3) $E > E_g$: Thermalization loss

Photons with energy larger than band gap E_g can promote the electron to excited state, but the

excess energy is quickly lost as heat by the carrier relax to the band edge. This process takes place on a pico-second scale [16], while the excited electrons remain in the excited state for a relatively long time. The absorbed photons achieve the same result as a photon with case 2).

The transmission loss and thermalization loss is the major factor to reduce the solar cell efficiency [17]. To reduce these losses, multiple band gap strategy is suggested such as multi-junction solar cell, intermediate band cell [18]-[20] and hot carrier solar cell [21]-[22].

In multiple band gap solar cell strategy, multi-junction is the most widely researched due to its simple structure and high efficiency. In this section, basic concept and advantages of multi-junction solar cell is introduced.

1.4.1 Multi-junction solar cells

One method to increase the efficiency of a solar cell is to split the spectrum and use a solar cell that is optimized to each section of the spectrum to reduce the thermalization and transmission losses. Series connected multi-junction solar cell, adding more subcell allows for each cell to be optimized to a narrower spectrum providing a higher efficiency.

Multi-junction solar cell is a promising structure for realizing high energy conversion efficiency by integrating subcells that have different absorption range of light, that is different band gap materials. The multi-junction cell is to stack difference band gap junctions in optical series and allow the wider band gap materials at the top to filter out most of the high energy photons, while less energetic photons pass through to smaller band gap materials as described in fig. 1-9.

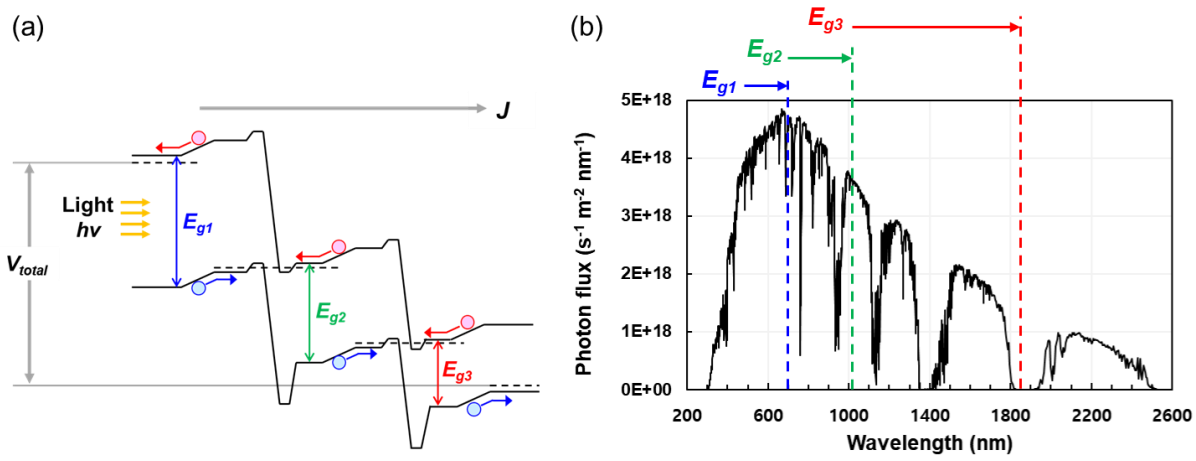

Fig. 1-9 Schematics of multi-junction solar cell: example of triple-junction solar cell. (a) Band diagram and (b) light absorption edges of each subcells.

Multi-junction solar cells can be individual cells, so called subcells, or also be connected in series. Series connected cells are simpler to fabricate but the current is the same though each cell so this restricts the bandgaps that can be used.

The maximum efficiency for a two-junction tandem under the AM1.5G spectrum under non-concentrated light is 47 % in theoretical calculation with the top cell has a band gap of 1.63 eV and the bottom cell has a band gap of 0.96 eV. As the number of band gaps increases the efficiency of the tandem cell also increases. Multi-junction solar cells consider each layer as one solar cell, and can output the maximum power when the current generated in each layer is constant. In such an optimized multijunction solar cell, the conversion efficiency of 69% under non-concentrated irradiation condition, and 86% under full concentration condition is obtained theoretically [13],[23]-[24].

1.4.2 Current matching in multi-junction solar cells

Current matching is a critical design limitation in 2-terminal multi-junction solar cells connected in series. When the amount of generated photocurrent differs from in each subcell, the extracted output current of the serially connected multijunction solar cell is limited to the smallest current of the subcell. Therefore, the subcells that generate the excess photocurrent is operated under non-optimized condition due to losses by recombination. To solve these problems, amount of photocurrent generated in each subcell has to be matched which is so called "current matching". Therefore, when designing a multi-junction solar cell, it is necessary to select appropriate bandgap materials that matches the amount of photocurrent generated in each subcell. However, it is very difficult to find a combination of semiconductor materials satisfying this requirement. To overcome this problem, multi-quantum well structure is proposed which will be discussed in chapter 2. The multi-quantum well structure is expected to achieve high efficiency of the multi-junction solar cell by tuning the bandgap of the semiconductor material.

1.4.3 III-V/Si tandem solar cells: cost reduction and efficiency enhancement

While the efficiency of Si based solar cell is saturated in last few decades the energy conversion efficiency of III-V based multi-junction solar cell has increasing continuously (fig. 1-8). III-V compound semiconductor based multi-junction solar cell recorded the highest energy conversion efficiency, in the all reported data, and now widely used in space application. However, it has not come into wide use for terrestrial use due to its high cost.

One of the most significant cost contributors in photovoltaic system is the cost of substrate. Solar panel

cost share 60% in the whole system of photovoltaics, and wafer cost is 50% of the total panel cost even in crystalline Si solar cell. In the case of GaAs, which is most common material as the epitaxial start layer for multi-junction cell, the cost of the substrate is higher than Si over 10 times.

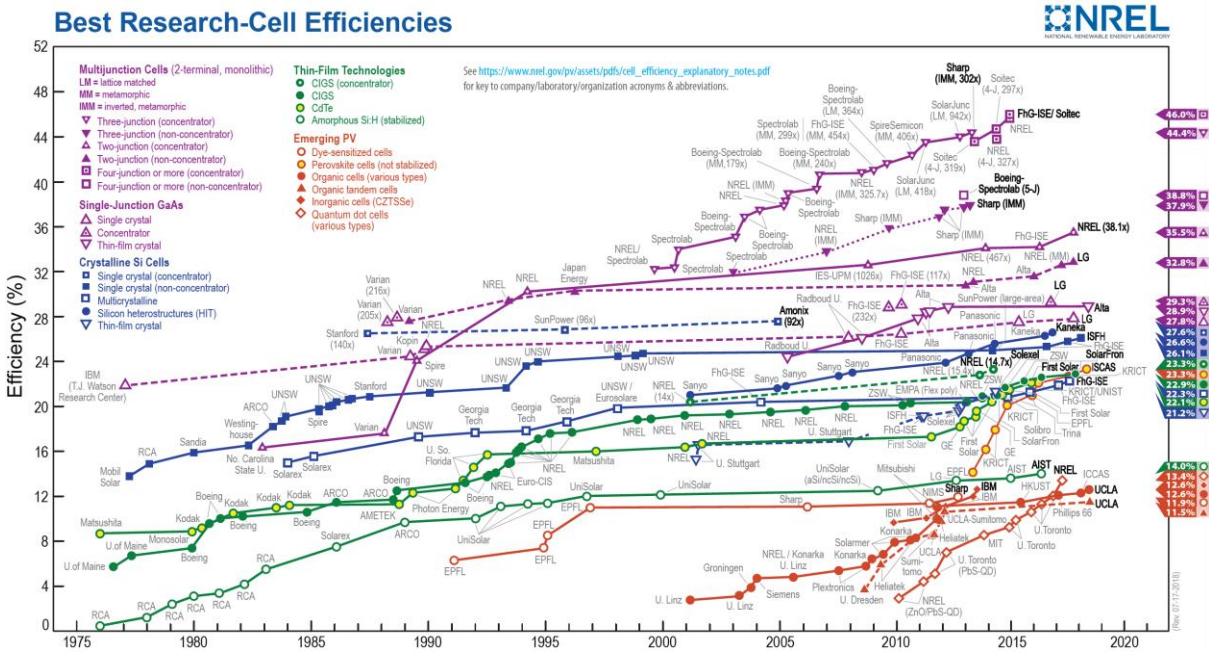

Fig. 1-10 Research cell record efficiency chart by NERL, 2018 [25]

From this background, in recent years, researches about III-V on Si multi-junction solar cells, using the merits of Si and III-V based multi-junction solar cells, are being studied variously [26]-[29].

✓ Advantages of the Si substrate

→ Large diameter substrate with low cost.

→ The manufacturing process is stable and suitable for mass production.

✓ Advantages of the III-V based multi-junction solar cell

→ Advantageous for fabricating multi-junction solar cells, therefore high efficiency can achievable.

By integrating III-V material on Si substrate, as well asthe cost reduction and high energy conversion efficiency are expected to be achieved in photovoltaic system.

1.5 III-V material integration approaches on Si

The techniques to integrate the III-V material on the SI substrate is categorized into two approaches [30]: 1) mechanical stacking (here, only 2-terminal structure is dealt with, therefore only the wafer bonding is introduced as a mechanical staking technique), and 2) heteroepitaxial growth (or monolithic). In this section, methods for integrating III-V material on Si substrate is briefly introduced.

1.5.1 Mechanical stacking methods

The biggest advantage of integration the III-V material on Si substrate by wafer bonding is that it does not depend much on the lattice mismatch. Therefore, wafer bonding enables ideal bandgap combination and material integration without the lattice mismatch constraint unlike the heteroepitaxial growth approach. From this attractive advantage, many studies have reported on III-V wafers bonded to Si structures using direct wafer bonding for solar cell application [31]-[37]. The most critical challenges for mechanical stacking for solar cell application are as below.

- → Post-growth bonding: wafer bonding is done first after growing on a III-V substrate.
- → The bonding temperature should be compatible with the III-V material and the Si substrate.
- → Electrically conductive bond layer is required to reduce the series resistance which degraded the cell performance.
- → The bonding layer has to be optically transparent to the active Si substrate.
- → Smooth bonding interface is required.

In the mechanical stacking approach, however, very critical demerit for solar cell application, which it requires III-V substrate, therefore the fabrication cost is not much reduced. Recently, to overcome this drawback, research on the reuse of III-V substrates is drawing attention [38]-[41].

1.5.2 Heteroepitaxial growth on Si substrates

The direct growth III-V material on Si substrate is a promising method for integrating high efficiency III-V based multi-junction solar cell on Si substrate due to utilization of single substrate and single epitaxial growth process.

For III-V based multi-junction solar cells, GaAs is the most used substrate as the growth start material.

Therefore, integration of GaAs on Si substrate is regardes as the initial for subsequent III-V top absorber stacking [42]-[44]. More recently, metamorphic buffer layer such as GaAsP or SiGe, for relaxing the stress from lattice mismatch between GaAs and Si, have got a lot of attention for GaAs heteroepitaxy on Si substrate [45]-[49].

The details about the heteroepitaxial growth of III-V material (mainly GaAs) is discussed in the next section.

1.6 III-V material heteroepitaxy on Si substrate: challenges for heteroepitaxy

Threading dislocations come from the property difference between III-V and Si causes degradation of the performance of solar cell especially owing to the open-circuit voltage decrease [50]-[53]. The difference of expansion coefficient causes micro cracks into the epitaxial layer, and it can be influence on the lifetime of solar cells [54]-[55]. For suppressing the performance degradation comes from the defects, the threading dislocation density (TDD) has to be lower than 10^6 cm^{-2} [56]-[57].

In this section, challenges in III/V heteroepitaxy on Si(1 0 0) substrates are introduced and the solutions for each problem are discussed.

1.6.1 Lattice mismatch

In epitaxial growth, lattice constant difference of epitaxial layer and substrate, called lattice mismatch, results in the accumulation of strain energy up to the point that the total strain energy exceeds the energy associated with some structural transformation in the film, and this causes misfit dislocations on grown epitaxial layer.

In the heteroepitaxy study of III-V material on Si substrate, GaAs is mainly studied because it is used mostly as a substrate of tandem solar cell. Therefore, in the following description GaAs is cited as III-V group material integrating on Si.

In the case of GaAs/Si crystal growth, there are large lattice mismatch of 4.1%, between GaAs (5.43Å) and Si (5.65Å) at 300K. The 4.1% lattice-mismatch between GaAs and Si makes the direct epitaxy of GaAs on Si extremely challenging, resulting in the formation of defects and dislocations such as threading dislocations and misfit dislocations. Such defects and dislocations have a detrimental impact on the minority carrier lifetime and hence the solar cell performance.

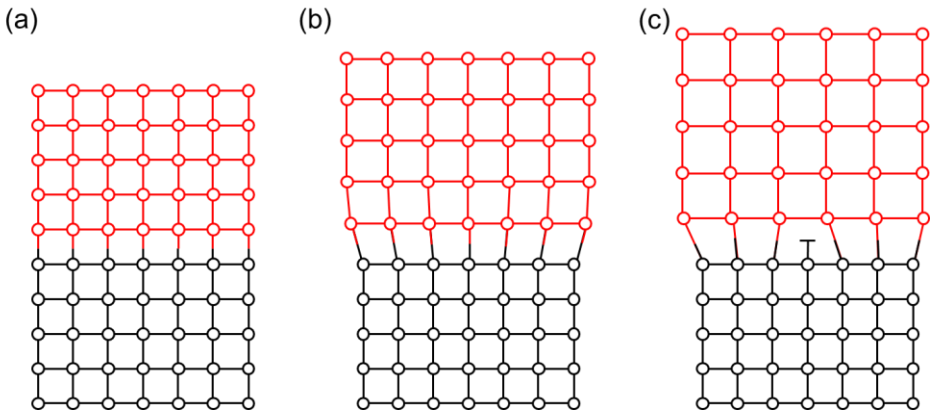

Fig. 1-11 Schematic of epitaxial layer: (a) lattice matched condition, (b) small lattice mismatch (under 0.1%), and (c) lattice mismatched.

Metamorphic buffer layer

To obtain high quality III-V epitaxial layer such as GaAs on Si substrate, metamorphic buffer layer is important for suppressing the dislocations. An appropriate buffer selection is extremely critical for the success of III-V material integration on Si by direct growth. Figure 1-12 describes the buffer structures for GaAs growth on Si.

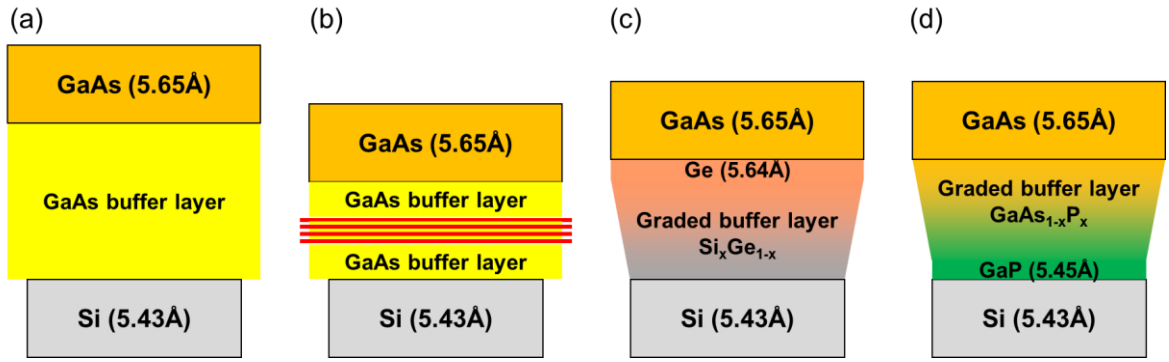

Fig. 1-12 Metamorphic buffer layer for GaAs on Si(1 0 0) heteroepitaxy: (a) GaAs buffer layer, (b) supperlattice layer in GaAs buffer layer, (c) SiGe graded buffer layer, and (d) GaAsP graded buffer layer on GaP/Si.

There are four major types of metamorphic buffer structures for relaxing the strain from the lattice mismatch between GaAs and Si as below.

1) GaAs bulk buffer layer [58]-[59]

Thick, enough to relax the strain from the large lattice mismatch, GaAs bulk layer is used for buffer layer.

2) GaAs buffer layer with superlattice [60]-[63]

InGaAs/GaAs or AlGaAs/GaAs supperlattice for blocking the threading dislocations from the GaAs/Si is inserted in GaAs bulk buffer layer.

3) Si_xGe_{1-x} graded buffer layer [64]-[67]

Gradually increase the proportion of Ge from the Si and finally bring to Ge. Ge which has very small lattice mismatch (0.13% at 300K) with GaAs, is used as seed layer for GaAs heteroepitaxy.

4) $GaAs_{1-x}P_x$ graded buffer layer [68]-[71]

Gradually increase the proportion of As from the GaP and finally bring to GaAs. GaP which has small lattice mismatch (0.35% at 300K) with Si is used as seed layer for GaAsP graded buffer growth.

Table. 1-1 Comparison of buffer layer structures.

	GaAs bulk	Supperlattice	Si_xGe_{1-x} graded	$GaAs_{1-x}P_x$ graded
Thickness	Thick (x)*	Thin (o)*	Thick (△)*	Thick (△)
Optical transparency to Si	Transparent (o)	Transparent (o)	Non-transparent (x)	Transparent (o)
Simplicity of process and design	Simple (o)	Complex (x)	Simple (o)	Simple (△)

***** (o) and (x) represents pros and cons. (△) is the neutral.

Graded buffer layer

Graded buffer layer is widely used in the metamorphic buffer layer for GaAs heteroepitaxy on Si substrate due to its simple structure, and comparably thin thickness comparing to GaAs bulk buffer layer. There are two approaches to obtain GaAs epitaxial layer on Si substrate by introducing graded buffer layer (fig. 1-13).

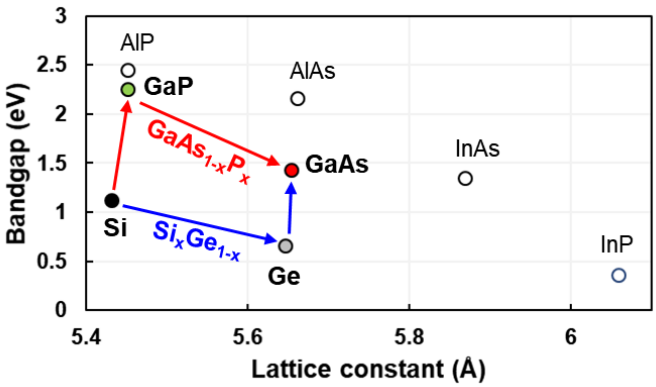

Fig.1-13 Strategies for graded metamorphic buffer layer: 1) $GaAs_{1-x}P_x$ from GaP/Si seed layer to GaAs, and 2) Si_yGe_{1-y} from Si to Ge.

The first approach is using Si_xGe_{1-x} graded buffer layer which is increasing the proportion of Ge gradually and finally bring to Ge which has small lattice mismatch with GaAs (0.13% at 300K). One of the inherent benefits of using graded Si_xGe_{1-x} buffer is the ability to realize high-quality, low TDD and relaxed Ge layers on Si substrate providing a Ge seed layer for subsequent GaAs growth. However, the band gap of Ge (0.66 eV at 300K) is smaller than Si (1.12 eV at 300K). Therefore, if Si_xGe_{1-x} buffer layer is applied, Si substrate can not be used as a active bottom cell.

The second approach is using GaAs1-xPx graded buffer layer, from GaP/Si seed layer as the growth start layer. GaAs layer can be obtained by gradually increasing of the proportion of arsenic in GaAsP buffer. The lattice constant of GaP is 5.45Å at 300K, and it has small lattice mismatch with Si substrate about 0.35%. The large band gap of $GaAs_{1-x}P_x$ buffer provides light transmission to the bottom Si subcell unlike the graded SiGe buffer approach. For these reasons, in this research, $GaAs_{1-x}P_x$ graded buffer layer on GaP/Si template is used for GaAsP top cell heteroepitaxy.

1.6.2 Antiphase domain

In addition to lattice mismatch, antiphase domain (APD) arising from the difference in polarization is also considered to be the major cause of dislocations. Si is a diamond cubic crystal which is consist of one kind of atom Si, so the crystal has no polarization. In III-V materials, on the other hand, the crystal is the zincblende cubic crystal which is consist of two (or more) kinds of atoms group-III and group-V, and the polarization is exist. This polarization difference between Si and III-V materials causes antiphase domain which is a type of defect. The atoms in the antiphase domain of a crystal are configured in the opposite order to the lattice system. In other words, an APD is a region formed from anti-site defects of a lattice and that's boundary is called antiphase domain boundary. A schematic of the antiphase domain boundary is shown in

fig. 1-14 (a).

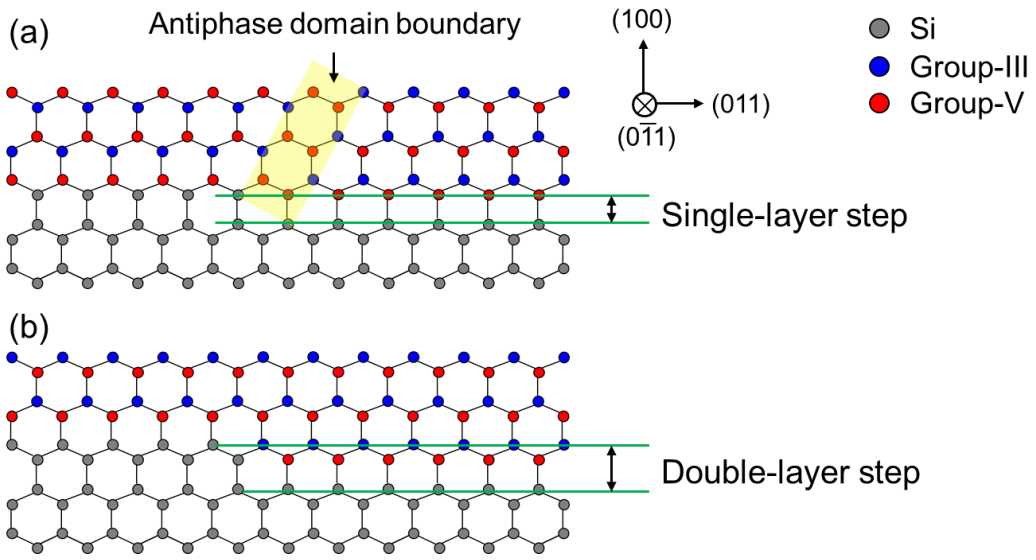

Fig. 1-14 Side view of III-V material on Si(1 0 0): III-V layer on (a) single-layer step surface and (b) double-layer step surface.

When the Si(1 0 0) surface has single-layer step which is monoatomic scale step, inappropriate binding of III-III (or V-V) is appeared along the step edge (fig. 1-14(a)). The APDs originated from polarization difference between III-V materials and Si is known as one of the biggest factors contributing to threading dislocations in III-V heteroepitaxial layers integrated on Si [72]-[73] and those dislocations degrade the solar cell performance [74]-[75].

To suppress such APDs, double-layer stepped (diatomic scale step) Si(1 0 0) surfaces shown in fig. 1-14(b) have to be prepared before heteroepitaxial growth of III-V layers on Si. From previous study, it is known that double-layer step is comparably easy to be formed on Si(1 0 0) surface with offcut surface of 2.5° or more [76]. Utilization of offcut Si substrates (4˚ - 6˚) is a good choice for forming the double-layer step surface and minimizing the formation of APDs , so the offcut substrate is widely used as the substrate for III-V material growth [77].

1.6.3 Thermal expansion coefficient

The inherent difference in the thermal expansion characteristics between GaAs(P) and Si lead to residual strain in the epitaxial films and also in the Si substrate such as microcrack and substrate bowing which could result in poor crystalline quality. In particular, the microcracks caused by difference of this thermal expansion properties is considered as the major fact for degrading the reliability of solar cells [78]-

[80] and this limit the device size and performance as well as the life time.

All objects have the property of being stretched or bulky as heat is applied. This is referred to as thermal expansion and the change rate of expansion by 1 K in temperature rise is represented as a thermal expansion coefficient. For the lattice constant of crystals, the thermal expansion coefficient (α_{th}) can be written as eq. (1.10)

$$\alpha_{th} = \frac{a_{T+\Delta T} - a_T}{a_T \, \Delta T} \tag{1.10}$$

Where, a_T and $a_{T+\Delta T}$ are the lattice constant at temperature T and $T+\Delta T$. The thermal expansion coefficient is the ratio of the lattice expansion by the temperature. The thermal expansion coefficient of GaAs is 6.4×10^{-6} K^{-1}, GaP is 4.7×10^{-6} K^{-1} [81] and of Si is 2.6×10^{-6} K^{-1} [82] at 300K, and those value increase with temperature increasing.

In the III-V crystal growth, the growth temperature is quite high 600 K - 800 K. To suppress the microcracks or other dislocations comes from the thermal expansion mismatch, it is extremely important to control the cooling step after the epitaxial growth. Another approach for reducing the thermal expansion coefficient mismatch impact on epitaxial layer, low temperature growth is highly preferred. To understand the correlation between thermal expansion mismatch and solar cell characteristics would be essential to validate the reliability and long-term robustness for III-V/Si solar cells.

1.6.4 GaP/Si template for heteroepitaxy seed layer

If the (Ge)/SiGe/Si template is used as a seed layer for GaAs epitaxy, Si substrates can not be used as bottom cell of multi-junction solar cell since the band gap of (Si)Ge is smaller than Si. To use active Si substrate as a bottom cell of III-V/Si multi-junction solar cell, large band gap material is required for the heteroepitaxy seed layer. From this point of view, GaP/Si template is a good choice as seed layer for III-V heteroepitaxial growth for multi-junction photovoltaic cell application.

GaP/Si template has benefits for using seed layer as below.

1) GaP is optically transparent to the Si
   - ✓ The band gap of GaP (2.45 eV at 300K) is larger than Si (1.12 eV at 300K), therefore the Si can be used as a bottom cell.
2) Small lattice mismatch with Si
   - ✓ 0.35% of lattice mismatch between GaP and Si at 300K.

3) Simple design for graded buffer

- ✓ Simple $GaAs_{1-x}P_x$ graded buffer layer can be used for relaxing the strain caused by lattice mismatch.

In this research, the GaP/Si template is used as seed layer for GaAsP heteroepitaxial growth on Si substrate for application to GaAsP/Si two-junction solar cell.

1.7 Outline of research

Main purpose of this research is that fabricate GaAsP heteroepitaxial layer on Si(1 0 0) substrates for low cost and high efficiency solar cell application by metal-organic vapor phase epitaxy.

Milestones in this research are,

1) Cell design

- ✓ Design the GaAsP top subcell with multi-quantum well structure for reducing the fabrication burden
- ✓ Predict the energy conversion efficiency with realistic carrier dynamic model for multi-quantum well layer.

2) Si(1 0 0) surface reconstruction

- ✓ Form the double-layer step on Si(1 0 0) surface in arsenic ambience.
- ✓ Clarify the relationship between process conditions (partial pressure of arsenic and hydrogen, surface reconstruction temperature and time, effect of Ga residuals) and surface anisotropy.
- ✓ Decide the surface preparation condition for succeeding GaP heteroepitaxy.

3) GaP/Si template fabrication

- ✓ Thin GaP epitaxial layer grown on double-layer stepped Si(1 0 0) surface.
- ✓ Verify the reproductivity by different types of reactors.

4) Metamorphic buffer layer design

- ✓ Design the number of steps and thickness for fully relaxed buffer layer.

5) GaAsP heteroepitaxy on GaP/Si template

In the main context, the fundamental theories related this research are explained chapter 2, and

experimental equipment and their principle is introduced in chapter 3.

In chapter 4, the method of designing for GaAsP top cell with multi-quantum well on Si bottom cell is explained. In this chapter, the carrier dynamics in multi-quantum wells (MQWs) is introduced, and the realistic energy conversion efficiency for MQWs-GaAsP/Si tandem solar cell is calculated. From the calculation results, the target structure for fabrication is determined.

In chapter 5, the fabrication methods and the results are discussed. At first, double-layer step formation on Si(1 0 0) surface in arsenic ambience is introduced. The relationship between process parameters, such as annealing time, temperature and partial pressure of H_2 and As, and surface states is verified. The second step is fabrication of GaP/Si template on double-layer stepped Si(1 0 0) surface. In next, before MQW-GaAsP heteroepitaxy on GaP/Si template, the $GaAs_{1-x}P_x$ graded buffer layer is designed by calculating the stress comes from lattice constant and thermal expansion coefficient mismatch. Then finally, GaAsP heteroepitaxial layer is integrated on Si(1 0 0) substrate.

1.8 References

[1] ″BP Statistical Review of World Energy”, June 2018, [Online]. Available: https://www.bp.com/en/global/corporate/energy-economics/statistical-review-of-world-energy.

[2] Hannah Ritchie and Max Roser, "Energy Production & Changing Energy Sources" [Online]. Available: https://ourworldindata.org/energy-production-and-changing-energy-sources.

[3] ″Annual Energy Outlook 2018”, Fab. 6, 2018, [Online]. Available: https://www.eia.gov.

[4] ″International energy outlook 2018”, July 2018, [Online]. Available: https://www.eia.gov/outlooks/ieo/

[5] ″世界のエネルギー事情″, [Online]. Available: https://www.kepco.co.jp/energy_supply/energy/nowenergy/world_energy.html

[6] International Energy Agency, "CO2 Emissions from Fuel Combustion 2018", [Online]. Available: https://webstore.iea.org/co2-emissions-from-fuel-combustion-2018

[7] International Renewable Energy Agency, “DATA METHODOLOGY”, [Online]. Available: http://dashboard.irena.org/download/Methodology.pdf

[8] International Renewable Energy Agency, “LCOE 2010-2017”, [Online]. Available:

http://resourceirena.irena.org/gateway/dashboard/?topic=3&subTopic=1065

[9] International Renewable Energy Agency, “Projected Costs of Generating Electricity 2015 Edition”, Sep. 2015.

[10] Christoph Kost, et al., “LEVELIZED COST OF ELECTRICITY RENEWABLE ENERGY TECHNOLOGIES”. Mar. 2018, Frounhofer, ISE.

[11] International Renewable Energy Agency, “Renewable Power Generation Costs in 2017”, Jan. 2018, [Online]. Available: http://irena.org/publications/2018/Jan/Renewable-power-generation-costs-in-2017

[12] M. Planck, "On the Low of Distribution of Energy in the Normal Spectrum", *Annalen der Physik* **4**, p.553, 1901.

[13] "THE PHYSICS OF SOLAR CELLS", Jenny Nelson, Imperial College Press, Reprinted 2010.

[14] "Terrestrial Photovoltaic Measurement Procedure", Report ERDA/NASA/1022-77/16, 1977.

[15] NREL, "Solar spectra", [Online]. Available: http://rredc.nrel.gov/solar/spectra/.

[16] P. Wurfel, "Physics of Solar Cells: From Basic Principals to Advanced Concepts", WILEY-VCH, 2009.

[17] C. H. Henry, "Limiting efficiencies of ideal single and multiple energy gap terrestrial solar cells", *J. Appl. Phys.* **51**, P.4494-4500, 1980.

[18] S. Kettemann, J. F. Guillemoles, "Limiting efficiency of LDS solar cells", *In Proc. 13th European Photovoltaic Solar Energy Conference*, 119, 1995.

[19] A. Luque and A. Marti, "Increasing the Efficiency of Ideal Solar Cells by Photon Induced Transitions at Intermediate Levels", *Phys. Rev. Lett.* **78** (26), 5014, 1997.

[20] M. A. Green, "Multiple band and impurity photovoltaic solar cells: General theory and comparison to tandem cells", *Prog. Photovoltaics* **9**, 287, 2001.

[21] M. C. Hanna, Z. Lu, and A. J. Nozik, "Hot carrier solar cells", *AIP Conference Proceedings* **404** (1), 309, 1997.

[22] D. Konig, K. Casalenuovo, Y. Takeda, G. Conibeer, J. F. Guillemoles, R. Patterson, L. M. Huang, M. A. Green, "Hot carrier solar cells: Principles, materials and design", *Physica E: Low-dimensional Systems and Nanostructures* **42** (10), p.2862-2866, 2010.

[23] S. P. Bremner, M. Y. Levy, C. B. Honsberg, “Analysis of tandem solar cell efficiencies under AM1.5G spectrum using a rapid flux calculation method”, *Prog. Photovoltaics: Research and Applications* **16**, p.225–233, 2008.

[24] A. S. Brown, M. A. Green, "Detailed balance limit for the series constrained two terminal tandem solar cell", *Physica E: Low-dimensional Systems and Nanostructures* **14** (1-2), p.96-100, 2002.

[25] NREL, “Research Cell Efficiency Records”, [Online]. Available: https://www.nrel.gov/pv/assets/pdfs/cell_efficiency_explanatory/notes.pdf.

[26] J. R. Lang, J. Faucher, S. Tomasulo, K. N. Yaung, and M. L. Lee, "Comparison of GaAsP solar cells on GaP and GaP/Si", *Appl. Phys. Lett.* **103**, 092102, 2013.

[27] K. N. Yaung, M. Vaisman, J. Lang, and M. L. Lee, "GaAsP solar cells on GaP/Si with low threading dislocation density", *Appl. Phys. Lett.* **109**, 032107, 2016.

[28] A. S. Gudovskikh, K. S. Zelentsov, A. I. Baranov, D. A. Kudryashov, I. A. Morozov, E. V. Nikitina, J. P. Kleider, "Study of GaP/Si heterojunction solar cells", *Energy Procedia* **102**, p.56-63, 2016.

[29] N. Jain, Y. Zhu, M. Clavel, and M. Hudait, "Performance Evaluation of Monolithically Integrated 3J InGaP/GaAs/Si Tandem Solar Cells for Concentrated Photovoltaics", *Proc. 40th IEEE PVSC*, 2014.

[30] N. Jain and M. K. Hudait, "III–V Multijunction Solar Cell Integration with Silicon: Present Status, Challenges and Future Outlook", *Energy Harvesting and Systems* **1** (3-4), p.121-145, 2014.

[31] S. Kim, D. Geum, M. Park, C. Kim, W. Choi, "GaAs solar cell on Si substrate with good ohmic GaAs/Si interface by direct wafer bonding", *SOLMAT* **141**, p.372-376, 2015.

[32] E. Jalaguier, B. Aspar, S. Pocas, J. F. Michaud, M. Zussy, A. M. Papon, M. Bruel, "Transfer of 3 in GaAs film on silicon substrate by proton implantation process", *Electron. Lett.* **34** (4), p.408-409, 1988.

[33] F. A. Kish, D. A. Vanderwater, and M. J. Peanasky, "Low-resistance Ohmic conduction across compound semiconductor wafer-bonded interfaces", *Appl. Phys. Lett.* **67** (14), 2060, 1995.

[34] G. Kastner, O. Breitenstein, R. Scholz, M. Reiche, "Compound semiconductor interfaces obtained by direct wafer bonding in hydrogen or forming gas", *J. Mater. Sci.* **13** (10), p.593-595, 2002.

[35] F. Shi, K. L. Chang, J. Epple, C. F. Xu, K. Y. Cheng, and K. C. Hsieh, "Characterization of GaAs-based n-n and p-n interface junctions prepared by direct wafer bonding", *J. Appl. Phys.* **92** (12), p.7544-7549, 2002.

[36] Y. C. Zhou, Z. H. Zhu, D. Crouse, and Y. H. Lo, "Electrical properties of wafer-bonded GaAs/Si heterojunctions", *Appl. Phys. Lett.* **73** (16), p.2337-2339, 1998.

[37] Justin R. Bickford, D. Qiao, P. K. L. Yu, and S. S. Lau, "Electrical characterization of GaAs metal bonded to Si", *Appl. Phys. Lett.* **89** (1), 012106, 2006.

[38] J. S. Ward, T. Remo, K. Horowitz, M, Woodhouse, B. Sopori, K. Van Sant, P. Basore, "Techno-economic analysis of three different substrate removal and reuse strategies for III-V solar cells", *Prog. Photovoltaics* **24** (9), p.1284-1292, 2016.

[39] G. J. Bauhuis, P. Mulder, E. J. Haverkamp, J. J. Schermer, E. Bongers, G. Oomen, W. Kostler, G. Strobl, "Wafer reuse for repeated growth of III–V solar cells", *Prog. Photovoltaics* **18** (3), p.155-159, 2010

[40] K. Lee, J. D. Zimmerman, Y. Zhang, S. R. Forrest, "Epitaxial lift-off of GaAs thin-film solar cells followed by substrate reuse", *IEEE 38th PVSC*, 2012.

[41] A. Van Geelen, P. R. Hageman, G. J. Bauhuis, P. C. Van Rijsingen, P. Schmidt, L. J. Giling, "Epitaxial lift-off GaAs solar cell from a reusable GaAs substrate", *Mat. Sci. Eng. B* **45** (1-3), p.162-171, 1997.

[42] S. M. Vernon, V. E. Haven, S. P. Tobin, and R. G. Wolfson, “Metalorganic Chemical Vapor Deposition of GaAS on Si for Solar Cell Applications”, *J. Cryst. Growth* **77**, p.530–538, 1986.

[43] M. Yamaguchi, A. Yamamoto, M. Tachikawa, Y. Itoh, and M. Sugo, “Defect Reduction Effects in GaAs on Si Substrates by Thermal Annealing”, *Appl. Phys. Lett.* **53**, p.2293–2295, 1988.

[44] T. Soga, T. Kato, M. Yang, M. Umeno, and T. Jimbo, “High Efficiency AlGaAs/Si Monolithic Tandem Solar Cell Grown by Metalorganic Chemical Vapor Deposition”, *J. Appl. Phys.* **78**, p.4196–4199, 1995.

[45] T. J. Grassman, A. M. Carlin, and S. A. Ringel, “Metamorphic GaAsP and InGaP Photovoltaic Materials on Si for High-Efficiency III-V/Si Multijunction Solar Cells”, *In Proc. IEEE 35th PVSC*, p.002029–002033, 2010.

[46] C. L. Andre, J. A. Carlin, J. J. Boeckl, D. M. Wilt, M. A. Smith, A. J. Pitera, M.L. Lee, E.A. Fitzgerald, S.A. Ringel, “Investigations of High-Performance GaAS Solar Cells Grown on Ge-Si1–x-Gex-Si Substrates”, *IEEE Transactions on Electron Devices* **52** (6), p.1055–1060, 2005.

[47] F. Dimroth, T. Roesener, S. Essig, C. Weuffen, A. Wekkeli, E. Oliva, G. Siefer, K. Volz, T. Hannappel, D. Haussler, W. Jager, A. W. Bett, “Comparison of Direct Growth and Wafer Bonding

for the Fabrication of GaInP/GaAs Dual-Junction Solar Cells on Silicon", *IEEE Journal of Photovoltaics* **4**, p.620–625, 2014.

[48] M. Diaz, L. Wang, A. Gerger, A. Lochtefeld, C. Ebert, R. Opila, I. Perez-Wurfl, A. Barnett, "Dual-Junction GaAsP/SiGe on Silicon Tandem Solar Cells", *In Proc. IEEE 40th PVSC*, 2014.

[49] Yaung, K. N., J. R. Lang, and M. L. Lee, "Towards High Efficiency GaAsP Solar Cells on (001) GaP/Si", *In Proc. IEEE 40th PVSC*, 2014.

[50] John C. Zolper and Allen M. Barnett, "The effect of Dislocations on the Open-Circuit Voltage of Gallium Arsenide Solar Cells", *IEEE Transactions on electron devices* **37** (2), p.478-484, 1990.

[51] M. Yamaguchi, "Dislocation density reduction in heteroepitaxial III-V compound films on Si substrates for optical devices", *J. Mater. Res.* **6** (2), p.376-384, 1991.

[52] S. M. Vernon, S. P. Tobin, M. M. Al-Jassim, R. K. Ahrenkiel, K. M. Jones, B. M. Keyes, "EXPERIMENTAL STUDY OF SOLAR CELLS PERFORMANCE VERSUS DISLOCATION DENSITY", *IEEE Conference on Photovoltaic Specialists*, 1990.

[53] M. Yamaguch, K. Lee, K. Araki, N. Kojima, and Y. Ohshita, "Potential and Activities of III-V/Si Tandem Solar Cells", *ECS Journal of Solid State Science and Technology* **5** (2), p.68-73, 2016.

[54] J. I. van Mölken, U. A. Yusufoglu, A. Safiei, H. Windgassen, R. Khandelwal, T. T. Pletzer, H. Kurz, "Impact of micro-cracks on the degradation of solar cell performance based on two-diode model parameters", *Energy Procedia* **27**, p.167-172 , 2012.

[55] M. Tachikawa, and H, Mori, "Dislocation generation of GaAs on Si in the cooling stage", *Appl. Phys. Lett.* **56**, p.2225-2227, 1990.

[56] M. Yamaguchi, K. Lee, K. Araki, N. Kojima, and Y. Ohshita, "Potential and activities of III-V/Si tandem solar cells", *ECS J. Solid State Sci. Technol.* **5** (2), p.68-73, 2016.

[57] J. C. Zolper, A. M. Barnett, "The effect of Dislocations on the Open-Circuit Voltage of Gallium Arsenide Solar Cells", *Transactions on electron devices* **37** (2), 1990.

[58] S. M. Vernon, S. P. Tobin, V. E. Haven, C. Bajgar, T. M. Dixon, "Efficiency Improvements in GaAS-on-Si Solar Cells", *In Proc. IEEE 20th PVSC*, p.481-485, 1988.

[59] S. M. Vernon, S. P. Tobin, V. E. Haven, L. M. Geoffroy, and M. M. Sanfacon, "High-Efficiency Concentrator Cells from GaAs on Si", *In Proc. IEEE 22nd PVSC*, p.353-357, 1991.

[60] Takano, Y., M. Hisaka, N. Fujii, K. Suzuki, K. Kuwahara, and S. Fuke, "Reduction of Threading

Dislocations by InGaAs Interlayer in GaAS Layers Grown on Si Substrates", *Appl. Phys. Lett.* **73**, p.2917-2919, 1998.

[61] T. Soga, T. Kato, M. Umeno, and T. Jimbo, "Photovoltaic Properties of an AlxGa1-xAs Solar Cell (x=0-0.22) Grown on Si Substrate by Metalorganic Chemical Vapor Deposition and Thermal Cycle Annealing", *J. Appl. Phys.* **79**, p.9375-9378, 1996.

[62] M. Yamaguchi, T. Nishioka, and M. Sugo, "Analysis of Strained-Layer Superlattice Effects on Dislocation Density Reduction in GaAs on Si Substrates", *Appl. Phys. Lett.* **54**, p.24-26, 1989.

[63] Y. Ohmachi, Y. Kadota, Y. Watanabe, and H. Okamoto, "High Quality GaAs on Si and Its Application to a Solar Cell", *MRS Online Proceedings Library* **144**, p.297-302, 1988.

[64] M. T. Currie, S. B. Samavedam, T. A. Langdo, C. W. Leitz, and E. A. Fitzgerald, "Controlling Threading Dislocation Densities in Ge on Si Using Graded SiGe Layers and Chemical-Mechanical Polishing", *Appl. Phys. Lett.* **72**, p.1718-1720, 1998.

[65] C. L. Andre, J. J. Boeckl, D. M. Wilt, A. J. Pitera, M. L. Lee, E. A. Fitzgerald, "Impact of Dislocations on Minority Carrier Electron and Hole Lifetimes in GaAs Grown on Metamorphic SiGe Substrates", *Appl. Phys. Lett.* **84**, p.3447-3449, 2004.

[66] M. R. Lueck, C. L. Andre, A. J. Pitera, M. L. Lee, E. A. Fitzgerald, and S. A. Ringel, "Dual Junction GaInP/GaAs Solar Cells Grown on Metamorphic SiGe/Si Substrates with High Open Circuit Voltage", *IEEE Electron Device Letters* **27**, p.142-144, 2006.

[67] M. Diaz, L. Wang, A. Gerger, A. Lochtefeld, C. Ebert, R. Opila, "Dual-Junction GaAsP/SiGe on Silicon Tandem Solar Cells", *In Proc. IEEE 40th PVSC*, 2014.

[68] J. F. Geisz, J. M. Olson, M. J. Romero, C. S. Jiang, and A. G. Norman, "Lattice-Mismatched GaAsP Solar Cells Grown on Silicon by Omvpe", *In Proc. of 4th World Conf. Photovoltaic Energy Conversion*, p.772-775, 2012.

[69] T. J. Grassman, J. A. Carlin, C. Ratcliff, D. J. Chmielewski, and S. A. Ringel, "Epitaxially-Grown Metamorphic GaAsP/Si Dual-Junction Solar Cells", *In Proc. IEEE 39th PVSC*, p.0149-0153, 2013.

[70] K. N. Yaung, J. R. Lang, and M. L. Lee, "Towards High Efficiency GaAsP Solar Cells on (001) GaP/Si", *In Proc. IEEE 40th PVSC*, 2014.

[71] T. Dimroth, T. Roesener, S. Essig, C. Weuffen, A. Wekkeli, E. Oliva, "Comparison of Direct Growth and Wafer Bonding for the Fabrication of GaInP/GaAs Dual-Junction Solar Cells on Silicon", *IEEE Journal of Photovoltaics* **4**, p.620-625, 2014.

[72] W. A. Harrison, E. A. Kraut, J. R. Waldrop, and R. W. Grant, “Polar heterojunction interfaces”, *Phys. Rev. B* **18**, 4402, 1978.

[73] H. Kroemer, “Polar-on-nonpolar epitaxy”, *J. Cryst. Growth* **81**, 193, 1987.

[74] M. Yamaguchi, A. Yamamoto, and Y. Itoh, “Effect of dislocations on the efficiency of thin-film GaAs solar cells on Si substrates”, *J. Appl. Phys.* **59**, 1751, 1986.

[75] M. Yamaguchi, “Dislocation density reduction in heteroepitaxial III-V compound films on Si substrates for optical devices”, *J. Mater. Res.* **6**, 2, 1991.

[76] B. S. Swartzentruber, Y.-W. Mo, M. B. Webb, and M. G. Lagally, “Scanning tunneling microscopy studies of structural disorder and steps on Si surfaces”, *J. Vac. ScI. Technol. A* **7** (4), 1989.

[77] Bolkhovityanov, Y. B., and O. P. Pchelyakov, “GaAs Epitaxy on Si Substrates: Modern Status of Research and Engineering”, *Physics-Uspekhi* **51** (5), p.437–456, 2008.

[78] M. Köntges, I. Kunze, S. Kajari-Schröder, X. Breitenmoser and B. Bjørneklett2, "Quantifying the risk of power loss in PV modules due to micro cracks", *25th European Photovoltaic Solar Energy Conference*, Valencia, Spain, 6-10 September 2010.

[79] P. Grunow, P. Clemens, V. Hoffmann, B. Litzenburger, L. Podlowski, "Influence of Micro Cracks in Multi-crystalline Silicon Solar Cells on the Reliability of PV Modules", *20th European Photovoltaic Solar Energy Conference*, Barcelona, Spain, 6 –10 June 2005.

[80] M. Tachikawa, and H. Mori, "Dislocation generation of GaAs on Si in the cooling stage", *Appl. Phys. Lett.* **56** (22), p.2225-2227, 1990.

[81] M. E. Straumanis, and J. P. Krumme, "Thermal Expansion Coeffiients and Lattice Parameters between 10°C and 65°C in the Systerm GaP-GaAs", *J. Electrochem. Soc.* **114** (6), p.640-641, 1967.

[82] Y. Okada, and Y. Tokumaru, "Precise determination of lattice parameter and thermal expansion coefficient of silicon between 300 and 1500 K", *J. Appl. Phys.* **56** (2), p.314-320, 1984.

Chapter 2 Theoretical background

2.1 Fundamental theory of solar cells

In chapter 1, basic principles of solar cells were introduced. In this section, more details about theoretical backgrounds for solar cells are reviewed.

There are two main theories for explaining current-voltage characteristics of solar cells: 1) detailed balance theory, and 2) drift and diffusion theory. Both of theories can derive the photo generated current described in chapter 1.

2.1.1 Detailed balance theory

One of the fundamental physical limitations on the performance of a solar cell arises from the detailed balance theory. When considering the micro state changing in the thermal equilibrium, the detailed balance theory in the photovoltaics refers that the probability balance between absorption and emission of photons. In the other words, the rate of emission of photons by solar cell has to be perfectly matched by the rate of photon absorption.

1) In equilibrium

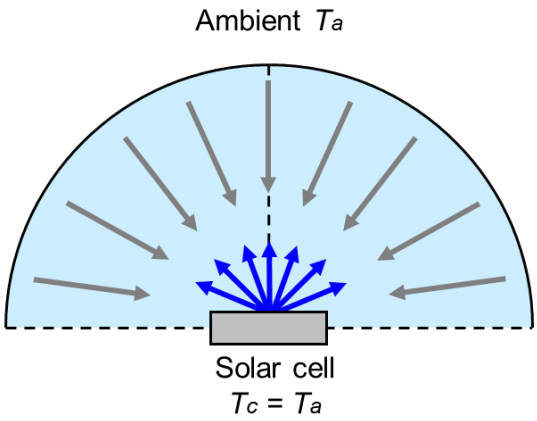

Fig. 2-1 Non-illumination system: a flat plate solar cell at the ambient temperature T_a.

In the dark (non-illumination) system, the photon flux from the ambience at the energy E, $b_a(E)$, is given by eq. (2.1).

$$b_a(E) = \frac{2F_a}{h^3c^2}\left(\frac{E^2}{e^{E/k_BT_a} - 1}\right) \tag{2.1}$$

Where, T_a is the temperature of ambience, and k_B, h, c are the constants [1]-[2]. The geometrical factor $F_a = \pi$, when assuming that ambient radiation is received over a hemisphere as shown in fig 2-1. The equivalent current density of absorption from the ambience, $j_{abs}(E)$ can be written as eq. (2.2), and it has to be balanced with emission current density $j_{emit}(E)$.

$$j_{abs}(E) = q\big(1 - R(E)\big)\, a(E)\, b_a(E) = j_{emit}(E) \tag{2.2}$$

$$j_{emit}(E) = q\big(1 - R(E)\big)\, \varepsilon(E)\, b_a(E) \tag{2.3}$$

Where, $R(E)$ and $a(E)$ represent the probability of reflection and absorption of photon energy E respectively. $\varepsilon(E)$ is the probability of photon emission and $\varepsilon(E) = a(E)$ in the detailed balance theory.

2) Under illumination

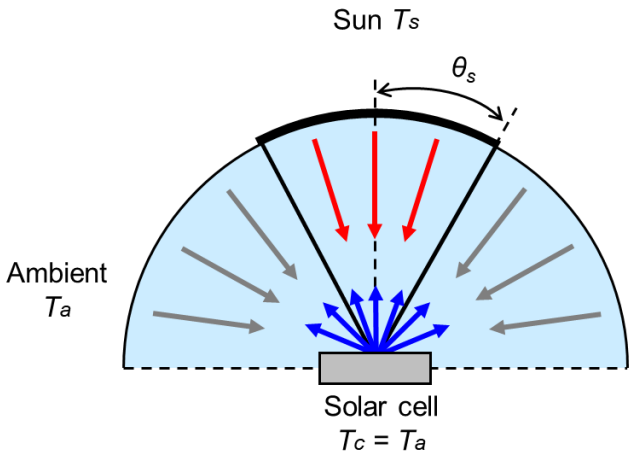

Fig. 2-2 Under illumination system: a flat plate solar cell irradiated by the sun light.

When the light from the sun at temperature T_s is irradiated to the flat plate solar cell as shown in fig. 2-2, the photon flux $b_s(E)$ from the sun is given by eq. (2.4).

$$b_s(E) = \frac{2F_s}{h^3c^2}\left(\frac{E^2}{e^{E/k_BT_s} - 1}\right) \tag{2.4}$$

Where, F_s is the geometrical factor by given as $\pi sin\theta_s^2$. The equivalent current density by photon absorption under illumination can be written as eq. (2.5).

$$j_{abs}(E) = q\big(1 - R(E)\big)\, a(E) \left[b_s(E) + \left(1 - \frac{F_s}{F_e}\right) b_a(E) \right] \tag{2.5}$$

The spontaneous emission photon flux from the cell, $b_e(E,\Delta\mu)$, is given by eq. (2.6) [3]-[4].

$$b_e(E, \Delta\mu) = \frac{2F_e n_s^2}{h^3 c^2} \left(\frac{E^2}{e^{(E-\Delta\mu)/k_B T_a} - 1} \right) \tag{2.6}$$

The cell is assumed to possess a uniform chemical potential, $\Delta\mu > 0$, as a result of the illumination, and to be in thermal equilibrium with the ambient at T_a. When the photon flux emitted from the cell (from a medium of refractive index n_s to the air n_0) with the angle within which emission is allowed as θ_c, the geometrical factor F_e can be written as eq. (2.7).

$$F_e \;=\; \pi \sin^2\theta_c \;=\; \pi \frac{{n_0}^2}{{n_s}^2} \tag{2.7}$$

The equivalent current density of emission is given as eq. (2.8).

$$j_{emit}(E) = q\big(1 - R(E)\big)\, \varepsilon(E)\, b_e(E, \Delta\mu) \tag{2.8}$$

It can be seen that eq. (2.8) is in the same form as eq. (2.3) for the cell in equilibrium that has no chemical potential elevated by light irradiation (that is, $b_a(E) = b_e(E,0)$). The probability of photon absorption $a(E)$ and photon emission $\varepsilon(E)$ has to be balanced. Therefore, the total equivalent current density $j_{total}(E)$ can be written as eq. (2.9).

$$j_{total}(E) = j_{abs}(E) - j_{emit}(E) = q\big(1 - R(E)\big) a(E) \left[b_s(E) + \left(1 - \frac{F_s}{F_e}\right) b_a(E) - b_e(E, \Delta\mu) \right] \tag{2.10}$$

The total current density can be divided into the net equivalent current density for photon absorption and emission as expressed in eq. (2.11) and eq. (2.12).

$$j_{abs(net)}(E) = q\big(1 - R(E)\big)\, a(E) \left[b_s(E) - \frac{F_s}{F_e} b_a(E) \right] \tag{2.11}$$

$$j_{emit(net)}(E) = q\big(1 - R(E)\big)\, a(E)\, [b_e(E, \Delta\mu) - b_e(E, 0)] \tag{2.12}$$

This j_{emit} represents the radiative recombination which is the unavoidable loss for solar cells.

3) Theoretical efficiency limitation

Detailed balance theory, reviewed in above, provides a method for calculating the maximum efficiency of photovoltaic devices. Originally the method was proposed by Shockley and Queisser in 1961 [5]. An

extended version was published in 1984 by Tiedje et al [6],[7]. A detailed explanation for theoretical limitation of energy conversion efficiency of solar cell will be given below.

The following assumptions are needed to obtain the theoretical efficiency limit of the solar cells with the detailed balance theory [1].

- ✓ For maximum photocurrent, the light absorption is assumed as following. The incident photons which have the energy over energy band gap of photoconverter (E_g) are perfectly absorbed in the cell. That is the external quantum efficiency *QE(E)* of the cell is set as below.

$$\begin{cases} QE(E) = 1, & E \geq E_g \\ QE(E) = 0, & E < E_g \end{cases}$$

- ✓ Each absorbed photon generates one electron-hole pair.
- ✓ There is no potential loss between photon absorption and charge collection to external circuit. The chemical potential is constant and equal to q times the applied bias V ($\Delta\mu = qV$) [8].

Short circuit current J_{sc}

When the θ_s is very small compared to the ambient, second term in eq. (2.11) can be neglected, and the photocurrent can be expressed in eq. (2.13).

$$J_{sc} = \int_0^\infty \eta_c(E) j_{abs(net)}\, dE \;\approx \int_0^\infty q\eta_c(E)\big(1 - R(E)\big)a(E)b_s(E)\, dE \tag{2.13}$$

Where, the η_c is the carrier collection efficiency, and in the ideal case, it has a value of 1. In the ideal photoconverter, the reflection at the surface is assumed as 0, so *a(E)* is equal to *QE(E)*. From this, eq. (2.13) can be written as eq. (2.14).

$$J_{sc} = q\int_0^\infty QE(E)b_s(E)\; dE = q\int_{E_g}^\infty b_s(E)\, dE \tag{2.14}$$

As it can be seen clearly from the eq. (2.14), the photocurrent is the function of only energy band gap of solar cell.

Dark current J_{dark}

Dark current J_{dark} is the flowing current through the cell in the dark with applied voltage V. Dark current is given by eq. (2.15).

$$J_{dark}(V) = \int_0^\infty j_{emit(net)}\, dE = \int_{E_g}^\infty q\big(b_e(E, qV) - b_e(E, 0)\big)\, dE \tag{2.15}$$

Theoretical efficiency limit of solar cells

From eq. (2.14) and eq. (2.15), the net photocurrent density *J(V)* can be written as below.

$$J(V) = J_{sc} - J_{dark}(V) = \int_{E_g}^\infty q\left[b_s(E) - \big(b_e(E, qV) - b_e(E, 0)\big)\right] dE \tag{2.16}$$

The *J(V)* has the approximate form as described in eq. (2.17), which is same as explained in chapter 1, eq. (1-9) for ideal diode.

$$J(V) = J_{sc} - J_0\big(e^{qV/k_BT} - 1\big) \tag{2.17}$$

Where, J_0 is the constant for the material which has dependence on the temperature [1]. As it can be seen in eq. (2.17), the photocurrent is dependent on the applied bias *V*. As *V* increases, the J_{dark} increases and net photocurrent decreases. At the open circuit voltage V_{oc}, the emission photon flux is exactly balanced with the absorption photon flux and the net photocurrent is zero.

The incident power density, P_s, from the sun is given by eq. (2.18).

$$P_s = \int_0^\infty E b_s(E_s) dE \tag{2.18}$$

The energy conversion efficiency of the photovoltaic cell is the ratio of the extracted power to supplied power as expressed in eq. (2.19).

$$\eta = \frac{V \times J(V)}{P_s} = \frac{\int_{E_g}^\infty E_g b_s(E)\, dE}{\int_0^\infty E b_s(E)\, dE} \tag{2.19}$$

The maximum efficiency can be achieved when the *V* satisfy the eq. (2.20).

$$\frac{d(J(V) \times V)}{dV} = 0 \tag{2.20}$$

If the incident power is fixed, the efficiency is only depending on the energy band gap of cell materials.

Assuming that the sun is the blackbody of 6000 K, the theoretical maximum efficiency of a single junction solar cell based on detailed balance theory is 31% at the energy band gap of 1.3 eV, reported by the Shockley-Queisser [5]. In the discussion above, the solar spectrum is described as the blackbody radiation spectrum at the temperature of particular T_s, but it can be replaced by arbitrary photon flux spectrum. The

calculated efficiency limit for the AM1.5 spectrum is up to 33% in the 1.4 eV band gap from 1-sun (non-concentrated solar irradiance).

2.1.2 Drift-diffusion model for solar cells

The detailed balance theory is simply a theory of the balance of photons, and it derives properties that do not depend on the structure of the device. In this section, current-voltage characteristics of semiconductor solar cells are discussed based on carrier drift and diffusion processes which take account of carrier dynamics within the cell.

The basic structure of semiconductor solar cells with p-n junction is shown at fig. 2-3.

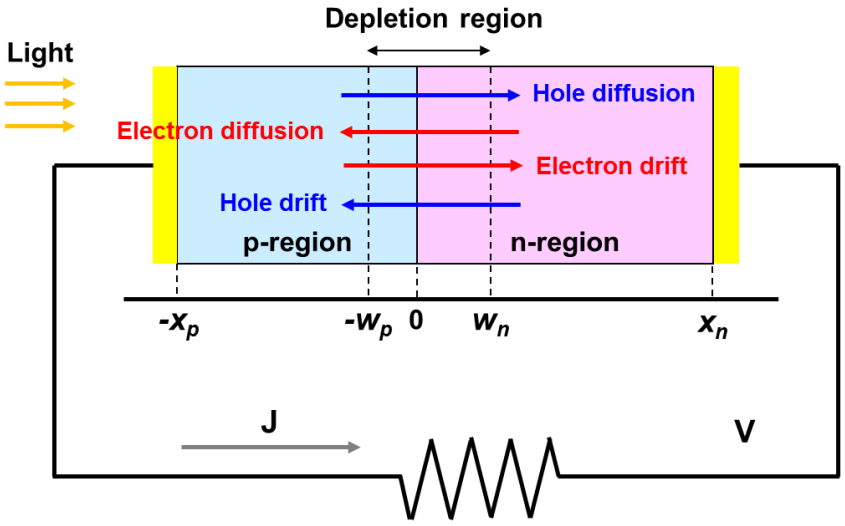

Fig. 2-3 A schematic layer structure of p-n junction solar cell.

For simplicity, all dynamics are considered in 1-dimension structure along the x axis as shown in the fig. 2-3, where the interface of p-region ($x < 0$) and n-region ($x > 0$) semiconductor is defined as $x = 0$. The x_p and x_n are the thickness of p-type and n-type semiconductor layer, and the junction is completely free of majority carriers for a depth w_p into p-region and w_n into n-region. About the doping concentration, N_a is the acceptor concentration in p-region and N_d is the donor concentration in n-region respectively.

The current-voltage characteristics of solar cells can be obtained by solving the semiconductor transport equations and Poisson's equation (eq. (2.21)-(2.25)) with boundary conditions at the p and n contacts and appropriate forms for the generation rate $G(x)$, recombination rates $U(x)$ and the electron and hole currents.

✓ Poisson's equation

According to Poisson's equation, the relation between the electrical potential $\phi(x)$ and carrier densities can be obtained as eq. (2.21).

$$\frac{d^2\phi(x)}{dx^2} = -\frac{q}{\varepsilon_s}(N_d(x) - N_a(x) + p(x) - n(x)) \tag{2.21}$$

Where, ε_s is the permittivity of semiconductor, q is the electronic charge, and $p(x)$ and $n(x)$ are the hole and electron density.

✓ Transport equation

The transport equations describe how carrier moves in the cell.

$$J_n = q\mu_n n(x)F + qD_n\frac{dn(x)}{dx} \tag{2.22}$$

$$J_p = q\mu_p p(x)F - qD_p\frac{dp(x)}{dx} \tag{2.23}$$

Where, F is the electric field, J_n is the electron current density, μ_n is the electron mobility and D_n is the electron diffusivity. Similarly, J_p is the hole current density, μ_p is the hole mobility and D_p is the hole diffusivity.

The first term is for drift current density (which means that carriers are driven by and electric field) and the second term is for diffusion current density (which means that carrier are driven by carrier concentration gradient).

✓ Continuity equation

The continuity equations describe the recombination, generation and transport of all carriers.

$$\frac{\partial n}{\partial t} = \frac{1}{q}\frac{\partial J_n}{\partial x} + G_n(x) - U_n(x) \tag{2.24}$$

$$\frac{\partial p}{\partial t} = -\frac{1}{q}\frac{\partial J_p}{\partial x} + G_p(x) - U_p(x) \tag{2.25}$$

Where, $U_n(x)$ ($U_p(x)$) is the recombination rate and $G_n(x)$ ($G_p(x)$) is the generation rate for electron (hole) at the point. For band-to-band generation and recombination process, the rates for electron and hole are equal, therefore $G_n(x) = G_p(x) = G(x)$ and $U_n(x) = U_p(x) = U(x)$. The generation rate and recombination rate are given by eq. (2.26)-(2.27).

$$G(E,x) = \big(1 - R(E)\big)a(E)b_s(\mathrm{E})e^{-\int_{-xp}^{x} a(E,x')\,dx'} \tag{2.26}$$

Where, *R(E)* and *a(E)* are probability of reflection and absorption of the photon flux, and $b_s(E)$ is the incident photon flux.

$$\begin{cases} U(x) = \dfrac{n - n_0}{\tau_n} & \text{for } x < 0 \\ U(x) = \dfrac{p - p_0}{\tau_p} & \text{for } 0 < x \end{cases} \tag{2.27}$$

Where, n_0 (p_0) is the electron (hole) concentration in the n-region (p-region), and τ_n and τ_p are the minority carrier lifetime in each region.

The equations listed above are difficult to solve without several simplifying assumptions, in addition to the assumption of a 1-dimensional layer structure as below [7].

Depletion approximation

1) The electric field is localized to the junction region and the electric field in the neutral region ($x < w_n$ or $x < -w_p$) is negligible.

2) There are no free carriers in depletion region ($n(x) = p(x) = 0$ for $-w_p < x < w_n$).

$$\frac{1}{q}\frac{\partial J_{n/p}}{\partial x} = \pm(U - G) = 0$$

3) Quasi-Fermi levels are approximately constant in the depletion region and split by applied voltage *V*.

4) Majority carrier density (N_a and N_d) are constant in the respective n- / p-regions and much more than minority carrier density.

Depletion region (Space charge region (SCR)) width w_{scr}

Depletion width can be obtained by solving the Poisson's equation with the boundary conditions are given as eq. (2.28).

$$\begin{cases} \phi = 0 & \text{for } x = -w_p \\ \phi = V_{bi} & \text{for } x = w_n \end{cases} \tag{2.28}$$

Where, V_{bi} is the built-in voltage across the p-n junction (difference in Fermi-levels between the n and p-type semiconductor).

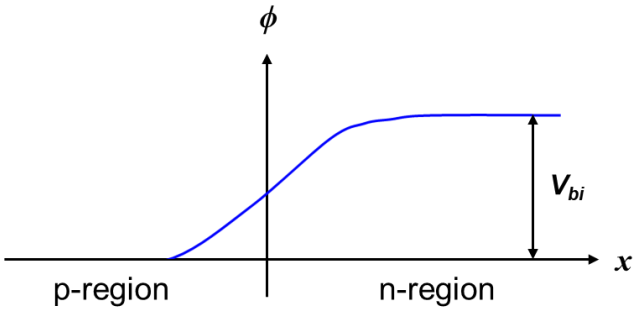

Fig. 2-4 Potential variation across the p-n junction, assuming that the voltage on the p-type side is zero.

Obtained potential ϕ is,

$$\begin{cases} \phi = \dfrac{qN_a}{2\varepsilon_s}(x + w_p)^2 & \text{for} \quad -w_p < x < 0 \\ \phi = -\dfrac{qN_d}{2\varepsilon_s}(x - w_n)^2 & \text{for} \quad 0 < x < w_n \end{cases} . \tag{2.29}$$

From these, the depletion region width w_{scr} is,

$$w_{scr} = w_n + w_p = \sqrt{\frac{2\varepsilon_s}{q}\left(\frac{1}{N_d} + \frac{1}{N_a}\right) V_{bi}} . \tag{2.30}$$

The depletion region width becomes thinner as p-doping or n-doping is increasing.

Current in neutral region

✓ Current in n-region ($x > w_n$)

The minority carrier population in the n-region follows eq. (2.31) from the continuity equation and transport equation.

$$\frac{d^2p}{dx^2} - \frac{p - p_0}{{L_p}^2} + \frac{G(E,x)}{D_p} = 0 \tag{2.31}$$

Where, L_p is the hole diffusion length given by $L_p = \sqrt{\tau_p D_p}$.

At the boundary, $n(x)$ satisfies following equations. The first boundary condition

$$p - p_0 = \frac{{n_i}^2}{N_d}\left(e^{\frac{qV}{k_B T}} - 1\right) \qquad \text{at} \quad x = w_n \tag{2.32}$$

and second boundary condition

$$-D_p \frac{dp}{dx} = S_p(p(x_n) - p_0) \qquad \text{at} \quad x = w_n \ . \tag{2.33}$$

Where, n_i is the intrinsic carrier density and p_0 is the equilibrium hole density in the n-region given by $p_0 = n_i^2 / N_d$, and S_p is the surface recombination rate of holes.

By solving the continuity equation with the boundary conditions described above, the hole current density $j_p(E, w_n)$ in n-region can be derived as equation (2.34).

$$j_p(E, w_n) = -\frac{q\big(1 - R(E)\big)b_s(E)a(E)L_p}{a(E)^2{L_p}^2 - 1}\, e^{-a(E)(x_p + w_n)}$$

$$\times\left[\frac{\left(\frac{S_p L_p}{D_p}\cosh\frac{x_n - w_n}{L_p} + \sinh\frac{x_n - w_n}{L_p}\right) - \left(\frac{S_p L_p}{D_p} - a(E)L_p\right)e^{-a(E)(x_n - w_n)}}{\frac{S_p L_p}{D_p}\sinh\frac{x_n - w_n}{L_p} + \cosh\frac{x_n - w_n}{L_p}} - a(E)L_p\right]$$

$$+\frac{qD_p p_0\left(e^{qV/k_B T} - 1\right)}{L_p}\left[\frac{\frac{S_p L_p}{D_p}\cosh\frac{x_n - w_n}{L_p} + \sinh\frac{x_n - w_n}{L_p}}{\frac{S_p L_p}{D_p}\sinh\frac{x_n - w_n}{L_p} + \cosh\frac{x_n - w_n}{L_p}}\right] \tag{2.34}$$

This can be expressed as,

$$j_p(E, w_n) = j_{ph,p}(E, w_n) + j_{dark,p}(E, w_n), \tag{2.35}$$

where, $j_{ph,p}$ is the photo-generated current and $j_{dark,p}$ is the dark current in n-region. From these, the current density at $x = w_n$ can be obtained as eq. (2.36).

$$J_p(w_n) = \int_0^\infty j_{ph,p}(E, w_n)\, dE + j_{dark,p}(V, w_n) \tag{2.36}$$

✓ Current in p-region ($x < -w_p$)

The minority carrier population in the p-region follows eq. (2.37) from the continuity equation and transport equation.

$$\frac{d^2 n}{dx^2} - \frac{n - n_0}{{L_n}^2} + \frac{G(E, x)}{D_n} = 0 \tag{2.37}$$

Where, L_n is the electron diffusion length given by $L_n = \sqrt{\tau_n D_n}$.

At the boundary, *n(x)* satisfies following boundary conditions. The first boundary condition

$$n - n_0 = \frac{{n_i}^2}{N_a}\left(e^{\frac{qV}{k_B T}} - 1\right) \qquad \text{at} \quad x = -w_p \tag{2.38}$$

and second boundary condition

$$D_n \frac{dn}{dx} = S_n\big(n(-x_p) - n_0\big) \qquad \text{at} \quad x = -w_p \ . \tag{2.39}$$

Where, n_i is the intrinsic carrier density and n_0 is the equilibrium electron density in the p-region given by $n_0 = {n_i}^2 / N_a$, and S_n is the surface recombination rate of electrons.

By solving the continuity equation with the boundary conditions described above, the electron current density $j_n(E, -w_p)$ in p-region can be derived as equation (2.40).

$$j_n\big(E, -w_p\big) = -\frac{q\big(1 - R(E)\big)b_s(E)a(E)L_n}{a(E)^2{L_n}^2 - 1}$$

$$\times\left[\frac{\left(\frac{S_n L_n}{D_n}\cosh\frac{x_p - w_p}{L_n} + \sinh\frac{x_p - w_p}{L_n}\right)e^{-a(E)(x_p - w_p)} - \left(\frac{S_n L_n}{D_n} - a(E)L_n\right)}{\frac{S_n L_n}{D_n}\sinh\frac{x_p - w_p}{L_n} + \cosh\frac{x_p - w_p}{L_n}} + a(E)L_n e^{-a(E)(x_p - w_p)}\right]$$

$$+\frac{qD_n n_0\big(e^{qV/k_B T} - 1\big)}{L_n}\left[\frac{\frac{S_n L_n}{D_n}\cosh\frac{x_p - w_p}{L_n} + \sinh\frac{x_p - w_p}{L_n}}{\frac{S_n L_n}{D_n}\sinh\frac{x_p - w_p}{L_n} + \cosh\frac{x_p - w_p}{L_n}}\right] \tag{2.40}$$

This can be expressed as,

$$j_n\big(E, -w_p\big) = j_{ph,n}\big(E, -w_p\big) + j_{dark,n}\big(E, -w_p\big), \tag{2.41}$$

where, $j_{ph,n}$ is the photo-generated current and $j_{dark,n}$ is the dark current in p-region. From these, the current density at $x = -w_p$ can be obtained as eq. (2.42).

$$J_n\big(-w_p\big) = \int_0^\infty j_{ph,n}\big(E, -w_p\big)\, dE + j_{dark,n}\big(V, -w_p\big) \tag{2.42}$$

Current in depletion region

The current density in depletion region, J_{scr} , can be obtained by integrating the eq. (2.24)-(2.25) as below [1].

$$J_{scr} = \int_{-w_p}^{w_n} q\,(U - G)\,dx \tag{2.43}$$

The depletion region current can be divided into recombination due to applied bias V, and generation due to light irradiation. There are two types of recombination processes: radiative recombination, and non-radiative recombination including Shockely Read Hall (SRH) and Auger recombination process. Current density of radiative recombination, $J_{rec,rad}$, and of non-radiative recombination mainly caused by SRH process, $J_{rec,SRH}$, are shown in equations (2.44) and (2.45).

$$\begin{aligned} J_{rec,rad}(\mathrm{V}) &= \int_{-w_p}^{w_n} qU_{rad}(x)\,dx \\ &= q\int_{-w_p}^{w_n} \frac{2\pi}{h^3c^2}\left[\int_0^{\infty} \frac{a(E)E^2}{e^{(E-qV)/k_BT}-1}dE - \int_0^{\infty} \frac{a(E)E^2}{e^{E/k_BT}-1}dE\right]dx \\ &\approx q\int_{-w_p}^{w_n} B_{rad}{n_i}^2\left(e^{qV/k_BT}-1\right)dx \end{aligned} \tag{2.44}$$

Where, the recombination constant, B_{rad}, is a material-specific property that does not depend on the carrier density.

$$\begin{aligned} J_{rec,SRH}(\mathrm{V}) &= \int_{-w_p}^{w_n} qU_{SRH}(x)\,dx \\ &= q\int_{-w_p}^{w_n} \frac{np - {n_i}^2}{\tau_{n,SRH}(p+p_t) + \tau_{p,SRH}(n+n_t)}\,dx \\ &\approx \frac{qn_i(w_n + w_p)}{\sqrt{\tau_{n,SRH}\tau_{p,SRH}}} \frac{\pi k_BT \sinh\frac{qV}{2k_BT}}{q(V_{bi}-V)} \end{aligned} \tag{2.45}$$

Where, n_t (p_t) is the value of the electron (hole) density when the electron (hole) Fermi level E_{fn} (E_{fp}) is equal to the carrier trap level E_t, and can be written as eq. (2.46)-(2.47).

$$n_t = n_i e^{\frac{E_t - E_i}{k_BT}} \tag{2.46}$$

$$p_t = n_i e^{\frac{E_i - E_t}{k_BT}} \tag{2.47}$$

Where, E_i is the junction of x, given by eq. (2.29). The generation term in Jscr in eq. (2.43) can be written as eq. (2.48) by eq. (2.26).

$$j_{scr,gen}(E) = -q\int_{-w_p}^{w_n} G(E,x)\,dx$$
$$= -q\int_{-w_p}^{w_n} \big(1-R(E)\big)a(E)b_s(\mathrm{E})e^{-\int_{-x_p}^{x} a(E,x')\,dx'}\,dx$$
$$= qb_s(E)(1-\mathrm{R(E)})e^{-a(E)(x_p-w_p)}(1-e^{-a(E)(w_p+w_n)}) \quad (2.48)$$

From above equations, total current density in depletion region Jscr(V) can be obtained as eq. (2.49).

$$J_{scr}(\mathrm{V}) = \frac{qn_i(w_n+w_p)}{\sqrt{\tau_{n,SRH}\tau_{p,SRH}}}\frac{\pi k_B T\sinh\frac{qV}{2k_BT}}{q(V_{bi}-V)} + q\int_{-w_p}^{w_n} B_{rad}{n_i}^2\big(e^{qV/k_BT}-1\big)\,dx$$
$$-q\int_0^{\infty} b_s(E)\big(1-\mathrm{R(E)}\big)e^{-a(E)(x_p-w_p)}\big(1-e^{-a(E)(w_p+w_n)}\big)\,dE \quad (2.49)$$

Total current density

The net current is given by the sum of $J_p(w_n)$, $J_n(-w_p)$ and J_{scr} described in above (eq. (2.36), (2.42), and (2.49)).

$$J(V) = -J_p(w_n) - J_n(-w_p) - J_{scr}(\mathrm{V}) \quad (2.50)$$

Dark current $J_{dark}(V)$

In the dark, $b_s(E) = 0$ for all energy rage E, therefore the first term of eq. (2. 34), (2.40) and the third term of eq. (2.49) are zero. The dark current can be expressed as approximated form shown in eq. (2.51).

$$J_{dark}(V) = \left(\frac{qn_i{}^2D_n}{N_aL_n}+\frac{qn_i{}^2D_p}{N_dL_p}\right)\big(e^{qV/k_BT}-1\big) + \frac{qn_i(w_n+w_p)}{\sqrt{\tau_n\tau_p}}\big(e^{qV/2k_BT}-1\big)$$
$$+qB_{rad}n_i{}^2(w_n+w_p)\big(e^{qV/k_BT}-1\big)$$
$$= J_{diff,0}\big(e^{qV/k_BT}-1\big) + J_{SRH,0}\big(e^{qV/2k_BT}-1\big) + J_{rad,0}\big(e^{qV/k_BT}-1\big)$$
$$= J_1\big(e^{qV/k_BT}-1\big) + J_2\big(e^{qV/2k_BT}-1\big) \quad (2.51)$$

Short circuit current J_{sc}

Under illumination, $V = 0$ therefore the second term of eq. (2. 34), (2.40) are zero. For the depletion region current, there is no recombination in this condition, therefore $J_{scr} = J_{gen}$. The photocurrent J_{sc} can be

written as eq. (2.52).

$$J_{sc} = \int_0^\infty j_{sc}(E)\ dE = -\int_0^\infty \left(j_n(E,-w_p) + j_p(E,w_n) + j_{gen}(E)\right) dE \tag{2.52}$$

From the equations discussed in above, the net current of photovoltaic cell can be obtained as below.

$$J(V) = J_{sc} - J_{dark}(V) = J_{sc} - J_1\left(e^{qV/k_BT} - 1\right) - J_2\left(e^{qV/2k_BT} - 1\right) \tag{2.53}$$

In the case of ideal cell, non-radiative recombination does not occur, therefore the dark current is considered as only caused by diffusion of minority carrier, $J_{diff,0}\left(e^{qV/k_BT} - 1\right)$. The net current density in the ideal photoconverter, can be described as eq. (2.54).

$$J(V) = J_{sc} - J_{diff,0}\left(e^{qV/k_BT} - 1\right) = J_{sc} - J_0\left(e^{qV/k_BT} - 1\right) \tag{2.54}$$

2.2 Fundamental physics of multi-quantum wells

As introduced briefly in chapter 1, multi-quantum wells (MQWs) layer in i-region between the p-n junction in the photovoltaic cell is a promising structure for tuning the bandgap of cell materials. However, carrier dynamics in the low dimensional quantum wells structure show different characteristics form compare to the bulk matrix. In this section, several important physics related to MQWs solar cell are introduced.

2.2.1 Characteristics of strain-balanced MQW solar cells

The new types of solar cells with multi-quantum wells (MQWs) are proposed for current matching of multi-junction solar cells [10]-[12]. MQWs solar cell was proposed by Barnman in 1990 [10] to increase the efficiency of multi-junction solar cells, and then MQWs structures made of various III-V materials such as InGaAs/GaAsP, GaAs/AlAsP, and InGaAsP/InP have been studied.

The strain-balanced MQWs structure is a technique of alternately stacking well-layer (large lattice constant mateiral) and barrier-layer (small lattice constant material) on a bulk matrix with ~nm scale, thereby compensate the stress comes from lattice mismatch. It is an idea to fabricate the MQWs layer without causing lattice relaxation, and application to solar cell was proposed by Ekins-Daukes [12]. The strain-balancing condition in MQWs layer is satisfied when the average lattice constant in the MQWs region, a_{ave}, is equal to the lattice constant of bulk material, a_{bulk}, as shown in eq (2.55).

$$a_{ave} = \frac{t_{well}a_{well} + t_{barrier}a_{barrier}}{t_{well} + t_{barrier}} = a_{bulk} \tag{2.55}$$

Where, t_{well} ($t_{barrier}$) is the thickness of well-layer (barrier-layer), and a_{well} ($a_{barrier}$) is the lattice constant of the well-layer (barrier-layer) material.

The typical current-voltage characteristics and quantum efficiency of solar cell with InGaAs/GaAsP MQWs with various number of QW layers is shown in fig. 2-5.

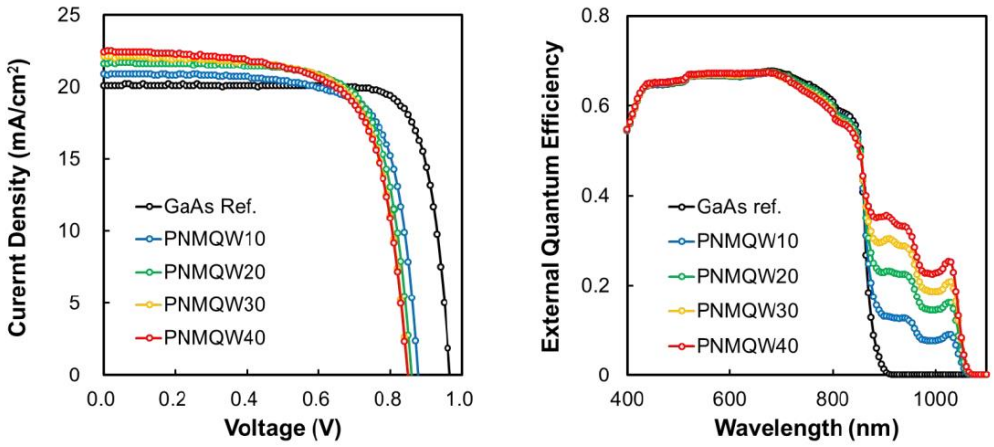

Fig. 2-5 Current-voltage curve and quantum efficiency spectra of InGaAs/GaAsP MQWs solar cells with various period numbers [13].

Spectral response of light absorption beyond the band edge of the bulk matrix material (here, the GaAs, having the light absorption edge at ~890 nm) and be obtained due to absorption of low energy photons in the MQWs layer. As the period number of MQWs increasing, J_{sc} is enhanced by the additional photocurrent , but carrier collection at forward bias that weaken the built-in potential. As a result, photocurrent decreases as the forward bias increasing, therefore the *FF* is degraded. However, it has been reported that the recombination current, caused by a high carrier concentration in a well-layer due to carrier confinement, is increased, so that the open-circuit voltage is lowered as compared with a single-junction cell of a bulk material [14]-[15]. In other hand, MQWs facilitate the radiative recombination of carriers by concentrating carriers in narrow-gap wells [16], which in turn suppresses non-radiative recombination and thus heat dissipation. In multi-junction cells, radiative recombination enhances luminescence coupling and makes a cell more tolerant against current mismatch induced by spectrum fluctuations of the solar irradiation [17].

From these reasons, the MQW is considered as a promising structure for tuning the energy bandgap of a subcell in the multi-junction solar cells and enhancing the efficiency.

In the next section, the carrier dynamics in the quantum well is discussed.

2.2.2 Band gap in quantum wells

When a material having a lattice constant different from that of the substrate is grown, the growth layer is crystal-grown while undergoing strain on the substrate. When strain-balancing MQWs is grown on the bulk material, well-layer material having a smaller lattice constant than bulk matrix is under tensile strain and barrier-layer material having large lattice constant is under compressive strain as shown in fig. 2-6.

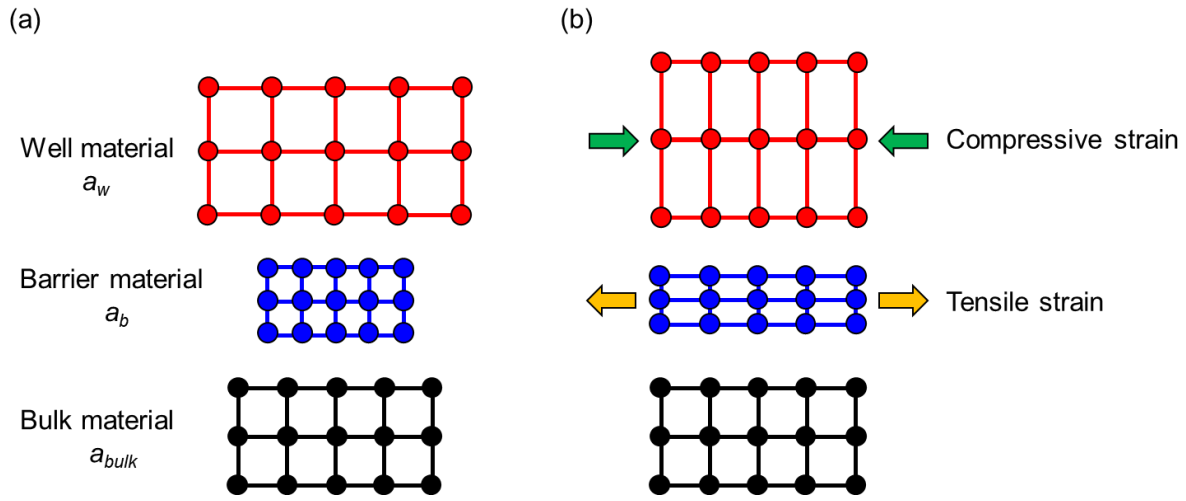

Fig. 2-6 Schematics of illustration for bulk material with two lattice mismatched materials which are for well and barrier layer. (a) is for unstrained condition and (b) is for strained situation.

The strain in the epitaxial layers, well and barrier, acts to change the crystal lattice geometry, therefore the electronic structure is also changed. In this section, the modified band gap by strain is discussed with the strain impact on the band edge profiles [9].

2.2.2.1 Strain in quantum wells

The strain tensor ϵ and the stress tensor σ are the tensor amounts which connected by Hooke's law, and can be expressed by the following equations (eq. (2.56)-(2.57)) using the elastic compliance constant S and elastic stiffness coefficient C.

$$\epsilon_{ij} = \sum_{k=1}^{3}\sum_{l=1}^{3} S_{ijkl}\sigma_{kl} \,. \tag{2.56}$$

$$\sigma_{ij} = \sum_{k=1}^{3}\sum_{l=1}^{3} C_{ijkl}\epsilon_{kl} \tag{2.57}$$

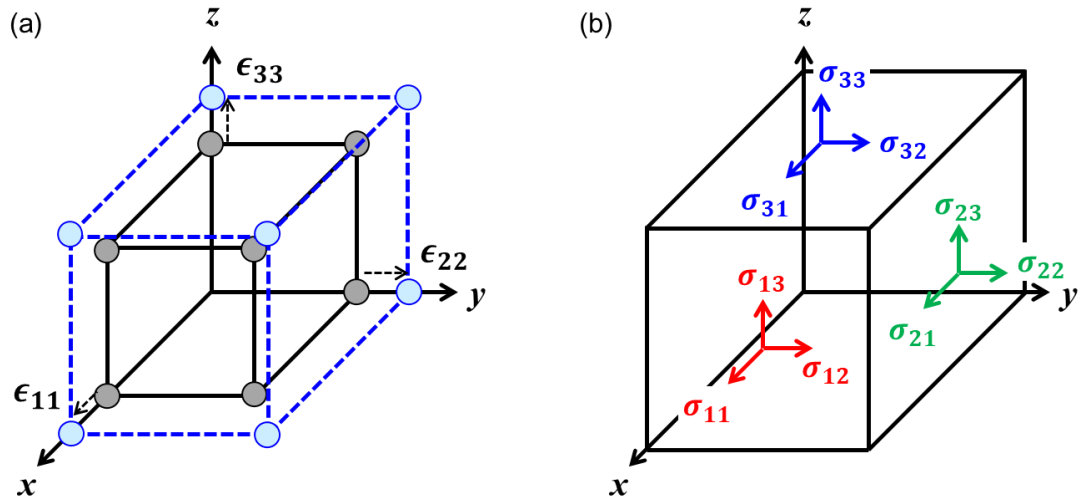

Fig. 2-7 Schematics illustration of (a) the strain components (ϵ_{11}, ϵ_{22}, ϵ_{33}), and (b) stress components σ_{ij} on the crystal.

These can be concisely represented by the following matrix notation as in eq. (2.58)-(2.59).

$$\epsilon = \begin{pmatrix} \epsilon_{11} & \epsilon_{12} & \epsilon_{13} \\ \epsilon_{21} & \epsilon_{22} & \epsilon_{23} \\ \epsilon_{31} & \epsilon_{32} & \epsilon_{33} \end{pmatrix} = \begin{pmatrix} \epsilon_1 & \frac{1}{2}\epsilon_6 & \frac{1}{2}\epsilon_5 \\ \frac{1}{2}\epsilon_6 & \epsilon_2 & \frac{1}{2}\epsilon_4 \\ \frac{1}{2}\epsilon_5 & \frac{1}{2}\epsilon_4 & \epsilon_3 \end{pmatrix} \tag{2.58}$$

$$\sigma = \begin{pmatrix} \sigma_{11} & \sigma_{12} & \sigma_{13} \\ \sigma_{21} & \sigma_{22} & \sigma_{23} \\ \sigma_{31} & \sigma_{32} & \sigma_{33} \end{pmatrix} = \begin{pmatrix} \sigma_1 & \sigma_6 & \sigma_5 \\ \sigma_6 & \sigma_2 & \sigma_4 \\ \sigma_5 & \sigma_4 & \sigma_3 \end{pmatrix} \tag{2.59}$$

The elastic stiffness coefficient C_{ij} is the (6x6) matrix that having 36 independent constants for defining elastic properties of the crystals. However, crystal lattices generally exhibit specific symmetry, reducing the number of constants needed to account for elastic behavior of the crystals. In the case of cubic crystals including diamond (Si, Ge, etc.) and zincblende crystals (GaAs, GaP, InP, etc.), the number of independent matrix components required are 3, due to its high symmetric property.

$$\begin{bmatrix}\sigma_1\\ \sigma_2\\ \sigma_3\\ \sigma_4\\ \sigma_5\\ \sigma_6\end{bmatrix}=\begin{bmatrix}C_{11} & C_{12} & C_{12} & 0 & 0 & 0\\ C_{12} & C_{11} & C_{12} & 0 & 0 & 0\\ C_{12} & C_{12} & C_{11} & 0 & 0 & 0\\ 0 & 0 & 0 & C_{44} & 0 & 0\\ 0 & 0 & 0 & 0 & C_{44} & 0\\ 0 & 0 & 0 & 0 & 0 & C_{44}\end{bmatrix}\begin{bmatrix}\epsilon_1\\ \epsilon_2\\ \epsilon_3\\ \epsilon_4\\ \epsilon_5\\ \epsilon_6\end{bmatrix} \tag{2.60}$$

Strain in very thin zinc blende crystals such as QW layer on thick bulk matrix can be described with biaxial stresses. Therefore, the stress has only two diagonal components, σ_1 and σ_2, while the *z*-direction (which is the direction of epitaxial growth) component σ_3 and other shear components are zero. The stress in the grown quantum well layer can be expressed as eq. (2.61).

$$\sigma=\begin{pmatrix}\sigma_1 & 0 & 0\\ 0 & \sigma_2 & 0\\ 0 & 0 & 0\end{pmatrix}. \tag{2.61}$$

The existence of biaxial stress results in the appearance of an in-plane strain, and such the in-plane deformation can be calculated by eq. (2.62).

$$\epsilon_{in}=\frac{a_{bulk}-a_{QW}}{a_{QW}}=\Delta a \tag{2.62}$$

Where, ϵ_{in} is the in-plane strain tensor, and a_{bulk} and a_{QW} is the lattice constant of bulk material and grown QW material. When the lattice constant of grown layer is larger than bulk material, ϵ_{in} have negative value and this represents the compressive strain, and vice versa for tensile strain.

The strain tensor ϵ_1, ϵ_2, and ϵ_3 can be obtained as eq. (2.63)-(2.64) from eq. (2.60)-(2.61).

$$\epsilon_1=\epsilon_2=\epsilon_{in} \tag{2.63}$$

$$\epsilon_3=-\nu\epsilon_1=-2\frac{C_{12}}{C_{11}}\epsilon_1 \tag{2.64}$$

There is no stress component in the *z*-direction, but the lattice constant is forced to change due to Poisson effect. Therefore, the perpendicular strain is induced due to the in-plane stress, and the ratio of lattice constant change in *z*-direction is called Poisson's ratio which is written as ν in eq. (2.64).

From above equations, the complete strain tensor matrix for quantum well can be written as eq. (2.65).

$$\epsilon=\begin{pmatrix}\epsilon_1 & 0 & 0\\ 0 & \epsilon_1 & 0\\ 0 & 0 & -2\frac{C_{12}}{C_{11}}\epsilon_1\end{pmatrix} \tag{2.65}$$

2.2.2.2 Band profiles in quantum wells

Band edge shift induced by strain can be derived by **k.p** perturbation theory using Pikus-Bir Hamiltonian [9] and model solid approximation [18]-[19]. Here, the modified band edge profile by strain is discussed with model solid method.

✓ Conduction band edge E_c

Conduction band shift ΔE_c is given by eq. (2.66) [9].

$$\Delta E_c = a_c \frac{\Delta V}{V} = a_c(\epsilon_1 + \epsilon_2 + \epsilon_3) = 2a_c\left(1 - \frac{C_{12}}{C_{11}}\right)\epsilon_1 \tag{2.66}$$

Where, a_c is the conduction band deformation potential. The band edge for conduction band can be obtained as,

$$E_c = E_{c0} + \Delta E_c\,. \tag{2.67}$$

Where, E_{c0} is the conduction band edge under unstrained condition.

✓ Valence band edge E_v

The band edge shift for three valence bands (for heavy hole band, light hole band and spin orbit splitting band) at **Γ** (**k** = 0) point respect to average of three uppermost valence bands $E_{v,av}$ is given by eq (2.68).

$$\Delta E_{v,HH} = \frac{\Delta_0}{3} - \frac{1}{2}\delta E_v$$

$$\Delta E_{v,LH} = -\frac{\Delta_0}{6} + \frac{1}{4}\delta E_v - \frac{1}{2}\sqrt{{\Delta_0}^2 + \Delta_0\delta E_v + \frac{9}{4}{\delta E_v}^2}$$

$$\Delta E_{v,SO} = -\frac{\Delta_0}{6} + \frac{1}{4}\delta E_v + \frac{1}{2}\sqrt{{\Delta_0}^2 + \Delta_0\delta E_v + \frac{9}{4}{\delta E_v}^2} \tag{2.68}$$

Where the deformation factor δE_v alone the [001] is given by eq. (2.69) with the shear deformation potential b for a tetragonal symmetry in cubic crystal.

$$\delta E_v = 2b(\epsilon_3 - \epsilon_1) = -2b\left(1 + \frac{2C_{12}}{C_{11}}\right)\epsilon_1 \tag{2.69}$$

✓ Band gap E_g in strained quantum well

The modified band gap by strain can be obtained by finding the difference between the conduction band edge and the upmost valence band edge (usually for heavy hole). The valence band edge for heavy hole $E_{v,HH}$ is given as eq. (2.70).

$$E_{v,HH} = E_{v,av} + \Delta E_{v,HH} \tag{2.70}$$

From above equations, the modified band gap can be calculated as eq. (2.71).

$$\begin{aligned} E_g &= E_c - E_v \\ &= (E_{c0} + \Delta E_c) - \left(E_{v,av} + \Delta E_{v,HH}\right) \\ &= E_{g0} + \Delta E_c - \Delta E_{v,HH} \end{aligned} \tag{2.71}$$

Where, E_{g0} is the band gap under unstrained crystal.

2.3 References

[1] Jenny Nelson, "THE PHYSICS OF SOLAR CELLS", Imperial College Press, Reprinted 2010.

[2] P. Würfel, "Physics of Solar Cells: From Basic Principles to Advanced Concepts", WILEY-VCH, 2009.

[3] P. Wurfel, "The chemical potential of radiation", *J. Phys. C* **15** (18), 3697, 1982.

[4] A. De Vos, "Endoreversible thermodynamics of solar energy conversion", Oxford University Press, 1992.

[5] W. Shockley and H. J. Queisser, “Detailed Balance Limit of Efficiency of p-n Junction Solar Cells”, *J. Appl. Phys.* **32** (3), p.510-519, 1961.

[6] T. Tiedje, E. Yablonovitch, G. D. Cody, B. G. Brooks, “Limiting Efficiency of Silicon Solar Cells”, *IEEE TRANSACTIONS ON ELECTRON DEVICES* **31** (5), p.711-716, 1984.

[7] PVEducation, [Online]. Available: https://www.pveducation.org/index.php

[8] G. L. Araujo, A. Marti, "Absolute limiting efficiencies for photovoltaic energy conversion", *SOLMAT* **33** (2), p.213-240, 1994.

[9] Paul Harrison, Alex Valavanis, "Quantum Wells, Wires and Dots", WILEY, 4th addition printed in 2016.

[10] K. W. J. Barnham, G. Duggan, ”A new approach to high-efficiency multi-band-gap solar cells”, *J. Appl. Phys.* **67** (7), p.3490-3493, 1990.

[11] N. J. Ekins-Daukes, K. W. J. Barnham, J. P. Connolly, J. S. Roberts, J. C. Clark, G. Hill, and M. Mazzer, ”Strain-balanced GaAsP/InGaAs quantum well solar cells”, *Appl. Phys. Lett* **75** (26), p.4195-4197, 1999.

[12] N. J. Ekins-Daukes, J. M. Barnes, K. W. J. Barnham, J. P. Connolly, M. Mazzer, J. C. Clark, R. Grey, G. Hill, M. A. Pate, J. S. Roberts, "Strained and strain-balanced quantum well devices for high-efficiency tandem solar cells", *SOLMAT* **68** (1), P.71-87, 2001.

[13] M. Sugiyama, Y. Wang, H. Fujii, H. Sodabanlu, K. Watanabe and Y. Nakano, "A quantum-well superlattice solar cell for enhanced current output and minimized drop in open-circuit voltage under sunlight concentration", *J. Phys. D: Appl. Phys.* **46**, 024001, 2013.

[14] N. G. Anderson and S. J. Wojtczuk, "Open-circuit voltage characteristics of InP-based quantum well solar cells", *J. Appl. Phys.* **79** (4), p.1973-1978, 1996.

[15] Y. Wang, Y. Wen, M. Sugiyama and Y. Nakano, "InGaAs/GaAsP strain-compensated superlattice solar cell for enhanced spectral response", *IEEE 35th PVSC*, Hawaii, 2010.

[16] T. Inoue, K. Toprasertpong, A. Delamarre, K. Watanabe, M. Paire, L. Lombez, J.-F. Guillemoles, M. Sugiyama, and Y. Nakan, “Quasi-Fermi level splitting evaluation based on electroluminescence analysis in multiple quantum well solar cells for investigating cell performance under concentrated light”, in *Physics, Simulation, and Photonic Engineering of Photovoltaic Devices V, SPIE Photonics West* (Feb. 13-18, 2016, San Francisco, USA), p. 974316, 2016.

[17] A. S. Brown and M. A. Green, “Radiative coupling as a means to reduce spectral mismatch in monolithic tandem solar cells tacks - Theoretical considerations”, Proc. *IEEE 29th PVSC*, p.868, 2002.

[18] C. G. Van de Walle and R. M. Martin, "Theoretical calculations of heterojunction discontinuities in the Si/Ge system", *Phys. Rev. B* **34** (8), 5621, 1986.

[19] C. G. Van de Walle, "Band lineups and deformation potentials in the model-solid theory", *Phys. Rev. B* **39** (3), 1871, 1989.

Chapter 3 Experimental equipment

3.1 Metal-organic vapor phase epitaxy (MOVPE)

Epitaxial growth, also called epitaxy, refers to the deposition of a crystal layer having the same orientation relationship over a substrate crystal [1]-[2]. Epitaxial growth is widely used not only in the production of various semiconductor devices but also in the growth of polymers, and recently is being utilized in a wide range of fields from inorganic materials to organic materials. There are several techniques for epitaxy of III-V materials: liquid phase epitaxy (LPE), vapor phase epitaxy (VPE) and molecular beam epitaxy (MBE) which are classified according to the transportation phase of precursors. VPE is also divided into metal-organic vapor phase epitaxy (MOVPE) and chloride vapor phase epitaxy (ClVPE) depending on the type of precursors. Among these techniques, MOVPE is the most promising method for industrial use for epitaxial growth of III-V materials due to its large scale reactor.

MOVPE is the epitaxial growth method in which a thin film is deposited on a substrate by introducing metal organic source gases into a crystal growth reactor. In the MOVPE, the pressure of the epitaxial growth reactor is set higher than that in the MBE chamber, and the metal organic source gases are introduced into the carrier gas (mainly hydrogen is used) flow to reach the vicinity of the substrate. The precursor molecules are decomposed by chemical reaction in the gas flow region or on the surface of the substrate and attached on the crystal as an atom which is composing epitaxial layer. In this research, a horizontal reactor (AIX200/4, AIXTRON) is used as shown in fig. 3-1.

The liquid state metal organic sources are kept in bubblers, and gas state sources at the saturated vapor pressure are extracted by bubbling with high purity hydrogen carrier gas. The saturated vapor pressure p (Torr) is dependent on the holding temperature, following the Antoine eq. (equation 3.1).

$$\log_{10} p = A - \frac{B}{C + T} \tag{3.1}$$

Where, T (K) is bubbler temperature and A, B and C are Antoine constants. For simplicity, C is set to zero.

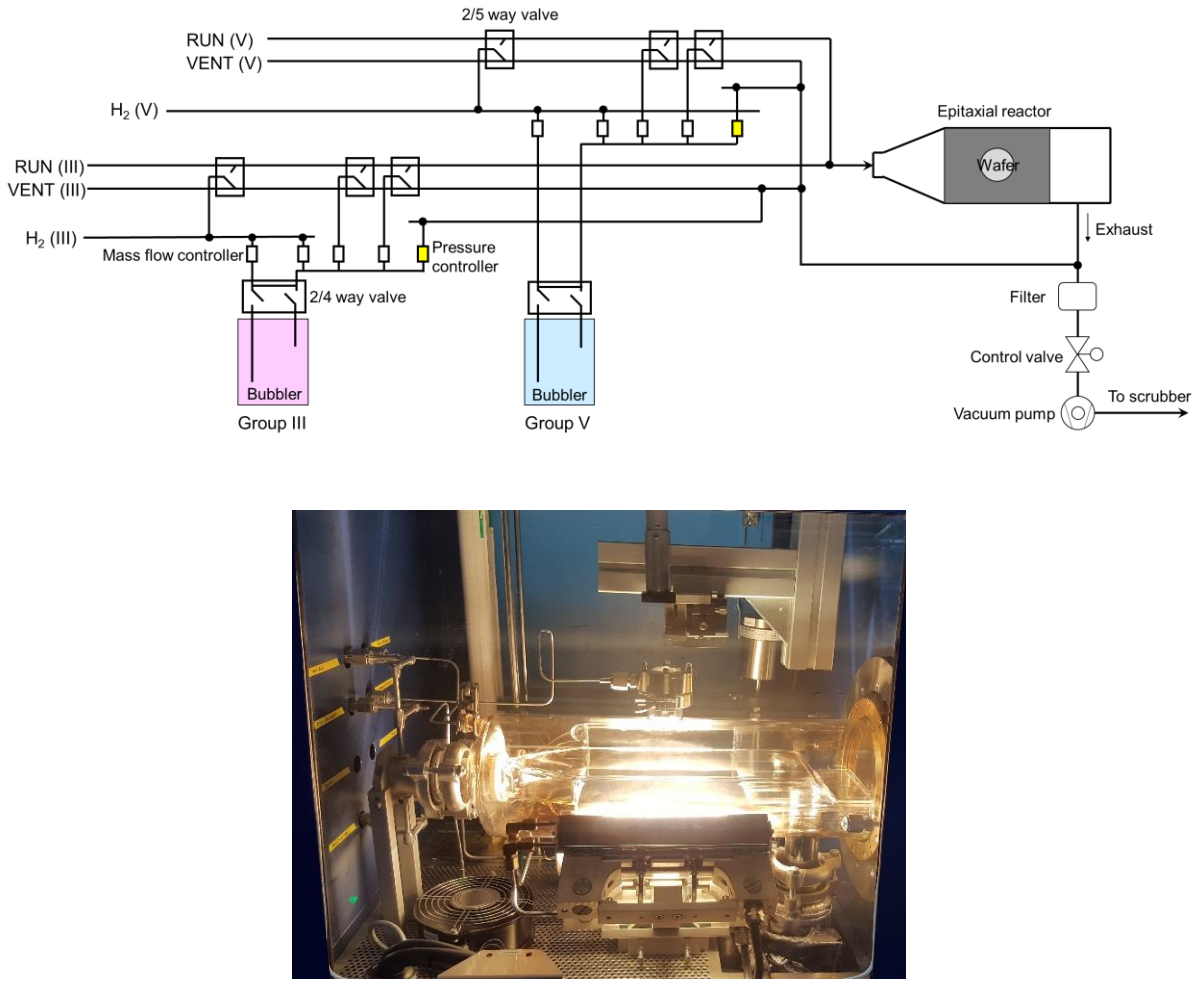

Fig. 3-1 A schematic of MOVPE system and a picture of MOVPE reactor (AIX200/4, AIXTRON) used in this research.

Tertiary-butyl arsine (TBA: $(CH_3)_3CAsH_2$), tertiary-butyl phosphine (TBP: $(CH_3)_3CPH_2$), and trimethyl gallium (TMGa: $(CH_3)_3Ga$) are used as a precursor of group-V and group-III (fig. 3-2) and hydrogen gas is used for carrier gas in this study. The Antoine parameters A, B and melting points T_M, boiling points T_B, holding temperatures ($T_{bubbler}$) and pressures ($P_{bubbler}$) of each bubbler are listed in the table 3.1 (ref. [3]).

Table 3.1 Properties of metal organic precursors used in this research.

Source	A	B	T_M (°C)	T_B (°C)	$T_{bubbler}$ (°C)	$P_{bubbler}$ (mbar)
TMGa	8.07	1703	-15.8	55.8	17	1000
TBA	7.243	1509	-1	69	17	1000
TBP	7.586	1539	4	56.1	17	1000

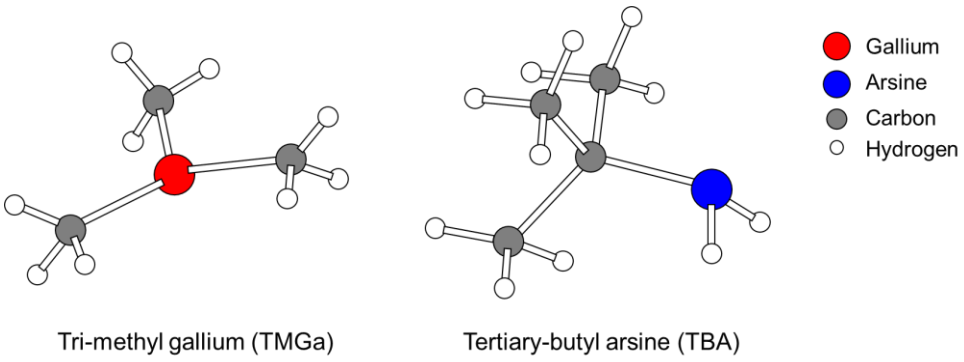

Fig. 3-2 Schematic diagrams of precursor molecules for TMGa and TBA

Sources extracted from bubblers are diluted by carrier gas, and then either injected to the epitaxial reactor through the run-line or discarded to vent-line. When the precursor inject line is opened and closed, dummy H_2 line is simultaneously closed and opened for suppressing the effect of gas flow rate changing during the growth which can cause laminar flow in the reactor. The mass flow controller and pneumatic valves control the gas flow in MOVPE system.

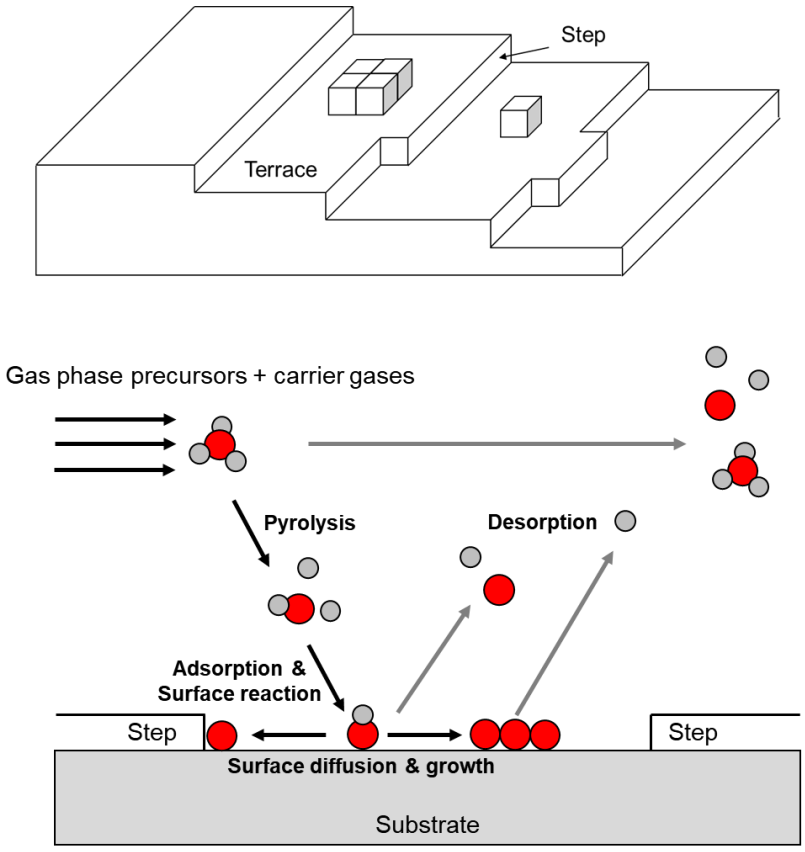

Fig. 3-3 A schematic of crystal growth dynamics in MOVPE.

The schematic of epitaxial growth dynamics in MOVPE is shown in fig. 3-3. In the MOVPE technique, the pressure of the reactor is set higher than MBE, and the gas phase precursors are introduced to the reactor mixed in the carrier gases. The gas flow rate in the reactor gradually increases from the completely stopped state on the substrate surface toward the main gas flow. The region where this flow velocity changes is called boundary layer. Since precursor molecules are consumed in the vicinity of the substrate, the source molecules diffuse through the boundary layer using the difference in concentration between the main flow and the substrate surface as a driving force. The precursors themselves and radicals generated by pyrolysis reach the substrate surface and adsorb. Thereafter, the diffuses on the substrate surface, and the radicals are decomposed at the step edge and the periphery of the island-like growth part which are rich in reactivity , and as a result, the crystal enters the crystal lattice position and the crystal grows. Among the radicals that have reached the surface, desorption may occur in the unreacted state even if it reaches the crystal. These reactions competitively occur in MOVPE growth.

3.2 Reflectance anisotropic spectroscopy (RAS)

3.2.1 Surface anisotropy and RAS

In MOVPE environment, hydrogen gas is flowing during the process as a carrier gas. Therefore, in-situ measurement such as XPS, LEED and STM for observing the surface states at ultra-high vacuum condition is not available. Reflectance anisotropy spectroscopy (RAS), however, is not required a vacuum state during the measurement, so it is considered as a in-situ measurement method for MOVPE process.

RAS is the optical measurement technique for the difference in reflectance of two beams of light that are shone in normal incident on a surface with different linear polarizations [4] as in eq. (3.2). It is also known as reflectance difference spectroscopy (RDS) [5]. The method was first introduced in 1985 for studying optical properties of the cubic semiconductors, silicon and germanium [6].

$$\frac{\Delta r}{r} = Re\left(\frac{\Delta r}{r}\right) + Im\left(\frac{\Delta r}{r}\right) = 2\frac{r_{[0\bar{1}1]} - r_{[011]}}{r_{[0\bar{1}1]} + r_{[011]}} \tag{3.2}$$

For a cubic crystal, the bulk is usually isotropic and the reflectance does not have polarization dependence. At the surface, however, there are a lot of dangling bonds and thus the atomic arrangement can be arranged as anisotropic, and it can be detected by the in-situ RAS measurement. The RAS is sensitive to surface of the cubic crystal, so it is used to analysis for the crystal surface study especially in surface recombination [6]-[15].

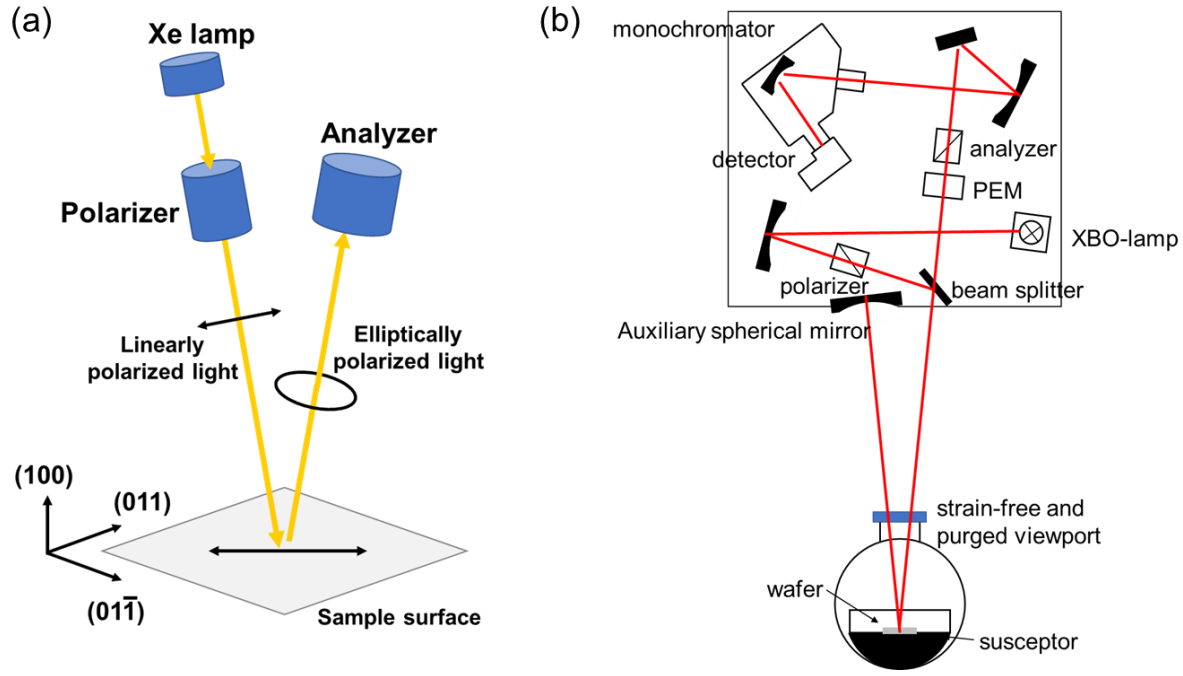

Fig. 3-4 RAS setup used in this research: (a) polarization of the light toward the sample, and (b) RAS system (EpiR-M TT, Laytec)

In this research, RAS system (EpiR-M TT, Laytec) is used as in-situ measurement for surface states of GaP/Si as well as Si(1 0 0) during MOVPE process as shown in fig. 3-4 (b). The incident light is perpendicular to the wafer surface and allows measurement of the surface reflectance for photon energies between 1.5 eV and 4.5 eV.

3.2.2 RAS of Si(1 0 0) surfaces

The surface morphology including not only the roughness but also the step structure, of the Si(1 0 0) substrate affects on the subsequent III-V material growth. The Si atoms on the (1 0 0) surface have two dangling bonds, and the surface atoms are re-arranged for reducing the number of dangling bonds on the surface [16], so reducing the surface energy [17]-[18].

In the MOVPE reactor, Since the hydrogen is always flowing in the MOVPE reactor during the growth, the chemical potential of hydrogen plays an important role in surface reconstruction process [18]-[23]. The monohydride-terminated Si dimer, which is a symmetrical structure in which each Si atom is bonded to one hydrogen atom, can be formed through thermal annealing under H_2 ambience. This process is depending on

the adsorption and desorption rates of the hydrogen atoms and the partial pressure of H_2 and temperature [19]-[23].

Figure 3-5 depicts different monohydride-terminated Si(1 0 0) surfaces, which differ in dimer orientation with reference to the step edges.

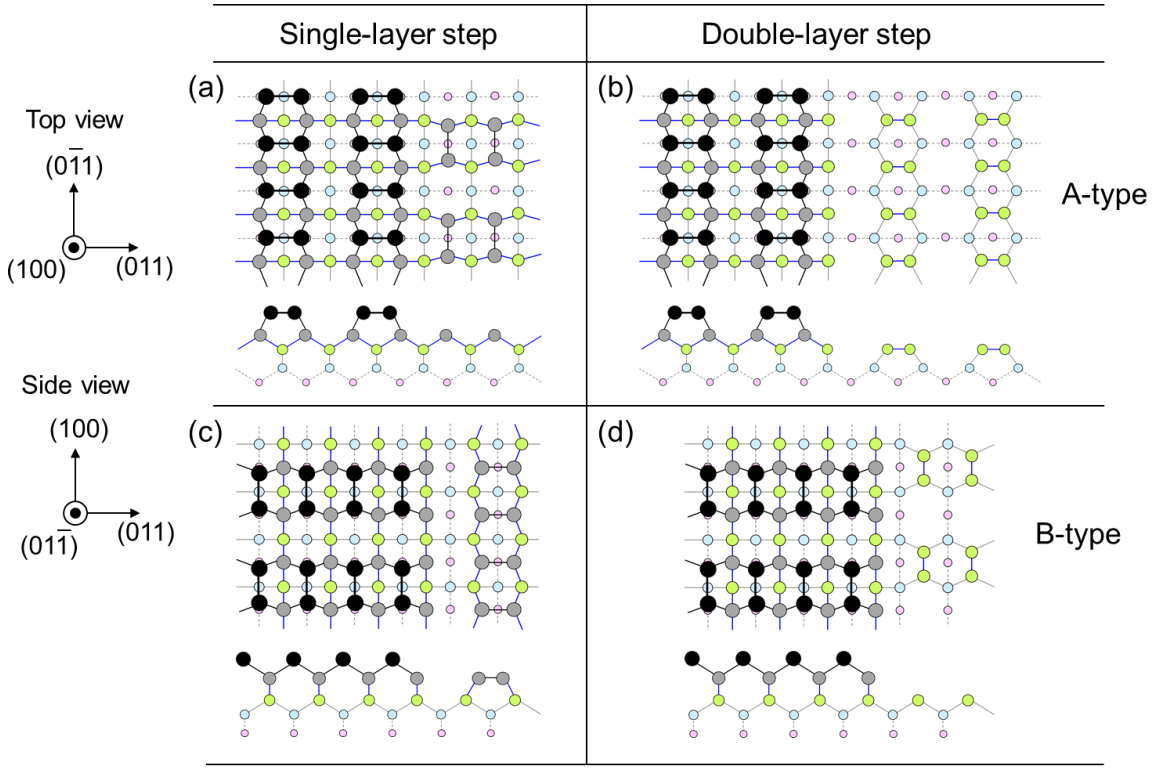

Fig. 3-5 Surface states of Si(1 0 0): top view and side view of (a), (c) single layer-step, (b) A-type double-layer step and (d) B-type double-layer step surfaces.

The surface with Si dimers whose dimer direction is formed in the perpendicular to the step edge is generally referred to as A-type surface as shown in fig 3-5 (a),(b). The B-type surface as shown in fig. 3-5 (c),(d) refers that the dimer direction on the surface is formed in parallel direction to step edge. In the case of single-layer step surface as shown in fig. 3-5 (a) and (c), both of A- and B-type surface exist, and these surfaces are called mixed surface in this study. For double-layer step surface depicted in fig. 3-5 (b) and (d), the dimer direction is arranged in one direction, that is, the anisotropy of the surface becomes maximum in these cases.

The RA signal reflects surface anisotropy, therefore the intensity of the RA signal increases as the surface is in a double-layer step state. The example of RA spectra for Si surfaces is shown in fig. 3-6.

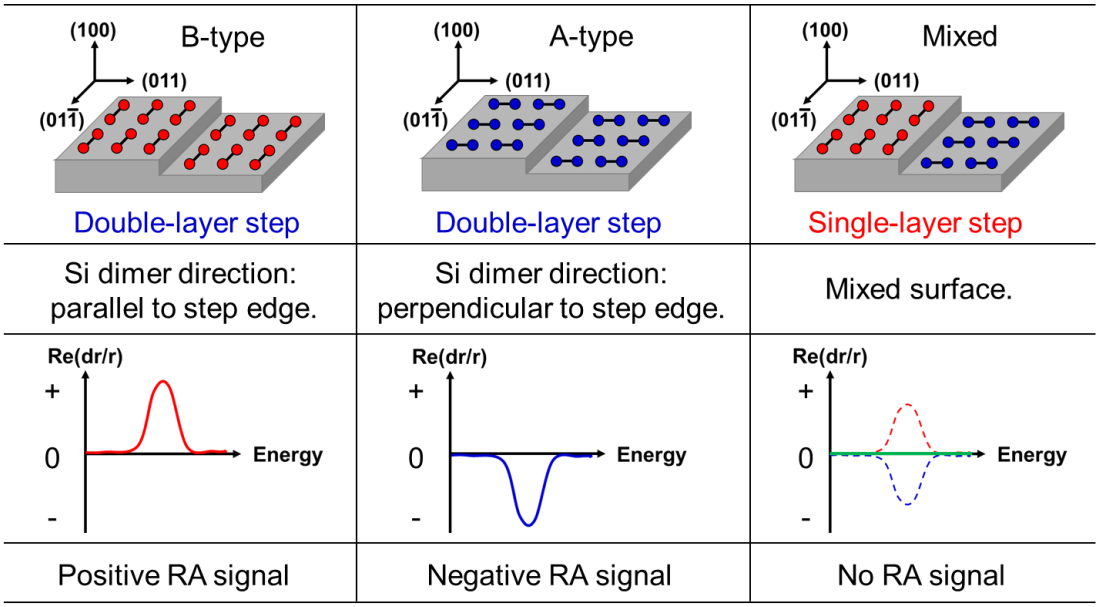

Fig. 3-6 Examples of RA spectra for Si surfaces: RA peak is appeared when the double-layer steps are formed on the surface.

Normalization factor in this research

The RA intensity is affected by lamp's emission and distortion of mirror or other misalignment of the system. Therefore, the RA intensity shows different value in difference measurement systems. In this research, in all the RA intensity is discussed with normalized value. The scaling factor is driven by comparing of the measurement of oxidized Si(1 1 0) surface reported in ref. [6].

3.3 Low energy electron diffraction (LEED)

Low Energy Electron Diffraction (LEED) is an analytical method of diffraction phenomenon of electrons with low energy of several hundred eV or less (20-200 eV) or material structure using it, and is most common in the study of the structure of single crystal surface [27]. In the LEED apparatus, an electron beam generated from an electron gun is irradiated perpendicularly to a sample and an interference pattern of electrons backscattered from the sample is detected by a hemispherical fluorescent screen installed on the same side as the electron gun It is structured. A schematic diagram of the device is shown in fig. 3-7.

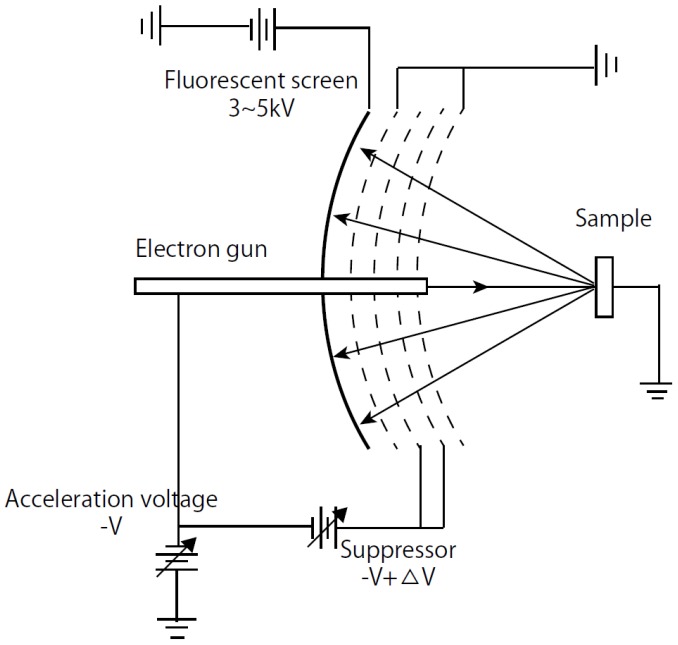

Fig. 3-7 A schematic of LEED system.

It is the basic principle of LEED to investigate the crystal structure of a substance by observing the diffraction caused by electron scattering from the crystal lattice of the sample. The wave length of low energetic electron can be expressed as eq. (3.3) from de Broglie's matter wave.

$$\lambda = \frac{h}{p} = \frac{h}{\sqrt{2meV}} \simeq \sqrt{\frac{150.412}{V\ [eV]}}\ [\text{Å}] \tag{3.3}$$

Where λ is the wavelength of electrons, h is Planck's constant, p is the momentum of electrons, m is the mass of electrons, e is the elementary charge, and V is the acceleration voltage of the electron beam. It is understood that the electron beam accelerated at 20 to 200 eV has a wavelength of about 0.87 - 2.74 Å. Since electrons with low energy can penetrate only a few atomic layers in a crystal, the perpendicular direction to the surface of the crystal can be neglected, and only the surface atoms are handled as a two-dimensional lattice.

The main reason for the high surface sensitivity of LEED is that the interaction between crystal and electrons is strong for low energy electrons. When the electrons penetrating the crystal, the primary electrons lose kinetic energy due to inelastic scattering processes such as plasmon and phonon excitation as well as electron-electron interaction. If the detailed properties of the inelastic process are not important, they are

generally treated assuming an exponential attenuation of the primary electron beam intensity I_0 in the propagation direction as expressed in eq. (3.4).

$$I(d) = I_0 \times e^{-d/\Lambda(E)} \tag{3.4}$$

Where d is the penetration depth and $\Lambda(E)$ is the inelastic mean free path (IMFP), defined as the distance an electron can travel before its intensity has decreased by the factor e^{-1}. The inelastic scattering process and the electron mean free path depend on the energy of the electrons but are relatively independent of the material. The mean free path is 5-10 Å in the energy range of electrons 20-200 eV [28].

In order to keep the sample clean and free from absorbing unwanted contaminants, LEED measurement is performed in an ultra-high vacuum (UHV) environment chamber (< 10^{-9} mbar).

Reciprocal space

Since the observation target of LEED is reciprocal space information of the crystal surface, in order to obtain information on the crystal structure of the sample from LEED, it is necessary to understand the relation between the reciprocal space and the real space.

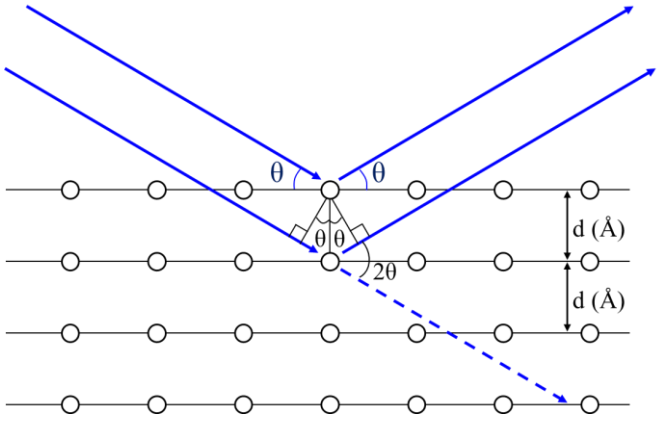

Fig. 3-8 A schematic representation of Bragg's Law.

As shown in fig. 3-8, when a wave of wavelength λ incident to the crystal surface of interplanar lattice spacing d at an angle of θ, if the optical path difference satisfies the condition of Bragg's reflection (eq. (3.5)), strong scattering is occurred due to diffraction interference.

$$n\lambda = 2d \sin\theta \tag{3.5}$$

When the plane wave is incident on the sample surface and is uni-scattered from it, its path can be described as fig. 3-9.

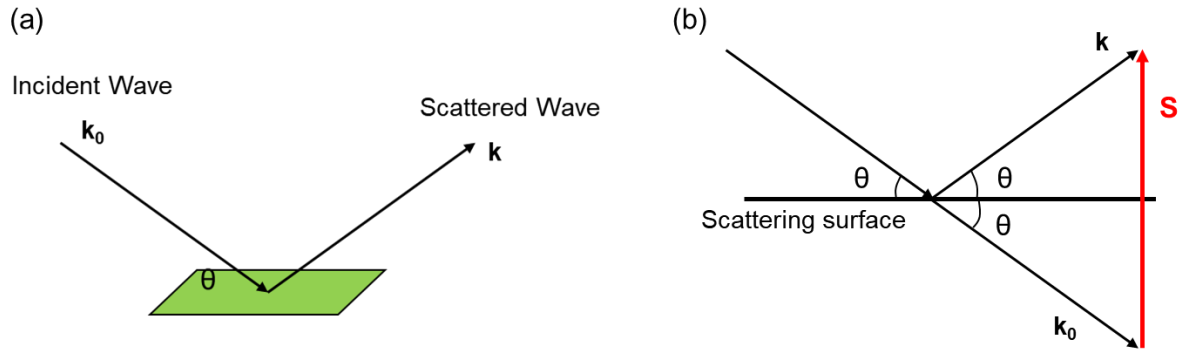

Fig. 3-9 Schematics of scattering vector, incident wave and scattered wave.

Where, **S** is the scattering vector defined by the wave vector of the incident wave and the scattered wave. When a plane wave traveling in the $\boldsymbol{k_0}$ direction is incident on the scattering source, the magnitude of $\boldsymbol{k_0}$ is,

$$|\boldsymbol{k_0}| = \frac{2\pi}{\lambda}. \tag{3.6}$$

Ewald construction is usually used for visually determining the scattering vector $\boldsymbol{S}$.

When considering a scattering surface such that incidence angle and reflection angle are same, $\boldsymbol{S}$ is obtained by eq. (3.7).

$$|\boldsymbol{S}| = 2|\boldsymbol{k}| \sin\theta = \frac{4\pi}{\lambda}\sin\theta = \frac{2\pi}{d}n \tag{3.7}$$

The $\boldsymbol{S}$ is 2π times the reciprocal of the lattice plane distance d, and the direction is perpendicular to the plane of the real space. That is, if the reciprocal lattice point is on the Ewald sphere, it means that the reciprocal lattice vector and the scattering vector coincide.

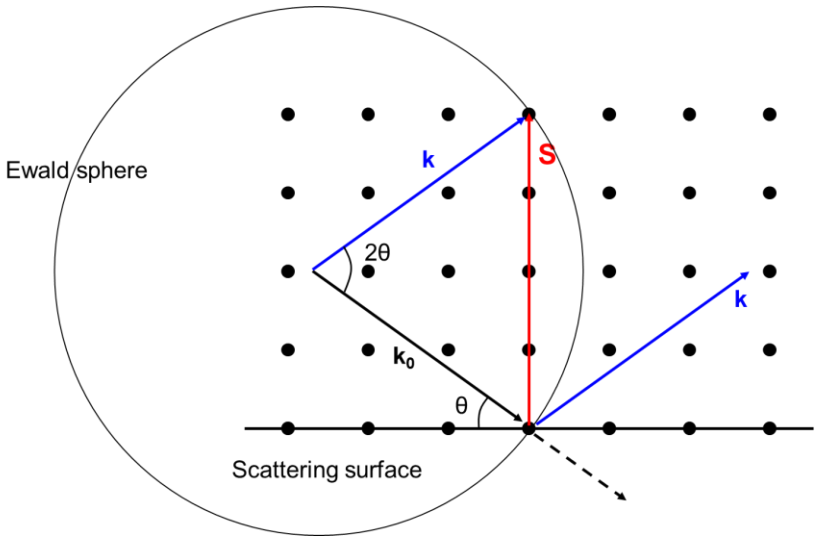

Fig. 3-10 A schematic of Ewald construction.

Since the hemispherical fluorescent screen used in LEED can be said to be an enlarged Ewald sphere, the pattern of the reciprocal lattice of the two-dimensional lattice of the crystal surface is observed on the screen.

3.4 X-ray photoelectron spectroscopy (XPS)

When a substance such absorbs an electromagnetic wave having a wavelength shorter than a specific wavelength (and therefore has a high energy), the phenomenon of emitting electrons is called a photoelectric effect, and the electrons emitted at this time are called photoelectrons. Photoemission Spectroscopy (PES) is a method of measuring the energy of photoelectrons emitted outside a sample (solid or gas) with a certain energy by utilizing a photoelectric effect, and analyzing the electronic state of the sample. There are X-ray Photoemission Spectroscopy (XPS) using X-rays and ultraviolet photoemission spectroscopy (UPS) using ultraviolet rays according to the irradiation light source in the PES. XPS is used to observe the electron state of core level and UPS to investigate the electron state in the valence band. In this research, XPS was used for analyzing surface chemical composition of the Si samples.

XPS also known as electron spectroscopy for chemical analysis (ESCA) enables observation of chemical compositions on the surfaces [29]-[31]. XPS is a surface-sensitive quantitative spectroscopic technique that measures the elemental composition on the surface. The XPS spectrum is obtained by simultaneously measuring the kinetic energy and the number of electrons from the sample surface (0 to several tens of nm on the top) while X-ray beam is irradiated on the sample. In order to keep the sample

clean and free from absorbing unwanted contaminants, XPS measurement requires HV (~ 10^{-8} mbar) or UHV (< 10^{-9} mbar) conditions.

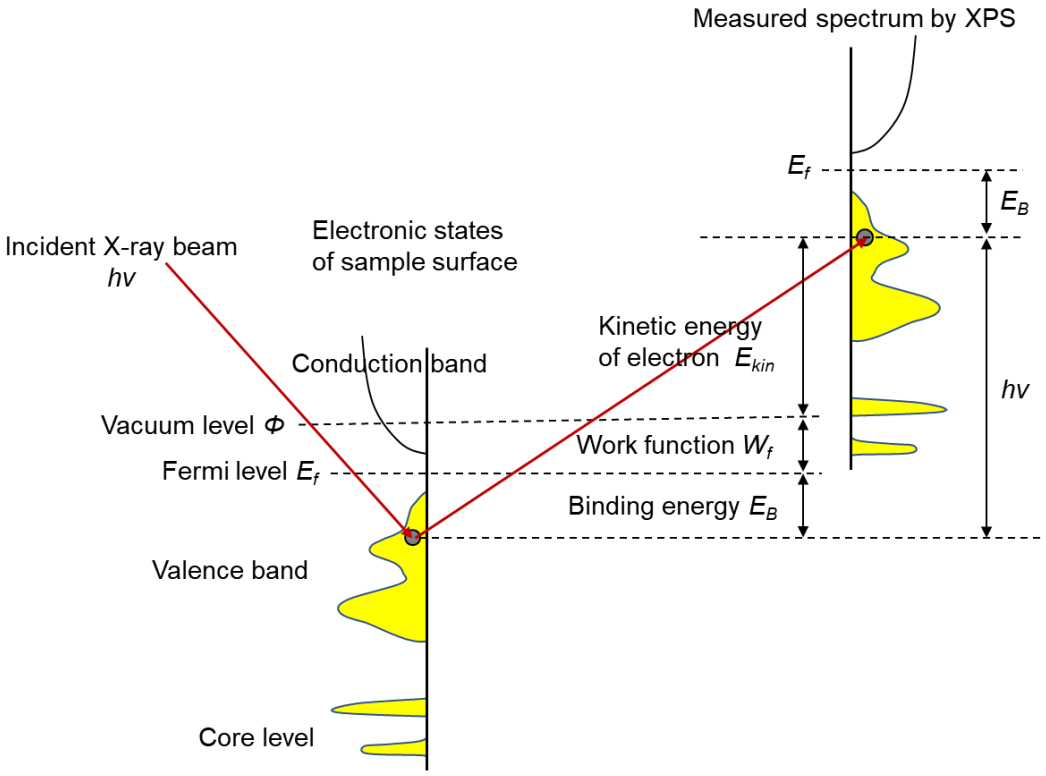

Fig. 3-11 Principle of photoelectron spectroscopy.

By the energy of incident X-ray beam and the kinetic energy of emitted photoelectrons, it is possible to investigate the electronic state in the solid as shown in fig. 3-11. When X-ray beam is incident on a solid surface, electrons having binding energy in the substance lose energy by the binding energy and work function from the energy received from the incident photon and are emitted from the solid surface (eq. (3.8)).

$$E_{kin} = hv - W_f - E_B \tag{3.8}$$

Where, E_B is the binding energy of the electron, hv is the energy of the X-ray photons being used, E_{kin} is the kinetic energy of the electron as measured by the instrument and W_f is the work function dependent on both the spectrometer and the material.

Because the energy of an X-ray beam and the wavelength are known (in this research, monochromatic Al K_α X-ray, hv = 1486.7 eV was used), and because the kinetic energies of emitted electrons are measured, the electron binding energy of each emitted electrons can be determined based on the work of Ernest

Rutherford (1914). This equation is a conservation of energy equation. The work function term is an adjustable instrumental correction factor that accounts for the few eV of kinetic energy given up by the photoelectron as it becomes absorbed by the detector, but it is a constant that rarely needs to be adjusted in practice.

3.5 Atomic force microscopy (AFM)

Atomic force microscopy (AFM) also called as force microscopy (SFM) is a one of the scanning prove microscopy (SPM) most widely used, which has a high resolution on the order of fractions of a nm.

The surface morphology by the AFM is obtained a 3-dimensional image by recording the change in the force using the contact force between the sample and the probe using a probe mounted on the AFM, rather than forming the image using a lens. AFM can be operated in vacuum, air and solution, unlike the case of STM, so its application range is wide. A schematic of principle for AFM is shown in fig. 3-12.

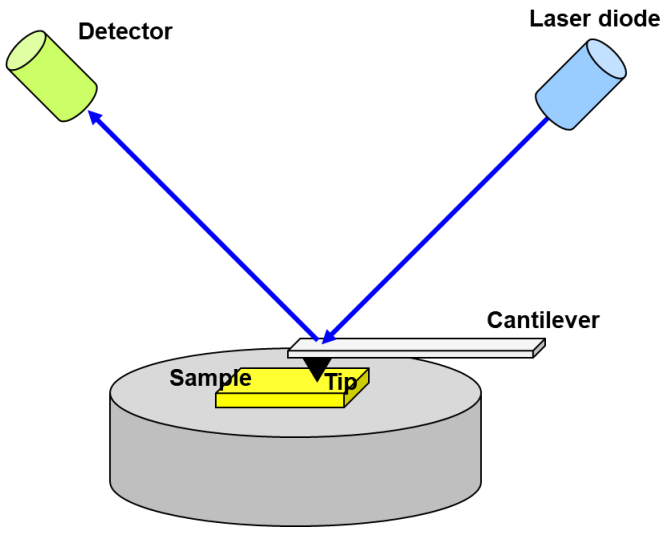

Fig. 3-12 A schematic of AFM measurement on the sample surface.

AFM uses a small rod called cantilever, which is made of micromachining instead of tungsten needles. By utilizing the interaction forces between atoms, both conductors and non-conductors can be observed, regardless of the electrical properties of the sample.

When the probe approaches to the sample surface, an interaction force is generated between the atoms at the tip of the probe and the atoms on the surface of the sample, and the sample results in deformation of the cantilever according to the law of the hook [32]. At this time, the angle of reflection of the laser beam on

the cantilever surface is measured by Photodiode to find out the surface curvature.

There are two types of measurement categorized into contact mode and non-contact mode.

✓ Contact mode

The AFM of the contact mode uses the repulsive force, and the distance and the force (1 ~ 10nN) are very fine. This force causes the probe bending and its degree of deformation is measured by reflecting the laser onto the probe and detecting it using a photodiode.

✓ Non-contact mode

Non-contact mode AFM is a method suitable for measuring materials that are susceptible to scratches due to their low force (0.01 to 0.1nN) as low as 1/100 of contact mode. In the non-contact mode, when the probe is forced to vibrate near the natural frequency and then brought close to the surface of the material, this natural frequency changes due to the influence of the force, and the change in amplitude and phase caused by the vibration is measured.

3.6 X-ray diffraction (XRD)

The incident x-ray vibrates the atoms in crystal, and some of x-ray diffracted, and their diffraction angles and intensities reflect the inherent material properties. By using this x-ray diffraction, information relating to the components and thickness of the crystalline material contained in the sample can be obtained. This analytical method for obtaining information on the structure of the crystalline material is x-ray diffraction (XRD).

✓ Principle of x-ray diffraction

If the sample has a lattice structure with an atomic spacing d as shown in fig. 3-13(b), when an x-ray having a wavelength λ is irradiated with an incident angle θ, the x-ray is scattered in all directions by the atom. When the light path difference of the scattered x-ray is an integer multiple of the wavelength of the incident x-ray, it is strengthened by the coherent effect. This phenomenon is referred to as a "diffraction", and the x-ray thus generated is referred to as a diffraction x-ray. The relationship between the wavelength of the incident x-ray and the incident angle and the lattice plane spacing is following the Bragg's law as described in eq. (3.5). From the Bragg's law, when the x-ray incident angle θ is determined, the lattice spacing d can be obtained.

✓ XRD measurement

A schematic of typical diffractometer for XRD measurement is shown in fig. 3-13(a). For XRD, the

angle 2θ, which reflects the geometry of the measurement system, is used rather than θ, which is the angle between the incident x-ray and the sample surface. When the intensity of the diffracted x-ray is recorded while changing the angle of the incident x-ray continuously, a plurality of diffraction peaks having different intensities appear, and a specific diffraction pattern can be obtained therefrom. The crystal structure of the crystalline material atoms differs depending on the material, and therefore the diffraction pattern can be regarded as a material-specific property.

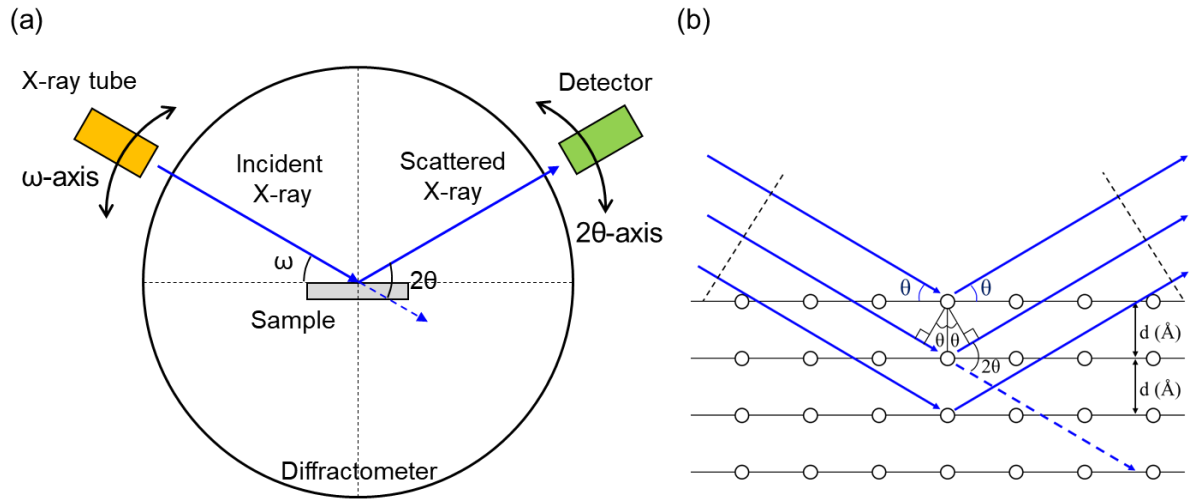

Fig. 3-13 (a) A schematic of typical diffractometer for XRD measurement, and (b) principle of X-ray diffraction by crystal with lattice plane distance of d.

The XRD diffractometer consists of an x-ray generator, a goniometer, which is an angle 2θ detector, a detector that measures diffracted x-rays, and control arithmetic units. The measurement methods are as below. In the XRD measurement system, rotate the sample to scan the ω-axis, since the x-ray tube is always fixed in all measurements.

→ ω-2θ scan: the most commonly used axis, rotate the sample (ω) and the detector (2θ).

→ 2θ scan: sample is fixed (fixed ω), and only rotate the detector (2θ). It is used to increase the amount of incident x-ray to the sample when measuring thin film, but the information about the direction is not obtained.

→ ω scan: detector is fixed (fixed 2θ), and only rotate the sample (ω).

3.7 References

[1] L. Royer, "Recherches experimentales sur l'epitaxie ou orientation mutuelle de cristaux d'especes differentes", Bull. Soc. Franc. Min. 51, p.7-154, 1928.

[2] 中嶋一雄：エピタキシャル成長のメカニズム（編集），共立出版， 2002.

[3] G. B. Stringfellow, "Organometallic Vapor-Phase Epitaxy - Theory and Practice", Academic Press, 2nd edition in 1999.

[4] Peter Y. Yu and Manuel Cardona, "Fundamentals of Semiconductors", Springer, 2005.

[5] P. Weightman, D. S. Martin, R. J. Cole, T. Farrell, "Reflection anisotropy spectroscopy", Reports on Progress in Physics 68 (6), 1251, 2005.

[6] D. E. Aspnes and A. A. Studna, "Anisotropies in the Above-Band-Gap Optical Spectra of Cubic Semiconductors", Phys. Rev. Lett. 54 (17), p.1956-1959, 1985.

[7] D. E. Aspnes, J. P. Harbison, A. A. Studna, and L. T. Florez, “Application of reflectance difference spectroscopy to molecular-beam epitaxy growth of GaAs and AlAs”, J. Vac. Sci. Technol. A 6, p.1327-1332, 1988.

[8] I. Kamiya, D. E. Aspnes, H. Tanaka, L. T. Florez, J. P. Harbison, and R. Bhat, “Surface science at atmospheric pressure: Reconstructions on (001) GaAs in organometallic chemical vapor deposition”, Phys. Rev. Lett. 68 (5), p.627–630, 1992.

[9] W. G. Schmidt, N. Esser, A. M. Frisch, P. Vogt, J. Bernholc, F. Bechstedt, M. Zorn, Th. Hannappel, S. Visbeck, F. Willig, and W. Richter, “Understanding reflectance anisotropy: Surface-state signatures and bulk-related features in the optical spectrum of InP(001)(2x4)”, Phys. Rev. B 61 (24), p.R16335(R), 2000.

[10] Y. C. Chang and D. E. Aspnes, "Theory of dielectric-function anisotropies of (001) GaAs (2×1) surfaces", Phys. Rev. B 41 (17), p.12002, 1990.

[11] D. E. Aspnes, Y. C. Chang, A. A. Studna, L. T. Florez, H. H. Farrell, and J. P. Harbison, "Direct optical measurement of surface dielectric responses: Interrupted growth on (001) GaAs", Phys. Rev. Lett. 64 (2), p.192, 1990.

[12] A. B. Muller, F. Reinhardt, U. Resch, W. Richter, K. C. Rose, U. Rossow, "Hydrogen-terminated Si(100) surfaces investigated by reflectance anisotropy spectroscopy", Thin Solid Films 233 (1-2), p.19-23, 1993.

[13] L. Kipp, D. K. Biegelsen, J. E. Northrup, L.-E. Swartz, and R. D. Bringans, "Reflectance Difference Spectroscopy: Experiment and Theory for the Model System Si(001):As and Application to Si(001)", Phys. Rev. Lett. 76, p.2810, 1996.

[14] O. Supplie, S. Bruckner, O. Romanyuk, H. Doscher, C. Hohn, M. M. May, P. Kleinschmidt, F. Grosse, and T. Hannappel, "Atomic scale analysis of the GaP/Si(100) heterointerface by in situ reflection anisotropy spectroscopy and ab initio density functional theory", Phys. Rev. B 90, 235301, 2014.

[15] A. Paszuk, O. Supplie, B. Kim, S. Bruckner, M. Nandy, A. Heinisch, P. Kleinschmidt, Y. Nakano, M. Sugiyama, T. Hannappel, "GaAsP/Si tandem solar cells: In situ study on GaP/Si:As virtual substrate preparation", SOLMAT 180, p.343-349, 2018.

[16] R. E. Schlier and H. E. Farnsworth, "Structure and Adsorption Characteristics of Clean Surfaces of Germanium and Silicon", J. Chem. Phys. 30 (4), p.917, 1959.

[17] R. M. Tromp, R. J. Hamers, and J. E. Demuth, "Si(001) Dimer Structure Observed with Scanning Tunneling Microscopy", Phys. Rev. Lett. 55 (12), p.1303, 1985.

[18] Robert A. Wolkow, "Direct observation of an increase in buckled dimers on Si(001) at low temperature", Phys. Rev. Lett. 68 (17), p.2636, 1992.

[19] T. Aoyama, K. Goto, T. Yamazaki, and T. Ito, "Silicon (001) surface after annealing in hydrogen ambient", Journal of Vacuum Science & Technology A 14, p.2909, 1996.

[20] H. Bender, S. Verhaverbeke, M. Caymax, O. Vatel, and M. M. Heyns, "Surface reconstruction of hydrogen annealed (100) silicon", J. Appl. Phys. 75 (2), 1207, 1994.

[21] John J. Boland, "Structure of the H-saturated Si(100) surface", Phys. Rev. Lett. 65 (26), 3325, 1990.

[22] Y. J. Chabal and K. Raghavachari, "Surface Infrared Study of Si(100)-(2×1)H", Phys. Rev. Lett. 53 (3), 282, 1984.

[23] T. Komeda and Y. Kumagai, "Si(001) surface variation with annealing in ambient H2", Phys. Rev. B 58 (3), 1385, 1998.

[24] L. Toben, T. Hannappel, K. Moller, H. J. Crawack, C. Pettenkofer, F. Willig, "RDS, LEED and STM of the P-rich and Ga-rich surfaces of GaP(1 0 0)", Surface Science 494 (1), p.755-760, 2001.

[25] N. Esser, W. G. Schmidt, J. Bernholc, A. M. Frisch, P. Vogt, M. Zorn, M. Pristovsek, W. Richter, F. Bechstedt, T. Hannappel and S. Visbeck, "GaP(001) and InP(001): Reflectance anisotropy and

surface geometry", J. Vac. Sci. Technol. B 17 (4), p.1691-1696, 1999.

[26] H. Doscher and T. Hannappel, "In situ reflection anisotropy spectroscopy analysis of heteroepitaxial GaP films grown on Si(100)", J. Appl. Phys. 107, 123523, 2010.

[27] K. Oura, V. G. Lifshifts, A. A. Saranin, A. V. Zotov, M. Katayama, "Surface Science", Springer-Verlag, Berlin Heidelberg New York. p. 1–45, 2003.

[28] M. A. Van Hove, W. H. Weinberg, C. M. Chan, "Low-Energy Electron Diffraction", Springer-Verlag, Berlin Heidelberg New York, 1986.

[29] K. Siegbahn, K. Edvarson, "β-ray spectroscopy in the precision range of 1 : 105", Nuclear Physics 1 (3), p.137-159, 1956.

[30] C. Nordling, S. Hagstrom and K. Siegbahn, "Application of Electron Spectroscopy to Chemical Analysis", Zeitschrift fur Physik 178 (5), p. 433–438, 1964.

[31] Ha. Siegbahn, "Electron Spectroscopy for Chemical Analysis of Liquids and Solutions", J. Phys. Chem. 89, p.897-909, 1985.

[32] B. Cappella, G. Dietler, "Force-distance curves by atomic force microscopy", Surface Science Reports 34 (1-3), p. 1-104, 1999.

Chapter 4 Device design of MQW based GaAsP/Si tandem solar cell

III-V top absorber integrated on active Si substrate is a promising structure for realizing high energy conversion efficiency solar cells with low production cost. However, there are still remaining challenges to integrate III-V material on Si substrate by epitaxial growth due to its differences of material properties such as lattice constant, thermal expansion coefficient and polarization. To suppress the cell performance degradation, the threading dislocation density (TDD) has to be lower than 10^6 cm^{-2} in the epitaxial layer for top absorber [1]-[4].

In this research, $GaAs_{0.5}P_{0.5}$ matrix top subcell with multi-quantum well (MQW) layers is proposed as a new approach for mitigating the stress for heteroepitaxial growth on Si(1 0 0) surfaces and extending the photon absorption range. In addition, the concept of effective mobility [5] is introduced for representing carrier dynamics in the quantum well layer, and the realistic efficiency of GaAsP/Si tandem solar cell is calculated with effective mobility and carrier collection model [6] in the MQWs layer.

4.1 Concept of MQW based GaAsP/Si tandem solar cells

The theoretical efficiency of ideal two-junction solar cell with active Si substrate is 45% when it has the top absorber with band gap of 1.73 eV material under nonconcentrated AM1.5 irradiance (in the idealized detailed balance limit) [7]. When it comes to the $GaAs_{1-x}P_x$ compound semiconductors, which can be grown on GaP/Si template with simple GaAsP graded metamorphic buffer layer, the band gap of 1.73 eV can be achieved with $GaAs_{0.75}P_{0.25}$. Current matched top subcell, $GaAs_{0.75}P_{0.25}$, contains arsenic as 75%. High arsenic proportion in the top absorber causes not only large lattice mismatch of 3.1% with GaP/Si template but also large expansion coefficient [8], therefore more challenging to heteroepitaxy on Si.

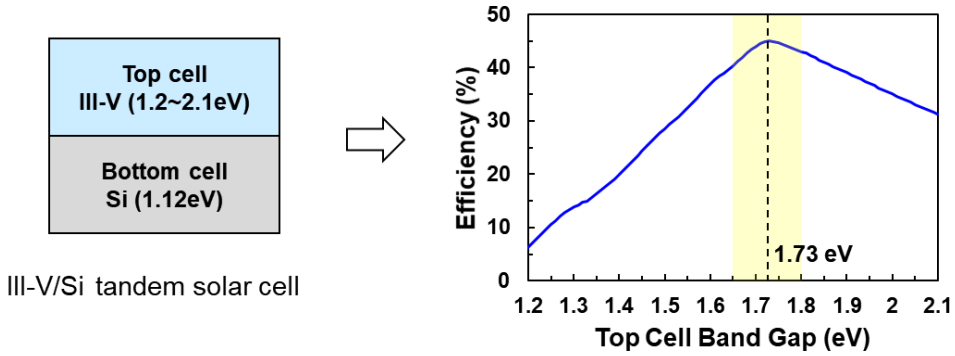

Fig. 4-1 Theoretical energy conversion efficiency for III-V/Si two-junction solar cells.

In this research, a new concept for III-V/Si two-terminal multi junction solar cell with inserting strain-balanced multi-quantum well in the GaAsP matrix is suggested. A device concept for this multi-quantum well based top absorber should be considered following contents.

1) Top absorbers have direct band gaps in the range of 1.65 to 1.8 eV which can yield high energy conversion efficiency when it is integrated on active Si of 1.12 eV.
2) Designed GaAsP matrix with low arsenic component: reducing the lattice mismatch and expansion coefficient with Si substrate.
3) Current matching in GaAsP/Si tandem solar cell: strain-balancing multi-quantum wells are applied for extending light absorption in top absorber.
4) High internal quantum efficiency.
5) Reduced material consumption.

The optimum top absorber band gap of 1.73 eV [9] could, for example, be achieved with GaAsP alloys containing 75% of As [10]-[11]. However, 75% of As translates to a large lattice mismatch of 3.1% between the top cell and a GaP/Si seed layer (even in the fully relaxed GaP on Si, the lattice mismatch is 2.8%), which requires a thick graded buffer layer (4~5 μm) [11].

Incorporation of less As component would decrease the lattice mismatch and thermal mismatch by that the minimum buffer thickness. However, it would also increase the absorption edge energy of the GaAsP top cell and by that reduce the device efficiency due to increased current mismatch to the Si subcell. To overcome this trade-off limitation, a GaAsP/Si two-junction solar cell with MQWs in the top absorber, as shown in fig. 4-2, is proposed as a new structure. As an example, $GaAs_{0.5}P_{0.5}$ is adopted as matrix of the top cell. The corresponding band gap of 2.05 eV is not suitable for high efficiency solar energy conversion due to current mismatch with Si bottom cell. However, by inserting MQWs layer in the top cell, the absorption edge can be shifted to longer wavelengths [12]-[14] and thus the current mismatch with regard to the Si cell can be

mitigated. $GaAs_{0.5}P_{0.5}$ can reduce the lattice mismatch to GaP/Si to about 1.8% compared with 2.8% for $GaAs_{0.75}P_{0.25}$. Moreover, the thermal expansion coefficient decreases about 4.3×10^{-7} K^{-1} at 300K so that there will be more gain in the high growth temperature. By these, the thickness of the metamorphic buffer layer can be substantially decreased. In addition, MQWs facilitate the radiative recombination of carriers by concentrating carriers in narrow-gap wells [15], which in turn suppresses non-radiative recombination and thus heat dissipation. In multi-junction cells, radiative recombination enhances luminescence coupling and makes a cell more tolerant against current mismatch induced by spectrum fluctuations of the solar irradiation [16]. For on-Si cells, in which the crystal quality of III-V layers tends to be worse than the layers on native substrates, the efficiency of radiative recombination tends to be degraded significantly and the ability of MQWs to enhance radiative recombination will be quite vital for achieving high efficiencies with III-V on Si tandem solar cells.

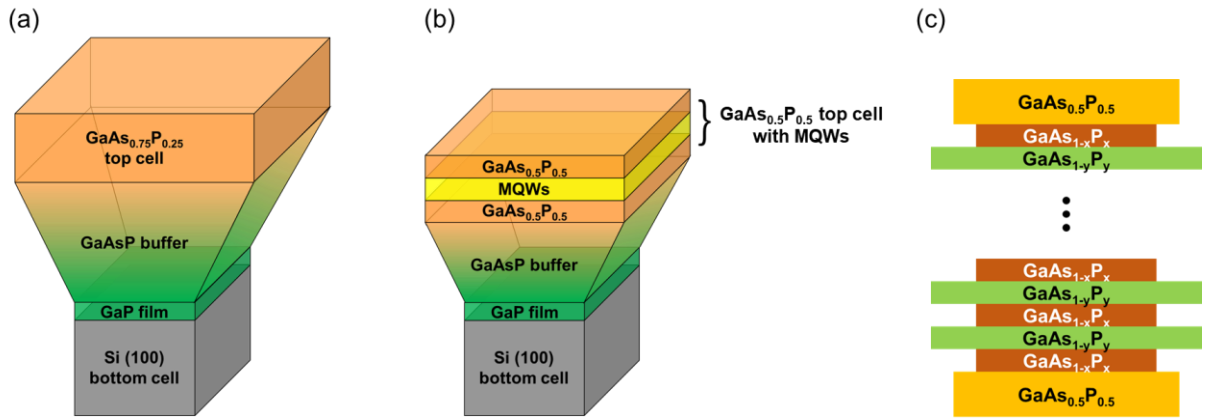

Fig. 4-2 A schematic of GaAsP/Si tandem solar cells: (a) $GaAs_{0.75}P_{0.25}$ on Si bottom cell which can achieve the theoretical maximum energy conversion efficiency, and (b) MQWs based $GaAs_{0.5}P_{0.5}$/Si tandem solar cell model which can reduce lattice mismatch between GaAsP top cell and Si bottom cell. (c) A schematic of multi-quantum well inserted in top cell [7].

In this research, the new structure of $GaAs_{0.5}P_{0.5}$/Si two-junction solar cell with MQWs in the top absorber is presented and estimated obtainable efficiency. To be specific, the energy conversion efficiency of such a tandem cell is predicted as a function of the structure of MQWs, such as the atomic content, thickness and stacking number. The model applied in this research is realistic in the sense that it takes the drawbacks of MQWs, such as limited light absorption and the bottleneck of carrier collection from the confinement states, into account.

4.2 Carrier collection process in multi-quantum well solar cells

Carrier dynamics in low dimensional multi-quantum well layers are different from the characteristics

in the bulk matrix. Effective mobility model in the quantum wells [5] is introduced for reflecting the realistic carrier behavior in MQWs-$GaAs_{0.5}P_{0.5}$ top subcell. In this section, the details about concept for effective mobility and carrier collection efficiency in MQWs layer [6] is explained.

4.2.1 Effective mobility for multi-quantum well

The carrier effective mobility in the quantum well layer is the concept for simplifying the carrier dynamics in periodic quantum well layers as shown in fig. 4-3. The effective carrier mobility μ_{eff} is obtained by formulating cascaded carrier escape events in periodic MQWs, and the rate of carrier escape from a well incorporates both thermionic and direct, thermionic assisted tunneling processes [5].

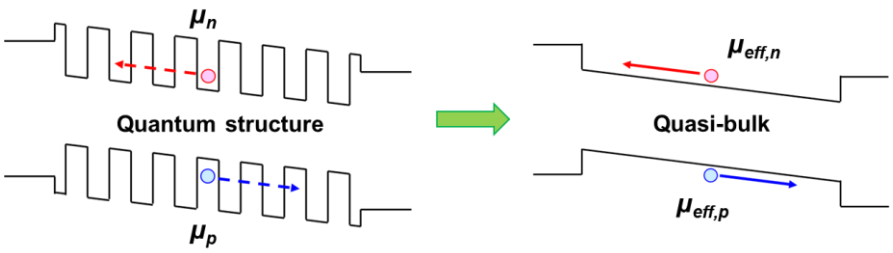

Fig. 4-3 A concept for effective mobility: simplify the carrier transport in low dimensional quantum well structure as a transport in quasi-bulk.

Figure 4-4 shows a schematic of the carrier transport in a quantum well to adjacent quantum well. The carrier escape rate from *i*th quantum well to adjacent well can be written in eq. (4.1).

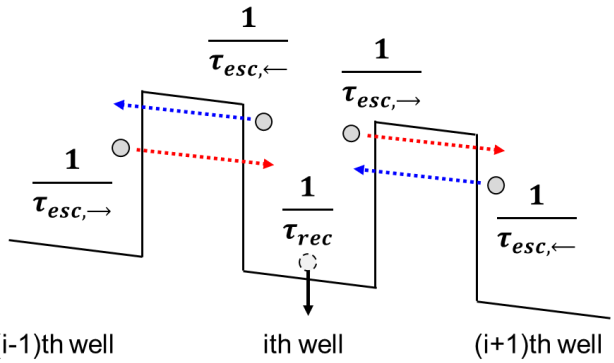

Fig. 4-4 A schematic of carrier transport in quantum well. Where, $1/\tau_{esc}$ is the carrier escape rate and ←, → represent the direction of escape. The $1/\tau_{rec}$ is the carrier recombination rate.

$$\frac{dn_i}{dt} = \frac{n_{i-1}}{\tau_{esc,\rightarrow}} - \frac{n_i}{\tau_{esc,\leftarrow}} - \frac{n_i}{\tau_{esc,\rightarrow}} - \frac{n_i}{\tau_{rec}} + \frac{n_{i+1}}{\tau_{esc,\leftarrow}} \tag{4.1}$$

Where, n_i is the carrier density in ith quantum well. By using Fokker-Plank approximation, the averaged carrier velocity in the quantum well layers can be obtained as eq. (4.2) [17]-[18].

$$\upsilon = L\left(\frac{1}{\tau_{esc,\rightarrow}} - \frac{1}{\tau_{esc,\leftarrow}}\right) \tag{4.2}$$

Where L is the thickness of a periodic quantum well which is the summation of well thickness L_w and barrier thickness L_b. This averaged carrier velocity is regraded as a carrier effective mobility in the MQWs layer.

The carriers in the quantum well can escape from the well by three processes which are thermionic escape, direct tunneling escape and thermionic assisted tunneling process as depicted in fig. 4-5.

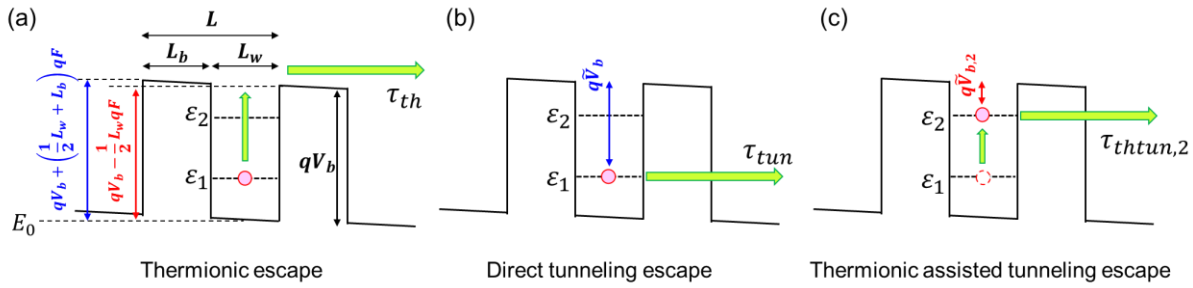

Fig. 4-5 Schematics band edge diagrams: (a) band parameters and thermionic escape process, (b) effective barrier height for ground state and direct tunneling escape process, and (c) effective barrier height for excited state (i=2) and thermal assisted tunneling escape process.

Where the E_0 is the band edge energy and qV_b is the band-offset or barrier height. The ε_i represents the ground state and excited states and F is the applied electrical field. In this scheme, the effective barrier height $q\tilde{V}_b$ is given in eq. (4.3).

$$q\tilde{V}_b = qV_b - \varepsilon_1 \tag{4.3}$$

The details about deriving the equations of carrier effective mobility for each escape processes are explained in ref.[5]. In this section, only simple scheme of each mobilities and equations is introduced.

1) Effective mobility by thermionic escape: μ_{th}

To escape from the well by thermionic process, the total energy over $E_0 + qV_b + \left(\frac{1}{2}L_w + L_b\right)qF$ is required. The effective mobility by thermionic escape process can be derived from the distribution function, and photocurrent density which is generated by thermionic escape.

$$\mu_{th} = \frac{m_{3D}^*}{m_{in,1}^*}\frac{qL^2}{h}\left(1+\mu_{3D}\sqrt{\frac{8m_{3D}^*V_b}{qL^2}}\right)e^{-q\tilde{V}_b/k_BT} \tag{4.4}$$

Where, m_{3D}^* and $m_{in,1}^*$ are the effective mass of carriers in the continuum levels and in-plain effective mass for ground state.

2) Effective mobility by direct tunneling escape: μ_{tun}

The effective mobility by tunneling escape can be derived by semiclassical analyzing [19]-[20] and assumption that the tunneling transport is dominated by the sequential tunneling [21].

$$\mu_{tun} = \sqrt{\frac{m_{3D}^*}{m_{per,1}^*}}\sqrt{\frac{\varepsilon_1}{q\tilde{V}_b}}\frac{qL_bL^2}{L_w\hbar}e^{-\frac{2L_b}{\hbar}\sqrt{2m_b^*q\tilde{V}_b}} \tag{4.5}$$

Where, $m_{per,1}^*$ and m_b^* are the perpendicular effective mass in the ground state and effective mobility in the barrier layer, and $\hbar$ is the reduced Plank's constant.

3) Effective mobility by thermionic assisted tunneling escape: μ_{thtun}

Thermionic assisted tunneling is the tunneling escape for the carriers which are in the excited states (i≥2) as shown in fig. 4-5(c).

$$\mu_{thtun} = \sum_{i\geq 2}\sqrt{\frac{m_b^*}{m_{per,i}^*}}\frac{m_{in,i}^*}{m_{in,1}^*}\sqrt{\frac{\varepsilon_i}{q\tilde{V}_{b,i}}}\frac{qL_bL^2}{L_w\hbar}e^{-\frac{(\varepsilon_i-\varepsilon_1)}{k_BT}}e^{-\frac{2L_b}{\hbar}\sqrt{2m_b^*q\tilde{V}_{b,i}}} \tag{4.6}$$

Where, $m_{per,i}^*$ / $m_{in,i}^*$ are the perpendicular / in-plain effective mobility in the *i*th state, and $q\tilde{V}_{b,i}$ is the effective barrier height for the carrier in the *i*th state

The total carrier effective mobility can be expressed as the summation of effective mobility by entire escape processes.

$$\mu_{eff} = \mu_{th} + \mu_{tun} + \sum\nolimits_{i\geq 2}\mu_{thtun,i} \tag{4.7}$$

4.2.2 Carrier collection efficiency in quantum well layer

The carrier collection efficiency (CCE) describes the probability that a carrier generated by light

absorption in a certain region of the cell will be collected by the p-n junction and therefore contribute to the light-generated current (CCE = $J_{out}/J_{generated}$). By applying multi-quantum well in the absorber, the effective band gap can be reduced and the absorption energy range can be extended.

However, it is difficult to collect the carrier through the MQWs layer due to its potential barrier. The confined carriers in the quantum well layer recombines and do not contribute to photocurrent. For dealing with this problem, the theoretical model for the carrier collection mechanism in the quantum well layer is proposed in ref. [6] by experimental and simulation method.

1) Carrier collection: Transport crossing the MQWs layer

Carrier density increases in the MQW layer due to the flow of photocurrent penetrating through the MQW layer, and decreases due to the Shockly Read Hall (SRH) recombination. When there is the hole-rich and electron-rich region in the MQWs layer, the carrier collection efficiency for minority carrier can be written as eq. (4.8) by considering these carrier density change.

$$CCE_{n\ (or\ p)} = exp\left(-\frac{L_{minor}}{L_d}\right) \tag{4.8}$$

Where, L_{minor} is the length of minority carrier region and L_d is the drift length of minority carrier in the MQWs layer.

2) Carrier collection: Collection efficiency for carriers generated in MQWs layer

The CCE for carriers which are generated in the MQWs is given by eq. (4.9).

$$CCE_{direct} = \frac{L_{p>n}}{L_{MQW}} exp\left(-\frac{L_{p>n}}{2L_{d,n}}\right) + \frac{L_{n>p}}{L_{MQW}} exp\left(-\frac{L_{n>p}}{2L_{d,p}}\right) \tag{4.9}$$

Where, L_{MQW} represents the total thickness of MQWs, $L_{p>n}$ and $L_{n>p}$ are the length of hole-rich and electron-rich region. The $L_{d,n}$ and $L_{d,p}$ are the drift length for electron and hole respectively.

The carrier collection efficiency of the absorber with MQWs has the maximum value when the distribution is symmetric, that is $L_{p>n} = L_{n>p} = \frac{1}{2}L_{MQW}$.

4.3 Realistic efficiency prediction of MQW based GaAsP/Si tandem solar cell

Based on the structure which is suggested in section 4.1, a realistic efficiency for MQW-$GaAs_{0.5}P_{0.5}$/Si

tandem solar cell can be calculated by introducing effective mobility model and carrier collection efficiency in the MQWs layer. The details about calculation methods for efficiency prediction and calculated results is discussed in this section.

4.3.1 Calculation method: structure of the GaAsP top cell with quantum wells

As mentioned in the previous section, $GaAs_{0.75}P_{0.25}$ top absorbers are required for GaAsP/Si current-matched dual junction solar cell. The As content can be significantly reduced by applying MQWs layer embedded in the GaAsP matrix. The amount of As incorporated into the host matrix is an important structural parameter for the overall efficiency. In this research, $GaAs_{0.5}P_{0.5}$ is adopted as bulk host material of the top absorber, which is arbitrarily chosen as a simple example. The efficiency predicted in this study, therefore, is not the maximum efficiency as a result of global optimization, which needs to be pursued in future work.

Strain-balanced multi-quantum well

For the MQWs, the content of wells and barriers are set to $GaAs_{1-x}P_x$ and $GaAs_{1-y}P_y$, respectively, and the thicknesses of well and barrier were set to L_w and L_b, respectively. Here, $x < 0.5 < y$ for strain balancing, and the P content for the barrier, y, is determined from the strain-balance condition shown in eq. (4.10), with the given P content in the well, x, and barrier thickness, L_b.

$$A_{MQW} = \frac{A_w L_w + A_b L_b}{L_w + L_b} = A_{bulk} \tag{4.10}$$

Where A_{bulk} is the lattice constant of the host $GaAs_{0.5}P_{0.5}$ layer. In this research, the thickness of a well L_w, is fixed at 5 nm for simplicity although it is also an important structural parameter and its optimization is subject to future survey. The barrier thickness, L_b, is set as a variable because it significantly affects the efficiency of carrier collection and the total thickness of MQWs layer. A_w and A_b represent the lattice constants of well and barrier, respectively, which are obtained according to x and y on the basis of Vegard's law between GaAs and GaP. The P contents in barrier calculated by the strain-balance condition is depicted in fig. 4-6.

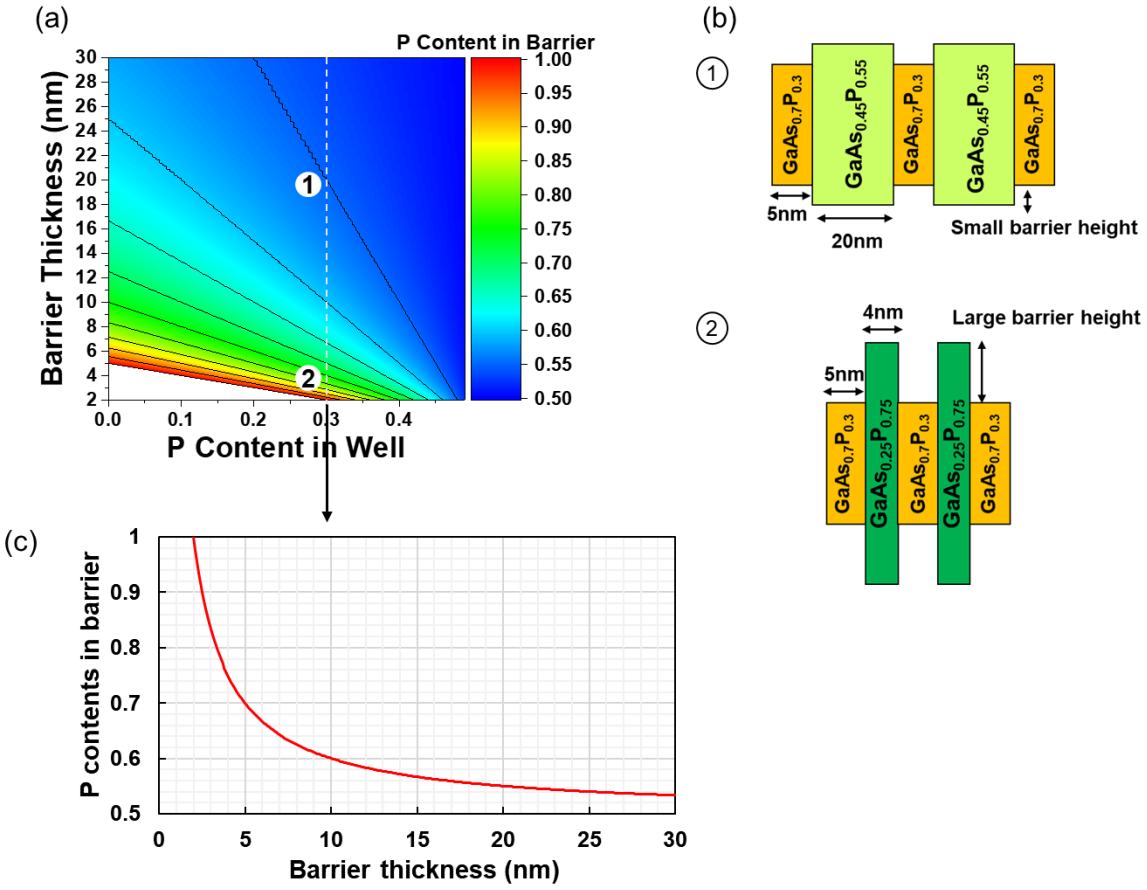

Fig. 4-6 P content in barrier that satisfies strain balancing of MQWs. For the white region, strain balancing is impossible for $GaAs_{1-x}P_x$ well / $GaAs_{1-y}P_y$ barrier system in the $GaAs_{0.5}P_{0.5}$ matrix.

It must be emphasized that L_w has only a small impact on the light absorption in the entire MQW structure. Although it is counterintuitive, the absorption coefficient in a well with significant carrier confinement is almost independent of its thickness for a photon energy range adjacent to its absorption edge, which is the functional energy range of quantum wells for our purpose. This physical principle implies that the light absorption near the absorption edge energy is almost proportional to the number of quantum wells, but not to their total thickness. Several experiments and theory supported this important design principle [22]-[24]. If multiple confinement states are included in a well, similar light absorption which is dependent on the number of wells takes place for each light absorption between the excited states. From the perspective of cost reduction, the thinner the MQW structure is, the less material is consumed. We thus focus on thinner quantum wells as long as strong quantum confinement never prevents the absorption edge energy of MQWs from reaching the desired value for current matching in tandem configuration.

4.3.2 Calculation method: assumption for evaluating light absorption and photocurrent in quantum well layers

The band gaps of the well and barrier were calculated taking into account the impact of strain, such as elastic stiffness, shear modulus and deformation potential. The band-edge energies were calculated following the method and parameters by Van de Walle [25], and all the parameters are indicated in Table. A-1. The absorption edge of the MQWs was obtained from the transition energies between the ground states and the *n*th excited states of the electrons and holes in a well. The quantum confinement energies were calculated using an effective-mass approximation for a rectangular confinement potential field, with an effective mass obtained using Vegard's law between GaAs and GaP.

There are several additional assumptions in the calculation.

(1) There is no optical loss in the metamorphic buffer layer and the GaP seed layer, so that there is no performance degradation due to these layers.

(2) 100% of light is absorbed in Si bottom cell and $GaAs_{0.5}P_{0.5}$ matrix, for the photon energy larger than the band gap.

(3) The absorption coefficient corresponding to the transition between the ground states of the electrons and holes in a well was set to 3.2×10^4 cm^{-1}, a value taken from the experimental result for InGaAs quantum wells [26], corresponding to 1.6% light absorption per a 5-nm-thick well and approximately 80% absorption in 100-period MQWs.

(4) The absorption between the excited states was considered up to the 6th excited state, which is the highest excited state that can be included in a well within the structural parameters assumed in this survey. The absorption coefficient for the photon energy below the absorption edge of $GaAs_{0.5}P_{0.5}$ takes staircase-like shape with the steps existing at the transition energies between the *n*th states. All the step height was assumed to be $3.2x10^4$ cm^{-1}, a value taken for the ground-state transition, that is the absorption was set to $3.2\times10^4\times n$ for *n*th energy state.

(5) A vertical single light path in the MQWs and AM1.5 global solar spectrum was set as the incident light condition.

Here, we only consider about direct bandedges, i.e., only Γ point in the band dispersion was considered, even though GaAsP with P content over 45% can be an indirect-band gap semiconductor. In the framework of the efficiency prediction, this is rationalized as the following.

1) As for light absorption, it is assumed that the photons with the energy larger than the absorption edge of $GaAs_{0.5}P_{0.5}$ host is 100% while the absorption by the $GaAs_{1-y}P_y$ barriers are neglected for simplification. Therefore, the indirect nature of GaAsP never affects the estimation of light absorption.

2) As for carrier transport, the band gap at Γ point is larger than the band gap at X point for an indirect-band gap $GaAs_{1-y}P_y$, i.e., the actual barrier height is lower than assumption was set in this research if Γ to X valley transition of carriers takes place. This means that the result from this survey may underestimate the effective mobility for the MQWs with indirect-band gap $GaAs_{1-y}P_y$ barriers, resulting in the prediction of lower efficiency.

These are potential source of uncertainties in the efficiency prediction, but we believe the impact is not large enough to sway the conclusion.

4.3.3 Estimaion of photovoltaic properties with realistic carrier collection efficiency

Photovoltaic properties were estimated on the basis of detailed balance theory incorporating limited light absorption. Here, the radiative limit of cell operation is considered in order to estimate the maximum efficiency that can be obtainable. For the silicon bottom cell, the flux of carriers to an external circuit is simply determined by the balance between light absorption and the radiative recombination of carriers at a given bias applied to the cell. For the top cell including MQWs, this assumption is inadequate since quantum confinement of carriers in the wells imposes a significant bottleneck of carrier extraction to an external circuit as explained at section 4.2. Such carrier collection can be assisted by the electric field applied over the MQW because the field makes the carrier escape from a well asymmetric, favoring the escape rate towards the downstream of the electric field [17],[25]. Degradation of carrier collection as a function of the bias voltage applied to a cell containing MQWs has been discussed quantitatively in terms of carrier collection efficiency (CCE) [6], which is a ratio of net photocurrent under a given bias $J_{ph}(V)$ with respect to the total light absorption in the active region (I_{abs}):

$$J_{ph}(V) = CCE(V) \times I_{abs} \tag{4.11}$$

Here, the photocurrent is estimated by this scheme for the property of the top cell.

In principle, CCE in a cell with MQWs can be obtained by cascaded escape and trap processes of a carrier. But numerical simulation including all the carrier transport processes is time consuming and is not suitable for the efficient structural optimization. Here, the MQWs are approximated as a quasi-bulk material and introduced a concept of effective carrier mobility μ_{eff} for the entire MQWs [18],[27]. As introduced in the previous section, the CCE is maximum when the distribution is symmetric, so the eq. (4.9) can be written as eq. (4.12).

$$CCE(V) = exp\left(-\frac{L_{MQW}}{4L_d(V)}\right) \tag{4.12}$$

where L_{MQW} is the total thickness of MQWs, and L_d is the average drift length of electrons and holes in the MQW region. The averaged drift length of carriers is expressed as eq. (4.13).

$$L_d = \frac{1}{2}\left[\mu_{eff,n}\tau_{rec,n}E(V) + \mu_{eff,p}\tau_{rec,p}E(V)\right] \tag{4.13}$$

where, τ_{rec} is the carrier recombination lifetime and $E(V)$ is the electric field at a bias voltage V, the subscripts n and p indicate electrons and holes respectively. In this calculation, τ_{rec} is set to 100 ns for both electrons and holes, an experimental value for a InGaAs-based MQW system [28].

The effective carrier mobility μ_{eff} is obtained by formulating cascaded carrier escape events in MQWs, and the rate of carrier escape from a well incorporates both thermionic and tunneling (direct and thermionic assisted) processes.

$$\mu_{th} = \mu_{th0}\left(\frac{\left({}^{1}/_{\tau_{esc\rightarrow}} - {}^{1}/_{\tau_{esc\leftarrow}}\right)L_{period}}{E}\right) \tag{4.13}$$

Where, τ_{esc} is the time constant of carrier escape, L_{period} is the period width of MQWs, the right arrow indicates the escape toward the downstream of the electric field and the left arrow toward the upstream. Considering the model for the escape time constant derived in section 4.2.1, the effective mobilities for the thermionic (μ_{th}) and tunneling processes (μ_{tun}) are expressed as following.

$$\mu_{th} = \mu_{th0}exp\left(\frac{-qV_b}{k_BT}\right) \tag{4.14}$$

$$\mu_{tun} = \mu_{tun0}exp\left(\frac{-2L_b\sqrt{2m_b^*qV_b}}{\hbar}\right) \tag{4.15}$$

Where, V_b is the barrier height, i.e. the energy difference between the ground confinement state in the well and the band edge of the barrier, m_b^* is the effective mass for carriers in the barrier, q is the elementary charge, k_B is Boltzmann's constant, T is the temperature, $\hbar$ is reduced Planck's constant, μ_{th0} and μ_{tun0} are the constants with weak dependency on the quantum well structure. Using the model in [5] within the parameter space in this survey, μ_{th0} ranged 1-10 cm^2/Vs and μ_{tun0} ranged 102-104 cm^2/Vs. The net effective mobility can be obtained as the summation of the effective mobilities for these processes.

4.4 Calculation results: efficiency of MQWs-GaAsP/Si tandem solar cell

4.4.1 Barrier height for strain-balanced MQW

The P contents in the barrier is decreasing with thicker barrier, when the thickness and P content for well layer is fixed as described in fig. 4-6. It means that a smaller P content in a well implies that the well is deeper. It is clear that a larger barrier P content, and hence a smaller lattice constant, is necessary to keep strain balancing for a thinner barrier. As a result, the band offset becomes larger for the combination of a small P content of the well and a small thickness of the barrier, as shown in fig.4-7.

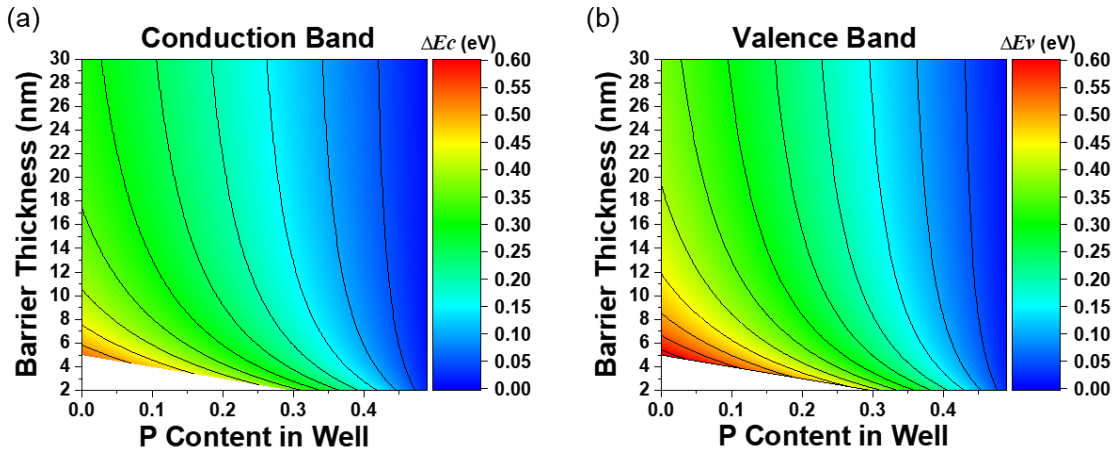

Fig. 4-7 (a) The conduction band offset ΔE_c and (b) the valence band offset ΔE_v for the strain-balanced MQWs composed of $GaAs_{1-x}P_x$ wells and $GaAs_{1-y}P_y$ barriers.

The energy barrier for the electrons and holes confined in a well is the energy difference between the ground-state confinement energy and the band edge energy of the $GaAs_{1-y}P_y$ barrier as shown in fig. 4-5. The value is slightly smaller than the conduction band offset for electrons and it is almost the same as the valence band offset for holes, as shown in fig. 4-8.

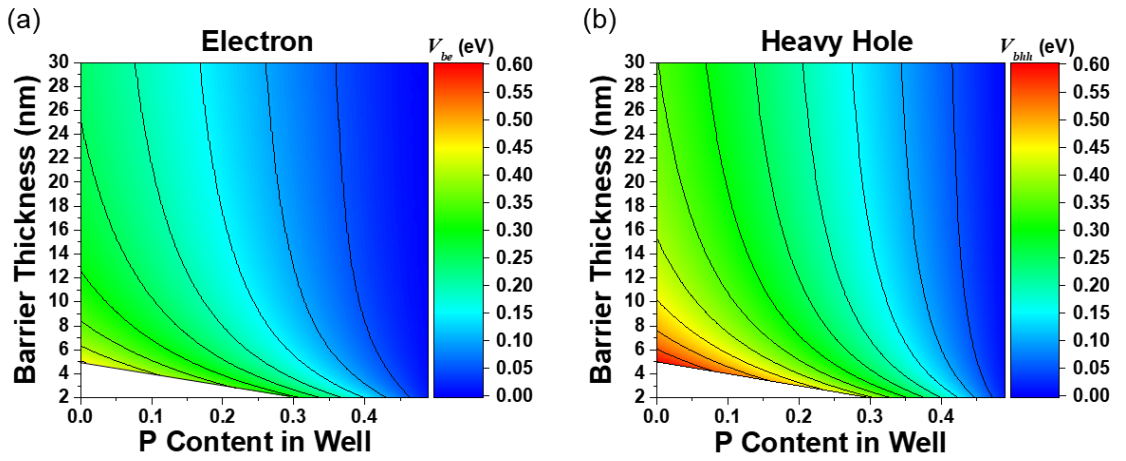

Fig. 4-8 Energy barrier height for (a) the electrons (V_{be}) and (b) the heavy holes (V_{bhh}) which are confined in a well.

4.4.2 Effective mobility of carriers in quantum well

The effective mobilities for electrons and holes can be obtained by according the model described in section 4.3. Figure 4-9 shows the calculated carrier effective mobility values considering the contributions of the thermionic and tunneling escape from the wells.

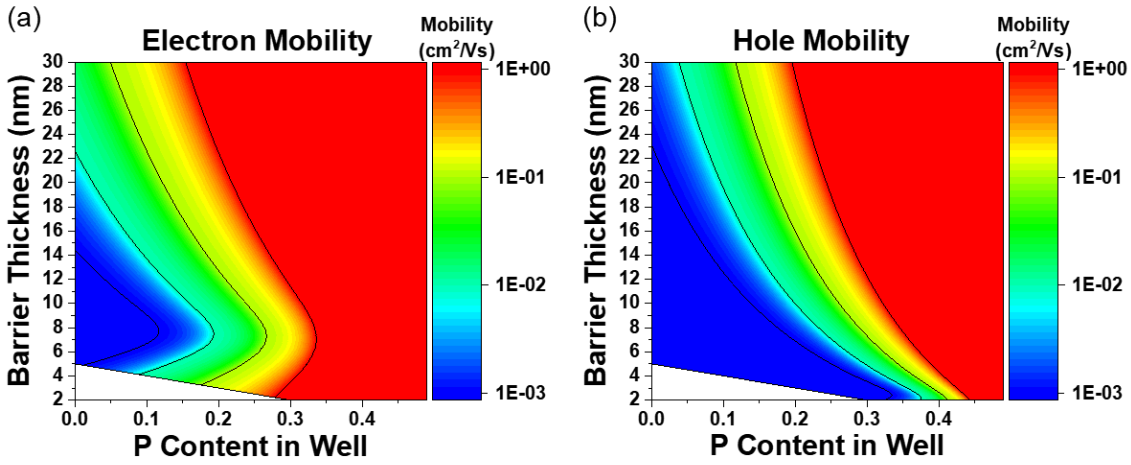

Fig. 4-9 Effective mobility for electrons and holes across the MQWs

The effective mobility takes the value below 1 cm^2/Vs due to cascaded escape/trap processes, and the value is in the range for bulk materials with inferior carrier transport such as amorphous silicon [29]. The value of effective mobility smaller than 1 cm^2/Vs has been observed in the time-of-flight measurement of

both electrons and holes in strain-balanced InGaAs / GaAsP quantum wells [30], which supports the reliability of our prediction. From eq. (4.14) and (4.15), the effective carrier mobility is particularly sensitive to the confinement barrier height in fig. 4-8. Therefore, the mobility value is larger for a P content in a well, a situation with shallower wells. As for the impact of the barrier thickness, the mobility takes larger values with thick barriers. This is a result of low P content in the barrier (fig. 4-6) which reduces the barrier height and facilitates thermionic escape of both electrons and holes and well agree with the tendency of barrier height as shown in fig. 4-9. For electrons alone, however, mobility gets larger with thinner barriers as well. This is brought about by the contribution of tunneling transport and is not effective for holes with larger effective mass than electrons.

4.4.3 CCE in quantum well and prediction of energy conversion efficiency

The carrier collection efficiency can be estimated by the carrier effective mobility values. The CCE is obtained by eq. (4.12) and (4.13), and realistic estimation of the photocurrent for the top cell with MQWs is possible on the basis of eq. (4.11).

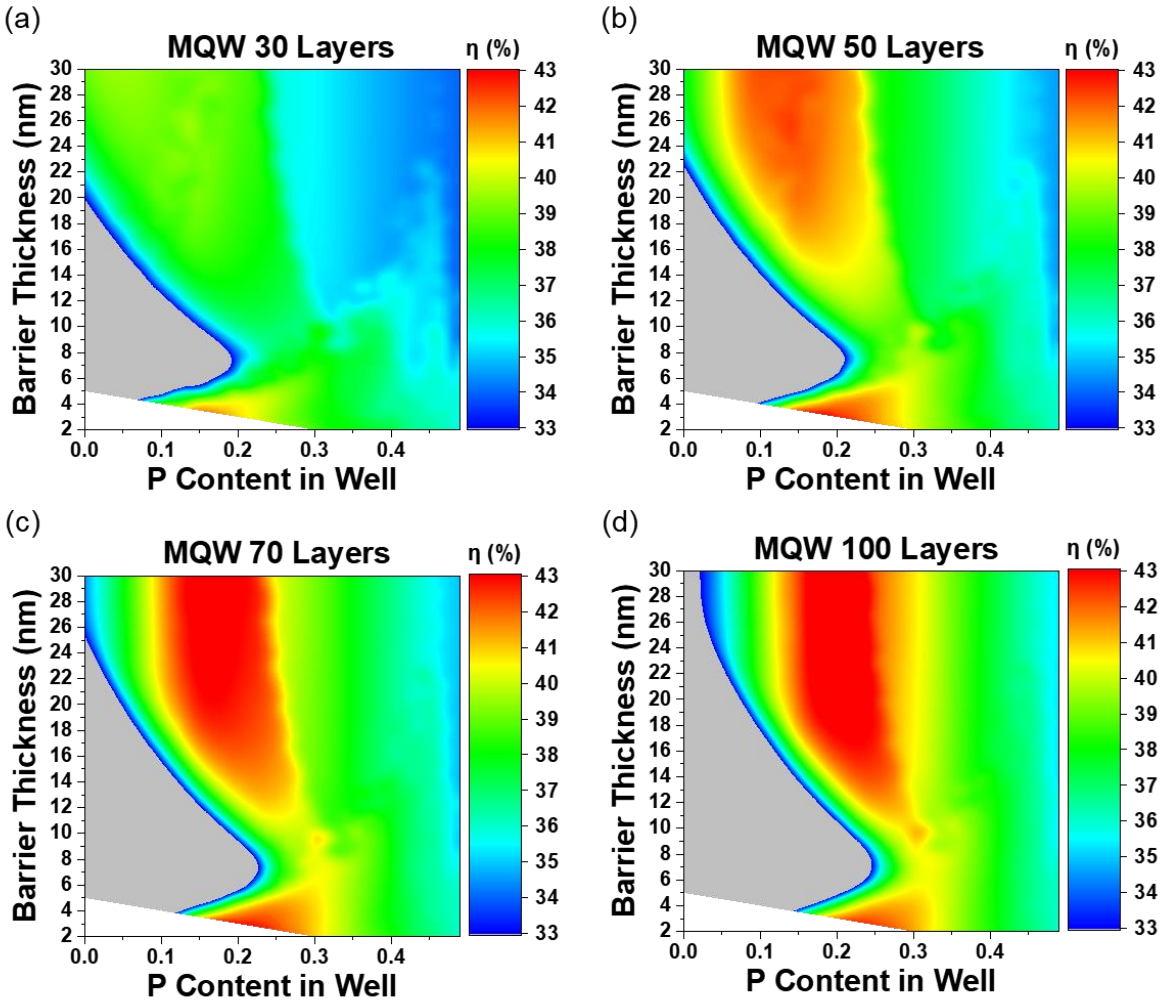

Fig. 4-10 Predicted efficiency of the two-junction cell consisting of a $GaAs_{0.5}P_{0.5}$ top absorber with GaAsP MQWs and a Si bottom cell for the cases with (a) 30, (b) 50, (c) 70 and (d) 100 periods of MQWs. The region filled with grey has no advantage over the theoretical efficiency limit of 33% for a Si single-junction solar cell

The predicted efficiency is plotted in fig. 4-10 as a function of both P content of the wells and the barrier thickness. In the contour plot of fig. 4-10, the region filled with grey has no advantage over the theoretical efficiency limit of 33% for a Si single-junction solar cell [31]. As for the impact of the barrier thickness, high efficiency can be achieved with either very thin barriers (under 4 nm with high P content) or very thick

barriers (approaching 30 nm with low P content). For the case of thin and high barriers, electron transport by tunneling contributes efficient carrier collection. For thick and low barriers, on the other hand, thermal escape is the mechanism of carrier collection.

The maximum efficiency is 44.22% for 100-period MQWs with 30-nm-thick barriers, while it is 42.62% for 70-period MQWs with 3-nm-thick barriers. The difference in the optimum barrier thickness originates from CCE limited by the MQWs layer.

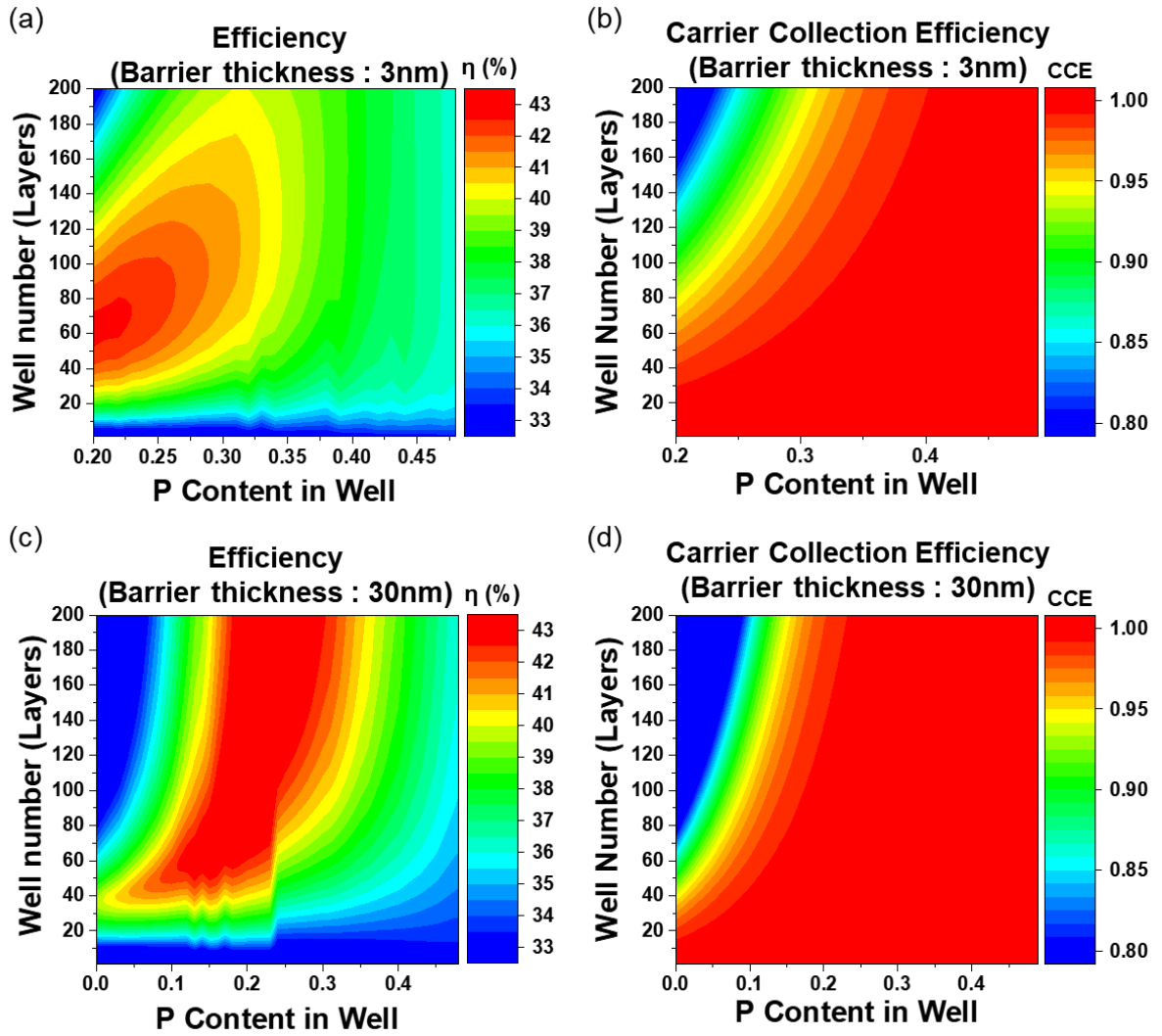

Fig. 4-11 Predicted efficiency of the two-junction cell consisting of a GaAs0.5P0.5 top cell with GaAsP MQWs and a Si bottom cell for the cases with 3-nm-thick barriers (a) and 30-nm-thick barriers (c). The corresponding values of carrier collection efficiency (CCE) are also shown at the maximum-power operation point of MQWs top cell in (b) and (d), respectively.

Figure 4-11 shows the predicted efficiency and the value of CCE for the MQW cells with the barrier thickness of 3 nm and 30 nm, which are the condition to obtain high efficiency. In the regime of deep wells, which is the region with P content in a well smaller than 0.3 for 3-nm-thick barriers, 0.15 for 30-nm-thick barriers, CCE is degraded with increasing the number of wells as described in fig. 4-11 (b) and (d). In this regime, the cell efficiency decreases with increasing number of wells due to its carrier trapping in the wells. In the regime of shallow wells, CCE is high enough to photocurrent extraction, with P content in a well larger than 0.4 for 3-nm-thick barriers and 0.2 for 30-nm-thick barriers. Therefore, the efficiency increases with the number of wells owing to enhanced light absorption. The same tendency is observed also for deep wells with a period smaller than 30. The discontinuity in fig. 4-11 (c) comes from the different number of excited states included in a well. The predicted efficiency takes the maximum (42.6 %) with 60-period MQWs for the barrier thickness of 3 nm, while the maximum of 44.22% was obtained with 200-period MQWs for the barrier thickness of 30 nm. The efficiency which can be achieved with 30-nm-thick barriers is higher than in the case of with 3-nm-thick barriers. However, the total thickness of MQWs reaches 7 μm to get the maximum efficiency for the former case, which does not satisfy our motivation of reducing the thickness of an entire III-V layers for cost reduction.

The recommended MQW structure is a 60-period stack consisting of 5-nm-thick $GaAs_{0.8}P_{0.2}$ wells and 3-nm-thick GaP barriers, resulting in the total thickness of 480 nm. The efficiency predicted for this structure (42.6%) is slightly inferior to a value (45.0%) predicted for a current-matched $GaAs_{0.75}P_{0.25}$/Si two-junction cell in our modeling framework. However, considering the advantage of the cell with MQWs to reduce the total thickness of III-V layers including the metamorphic buffer layers, the predicted efficiency as large as 42.6% is still attractive. It would be a good structure to balance the requirements of high efficiency, small material consumption, reduced time of the growth (since MQWs normally need lower growth rate than bulk layers) and the good crystal quality of MQWs (since larger number of stacking in MQWs can induce lattice relaxation due to both a slight deviation from strain balancing and inadequate interface treatment).

Furthermore, our calculation found that the efficiency of $GaAs_{0.75}P_{0.25}$/Si cell will drop significantly to 39.1% when the internal luminescence efficiency is as low as 0.1%, which is a reasonable value for a $GaAs_{0.75}P_{0.25}$ bulk cell with defects induced by the metamorphic growth on Si. Although the photocurrent from III-V/Si two-junction solar cell is limited by the III-V top subcell in the ideal case, Si subcell would generate still low current in actual devices, leaving a room for efficiency gain owing to the luminescence coupling from the top cell to the bottom cell. MQWs have the advantage of keeping the luminescence efficiency relatively high owing to the concentration of carriers in the wells. Inclusion of realistic values for internal luminescence efficiency is a target of future survey and we must note that no luminescence coupling effect is considered in the present work.

Quantum efficiency and current-voltage characteristics

Figure 4-12 shows the predicted external quantum efficiency (EQE) and current-voltage curve of $GaAs_{0.5}P_{0.5}$/Si dual junction solar cell with the above-mentioned 60-period $GaAs_{0.8}P_{0.2}$ (5 nm) / GaP (3 nm) MQWs, which yields 42.6% energy conversion efficiency, short circuit current of 20.7 mA/cm^2, open circuit voltage of 2.3V and fill factor of 89.3%. In the QE plot (a), the staircase-like absorption appears up to the 4th excited state in a well. This is a good example rationalizing the assumption of up to the 6th excited states in a well as explained in section 4.3.2. The energy spacing between higher excited states, such as the 5th and the 6th, is very close the absorption edge energy of $GaAs_{0.5}P_{0.5}$ matrix and the higher excited states than the 6th state do not contribute to the absorption spectrum in the photon energy range below the absorption edge of $GaAs_{0.5}P_{0.5}$ bulk layer.

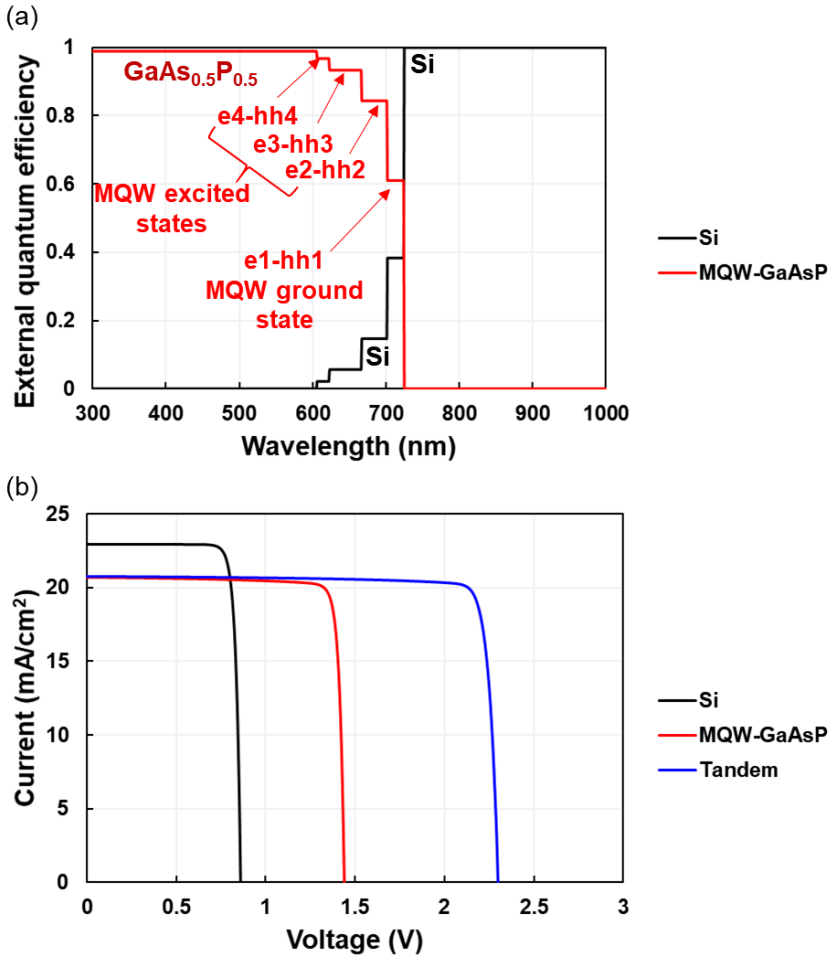

Fig. 4-12 (a) External quantum efficiency (EQE) and (b) current-voltage curve predicted for the $GaAs_{0.5}P_{0.5}$/Si two-junction cell with 60-period $GaAs_{0.8}P_{0.2}$ (5 nm) / GaP (3 nm) MQWs

Quantum efficiency and current-voltage characteristics by the number of QW layer

Figure 4-13 shows the predicted external quantum efficiency (EQE) and current-voltage curve of $GaAs_{0.5}P_{0.5}$/Si dual junction solar cell with the 10-period and 200-period $GaAs_{0.8}P_{0.2}$ (5 nm) / GaP (3 nm) MQWs.

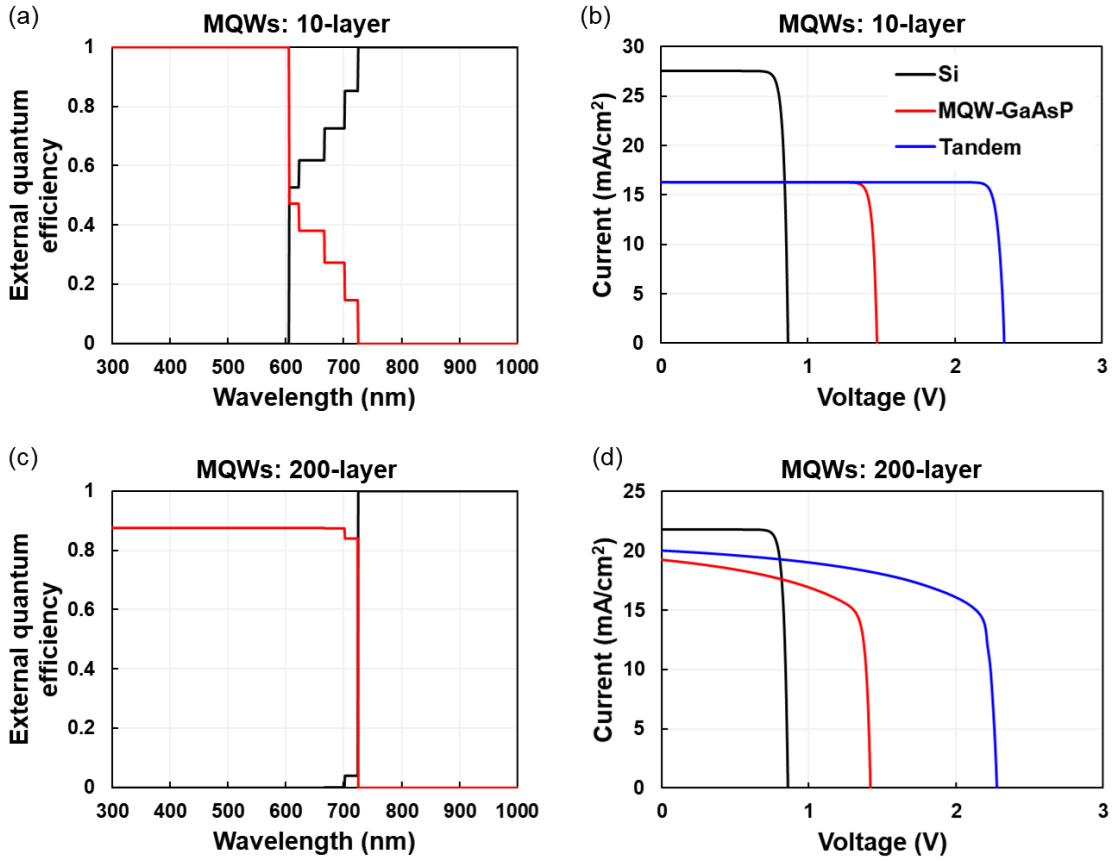

Fig. 4-13 (a) External quantum efficiency, and (b) current-voltage curve predicted for $GaAs_{0.5}P_{0.5}$/Si two-junction cell with 10-period $GaAs_{0.8}P_{0.2}$ (5 nm) / GaP (3 nm) MQWs. (c) External quantum efficiency, and (d) current-voltage curve predicted for $GaAs_{0.5}P_{0.5}$/Si two-junction cell with 200-period $GaAs_{0.8}P_{0.2}$ (5 nm) / GaP (3 nm) MQWs.

As explained in the previous section, as shown in fig. 4-11, CCE is high at thin (under 30-period MQWs) and is decreasing with the number of well layers in the deep well scheme. In 10-period MQWs, the fill factor is very high 93% due to its high carrier collection efficiency. However, the QE in the MQWs layer is low due to its short light absorption length. For the less energy absorption in MQWs, the current in the top absorber becomes small and the efficiency decreases (35.3%) owing to the current mismatch. In 200-period MQW, the light absorption in MQWs layer is increased due to the thick absorption length. However, the CCE is low as 30% in the 200-period MQWs. Therefore, it is hard to extract the photocurrent generated in

the top cell due to decrease of CCE for both of crossing and direct as introduced in section 4.2.2. From these, the fill factor is degraded to 71% and also the efficiency is degraded to 32.4%.

The predicted efficiency as described above provides a strong motivation to implement III-V on Si two-junction cells with a top $GaAs_{0.5}P_{0.5}$ cell that include MQWs consisting of GaAsP with different P contents. The structure potentially reduces the thickness of a metamorphic layer between Si and $GaAs_{0.5}P_{0.5}$ compared with the case with a bulk $GaAs_{0.75}P_{0.25}$ top cell, which would make it easier to implement III-V on Si cells by hetero-epitaxial growth. The efficiency might be further increased by the optimization of the P content of the GaAsP host and of the thickness of single well.

4.4.4 Feasibility of epitaxial growth for MQWs layer

Here, the feasibility of fabrication for designed MQWs is discussed.

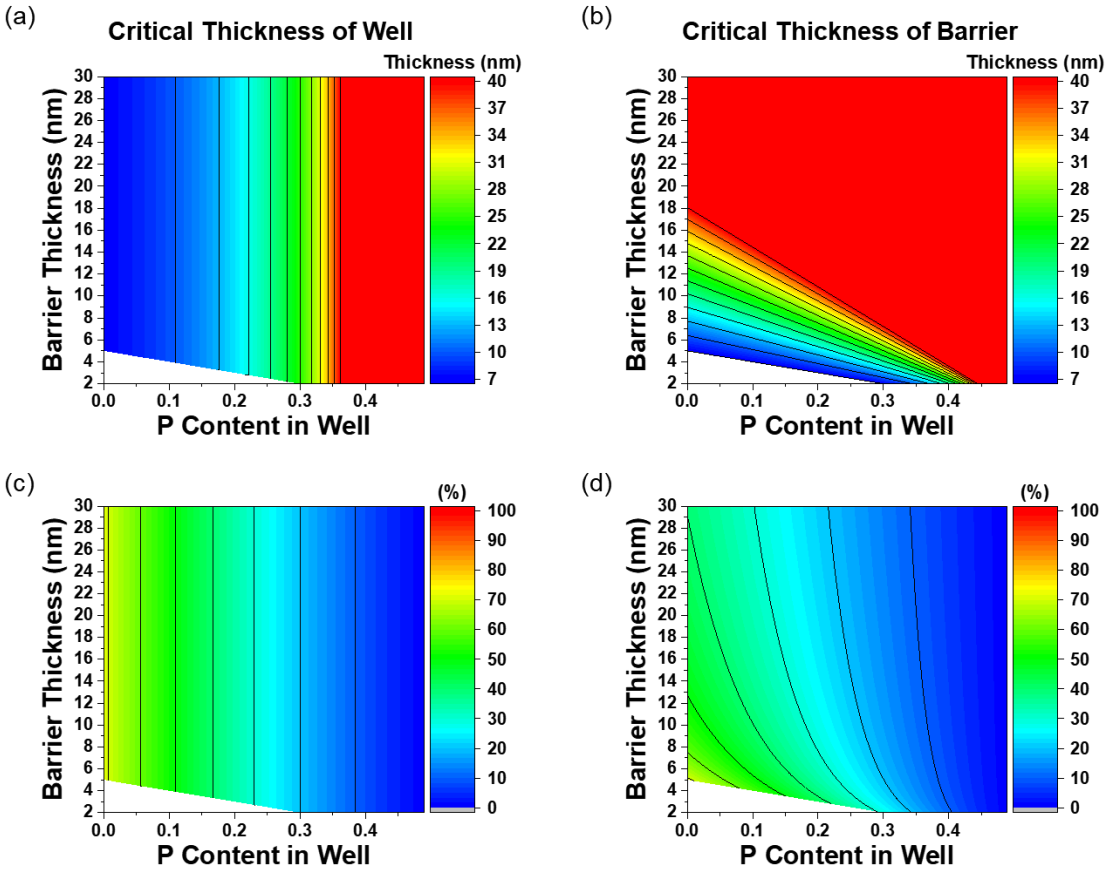

Fig. 4-14 Critical thickness by Matthews-Blakeslee model [32] for (a) a well and (b) a barrier with $GaAs_{0.5}P_{0.5}$ bulk matrix. The ratio of the designed layer thickness versus the calculated critical thickness is also shown for (c) a well and (d) a barrier.

The growth of strain-balanced MQWs needs to manage following things.

1) The strain accumulation both in an individual component layer and in the MQWs as a whole.

2) The hetero-interfaces between wells and barriers.

Here, all the MQWs are designed to keep strain balancing and we need to take care of the strain in an individual layer alone. Figure 4-14 shows the critical thickness for the well and barrier layers on the basis of Matthews-Blakeslee model [32]. The panels (a) and (b) indicate the values of critical thickness for the well and the barrier, respectively, and (c) and (d) show the the ratios of the designed layer thickness of the well (5 nm) and the barrier (a variable in the vertical axis) versus the corresponding critical thicknesses. Note that the P content in a well affects the critical thickness of the well layer itself, while the critical thickness of a barrier layer is determined by the P content in the barrier which depends on both the P content in a well and the thickness of the barrier, according to the strain-balancing criterion in eq. (4.10). As shown in fig. 4-14 (c) and (d), even in the most aggressive MQW structure, the thicknesses of the wells and the barriers are smaller than 71.4% of the corresponding critical thicknesses. The result suggests no possibility of crystal relaxation during the growth of the component layers in the MQWs.

As for the management of hetero-interfaces during the epitaxial growth by metal-organic vapor-phase epitaxy (MOVPE), the MQW structure under consideration just necessitates the content change of As and P. The exchange of As/P at hetero-interfaces has been explored for decades and it can be controlled by using optimized gas switching sequence on the basis of in-situ observation [33]-[34].

4.5 Summary of device design

In this research, a new structure for high-efficiency and low-cost III-V-on-Si dual junction solar cell with MQWs layer is proposed. The suggested $GaAs_{0.5}P_{0.5}$ top cell includes strain-balanced MQWs to facilitate sufficient light absorption while reducing the lattice mismatch between III-V layers and Si, and this allows to reduce the thickness of the metamorphic buffer layer compared to conventional $GaAs_{0.75}P_{0.25}$/Si solar cells.

Degradation of carrier collection efficiency (CCE) from the MQWs layer due to carrier confinement in the wells was incorporated in the efficiency prediction for the first time. According to the calculation in this research, either very thin (below 4nm) or very thick (over 30 nm) barriers are suitable for enhancing CCE, and the optimum stacking periods exists because increasing periods results in both the enhancement in light absorption and the degradation of CCE. By applying the calculated optimum MQWs in top absorber, the conversion efficiency can reach 42.6% if 60-periods MQWs composed of $GaAs_{0.8}P_{0.2}$ 5-nm-thick wells and 3-nm-thick GaP barriers are implemented as a QW structure. The total thickness of the MQWs is as small as

480 nm, in accordance with our motivation of thickness reduction, and no significant bottleneck is expected in the crystal growth. The structure is subject to further optimization regarding P content in the GaAsP host and the thickness of the wells.

4.6 References

[1] S. M. Vernon, S. P. Tobin, M. M. Al-Jassim, R. K Ahrenkiel, K. M. Jones and B. M. Keyes, "Experimenta study of solar cell performance versus dislocation density", *21st PVSC*, 1990. DOI: 10.1109/PVSC.1990.111619

[2] M. Yamaguchi, C. Amano, "Efficiency calculation of thin-film GaAs solar cells on Si substrates", *J. Appl. Phys.* **58** (9), p.3601-3606, 1985.

[3] T. Kieliba, S. Riepe, and W. Warta, "Effect of dislocations on open circuit voltage in crystalline silicon solar cells", *J. Appl. Phys.* **100**, 093708, 2006.

[4] M. Yamaguchi, K. Lee, K. Araki, N. Kojima, and Y. Ohshita, "Potential and activities of III-V/Si tandem solar cells", *ECS J. Solid State Sci. Technol.* **5** (2), p.68-73, 2016.

[5] K. Toprasertpong, S. M. Goodnick, Y. nakano, and M. Sugiyama, "Effective mobility for sequential carrier transport in multiple quantum well structures", *Phys. Rev. B* **96**, 075441, 2017.

[6] K. Toprasertpong, T. Inoue, Y. Nakano, M. Sugiyama, "Investigation and modeling of photocurrent collection process in multiple quantum well solar cells", *SOLMAT* **174**, p.146-156, 2018.

[7] B. Kim, K. Toprasertpong, A. Paszuk, O. Supplie, Y. nakano, T. Hannappel, M. Sugiyama, "GaAsP/Si tandem solar cells: Realistic prediction fo efficiency gain by applying strain-balanced multiple quantum wells", *SOLMAT* **180**, p.303-310, 2018.

[8] M. E. Straumanis, and J. P. Krumme, "Thermal Expansion Coeffiients and Lattice Parameters between 10°C and 65°C in the Systerm GaP-GaAs", *J. Electrochem. Soc.* **114** (6), p.640-641, 1967.

[9] H. Döscher, O. Supplie, M.M. May, P. Sippel, C. Heine, A.G. Muñoz, R. Eichberger, H.-J. Lewerenz, T. Hannappel, “Epitaxial III-V films and surfaces for photoelectrocatalysis", *ChemPhysChem.* **13** (12), p.2889-2909, 2012.

[10] J. F. Geisz, J.M. Olson, M. J. Romero, C. S. Jiang, and A. G. Norman, "Lattice-mismatched GaAsP solar cells grown on silicon by OMVPE", in: Proceedings of the *IEEE 4th World Conf. Photovolt. Energy Conf.* **1**, p.772, 2006.

[11] K. N. Yaung, M. Vaisman, J. Lang, M. L. Lee, "GaAsP solar cells on GaP/Si with low threading dislocation density", *Appl. Phys. Lett.* **109**, 032107, 2016.

[12] K. W. J. Barnhamg, G. Duggan, "A new approach to high-efficiency multi-band-gap solar cells", *J. Appl. Phys.* **67**, 3490, 1990.

[13] M. Sugiyama, Y. Wang, H. Fujii, H. Sodabanlu, K. Watanabe, N. Yoshiaki, "A quantum-well superlattice solar cell for enhanced current output and minimized drop in open-circuit voltage under sunlight concentration", *J. Phys. D. Appl. Phys.* **46**, 024001, 2013.

[14] H. Fujii, K. Toprasertpong, Y. Wang, K. Watanabe, M. Sugiyama, Y. Nakano, "100-period, 1.23-eV bandgap InGaAs/GaAsP quantum wells for high-efficiency GaAs solar cells: toward current-matched Ge-based tandem cells", *Prog. Photovolt. Res. Appl.* **22**, p.784, 2014.

[15] T. Inoue, K. Toprasertpong, A. Delamarre, K. Watanabe, M. Paire, L. Lombez, J.-.F. Guillemoles, M. Sugiyama and Y. Nakano, "Quasi-Fermi level splitting evaluation based on electroluminescence analysis in multiple quantum well solar cells forinvestigating cell performance under concentrated light", in: Proceedings of *SPIE 9743, Physics, Simulation, and Photonic Engineering of Photovoltaic Devices V, SPIE Photonics West* (Feb. 13-18, 2016, San Francisco, USA), p.974316, 2016.

[16] A.S. Brown, M.A. Green, "Radiative coupling as a means to reduce spectral mismatch in monolithic tandem solar cells tacks - Theoretical considerations", in: Proceedings of *29th IEEE PVSC*, p. 868, 2002.

[17] H. Schneider and K. v. Klitzing, "Thermionic emission and Gaussian transport of holes in a GaAs/AlxGa1-xAs multiplequantum-well structure", *Phys. Rev. B* **38**, 6160, 1988.

[18] K. Toprasertpong, T. Inoue, K.Watanabe, T. Kita,M. Sugiyama, and Y. Nakano, "Effective drift mobility approximation in multiple quantum-well solar cell", in: Proceedings of *SPIE 9743, Physics, Simulation, and Photonic Engineering of Photovoltaic Devices V*, 974315 (14 March 2016), 2016.

[19] S. A. Gurvitz, "Novel approach to tunneling problems", *Phys. Rev. A* **38**, 1747, 1988.

[20] I. A. Larkin, S. Ujevic, and E. A. Avrutin, "Tunneling escape time from a semiconductor quantum well in an electric field", *J. Appl. Phys.* **106**, 113701, 2009.

[21] A. Wacker and A. -P. Jauho, "Quantum Transport: The Link between Standard Approaches in Superlattices", *Phys. Rev. Lett.* **80**, 369, 1998.

[22] P. Blood, "On the dimensionality of optical absorption, gain, and recombination in quantum-confined structures", *IEEE J. Quantum Electron.* **36** (3), 354, 2000.

[23] H. Fujii, Y. Wang, K. Watanabe, M. Sugiyama, Y. Nakano, "High-aspect-ratio structures for efficient light absorption and carrier transport in InGaAs/GaAsP multiple quantum well solar cell", *IEEE J. Photovolt.* **3** (2), 859, 2013.

[24] K. Toprasertpong, H. Fujii, T. Thomas, M. Führer, D. Alonso-Álvarez, D.J. Farrell, K. Watanabe, Y. Okada, N.J. Ekins-daukes, M. Sugiyama, Y. Nakano, "Absorption threshold extended to 1.15 eV using InGaAs/GaAsP quantum wells for over-50%-efficient lattice-matched quad-junction solar cells", *Prog. Photovolt. Res. Appl.* **24** (4), 533, 2016.

[25] C.G. Van de Walle, "Band lineups and deformation potentials in the model-solid theory", *Phys. Rev. B* **39** (3), 1871, 1989.

[26] I. Serdiukova, C. Monier, M.F. Vilela, A. Freundlich, "Critical built-in electric field for an optimum carrier collection in multiquantum well p-i-n diodes", *Appl. Phys. Lett.* **74** (19), 2812, 1999.

[27] K. Toprasertpong, N. Kasamatsu, H. Fujii, T. Kada, S. Asahi, Y. Wang, K. Watanabe, M. Sugiyama, T. Kita, Y. Nakano, "Microscopic observation of carrier-transport dynamics in quantum-structure solar cells using a time-of-flight technique", *Appl. Phys. Lett.* **107** (4), 043901, 2015.

[28] K. Toprasertpong, T. Inoue, A. Delamarre, K. Watanabe, J.-F. Guillemoles, M. Sugiyama, Y. Nakano, "Electroluminescence-based quality characterization of quantum wells for solar cell applications", *J. Cryst. Growth* **464**, 95, 2017.

[29] E.A. Schiff, "Low-mobility solar cells: a device physics primer with application to amorphous silicon", *SOLMAT* **78**, p.1–4, 2003. 567.

[30] K. Toprasertpong, T. Tanibuchi, H. Fujii, T. Kada, S. Asahi, K. Watanabe, M. Sugiyama, T. Kita, Y. Nakano, "Comparison of electron and hole mobilities in multiple-quantum-well solar cells using a time-of-flight technique", *IEEE J. Photovolt.* **5** (6), 1613, 2015.

[31] W. Shockley, H.J. Queisser, "Detailed balance limit of efficiency of p-n junction solar cells", *J. Appl. Phys.* **32** (3), 510, 1961.

[32] J. W. Matthews, A. E. Blakeslee, “Defects in epitaxial multilayers: I. Misfit dislocations”, *J. Cryst. Growth* **27**, p.118-125, 1974.

[33] S. Sudo, Y. Nakano, M. Sugiyama, Y. Shimogaki, H. Komiyama, K. Tada, "In-situ As-P exchange monitoring in metal-organic vapor phase epitaxy of InGaAs/InP heterostructure by spectroscopic

and kinetic ellipsometry", *Thin Solid Films* **313-314**, p.604–608, 1998.

[34] M. Deura, Y. Shimogaki, Y. Nakano, M. Sugiyama, “Kinetic analysis of surface adsorption layer for InGaAsP-related binary materials using in situ RAS”, *J. Cryst. Growth* **310**, p.4736-4740, 2008.

Chapter 5 GaAsP on Si heteroepitaxy

III-V top cell integrated on active Si substrate is a promising structure for realizing a high efficiency solar cell with cost reduction [7]. Direct growth of III-V epitaxial layer on Si substrate by metal-organic vapor phase epitaxy (MOVPE) is a one of the favorable method for its process simplicity and productivity. Integration on Si substrate, however, have several challenges coming from the characteristic differences such as lattice constant, thermal expansion coefficient and polarization. GaP film is a good candidate as a starting layer for direct growth of III-V top absorber on an active Si substrate due to its optical transparency and lattice matching with Si [8]-[9].

Antiphase domains (APDs) originated from polarization difference between III-V and group-IV material is known as one of the biggest factors contributing to threading dislocations in III-V heteroepitaxial layers integrated on Si [10]-[11] and those dislocations degrade the solar cell performance [12]-[13]. Double-stepped Si surfaces have to be prepared before heteroepitaxial growth of III-V layers on Si to suppress such APDs.

Double-stepped Si surfaces can be achieved at comparatively low-temperature annealing under arsenic ambience in MOVPE chambers and subsequent GaP epitaxial layer could be grown on that surface [14]-[18]. Here, the surface state of Si substrate and grown GaP was analyzed by in-situ reflectance anisotropy spectroscopy (RAS) measurement in the MOVPE chamber during the processes. In the following sections, the experimental details and results for double-layer step formation and succeeding GaAsP/GaP/Si heteroepitaxy are discussed.

5.1 Double-layer step formation on Si(1 0 0)

To suppress dislocations comes from the antiphase domain, Si(1 0 0) surfaces have to be formed as double-layer step, before GaP heteroepitaxy on Si substrates. In the MOVPE reactor, different from the MBE process, it is difficult to make double-layer step on Si(1 0 0) surface even in using vicinal substrate due to the carrier gases in the reactor.

Double-layer step can be formed in the MOVPE with either hydrogen ambience [19]-[21] and arsenic ambience [22]-[23]. Among these techniques, what was mainly studied in the conventional surface reconstruction method was the double-layer step formation under pure H_2 ambience which is used for carrier gases. However, it requires high temperature around 1000 °C for removing the oxide layer on Si surface in H_2 process, which induces unintentional impurity diffusion on Si substrate and it results the degradation of

carrier lifetime in Si bulk [24]-[27]. To avoid unintentional impurity diffusion, lower process temperature is required than in H_2 ambience process. For this reason, in recent years, low temperature processes in As ambience have attracted attention. However, the relationship between the conditions for pretreatment of the Si surface under As ambience and the surface state has not been clarified yet.

The purpose of this research is clarifying the relationship between process parameters and surface reconstruction for optimizing the process conditions with As ambience MOVPE reactor. The experimental details and results are discussed in section 5.1.2-3.

5.1.1 Double-layer step formation in hydrogen ambience

Before discussing about As ambience process, the conventional H_2 ambience reconstruction is introduced in this section. Figure 5-1 shows a schematic of process flow for Si surface reconstruction under H_2 ambience under reactor pressure of 950 mbar.

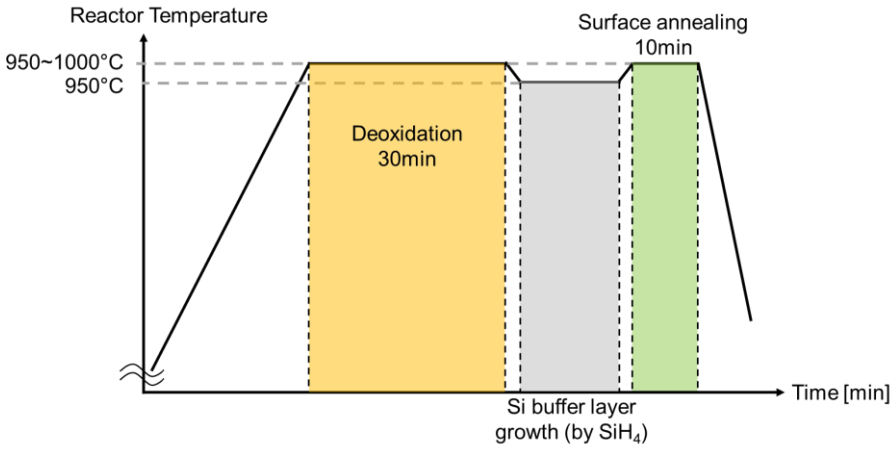

Fig. 5-1 A example schematic of process flow for Si(1 0 0) surface reconstruction with hydrogen ambience in MOVPE reactor [20], [28].

The conventional Si surface reconstruction process with H_2 is following the steps as below.

Step1) Thermal deoxidation on Si surface with high temperature (over 950 °C).

Step2) Si buffer layer growth.

Step3) Surface atom re-ordering.

In H_2 process, Si buffer layer is usually used for getting smooth surface after deoxidation step with high temperature. The precursor for Si growth is silane (SiH_4) which can be used as dopant for subsequent III-V heteroepitaxy.

The best surface reconstruction result for Si(1 0 0) double-layer step has reported was by the process under H_2 ambience with high temperature. However, mentioned in above, there are two concerning problems which need to be avoided. From these reasons, the As ambience Si surface reconstruction with lower temperature is preferred for solar cell application.

In following sections, the details of experimental conditions and results studied with As ambience in this research are discussed.

5.1.2 Arsenic modified Si surface

Surface reconstruction scheme: vacancy diffusion

Si dimers on the surface are moving by surface vacancy generation, diffusion, and annihilation at step edges, which may account for the formation of double-layer step structure. Figure 5-2 depicts a schematic for anisotropic Si vacancies diffusion.

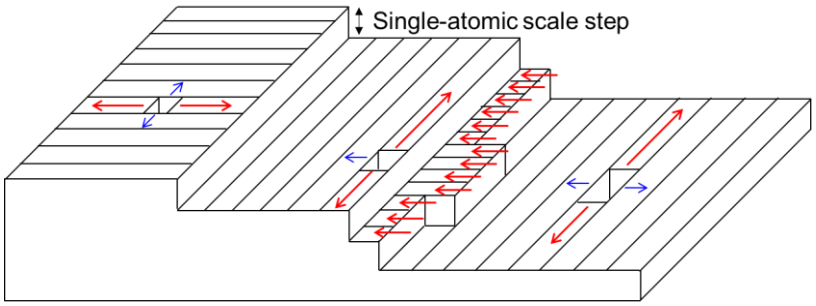

Fig. 5-2 A schematic for movement of vacancies: vacancies move fast along dimer direction. Where, the line direction corresponds to the dimer direction.

The vacancies diffuse to adjacent dimer, and annihilation at the end of the dimer rows. The vacancies preferred to move along the dimer rows, so the moving direction which are described as red arrow line in fig. 5-2 is faster than blue line.

In arsenic process, supply of arsenic precursors such as tertiary-butyl arsine (TBA) or arsine (AsH_3) during thermal deoxidation of the Si surface was known to decrease the required temperature below 900 °C [16], [29]-[30], due to its etching effect on oxide layer of As. In As ambience process, following steps are required.

1) As absorption on the Si surface: breaking the Si dimer and forming As terminated surface.

2) As desorption and surface re-ordering: generating the vacancies by As desorption and re-ordering the

surface atoms by vacancies diffusion.

The As is applied as etchant for SiO_x on Si surface so the process temperature for deoxidation can be lowered, however, it has to be considered about the roughened surface by etching. In the double-layer step formation with As ambience, it is crucial to control the process parameters for obtaining clear surface anisotropy.

Experimental method and results

Samples were prepared in a horizontal MOVPE reactor (AIX-200/4 and AIX-200 from Aixtron, AIX-200 reactor has an MOVPE-to-UHV transfer system [31]) and the whole process was monitored with in-situ RAS measurement (EpiR-M TT and EpiRAS-200 from Laytec). As precursors, tertiary-butyl arsine (TBA) is used with purified hydrogen carrier gases. P-type doped Si (100) substrates with 4° off cut towards the [111] direction were used in all process in this work. The Si substrate was loaded into the MOVPE chamber after wet-chemical processes as following.

1) Ultrasonic bath with isopropanol for 10 min.

2) Soaking in sulfuric acid-hydrogen peroxide mixture (SPM) solution at 180 °C for 10 min.

3) Dipping in 0.5 % HF solution at room temperature for 1 min.

The initial process condition for double-layer step was set by benchmarking ref.[17] which is the proposed condition from our co-worker group (TU Ilmenau, Thomas Hannappel Lab.).

Figure 5-3 shows the schematic of process flow for As modified double-layer step Si(1 0 0) surface formation.

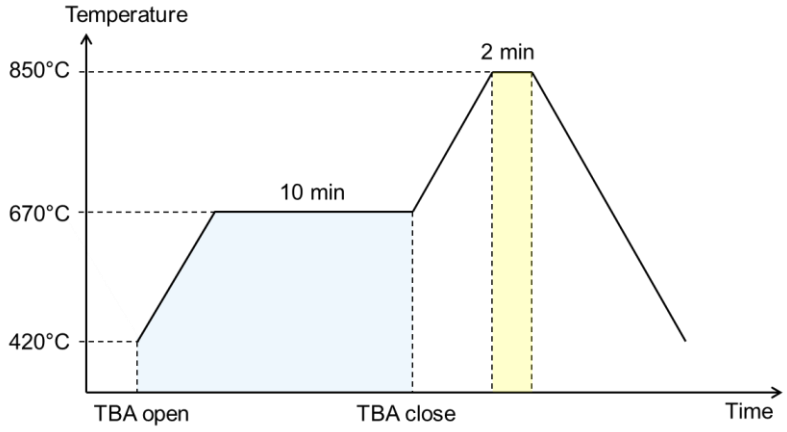

Fig 5-3 A schematic of process flow for Si(1 0 0) surface reconstruction process with As ambience.

The reactor pressure is 750 mbar, and partial pressure of arsenic is 0.896 mbar in this process. 670 °C which is slightly higher than the pyrolysis temperature [32] of TBA, but comparable to the decomposition temperature of arsine (AsH_3) which was used for As coating step. The TBA source is provided at 420 °C, and raise up to coating temperature, then kept at 670 °C for 10 min. The surface annealing temperature is as high as 850 °C (not the real surface temperature but the reactor temperature), and the surface reconstruction time is controlled by in-situ RA signal (the sample start to cool down when the peak at 3.2 eV has maximum value, and in this condition, it was 2min).

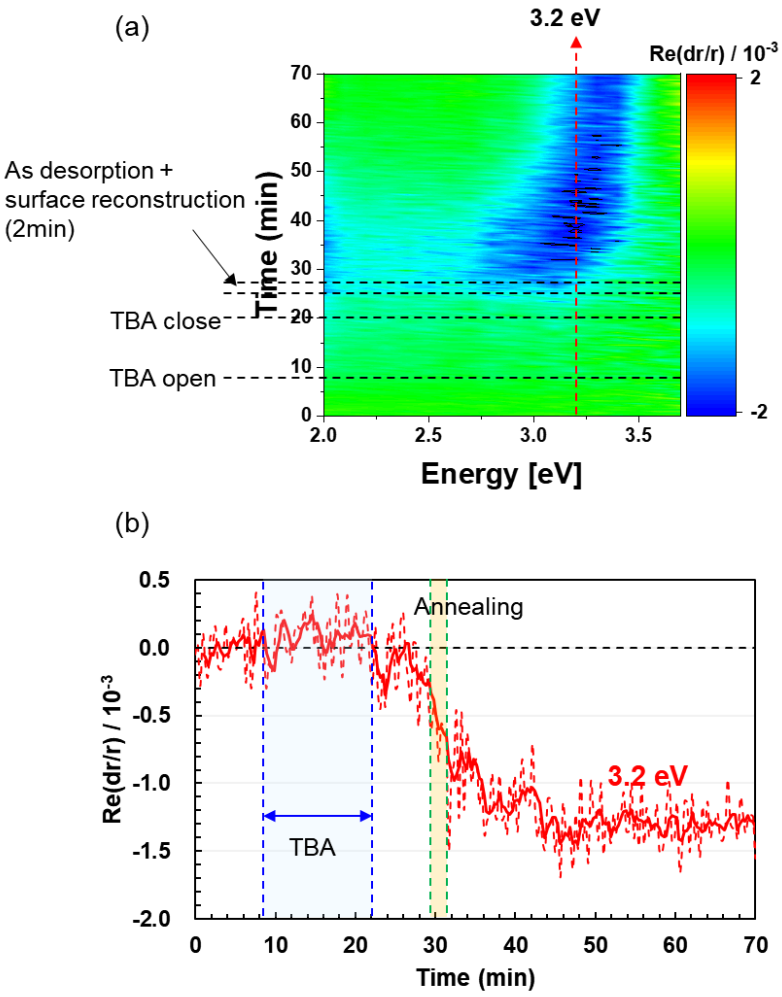

Fig 5-4 In-situ measured transient RA signal during the process: (a) color plot for whole range of energy, and (b) Transient RA for 3.2 eV. Where, the Transient RA for 3.2 eV is calculated value for subtracting the baseline. The dashed line in (b) is the time transient RA signal and solid line is the interval mean value of four measurement points.

Figure 5-4 shows the in-situ Transient RA. The dimer peak of Si-Si at 3.2 eV [33] appears after closing the TBA supply, and the peak intensity is increasing with annealing due to As desorption and surface re-

ordering by vacancies diffusion. Figure 5-5 shows the surface anisotropy measured by RA signal at room temperature.

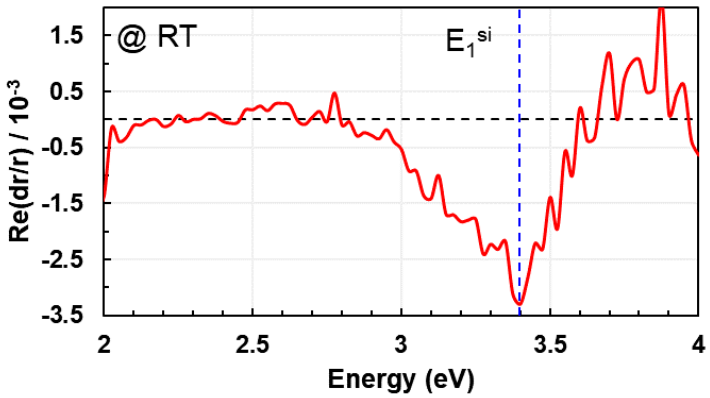

Fig 5-5 RA spectra measured at room temperature.

There is a clear anisotropic peak at 3.4 eV of Si E_1 energy level is [33] observed, and A-type double-layer step Si(1 0 0) surface is formed. In this section, the basic scheme of As ambience Si surface pretreatment and the experimental method are introduced.

In the following section, more detailed information about Si(1 0 0) surface reconstruction with As is discussed by using not only RAS but also XPS and LEED for clarifying the relationship between process parameters and surface states.

5.1.3 Si(1 0 0) surface preparation: process parameters and surface states

In this section, the relationship between process parameters and Si(1 0 0) surface states is discussed.

5.1.3.1 Robust process with arsenic

In many researches for Si surface treatment, it is concerned about the Si surface oxidation after removing the oxide layer on Si by wet-chemical etching, because the Si surface is easy to oxidize [34] in the air. Especially, in the surface reconstruction process, deoxidation is very important to subsequent III-V growth. From this concern, after the wet-chemical etching process, many researchers try to load samples into the MOVPE reactor in a short time so as not to be exposed to the air as much as possible.

Since As has an effect of etching the Si surface, differently from the H_2 ambience process, it can be considered that As ambience process is not much sensitive to the very thin oxide film produced by exposure

to air. In this work, we demonstrate the robustness of the Si deoxygenation and surface reconstruction process using As.

Here, two samples is prepared as following.

- ✓ Sample 1: The sample loaded into MOVPE chamber as soon after wet-chemical etching. (but even in this case, it takes about 20 min)
- ✓ Sample 2: The sample loaded into the pre-chamber of the MOVPE at the same time with sample1. However, it was stocked at a pre-chamber (filled with N_2 and O_2 < 0.1ppm) a day before load into reactor.

All process conditions including reactor pressure (750 mbar), temperature (As coating at 670 °C and surface reconstruction at 850 °C), process time (As coating 10 min and surface annealing 2 min) and partial pressure of As (0.896 mbar) is same as introduced in previous section.

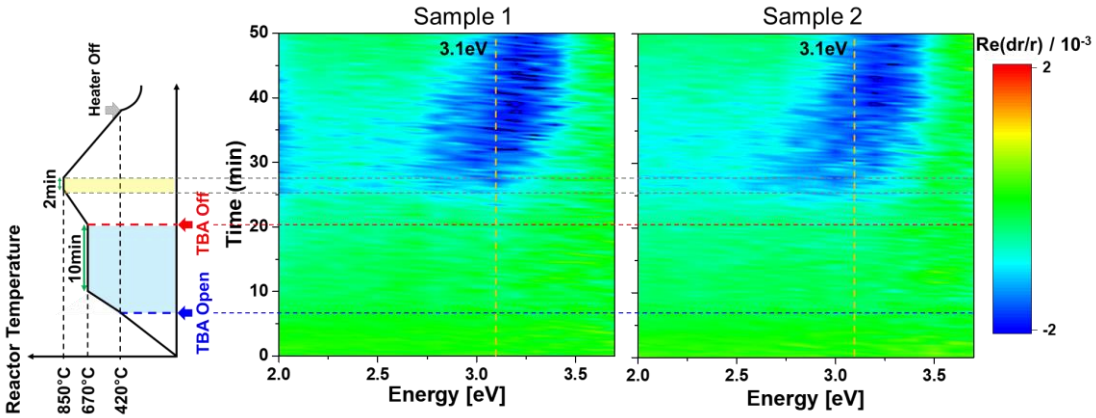

Fig. 5-6 In-situ Transient RA: 1) sample 1: sample loaded into reactor as soon as loading into the MOVPE pre-chamber, and sample 2: sample loaded into reactor after 1day kept in the pre-chamber.

Figure 5-6 shows the in-situ time transient RA during the process. Figure 5-7 describes the Transient RA for 3.1 eV, and RA spectra measured at room temperature.

From the above results, it is clear that the obtained anisotropic properties for Si surfaces from the two samples are identical. As expected for As etching effect on SiO_x on Si surface, As ambience process is not much sensitive to the very thin oxide film produced by exposure to air. However, the pre-chamber is not so oxygen rich environment, so additional exploration is needed for long exposure to atmospheric conditions.

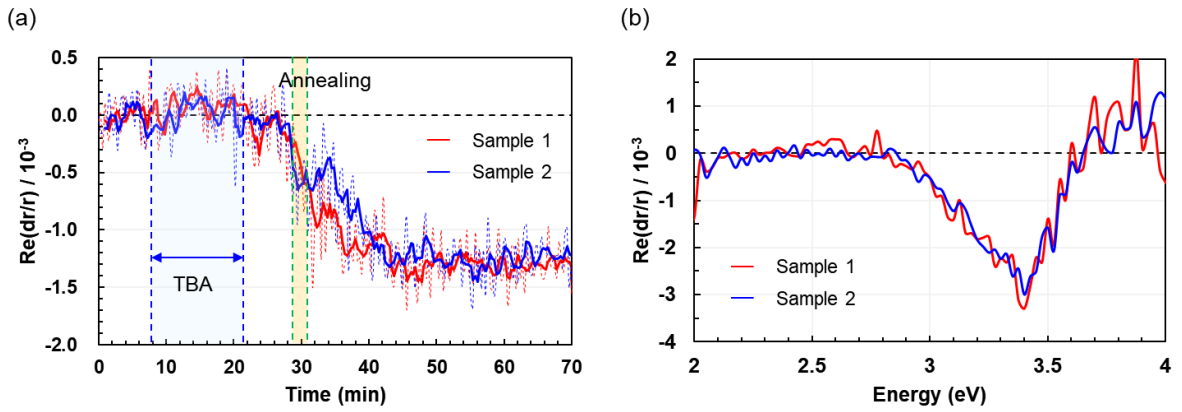

Fig. 5-7 In-situ measured transient RA signal during the process: (a) Transient RA for 3.1 eV, and (b) RA spectrum measured at room temperature. Where, the dashed line in is the time transient RA signal and solid line is the interval mean value of four measurement points.

5.1.3.2 Annealing condition and Si surface reconstruction

The thermal treatment condition is crucial for surface reconstruction [35], but the relationship between the thermal process condition and surface states has not been much investigated about As ambience process. Here, the following experiment was designed to investigate the process conditions of surface reconstruction.

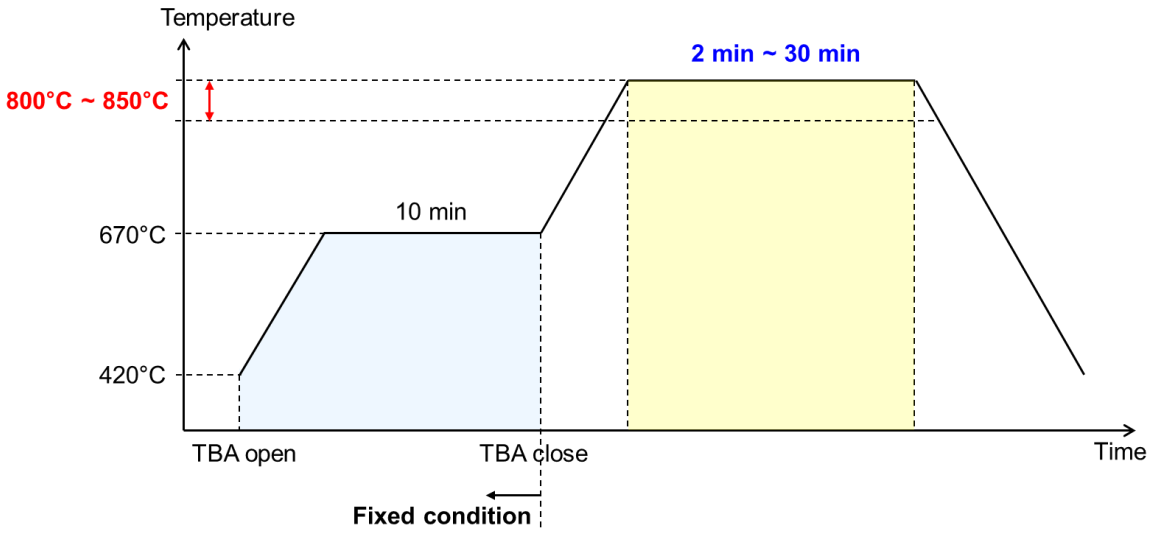

Fig. 5-8 A schematic of process flow: process parameters are verified in the range of 1) annealing temperature from 800 °C to 850 C°, and 2) annealing time from 2 min to 30 min. The other conditions such as the partial pressure of As, As coating temperature and time, and the reactor pressure are the same.

- ✓ The process conditions except thermal annealing conditions are same in all experiments.
  - → Reactor pressure: 750 mbar / As partial pressure: 0.896 mbar / As coating temperature: 670 °C / As coating duration: 10 min / Temperature raising time (total time for temperature ramp up form 670 °C to annealing temperature): 5 min.
- ✓ Total 13 samples are prepared in MOVPE reactor.
  - → Reactor temperature for annealing step: 800 °C / 825 °C / 850 °C
  - → Annealing time: 2 / 5 / 10 / 15 / 30 min
- ✓ RA signal is measured in rotation system for comparison.
  - → The RA signal measured in the rotation system represents the absolute value of the anisotropic signal. In the non-rotation system, the RA signal intensity depends on the sample input direction, so exact comparison is difficult. Therefore, for comparing every sample in same measurement condition, the rotation system is applied. However, when measuring the RA signal in a rotating environment, the intensity of the value may vary depending on the setting of the rotation speed, and the rotating speed is changing by reactor temperature and pressure. Therefore, this should be noted.

Figure 5-11 shows the RA intensity at 3.3 eV measured at 200 °C for each sample.

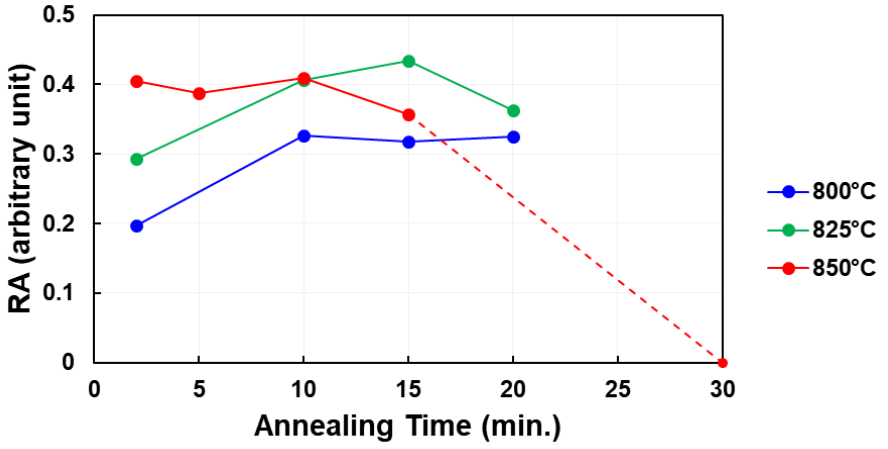

Fig. 5-9 Anisotropic signal intensity comparison: RA intensity at 3.3 eV measured at 200 °C, 750-mbar.

In fig. 5-9, the RA intensity shows clear dependency to the thermal treatment condition.

1) Annealing time can be shorten at high temperature.
2) Even in low temperature process of 825 °C, surface anisotropic signal intensity can be

obtained to the same level as 850 °C, but it requires longer time.

3) There is lower limit on annealing temperature: under 825 °C (expected sample surface temperature is lower than 800 °C), high RA intensity can not be obtained even with long time annealing.

4) The double-layer step surface that has been once formed disordered with long time annealing. This can be clearly seen in fig. 5-10 which shows RA signal measured during 30 min annealing at 850 °C.

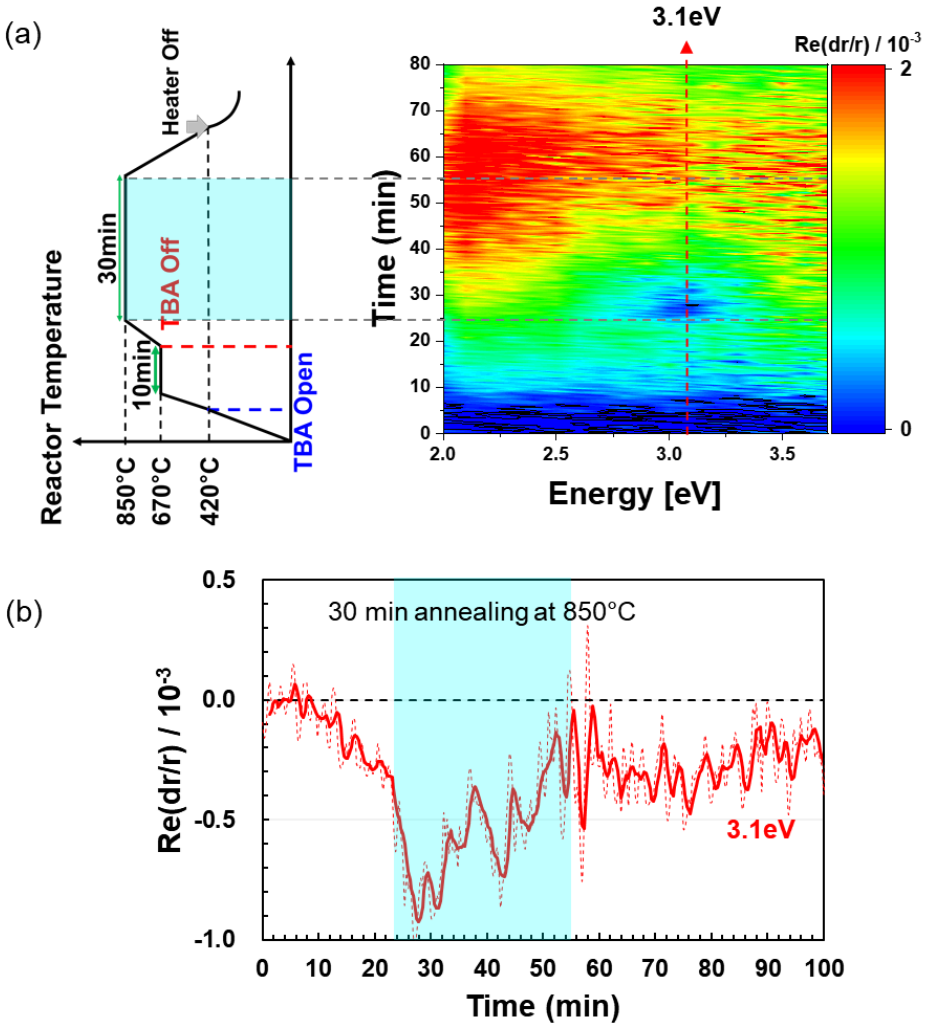

Fig. 5-10 (a) A schematic of process flow and correspondence time transient RA. (b) Time transient RA at 3.1 eV.

As shown in Figure 5-10, the RA intensity at 3.1 eV, indicating Si-Si dimer anisotropy, increases at the beginning of annealing and gradually decreases after 8 minutes. The Si surface eventually stabilizes in the

form of random state, since the process of surface reconstruction is the process by which atoms move to minimize surface free energy.

From the above results, it is verified that the thermal treatment condition and the surface states for Si surface reconstruction are strongly related. From the correlation, it is possible to deduce the optimal annealing time according to each annealing temperature. The results of the Si surface reconstruction using the thermal treatment conditions deduced from the above results are shown in fig. 5-11.

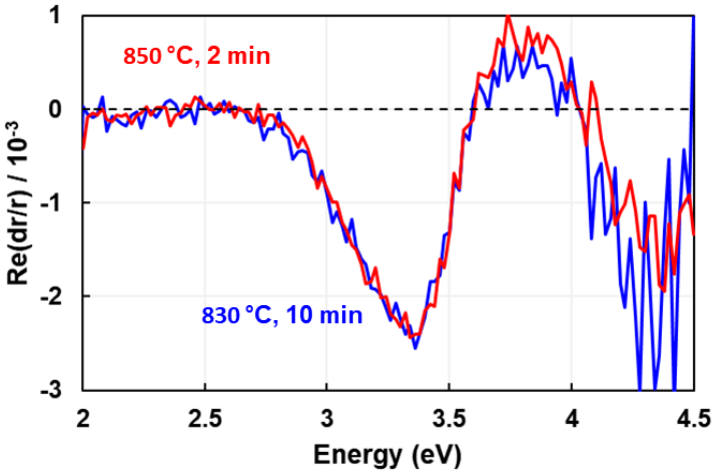

Fig. 5-11 RA spectra measured at 150 °C.

Two samples are prepared for demonstrating.

- ✓ Sample 1 (red line in fig. 5-11): Annealing at 850 °C during 2 min.
- ✓ Sample 2 (blue line in fig. 5-11): Annealing at 830 °C during 10 min.

These two samples, process was done in the totally same condition (reactor pressure: 750 mbar / partial pressure of As: 0.845 mbar) except the annealing thermal condition. The RA anisotropic signals measured in non-rotation system (in this experiment, the susceptor and sample are stationary and the sample is always tilted at 45 ° to the light direction) shows identical intensity of anisotropy spectrum for these two samples.

This study has revealed the relationship between thermal annealing condition and double-layer formation on Si(1 0 0) surface, and has proved its validity.

5.1.3.3 Partial pressure of arsenic and surface deoxidation

Surface oxide removal is another important process for double-layer step formation on the Si surface. In this section, the relationship between the partial pressure of As and oxide removal is discussed. Here, the

following experiment was designed to investigate the process conditions of surface reconstruction.

→ Sample 1: Reactor pressure: 750 mbar / partial pressure of As: 0.78 mbar

→ Sample 2: Reactor pressure: 950 mbar / partial pressure of As: 0.35 mbar

Except the above conditions, all the process conditions are same in the two experiments. Figure 5-12 shows a schematic for process flow in the experiments.

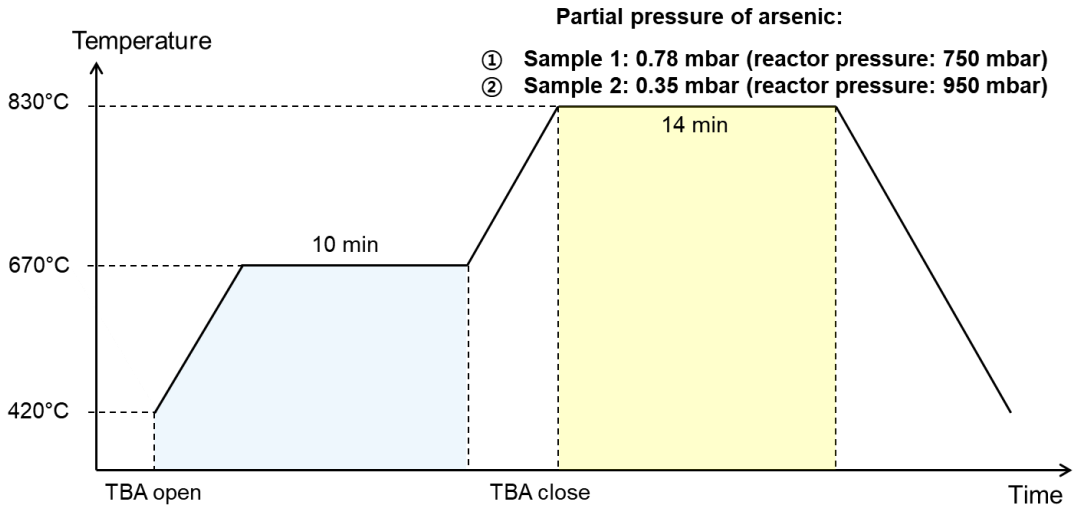

Fig. 5-12 A schematic of process flow: As coating at 670 °C during 10 min, and surface annealing at 830 °C during 14 min.

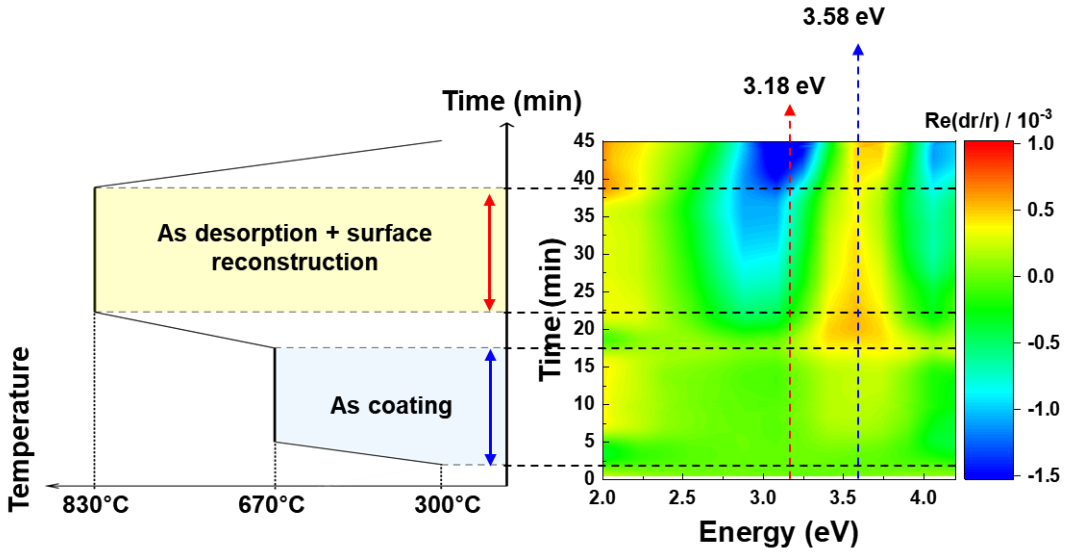

Fig 5-13 A schematic of process flow for Si(1 0 0) surface reconstruction process (left), and correspondence in-situ measured transient RA for sample 2.

Figure 5-13 shows the schematic of process flow and correspondence time transient RA for sample 2.

The TBA source is supplied at 420 °C, and raise up to coating temperature, then keep 670 °C 10 min. The surface annealing temperature is as high as 830 °C (not the real surface temperature but the reactor temperature), and the surface reconstruction time is controlled by in-situ RA signal (the sample start to cool down when the peak at 3.1-3.2 eV has maximum value, and in this condition, it was ~14min in both two conditions). In As coating step, the weak peak is appeared at 3.58 eV, which comes from the As terminated Si surface (As-Si or As-As [35]). More details about time transient RA spectrum for 3.18 eV (for Si dimer anisotropy at 830 °C) and 3.58 eV (for As terminated Si surface anisotropic peak at 830 °C) are described in fig. 5-14.

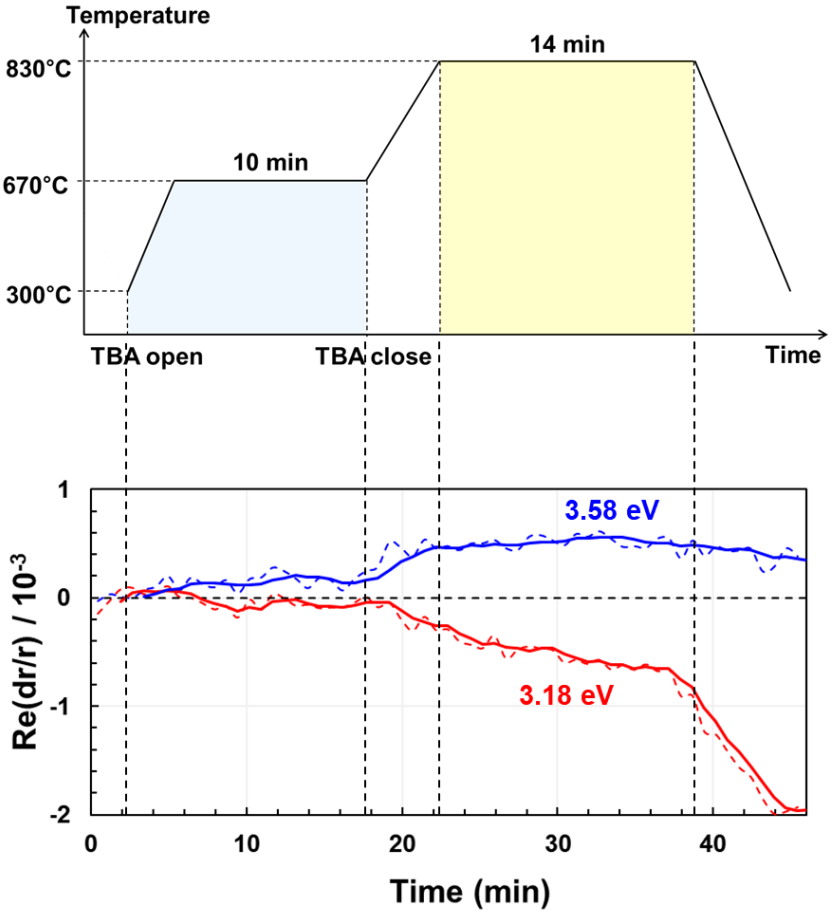

Fig 5-14 A schematic of process flow for Si(1 0 0) surface reconstruction process for sample 2, and correspondence with time transient RA of 3.18 eV (red line) and 3.58 eV (blue line). Where, the dashed line is the time transient RA signal and solid line is the interval mean value of three measurement points.

The dimer peak of Si-Si at 3.18 eV appears after closing the TBA supply, and the peak intensity is

increasing with annealing due to As desorption and surface re-ordering by vacancies diffusion. Figure 5-15 shows the comparison between sample 1 and sample 2 for the time transient RA at 3.18 eV.

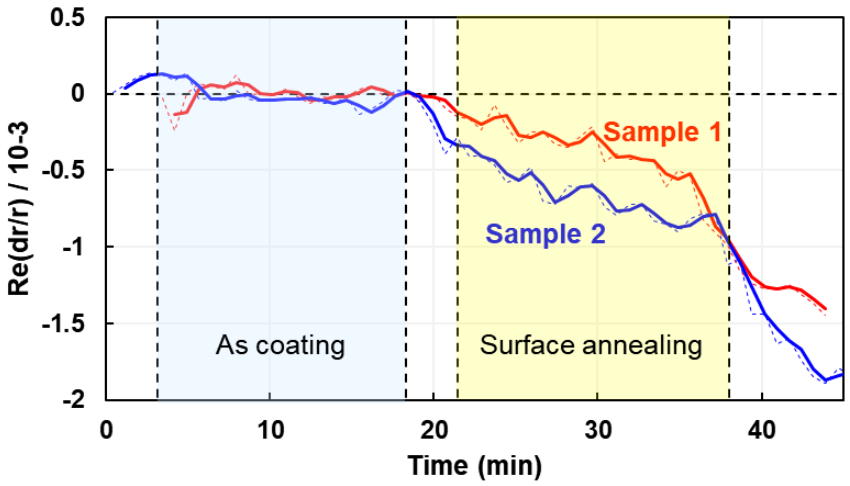

Fig 5-15 A schematic of process flow for Si(1 0 0) surface reconstruction process, and correspondence with time transient RA of 3.18 eV (red line) and 3.58 eV (blue line). Where, the dashed line is the time transient RA signal and solid line is the interval mean value of three measurement points.

It can be seen at fig. 5-15, RA intensity is increasing after stoping the TBA supply in both samples, but the increasing slopes are different in each condition. More details about this difference is discussed in following section, but the difference in the peak intensity is as a result of the difference in reactor pressure rather than due to differences in As partial pressures.

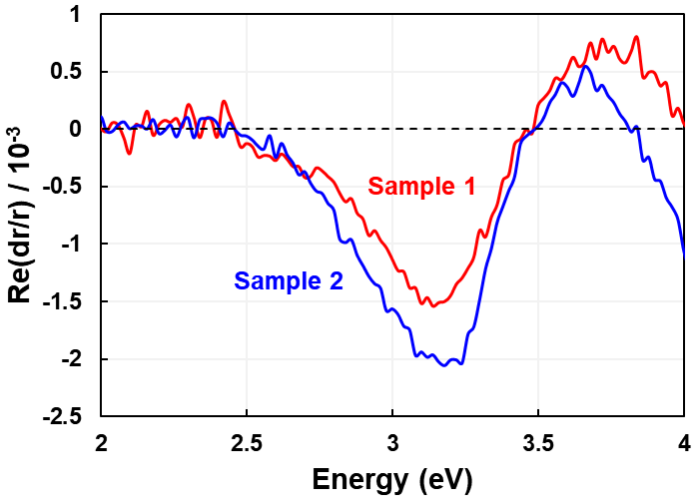

Fig 5-16 RA spectra measured at 420 °C.

Figure 5-16 shows the surface anisotropy measured by RA signal at 420 °C, and fig. 5-17 shows LEED images for prepared samples.

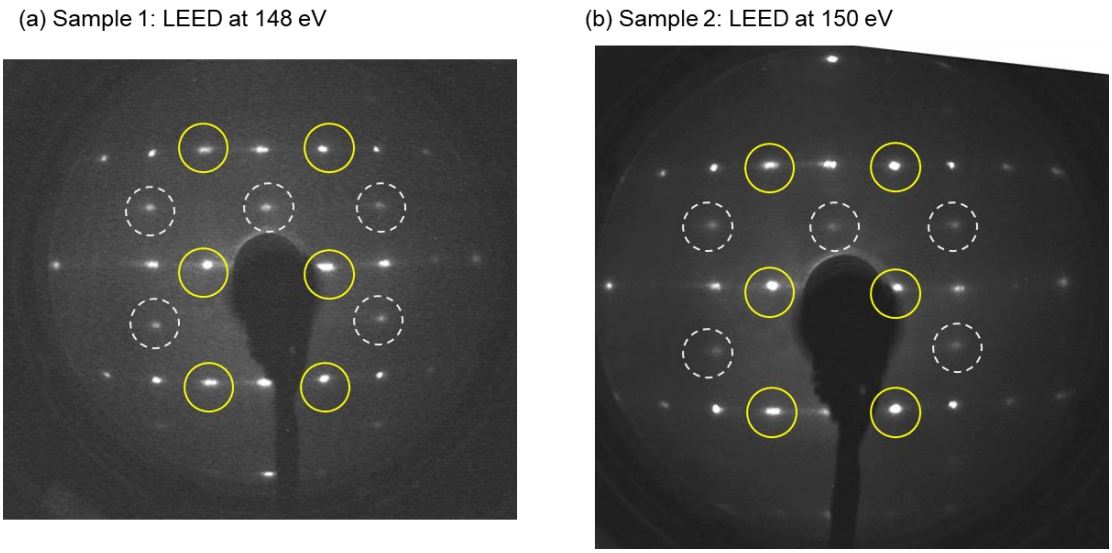

Fig 5-17 LEED image for prepared Si(1 0 0) surfaces for (a) sample 1, and (b) sample 2. Where, yellow and dashed circles mark spots at half order.

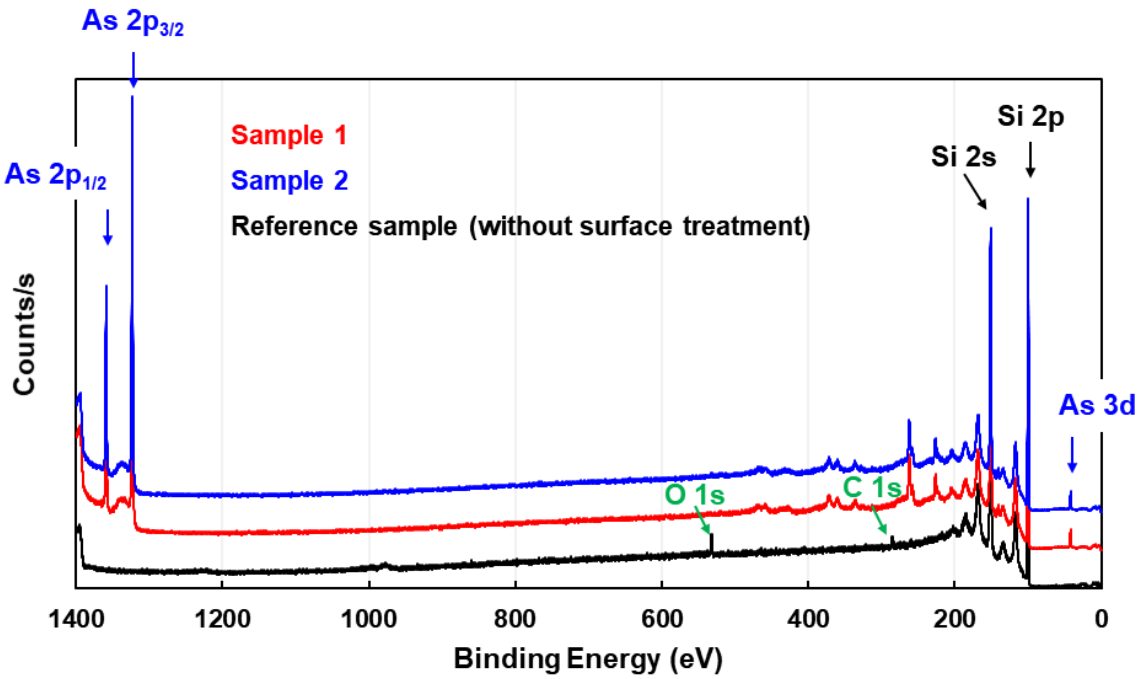

Fig 5-18 XPS spectrum: black line is for the sample before the surface preparation (loaded into XPS measurement chamber after wet-chemical etching), and red line is for the sample 1 and blue line is for the sample 2 after the surface treatment with As ambience.

Figure 5-16 shows anisotropic peak for Si-Si dimer and As terminated surface for A-type Si(1x2) surface, and LEED image shows the major spots for (1x2) structure but with weak (2x1) spots also. In the LEED images, sharp spots are clearly visible, and the minor peak for B-type surface is more clear at sample 1 than at sample 2. Quantitative comparison from LEED image and RA intensity is difficult, but it can be considered that sample 1 has larger domain region of B-type surface than sample 2.

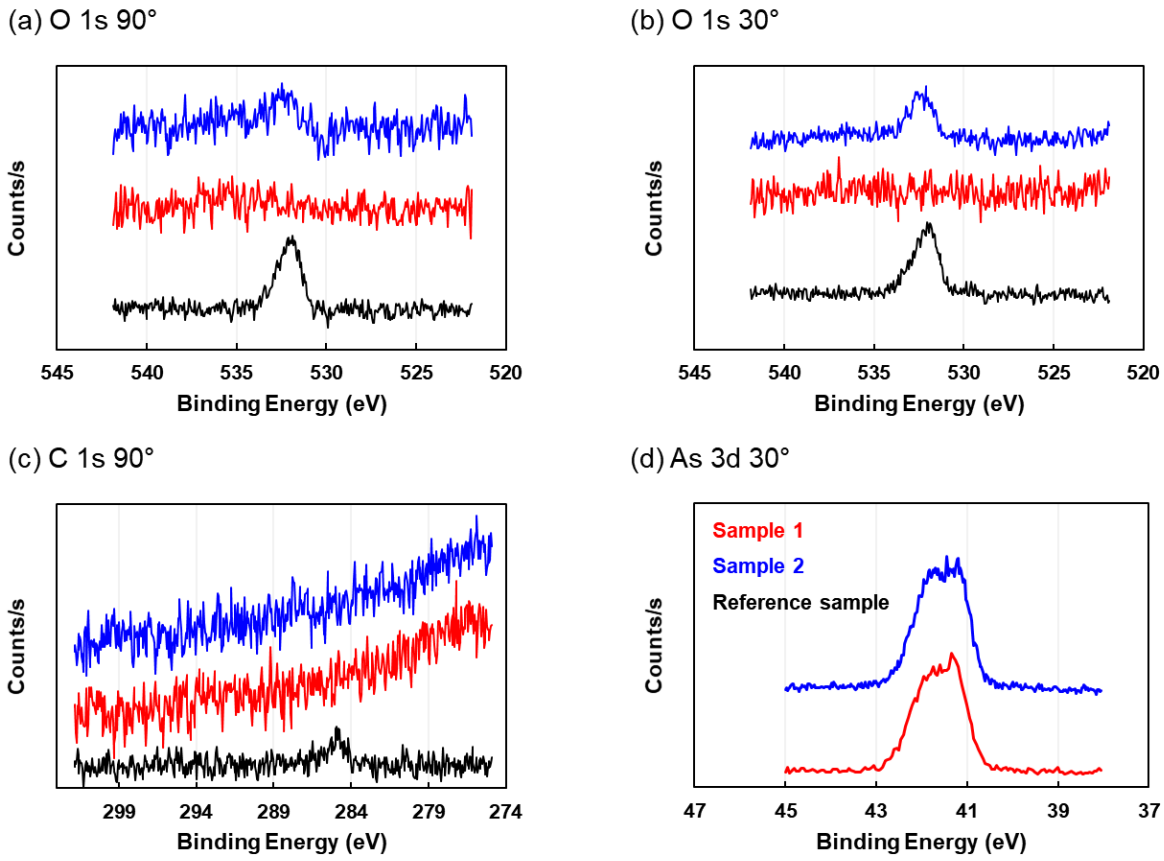

Fig. 5-19 XPS spectrum: (a) O 1s for 90° direction, (b) O 1s for 30° tilted direction, (c) C 1s, and (d) As 3d measurement for 30° tilted direction.

Figure 5-18 and 5-19 shows the XPS data for these samples to identifying the chemical components on the surface. When comparing the XPS data for before-process and after-process, the main focus is the presence of oxygen and carbon which affect surface reconstruction as well as subsequent crystal growth. The carbon was removed successfully in both samples, but still weak oxygen peak is remaining after As process in sample 2. The peak for oxygen for sample 2 is more clear at the 30° tilted measurement which can measure surface dominant data (fig. 5-20).

From these results, it was found that the complete removal of oxide film was difficult at low arsenic

partial pressure. Here, one more experiment is implemented for clarify the deoxidation condition by As, as shown in fig. 5-21.

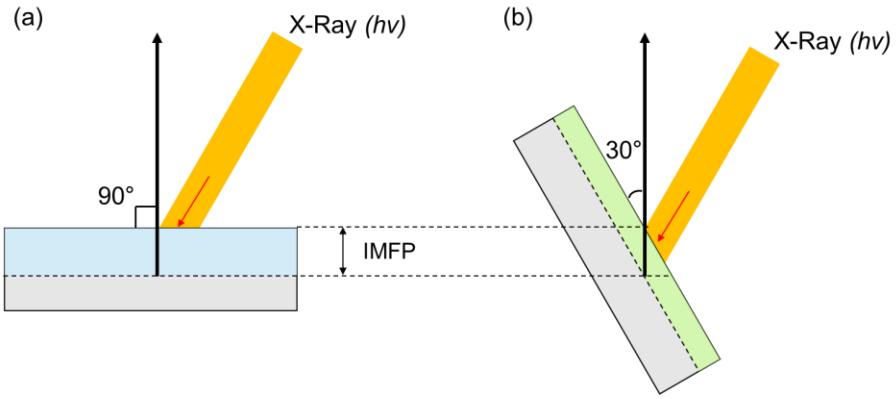

Fig. 5-20 Schematics of XPS measurement: (a) 90° and (b) 30° tilted measurement.

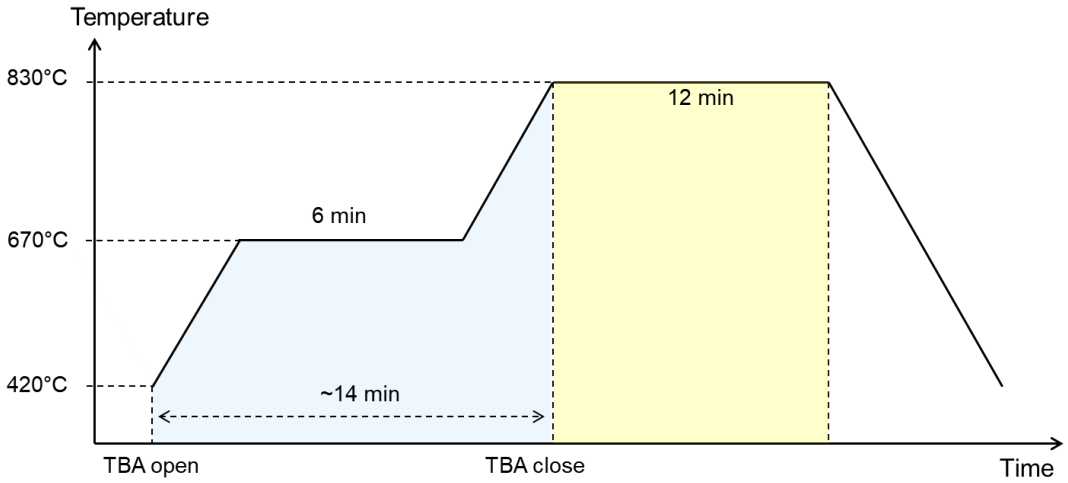

Fig 5-21 A schematic of process flow sample 3: all the conditions are same as sample 2, except As supplying temperature.

The sample 3 prepared with the same condition as sample 2 (reactor pressure: 950 mbar / partial pressure of As: 0.35 mbar / surface annealing temperature: 830 °C) except TBA supply temperature. For sample 3, unlike the previous process, the TBA supply was continued until the reactor temperature reached 830 °C. However, the entire exposure time to TBA is controlled as comparable to other samples (from 420 °C to 830 °C: ~14 min). This condition is intended to investigate the effect of etching temperature on the same arsenic partial pressure. However, it should be noted that long time exposure to TBA at high temperature roughen the Si surface [36], so it is considered in experimental design.

Figure 5-22 shows the RA spectrum measured at 420 °C and the LEED image for sample 3, and fig. 5-

23 shows XPS measurement data. The surface anisotropic signals measured from RAS and LEED are show totally same results for sample 2 and sample 3. From the viewpoint of double-layer formation, both process conditions can form A-type reconstructed surfaces with an RMS roughness ~1 Å.

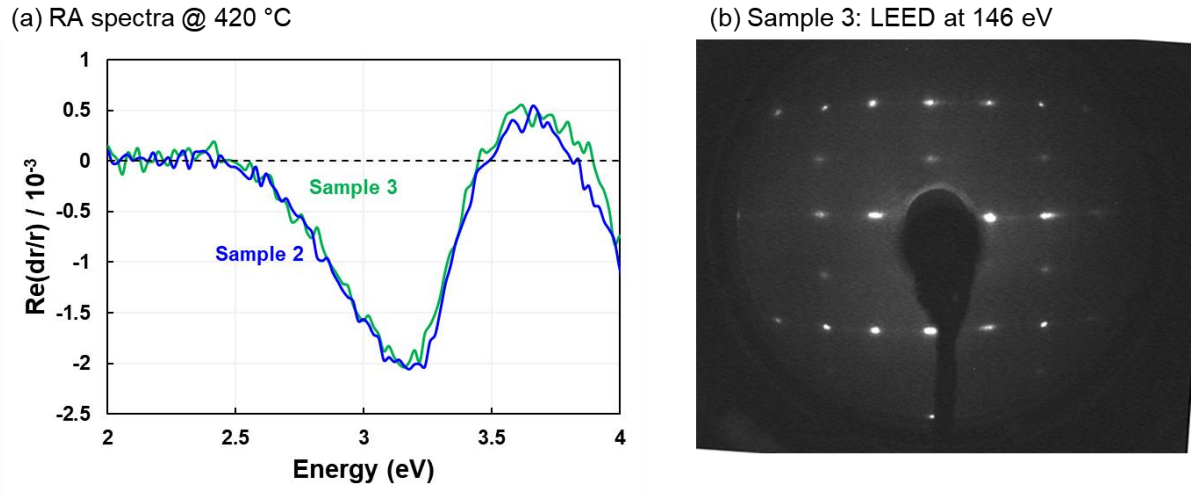

Fig 5-22 (a) RA spectra measured at 420 °C for sample 2 and sample 3, and (b) LEED image for sample 3.

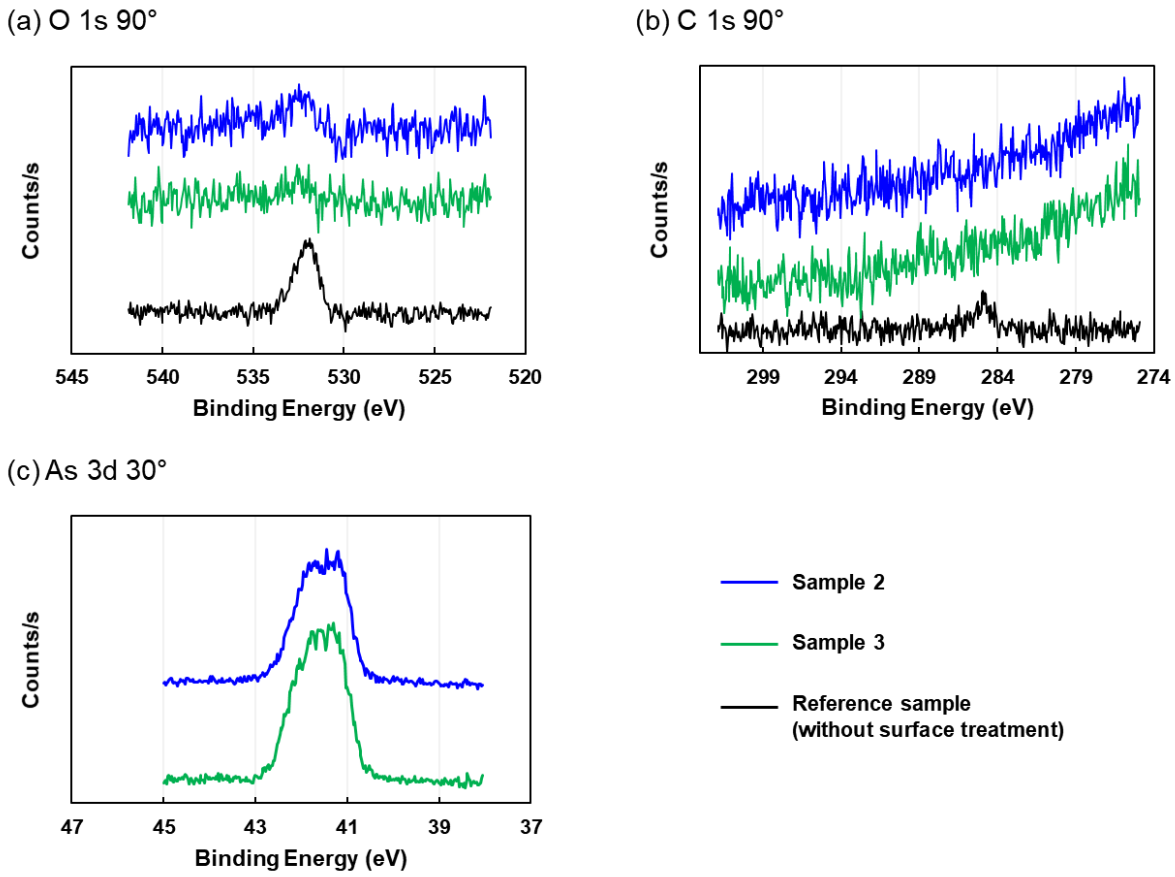

Fig 5-23 XPS spectrum: (a) O 1s and (b) C 1s measured at 90° direction, and (c) As 3d measurement for 30° tilted direction.

Figure 5-22 shows the XPS data for sample 2 and 3 for identifying the chemical components on the surface. The carbon was removed successfully in both samples. For the oxygen in Sample 3, the lower XPS peak intensity compared to Sample 2 can be observed, but still very weak peak is remaining.

From these results, it was verified that the partial pressure of As is an important factor in the removal of surface oxide film on Si, and the As treatment temperature also plays an important role on deoxidation process.

5.1.3.4 Partial pressure of hydrogen and surface reconstruction

As mentioned in the result of the previous part, the pressure of the reactor, which is almost same as the partial pressure of H_2, also plays an important role. Here, the effect of H2 partial pressure on double-layer step formation is discussed.

Figure 5-24 shows a schematic of process flow.

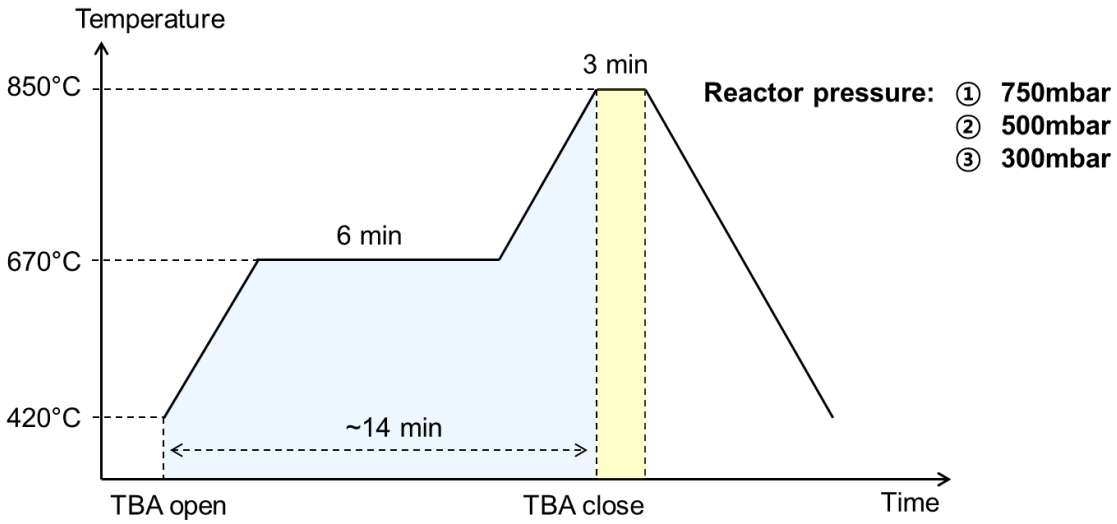

Fig 5-24 A schematic of process flow: Si(1 0 0) surface reconstruction in the reactor pressure of 750 mbar, 500 mbar, and 300 mbar with partial pressure of arsenic 0.846 mbar in all process.

Here, the As partial pressure for all conditions was 0.846 mbar which is enough high to remove the surface oxide as verified in previous works, and total As coating time was controlled about 14 min.

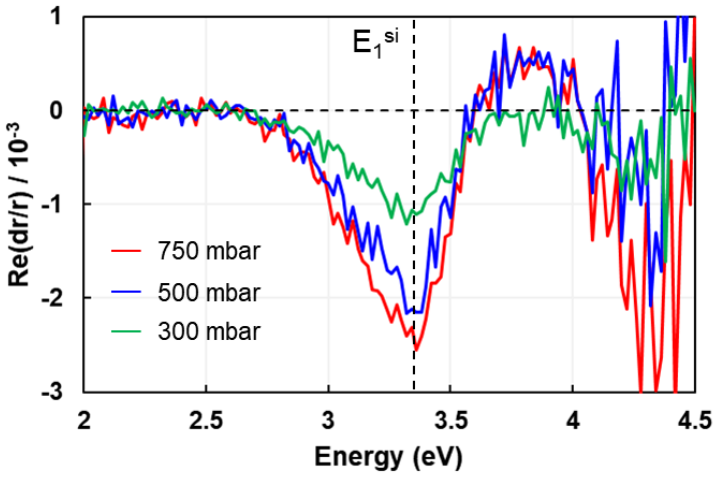

Fig. 5-25 RA spectrum measured at 150°C.

Surface anisotropic signal measured at 150 °C is shown in fig. 5-25. In all samples, RA peak is observed at 3.4 eV which is for Si dimer on the surface, but their intensity is different by each reactor pressure condition. From this tendency, it is clear that higher reactor pressure is required for single domain surface formation on Si(1 0 0). However, strictly speaking, this experimental design has two different conditions which is the pressure at As absorption step and the pressure at desorption + surface reconstruction step.

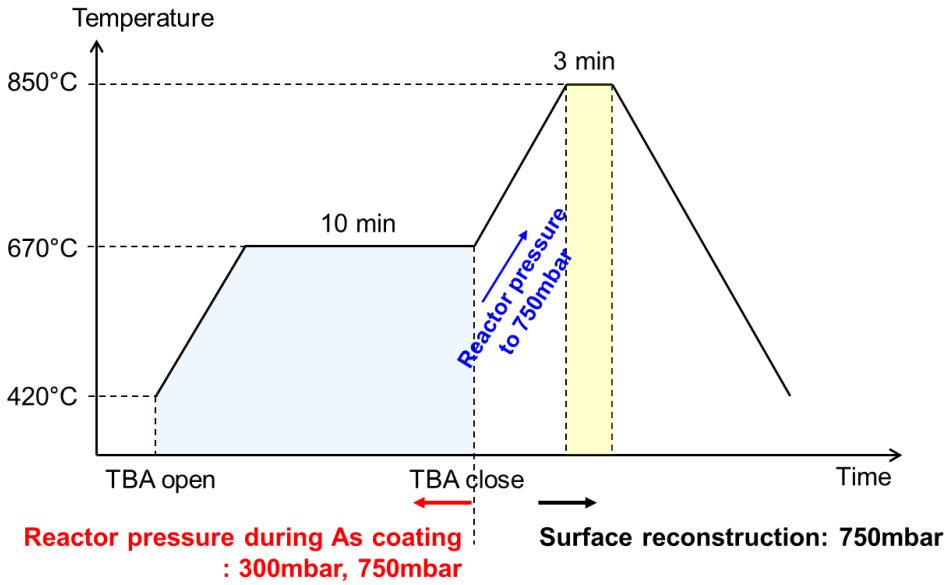

Fig. 5-26 A schematic of process flow: different reactor pressure (300 mbar and 750 mbar with the partial pressure of arsenic 0.846 mbar in each reactor conditions) is applied during As coating step. Then, after closing TBA supply, refill the reactor to 750 mbar, and surface annealed at 850 °C, 3 min.

To clarify the exact effect of reactor pressure on surface reconstruction, additional experiment was implemented as shown in fig. 5-27. In the As coating step, different reactor pressure but the same As partial pressure is applied as depicted in fig. 5-27. After stoping the TBA supply, reactor is refilled to 750 mbar with H_2.

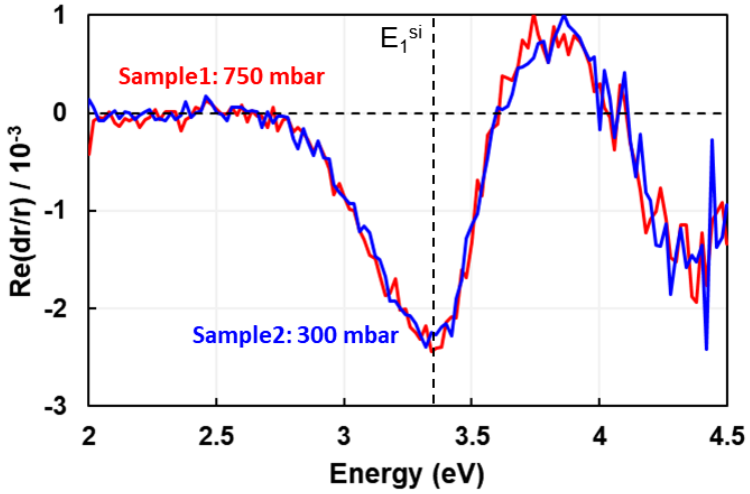

Fig. 5-27 RA spectrum measured at 150°C.

Surface anisotropic signal, measured at 150 °C as shown in fig. 5-27, shows identical intensity of anisotropy spectrum for these two samples.

From the above results, it can be seen that the partial pressure of arsenic greatly affects the removal of the oxide film on the surface, but does not affect the surface reconstruction. About the surface reconstruction process, it can be seen that the surface re-ordering by vacancies generation and diffusion, is strongly depends on the partial pressure of H_2 in the reactor.

5.1.4 Summary of Si(1 0 0) surface preparation conditions

In this research, the relationship between the process parameters and Si(1 0 0) surface reconstruction is verified. The results are summarized as below.

1) Annealing temperature and time

There is strong relationship between annealing time, temperature and surface anisotropy intensity.

- ✓ Lower temperature requires longer time to get strong surface anisotropic signal on Si(1 0 0).
- ✓ There is lower limit on annealing temperature. In this study, the maximum anisotropic signal intensity is decreased at low surface annealing below 825 °C (expected sample surface temperature is lower than 800 °C).
- ✓ Once formed double-layer step surface disordered with long time annealing.

2) Partial pressure of arsenic

Partial pressure of As and the As coating temperature are important parameters for removing oxide film on the Si(1 0 0) surface. In this research, 0.78mbar and 0.35mbar of As partial pressure, and 420 °C-670 °C / 420 °C-830 °C As supply condition are verified. In this work, it is verified that high As partial pressure and supply temperature is effective to remove the oxide layer.

Remaining oxide is not detected by RA signal which is the only in-situ measurement method in AIX-200/4 reactor or other MOVPE which has no transfer system (MOVPE-to-UHV). From these reasons, rather high As partial pressure and high temperature is used in this following experiments.

3) Partial pressure of hydrogen

Partial pressure of hydrogen is important parameter for As desorption and surface reconstruction. In this research, 300mbar, 500mbar, and 750mbar is verified. The RA intensity of the As terminated Si surface is very well correlated with the hydrogen pressure.

In order to obtain a strong anisotropic signal, it is advisable to carry out the process under the highest possible reactor pressure. The for the MOVPE reactors used in this research, the maximum available reactor pressure at 850 °C is, 1) AIX-200/4: 750 mbar, 2) AIX-2000HT: 750 mbar, and 3) AIX-200: 950 mbar (this reactor is not located in Tokyo Univ. but located in our co-work group TU Ilmenau, Germany).

From these results, a new condition for double-layer step formation on Si(1 0 0) is decided as below.

1) Rector pressure: 750 mbar
2) As partial pressure: 0.84 mbar
3) As supply temperature: 300 °C-850 °C (entire time is controlled as ~14 min)
4) Surface annealing temperature: 850 °C
5) Surface annealing time: 3 min

The RA data for above process condition is depicted in fig. 5-28 and 5-29.

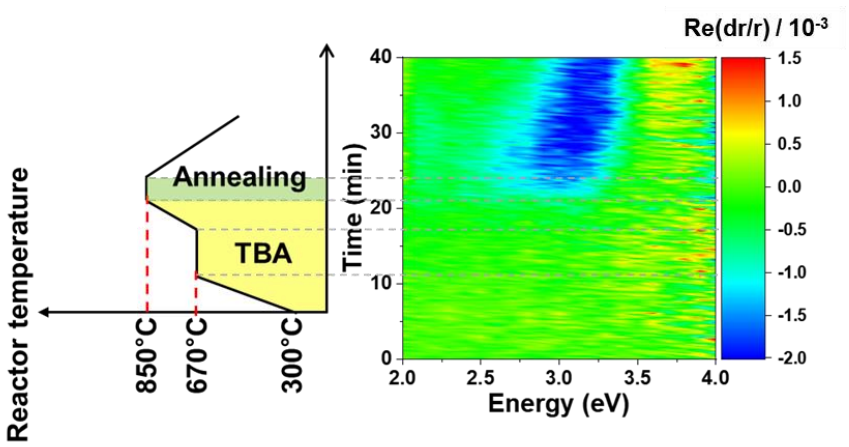

Fig. 5-28 A schematic of process flow and correspondence time transient RA.

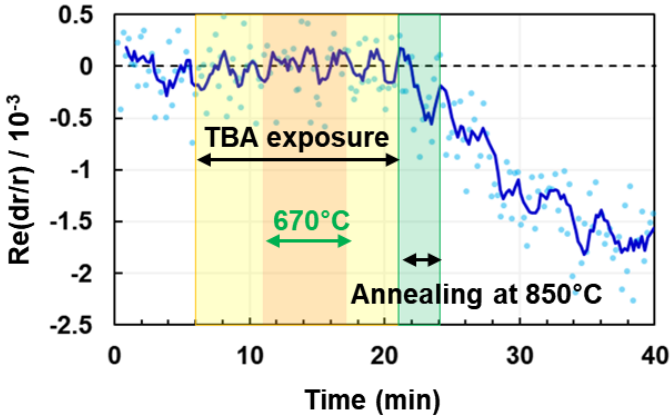

Fig. 5-29 Time transient RA at 3.1 eV.

The A-type Si(1 0 0) surface is successfully obtained by this process condition. In following sections, this surface reconstruction process condition is used for double-layer step formation on Si(1 0 0) for subsequent GaP growth.

5.2 GaP heteroepitaxy on Si(1 0 0) surface

GaP/Si template is a good candidate as a seed layer for subsequent GaAsP heteroepitaxy. In this research, the surface state of GaP(1 0 0) grown on double-layer stepped Si(1 0 0) surface is used as in-situ reference. The measured RA spectra of GaP/Si(1 0 0) surfaces have been established and benchmarked to surface science techniques in previous studies [37].

5.2.1 GaP heteroepitaxy on Si(1 0 0): surface states of GaP/Si

For GaP/Si(1 0 0) heteroepitaxy, a two-step process [41]-[42] was applied. GaP was nucleated with alternating (TBP, TMGa) pulses of 1.5s each (starting with TBP, no pause in between), at 420 °C in reactor pressure of 100 mbar with increased V: III ratio of 40, compared to growth. GaP epilayers were grown using TBP and TMGa at 595 °C, 50 mbar with V: III=13 during 150 sec. The grown epitaxial layer was analyzed by RA and XRD measurement data. The layer thickness of grown GaP was ~50 nm was obtained by ellipsometry measurement (growth speed: 20 nm / min).

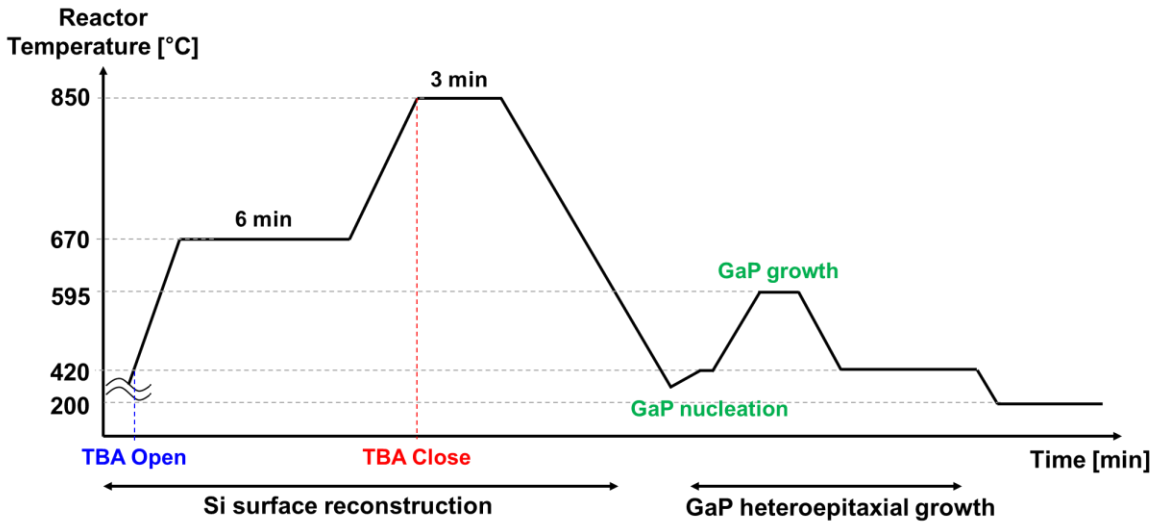

Fig. 5-30 A schematic of process flow for GaP/Si(1 0 0) heteroepitaxy.

Figure 5-31(a) shows the time transient RA measured during the entire process of GaP heteroepitaxy on prepared Si(1 0 0) surface. Figure 5-31(b) and (c) show the in-situ measured RA signals at the surface reconstruction step.

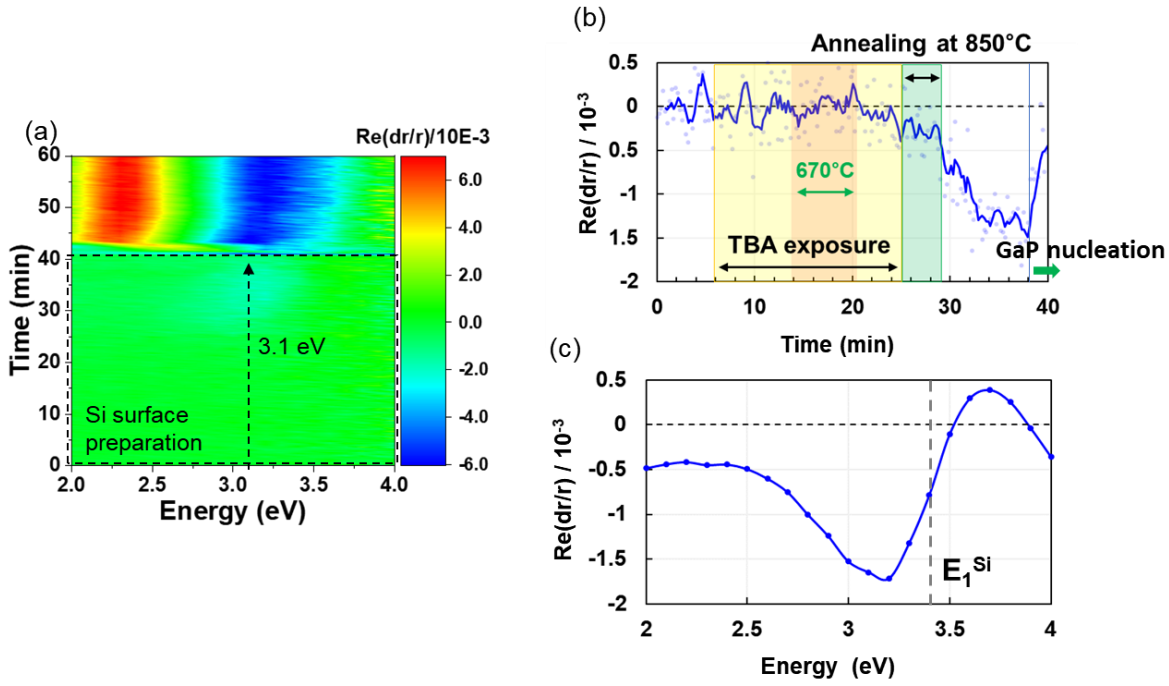

Fig. 5-31 (a) Color plot for time transient RA during the GaP growth on double-layer stepped Si surface. (b) Time transient RA at 3.1 eV, and (c) RA spectra measured at 420 °C.

RA spectra for Si(1 0 0) anisotropy measurement at 420 °C measured immediately before subsequent GaP growth on prepared Si(1 0 0) surface is shown in fig. 5-31(c). The clear anisotropic peaks are observed at 3.2 eV 3.7 eV which are derived from As terminated A-type Si(1 0 0) surface. From this, it could be deemed that the double-layer step surface was successfully formed on Si(1 0 0) surface.

Figure 5-32 shows the in-situ RA spectrum measured at GaP growth process step. It is the RA signal of the same sample as fig. 5-30, but it shows only the part of GaP growth step is picked up. The grey dashed lines represent the critical points energies of GaP [38].

The main characteristics of the RA signal on the reconstructed P-terminated (2x2)/c(4x2) GaP(1 0 0) surface are a minimum peak value at around 2.3 - 2.6 eV and maximum peak at 3.4 – 3.7 eV [37],[39]. The minimum peak is considered that comes from the transition of dimerized P atom which is not bound to H atom [39], and the maximum peak is associated with a E_1 transition [40].

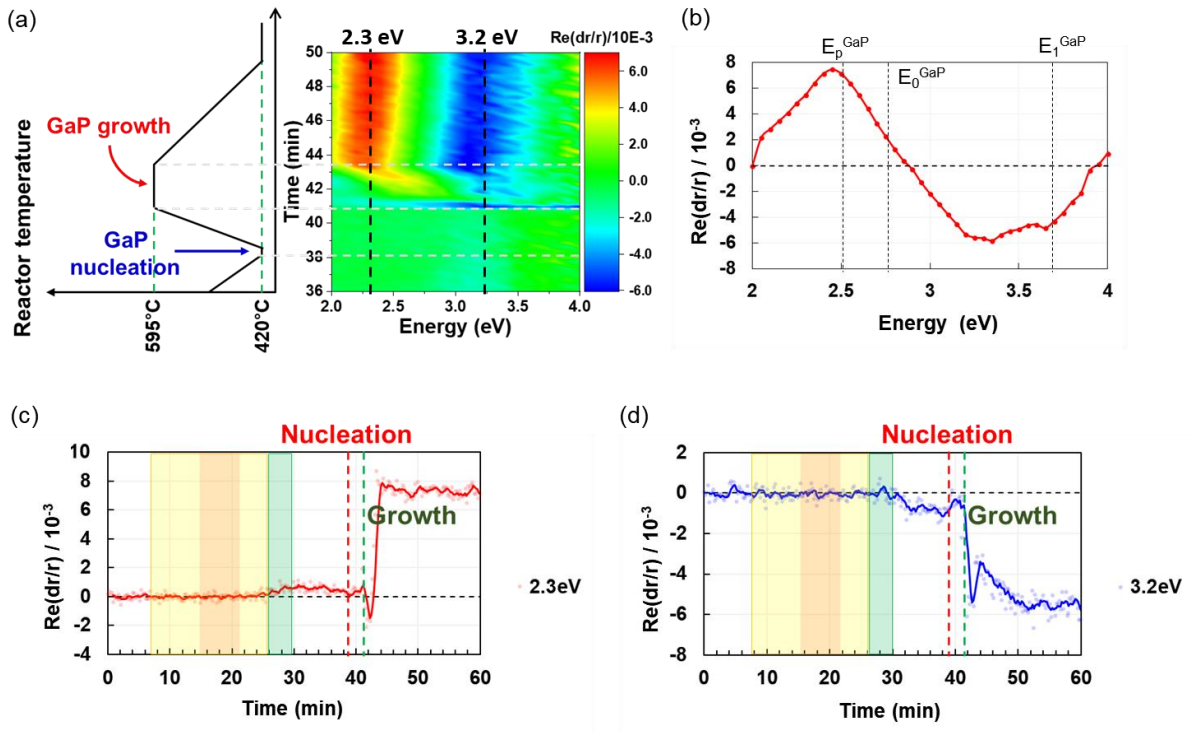

Fig. 5-32 (a) A schematic of process flow for GaP heteroepitaxy on double-layer stepped Si(1 0 0) surface and corresponding time transient RA. (b) RA spectra measured at 150 °C. Time transient RA for (c) 2.4 eV and (d) 3.2 eV which comes from P-rich (2x2)/c(4x2) A-type GaP surface anisotropy.

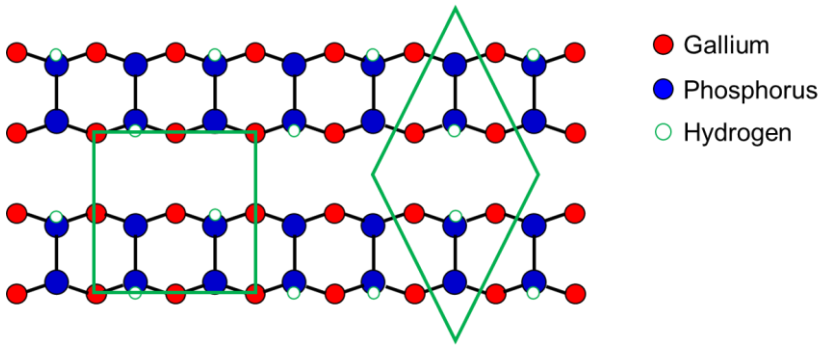

Fig. 5-33 Top view of surface state: P-rich GaP(1 0 0) (2x2)/c(4x2) surface.

From the above RAS signal, it was confirmed that A-type P-terminated GaP surface can be obtained when GaP is grown on the A-type double-layer step Si (1 0 0) surface. This can be used as an indicator in assessing the quality of epitaxial layer. However, since this shows information only about the surface morphology, additional analysis with TEM or XRD is necessary to discuss the crystal quality of the epitaxial layer.

5.2.2 X-ray diffraction of GaP on Si(1 0 0)

By conducting X-ray diffraction (XRD) measurement on crystals subjected to heteroepitaxial growth, it is possible to determine how well the orientations of grown crystals are aligned, how much distortion is present in the crystal, whether lattice defects or the like have not occurred Important information on the grown crystals can be obtained.

In this research, XRD measurement was performed as following to observe the characteristics of grown epitaxial layer.

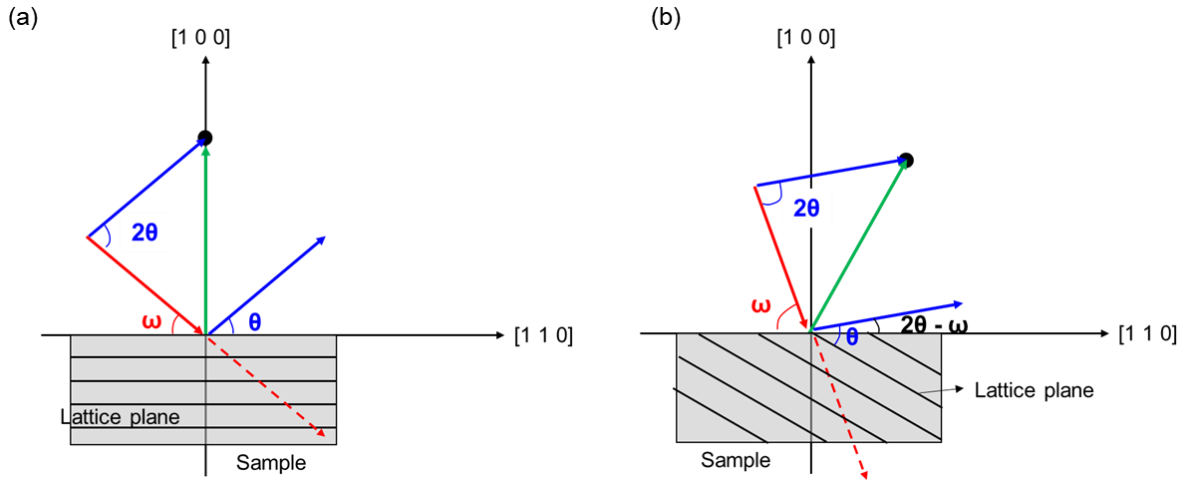

Fig. 5-34 Schematics of XRD measurement: (a) symmetrical reflection, and (b) asymmetric reflection.

By measuring the symmetrical reflection, the interplanar spacing / lattice constant in the direction perpendicular to the substrate crystal surface can be obtained. In addition to this, if we can measure the asymmetric reflection and measure the surface spacing of the surface tilted with respect to the surface, we can calculate the lattice constant in the direction parallel to the surface by calculation. The coordinates Q_x and Q_y of the reciprocal lattice space can be obtained from the following equations.

$$Q_x = \frac{1}{\lambda}(\cos(\omega) - \cos(2\theta - \omega)) \tag{5.1}$$

$$Q_y = \frac{1}{\lambda}(\sin(\omega) + \sin(2\theta - \omega)) \tag{5.2}$$

Where, λ is the wavelength of X-ray. In this research, Cu $K_{\alpha,1}$ with wavelength of 1.540598(Å) is used for measurement. The theoretical Bragg angle and corresponding for each material is summarized in Table. 5-1.

Table. 5-1 Calculated Bragg angle and corresponding Q_x, Q_y.

Material (Lattice constant Å)	Lattice plane (h k l)	2θ (°)	ω (°)	$Q_x \times 10000$	$Q_x \times 10000$
Si (5.43095)	(0 0 4)	69.1299	34.5649	0	7356.05
	(2 2 4)	88.0300	79.2794	-5201.516	7356.055
GaP (5.4512)	(0 0 4)	68.8368	35.5284	0	7337.83
	(2 2 4)	87.6194	79.0741	-5188.63	7337.83
GaAs (5.6533)	(0 0 4)	66.0528	33.0264	0	7075.51
	(2 2 4)	83.7516	77.1402	-5003.14	7075.51

This section provides additional XRD analysis for the samples that have already completed surface analysis in the previous section. Figure 5-35 shows the 2θ-ω scan data for (0 0 4) plane (symmetric reflection), and reciprocal space mapping (RSM) data for ($\bar{2}\ \bar{2}$ 4) plane (asymmetric reflection).

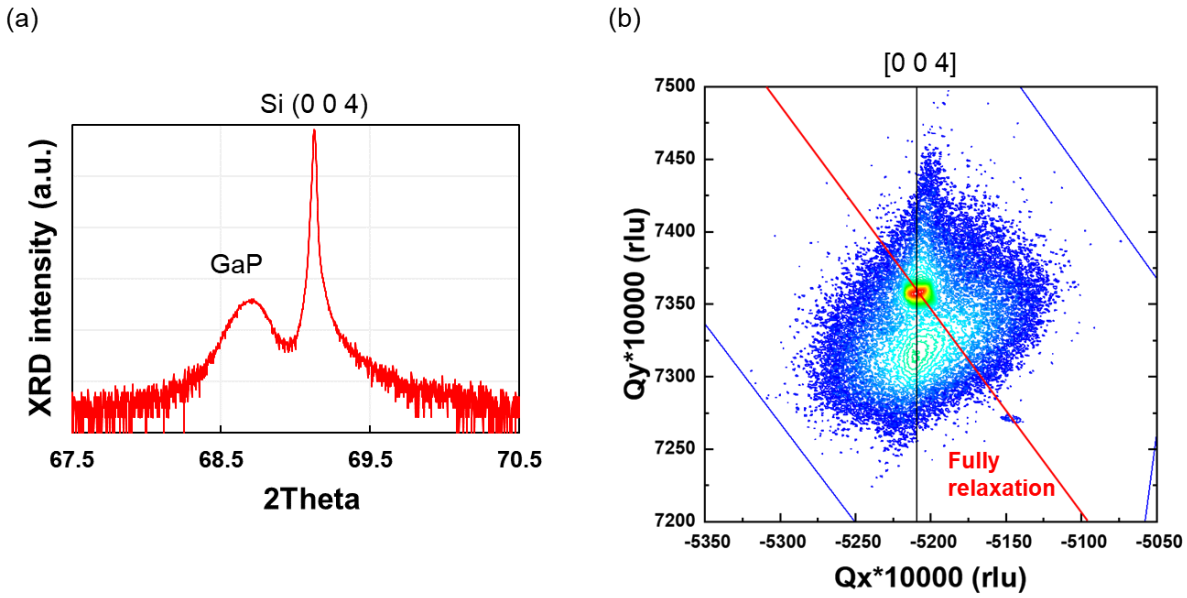

Fig. 5-35 (a) 2θ-ω scan data, and (b) RSM image for GaP/Si(1 0 0).

From fig. 5-35(b), it can be seen that the epitaxially grown GaP layer was obtained which was pseudo-morphic to Si. To further explain the structure of the epitaxial layer, the lattice plane distance of the grown

GaP layer is determined from the following equation.

$$d_{epi} = \frac{\sin(\theta_{sub})}{\sin(\theta_{epi})} d_{sub} \tag{5.3}$$

Where, the d_{epi} and d_{sub} are the lattice plane distance of epi-layer and substrate. The θ_{epi} and θ_{sub} represent θ values at which the XRD intensity is maximum for the epi-layer and the substrate.

The calculated lattice plane distance of GaP epitaxial layer from eq. (5.3) is 1.365 Å for (0 0 4) plane, it is slightly increased value comparing to the original GaP (1.3628 Å). The resultant GaP / Si structure is shown in fig. 5-36.

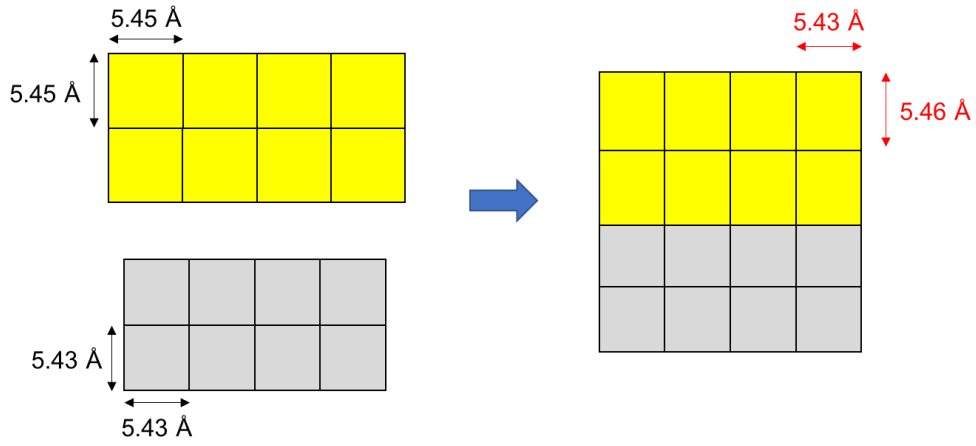

Fig. 5-36 The expected GaP epitaxial layer structure grown on Si substrate.

5.2.3 Effect of residues on GaP epitaxial layer

Double-stepped Si surfaces can be achieved at comparatively low-temperature annealing under arsenic ambient in MOVPE chambers and subsequent GaP epitaxial layer could be grown on that surface. In the succeeding growth, however, it is not possible to establish the same ambient condition in the reactor every time due to residual atoms (Ga, P and As) on the reactor wall, which was deposited in the preceding growth. The impact of residuals on GaP heteroepitaxial layer growth is still unclear because the previous works mainly deal with the preparation of double-layer stepped Si surfaces in the MOVPE reactor totally cleaned to be free from group-III contamination. In this study, we investigate about the impact of residuals on GaP film growth on Si(1 0 0) substrate and the method to remove the residuals in the reactor.

At first, three successive GaP growth experiments were conducted without additional reactor cleaning to determine the effect of the residue on GaP heteroepitaxy. The GaP growth conditions for each experiment

were exactly same as depicted in fig. 5-30.

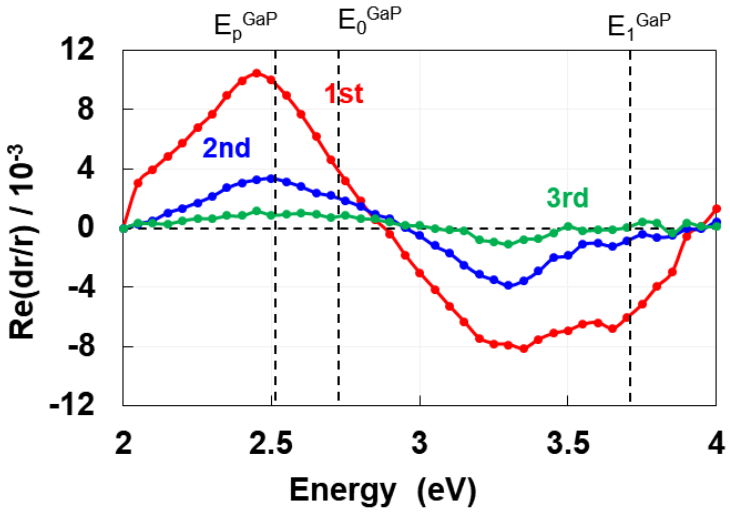

Fig. 5-37 RA spectrum measured at 150 °C for GaP/Si(1 0 0) surface.

The RAS signals measured at 150 °C are shown in fig. 5-37. In fig. 5-37, red line is for GaP surface grown in very clean reactor (only As existed on the reactor wall, without any group-III material). Blue line and green line show the GaP surface states which are conducted without additional cleaning for the reactor after the first growth (Ga, P and As atoms remained in the reactor from previous growth). The surface anisotropic peak intensity is drastically dropped in the blue line, and in the third growth, the anisotropic peak almost disappeared. It is difficult to predict the exact atomic arrangement of the GaP surface from the RAS signal, but it can be seen that at least the P-terminated A-type GaP/Si(1 0 0) surface is disordered.

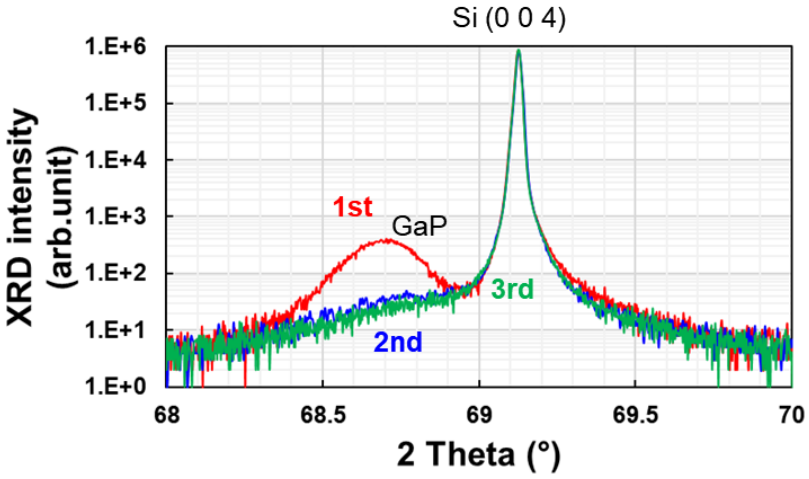

Fig. 5-38 2θ-ω measurement data for GaP/Si(1 0 0): lattice plane (0 0 4).

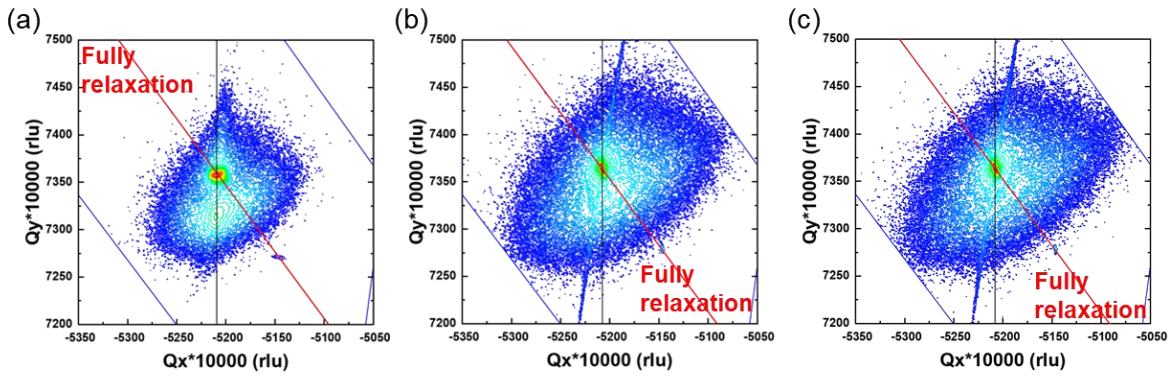

Fig. 5-39 RSM images for GaP/Si(1 0 0). Lattice plane: $(\bar{2}\ \bar{2}\ 4)$

XRD measurements were performed to determine the quality of the crystals. The XRD measurement results show almost the same results for the GaP epitaxial layers grown in the contaminated reactor. The RSM image of the GaP epitaxial layer grown in the contaminated reactor shows a broad and weak peak of GaP, while a clear peak without relaxation was obtained in the first sample, and the peak of GaP is spread over the complete relaxation line. Assuming that a GaP film of the same thickness is grown for the three samples, a broad and weak peak of XRD means that the atom arrangement of the crystal is not somewhat regular and thus the quality of the grown epitaxial crystal is not good.

In addition, although not attached here, about the RA signal for Si double-layer step formation, there was no anisotropic signal in both two samples which are grown in contaminated reactor. From these results with RAS and also with XRD, it is verified that the residue of the reactor has a significant influence on the subsequent growth.

Removal of the residues

In the following, three conditions of GaP growth process is discussed: GaP heteroepitaxial layer grown in (1) a clean reactor (possible residual is only As), (2) a contaminated reactor (Ga, P and As remained from the preceding GaP growth), and (3) a reactor after the removal of residuals (flushing the residuals by baking before the process). For the growth condition, almost same as in previous samples but only different from the As coating temperature as shown in fig. 5-40.

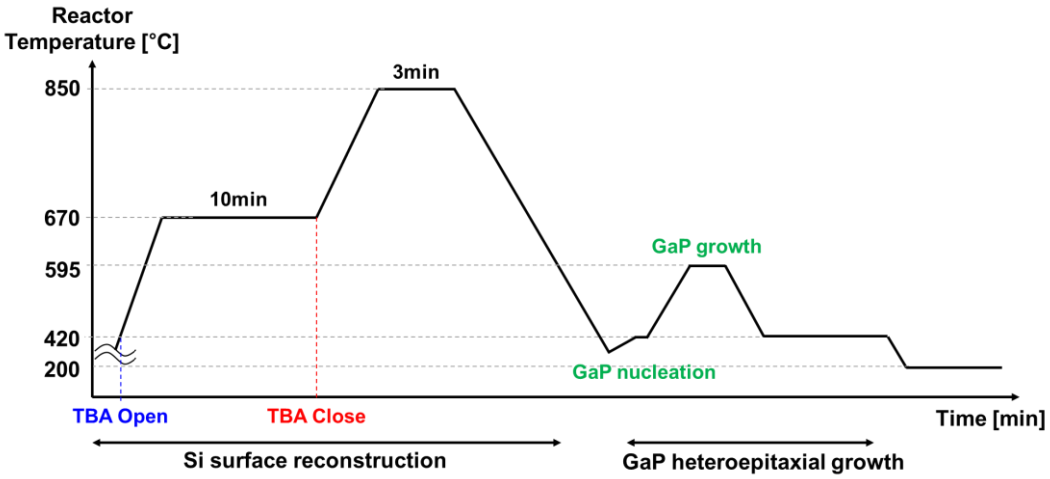

Fig. 5-40 A schematic of process flow for GaP growth on Si(1 0 0).

As-terminated Si surface was formed during TBA exposure at 670°C. The terminated As atoms desorbed during the annealing process at 850°C and surface atoms rearranged to have low surface energy. By the optimal annealing condition, the double-layer stepped Si(1 0 0) surface could be obtained. After the pretreatment of Si surface, subsequent GaP epitaxial layer was grown by two-step growth process as described in the begging of this section. Figure 5-41 shows the transient RA signal of the first sample which was prepared in the clean reactor.

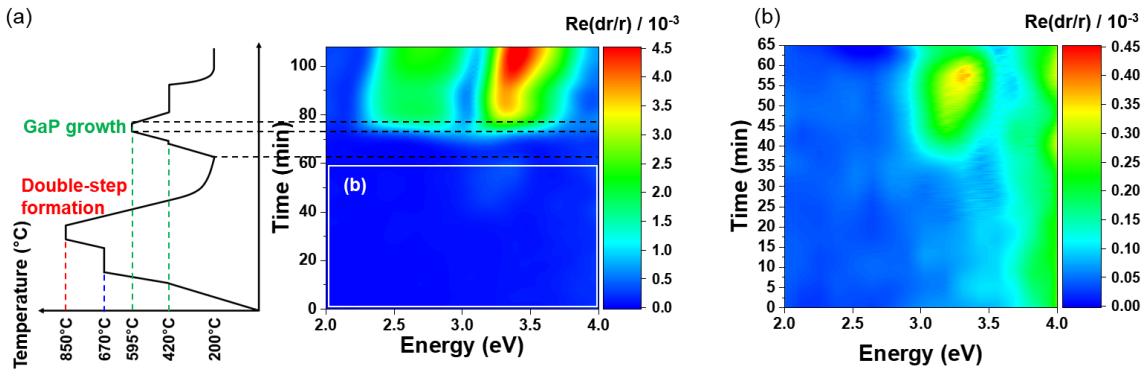

Fig. 5-41 (a) In-situ measured transient RA signal during GaP heteroepitaxial layer growth in the clean reactor. (b) The enlarged transient RA signal of the white box region in (a) which is for the Si(1 0 0) surface reconstruction process.

Here, the RA signal was measured with sample rotation and the signal shows the absolute value of RA. As shown in fig. 5-41, the peaks corresponding to the double-layer stepped Si(1 0 0) surface and the GaP layer on Si were observed. RA spectra measured after Si surface reconstruction at 400°C and after GaP

heteroepitaxial growth at 200°C are shown in fig. 5-42, respectively. The gray dashed lines indicate the critical point energies of Si [44] and GaP [45].

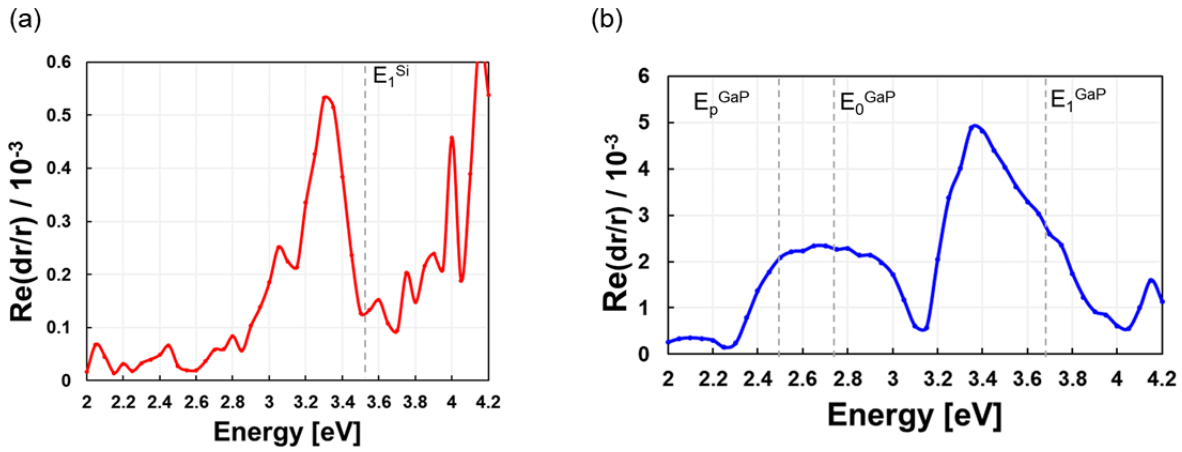

Fig. 5-42 (a) RA spectrum measured at 400°C after Si reconstruction process. (b) RA spectrum measured at 200°C after GaP layer growth.

RA signal peak corresponding to Si E_1 state was observed as shown in fig. 5-42(a). It could be deemed that the double-layer step surface was formed on Si (100) surface. In the subsequent GaP growth, GaP was grown for 90 sec on that surface after nucleation by pulsed TMGa and TBP. A broad peak at 2.5eV~3eV and a sharp peak around 3.4eV originated from the P-terminated (2×2)/c(4×2) reconstructed surface state of GaP heteroepitaxial layer was observed as shown in fig. 5-42(b) indicating the successful growth of GaP on Si(100) surface without substantial density of antiphase domains because the surface with large antiphase domains does not show RA signals due to random dimer direction on the surface.

Second sample was prepared in the contaminated chamber by using completely the same recipe as the first sample without any residue removal process before the growth. In this condition, remaining Ga, P and As atoms due to the first sample growth existed. Before moving to the third growth, we bake the reactor at 850 °C for 30 min under 100 mbar of H_2 ambient for flushing the residuals. The third sample was grown by using the same recipe as the previous ones except for the extended growth time of GaP from 90 sec to 150 sec (to sharpen the RA intensity peak [1]). RA spectra of these two samples were measured at 200 °C without sample rotation as shown in fig. 5-43. The RA spectra for the first sample was measured with rotation, as mentioned above, and the sign of RA signal for the first sample was turned to negative in the photon energy range of 2 - 3.15 eV for comparison with the other samples.

The RA intensity for second sample grown in the contaminated reactor is only 50% compared to the other samples in the photon energy range around 3.5 eV, and we could not observe the Si(1 0 0) anisotropy

signal during the surface preparation stage after TBA exposure. This degradation in the RA signal indicates the failure in the surface preparation of Si and the subsequent growth of GaP seems to be accompanied by a lot of antiphase domains. For the third sample growth, high temperature baking of the MOVPE chamber at 850 °C to flush the residuals was applied before the sample preparation, and the RA signal intensity was recovered to the similar level to the first same grown in the fresh reactor. This recovery of the RA signal indicates that Ga, P and As residuals could be flushed out with high temperature baking, and the GaP without noticeable antiphase domains was obtained.

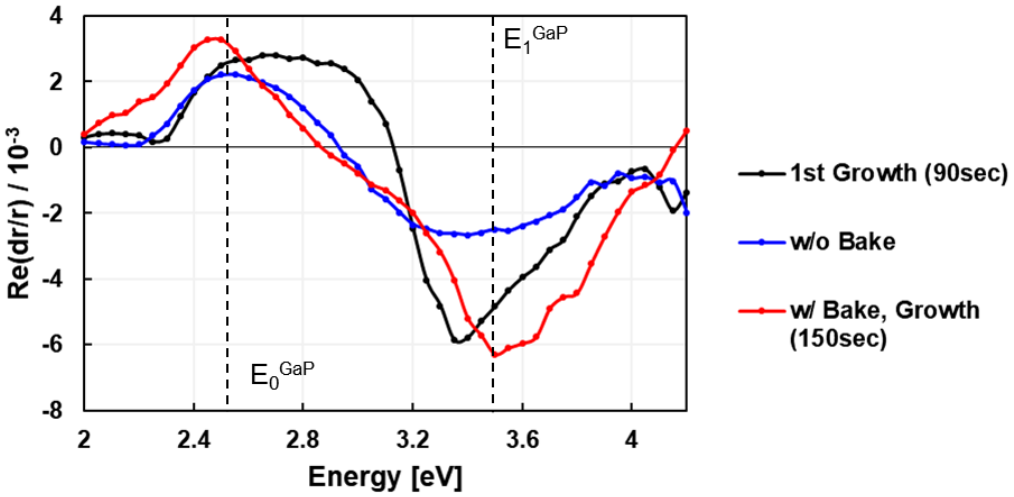

Fig. 5-43 Comparison of RA spectra for three conditions: GaP grown on Si (100) surface (1) in the clean reactor (2) in the contaminated reactor (3) after the MOVPE chamber baking.

Here, it is investigated about the impact of residuals in a MOVPE reactor on the heteroepitaxial growth of GaP on a Si (100) substrate. The existence of antiphase domains in the GaP layer on Si was related to the intensity of RA peaks corresponding to the (2×2)/c(4×2) reconstructed GaP surface. Si surface reconstruction was hindered even with a small amount of residue that was deposited during the growth of a GaP layer with only several tens of nanometers in thickness, as indicated by the degradation in the RA signal. To remove the contaminations in the reactor, we baked the reactor at high temperature of 850 °C for 30 min before loading a new sample in the MOVPE reactor to flush out residual contaminations. The RA signal was recovered to almost the same level as the initial sample grown in the flesh reactor, indicting the effectiveness of reactor baking on the growth of GaP without antiphase domains. However, after the growth of a thick GaP layer, baking will not be a good method for remove the contaminations in the reactor due to a risk of forming Ga metal droplets on the reactor wall, which will act as detrimental source of Ga evaporation in the succeeding run of Si surface preparation. More effective method of removing abundant Ga atoms from the reactor wall is a target of future study.

5.2.4 Regrowth of GaP on GaP/Si template

1) GaP/Si(1 0 0) template fabrication by AIX-2000HT reactor

As mentioned in the previous section, the environment in the reactor is very important for Si surface reconstruction and growth of subsequent GaP. Therefore, after every GaP growth, the reactor quartz tube should be cleaned with aqua regia, and the susceptor also should be cleaned with chlorine at a high temperature of over 1000 °C. Here, the fabrication of GaP / Si (1 0 0) template using another reactor (AIX-2000HT) is introduced.

Fig. 5-44 AIX-2000HT reactor.

Planetary reactor AIX-2000HT as shown in fig. 5-44 can fabricate the 7 samples of 2-inch wafers in one growth, and the reactor can be cleaned by introducing hydrogen chloride to the reactor. The process flow of GaP/Si(1 0 0) is as below (the Si surface preparation and GaP growth process are same as fig. 5-30).

Reactor cleaning by HCl (before loading a sample wafer into the reactor)

→ Reactor is cleaned by HCl at 800 °C, 750 mbar during 20 min.

→ After stopping the HCl supply, reactor was baked at 850 °C with hydrogen ambience for 30 min.

→ Before loading the Si wafer into reactor, one more baking process is done with As at 850 °C for 30min.

GaP heteroepitaxy on Si(1 0 0)

→ Si surface coating with As at 420 °C - 850 °C, 750 mbar.

→ Si surface annealing at 850 °C, 750 mbar during 3 min.

→ GaP was nucleated with alternating (TBP, TMGa) pulses of 1.5s each (starting with TBP, no pause in between), at 420 °C in reactor pressure of 100 mbar with increased V: III ratio of 40.

→ GaP epilayers were grown at 595 °C, 100 mbar with V: III=13 during 150 sec.

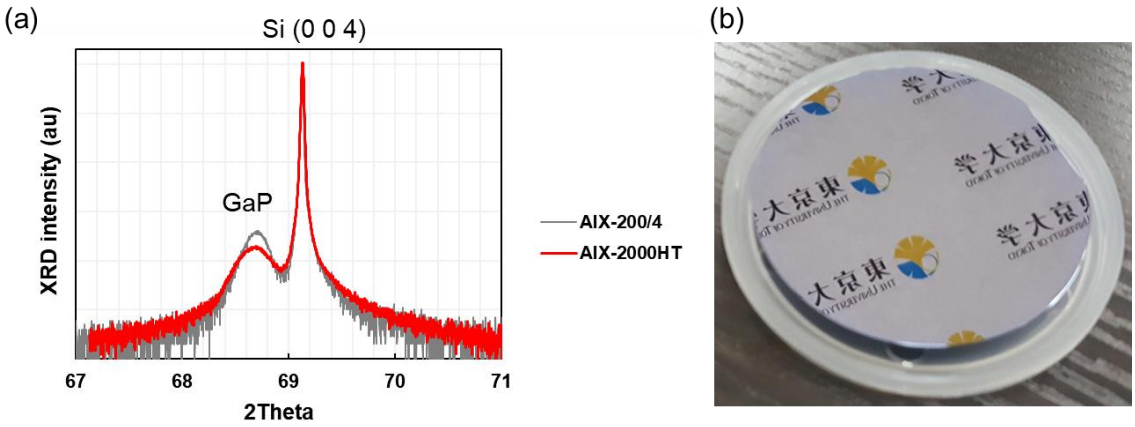

Fig. 5-45 (a) 2θ-ω measurement data. (b) Mirror-like surface is obtained.

2θ-ω measurement results of 2 samples which are prepared in AIX-200/4 and AIX-2000HT are shown in fig. 5-45(a), and the picture of the sample surface prepared in AIX-2000HT is shown in fig. 5-45(b). The full width at half maximum (FWHM) value of 2θ is 705 arcsec (for Si peak, 57 arcsec) and 820 arcsec (for Si peak, 65 arcsec) for AIX-200/4 sample and for AIX-2000HT sample respectively. For both of samples, mirror-like surfaces are visually observed, but the XRD measurements show that the GaP peak of the sample in the AIX-2000HT reactor is broader.

More details about crystal quality of GaP grown by AIX-2000HT reactor is discussed with TEM images shown in fig. 5-46. Figure 5-46(a), (b) and (c) show the cross-sectional view of grown GaP epitaxial layer. It can be seen that dislocations in the direction of 59 ° and 50 ° are generated with respect to the surface of Si(1 0 0) which is tilted 4 ° to the <1 1 1> direction. Considering that the angle formed by the (1 1 1) lattice plane and the (1 0 0) plane is 54.7 °, it can be considered that these dislocations are generated along the (1 1 1) plane. That is, it can be regarded as dislocations due to APD. The grown GaP layer has many antiphase boundaries and the thickness distribution is uneven (25 nm ~ 45 nm). About the dislocation density counted by plane view of TEM images, over 10^{10} cm^{-2} is observed.

Although the single domain surface was not obtained, it is meaningful that a 2-inch wafer size GaP / Si (1 0 0) template was fabricated in a reactor with HCl cleaning treatment at 800 °C. There are still remaining studies to optimize the process parameters for Si surface preparation and GaP growth in the AIX-2000HT reactor, because there are process conditions differences which comes from the reactor environment (such

as the difference between the reactor temperature and the actual sample surface temperature) between these two types of reactors. However, if it is possible to fabricate a GaP/Si(1 0 0) template by using this planetary reactor, 7 samples can be obtained at one growth and the burden of susceptor cleaning can be reduced.

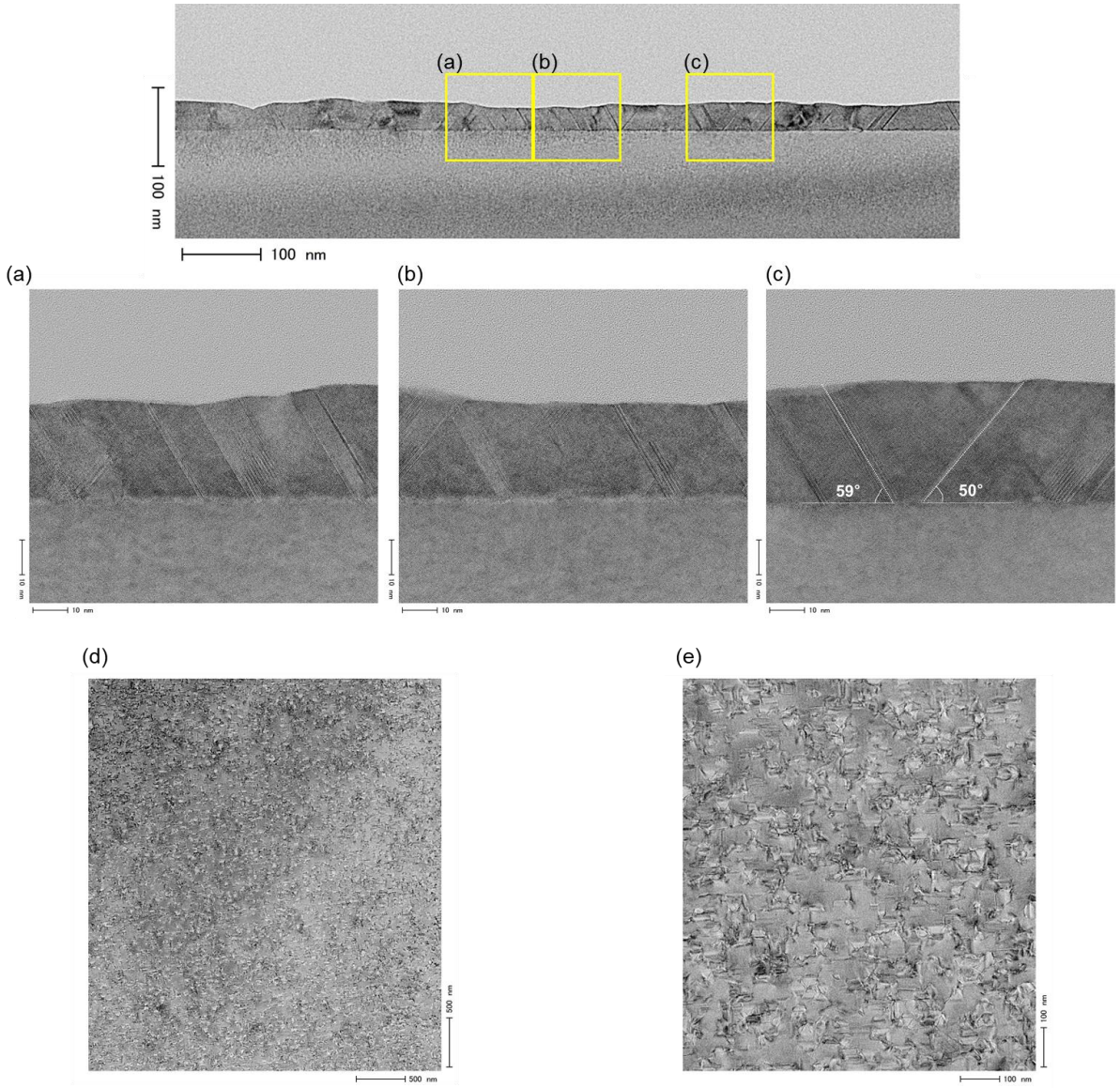

Fig. 5-46 TEM image for GaP/Si(1 0 0) template prepared in AIX-2000HT reactor. (a)-(c) are cross-sectional image and (d)-(e) are plane view of the sample.

2) GaP/Si(1 0 0) template

The Ga(As)P growths which are discussed in the following sections are implemented on the GaP/Si(1 0 0) templates which are fabricated in AIX-2000HT reactor at one growth.

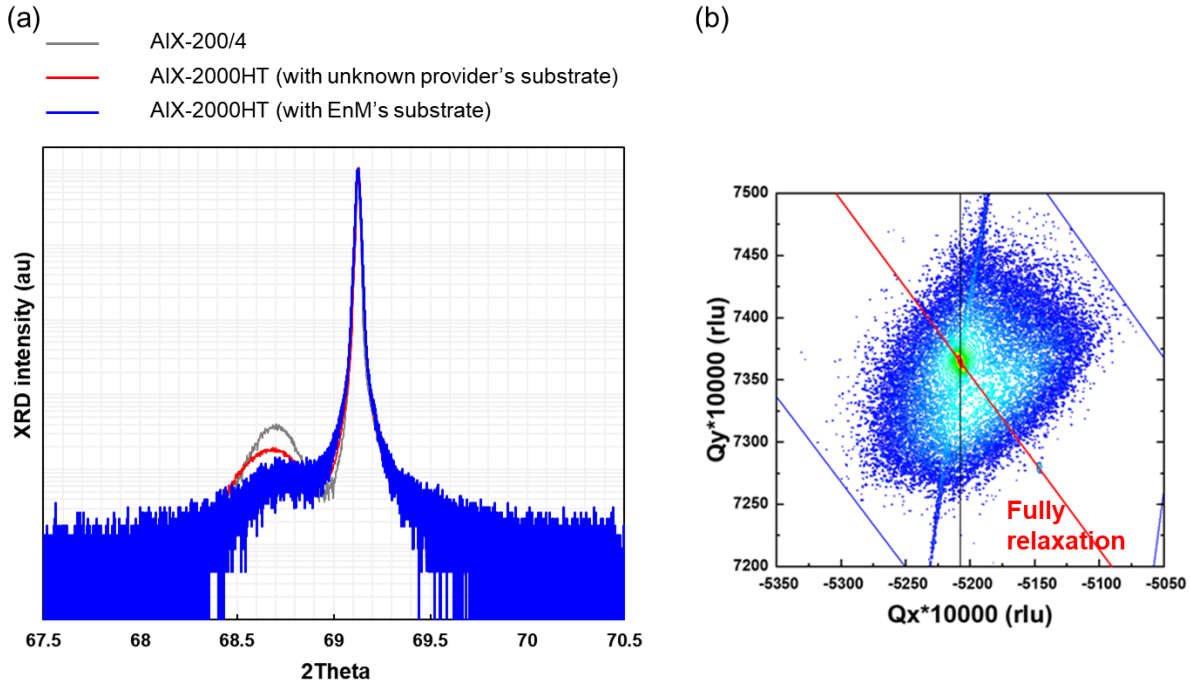

Fig. 5-47 (a) 2θ-ω measurement data for (0 0 4) plane, and (b) RSM image for ($\bar{2}$ $\bar{2}$ 4) plane of GaP/Si(1 0 0) template grown in AIX-2000HT reactor.

2θ-ω measurement data is shown in fig. 5-47(a), and the RSM image is shown in fig. 5-47(b). In 2θ-ω measurement, very broad and weak peak of GaP is observed. RSM also shows the broad and weak GaP peak, and the peak is broadening to fully relaxation line. About the sample surface, mirror-like surfaces are visually observed, but slightly darker than previous sample depicted in fig. 5-45.

For this samples, the double-layer step is not well formed due to the inherent surface morphology issue of the wafer itself (details are introduced in Appendix B), so the fabricated GaP/Si(1 0 0) template does not show well-ordered characteristics. However, since the surface of the GaP-coated Si is hard to generate an oxide film and can be removed at a low temperature, this has high prospective to application.

3) GaP regrowth on the GaP/Si(1 0 0) template

Here, the results of GaP regrowth on the GaP/Si(1 0 0) template which is expressed in above is discussed. Process flow for GaP regrowth on GaP/Si(1 0 0) is depicted in fig. 5-48.

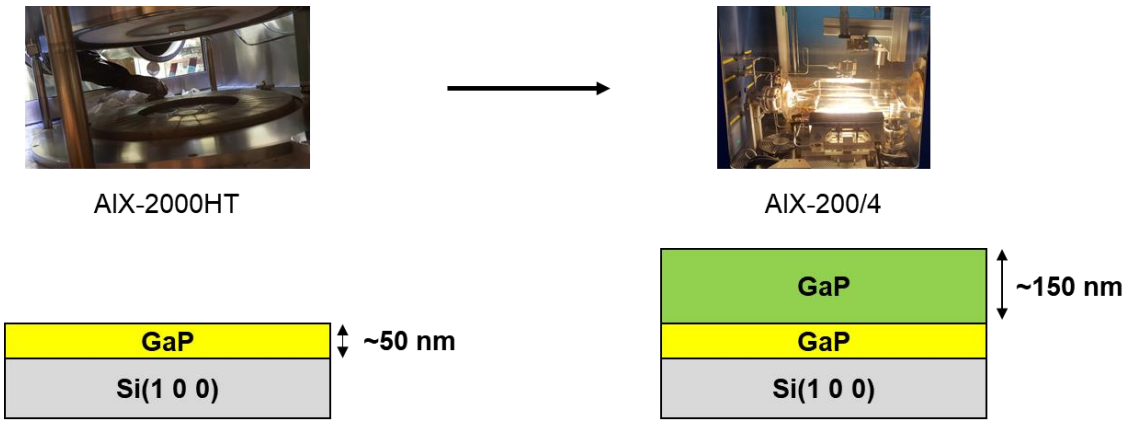

Fig. 5-48 A schematics of process flow and structure of heteroepitaxy: GaP regrowth in the AIX-200/4 reactor on GaP/Si(1 0 0) template prepared in the AIX-2000HT reactor.

GaP growth is conducted at AIX-200/4 reactor using GaP/Si(1 0 0) template prepared in AIX-2000HT. The experimental details are as below.

- ✓ Bake at 650 °C with TBP during 20 min: remove the surface oxide layer.
- ✓ GaP epilayers were grown at 700 °C, 100 mbar with V (TBP):III (TMGa) = 8, during 8 min (growth rate: 20 nm / min).

2θ-ω measurement data and RSM image are shown in fig. 5-49 (a) and (b), and the picture of the sample surface prepared is shown in fig. 5-49(c).

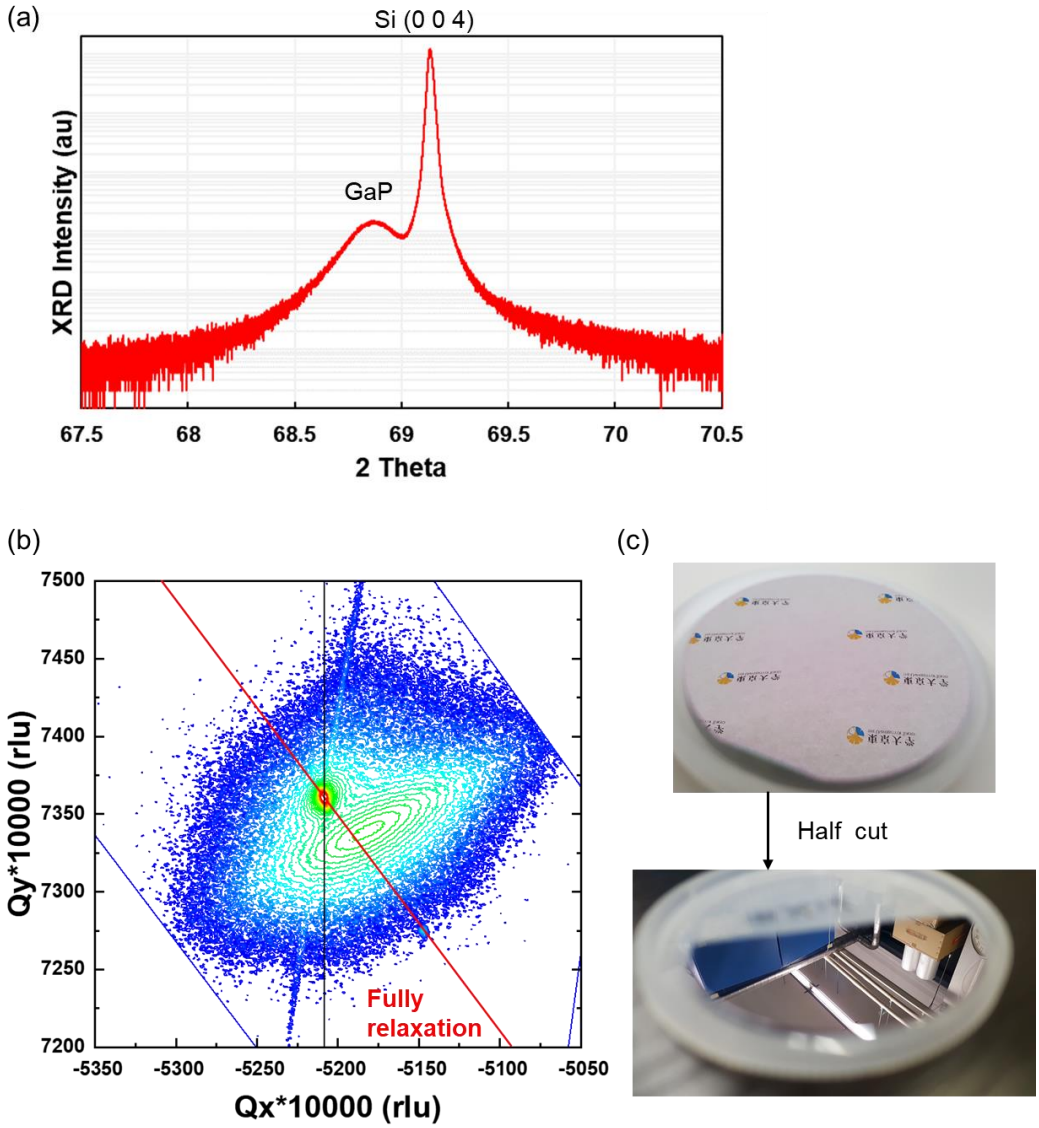

Fig. 5-49 (a) 2θ-ω measurement data for (0 0 4) lattice plane, and (b) RSM image for ($\bar{2}$ $\bar{2}$ 4) plane of regrown GaP sample (in AIX-200/4 reactor) on GaP/Si(1 0 0) template (prepared in AIX-2000HT reactor). (c) A slightly dark (with a purple color), but mirror-like surface was obtained.

From the XRD measurement data, in the both of 2θ-ω scan and reciprocal space scan, fully relaxed GaP epitaxial layer is observed, and the mirror-like surface but slightly dark (not white but slightly purple) is also obtained.

It can be verified that fully related thick (hundreds of nm) GaP epitaxial layer can be grown on the GaP/Si(1 0 0) quasi-substrate even though that crystal quality of template is not so high.

5.3 GaAsP heteroepitaxy on GaP/Si

5.3.1 Calculation method for lattice deformation in heteroepitaxy

Lattice strain originates from mismatch of the substrate lattice, and film surface, and the lattice is deformed when materials with different lattice constants are integrated by heteroepitaxy. In deformed lattice, the lattice plane distance and direction are different from undeformed lattice, so the XRD characteristics is also different.

In the reciprocal lattice space, the fluctuation of the lattice plane orientation of the crystal is observed as the spread of the Bragg point on the spherical surface centering on the origin. On the other hand, the change in the lattice spacing of crystals is observed as a change in the radial direction in the reciprocal lattice space. In order to observe this change, measurements called ω-2θ measurement are made.

In this section, a method of calculation for the lattice parameters, such as lattice constant and components, of the epitaxial layer considering the lattice strain from the measured XRD data is introduced.

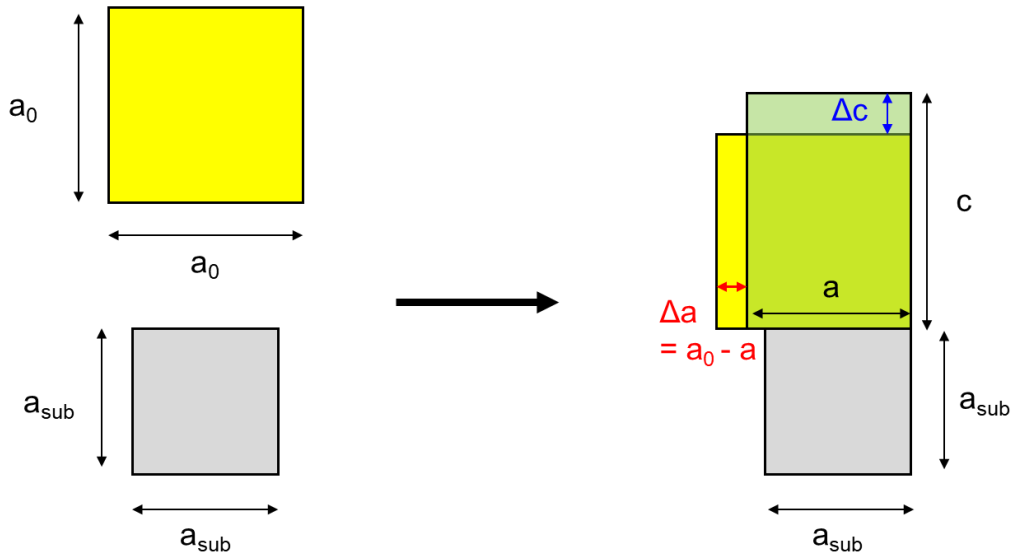

Fig. 5-50 A schematic of lattice deformation.

When considering a heteroepitaxy as shown in Figure 5-50, the deformed lattice parameters can be estimated as follows. Where, a_{sub} and a_0 are the lattice constant of substrate and the lattice constant of epitaxial film in the absence of strain, and a and c are deformed lattice constant which of in plane direction (transverse) and crystal growth direction (longitudinal).

In estimating the lattice deformation in heteroepitaxy of $GaAs_{1-x}P_x$ on GaP/Si(1 0 0), the elastic stiffness constants are used as following values.

- ✓ Elastic stiffness for GaP: C_{11} = 14.39 / C_{12} = 6.52
- ✓ Elastic stiffness for GaAs: C_{11} = 12.23 / C_{12} = 5.71
- ✓ Elastic stiffness for $GaAs_{1-x}P_x$: $C_{11} = 14.39 \times x + 12.23 \times (1-x)$ / $C_{12} = 6.52 \times x + 5.71 \times (1-x)$

Poisson's ratio ν, which is the ratio between the transverse strain and the longitudinal strain, is expressed as eq. (5.4).

$$\nu = \frac{C_{12}}{C_{11} + C_{12}} \tag{5.4}$$

For $GaAs_{1-x}P_x$, the Poisson's ratio has a value of 0.312 – 0.318 in the range from x = 0 to x = 1. Here, the average value of Poisson's ratio, 0.315 is used for all estimation. From this, the relation between deformed lattice constant, in plane direction a and crystal growth direction c, can be expressed as follows.

$$c = a + \frac{1+\nu}{1-\nu}\Delta a = a + \frac{1+\nu}{1-\nu}(a_0 - a) \tag{5.5}$$

With respect to a crystal growing while undergoing some restraint from a substrate crystal on a substrate crystal, it is impossible to know the original lattice constant (when there is no deformation) merely by measuring the lattice spacing of one face of the crystal. This is because it is impossible to know how much the change in the measured interplanar spacing depends on the change in the lattice constant of the grown crystal and how much it is derived from the distortion due to constraint to the substrate crystal. On the other hand, if the surface spacings of a plurality of planes which are not parallel to each other are measured, it is possible to know how much the grown crystal is distorted and also to estimate the lattice constant in the unstrained state. When the crystal axis in the epitaxial growth direction is taken as the c-axis, the interplanar spacing in the c-axis direction of the GaAsP layer grown on the GaP/Si(1 0 0) crystal, can be obtained by measuring the diffraction of the (0 0 4) lattice plane, and lattice plane distance (d_{004}) can be estimated as eq. (5.6).

$$d_{004} = \frac{1}{4}c \tag{5.6}$$

However, from this interplanar spacing, lattice constant of GaAsP can not be decided immediately, so additional information is required for estimating. In this case, if asymmetry reflection measurement such as d_{224} is determined by diffraction measurement of the (2 2 4) plane, the transverse lattice constant a and longitudinal lattice constant c can be determined as below.

$$d_{224} = \frac{1}{\sqrt{\frac{8}{a^2} + \frac{16}{c^2}}} \tag{5.7}$$

$$a = \frac{1}{\sqrt{\frac{1}{8d_{224}^2} - \frac{1}{8d_{004}^2}}} \tag{5.8}$$

From above equations, the a_0 can be estimated.

$$a_0 = \frac{2\nu}{1+\nu}a + \frac{1-\nu}{1+\nu}c \tag{5.9}$$

It is known that the lattice constant of unstrained $GaAs_{1-x}P_x$ (a_{GaAsP}) changes linearly from the lattice constant of GaP (a_{GaP}) to the lattice constant of GaAs (a_{GaAs}) depending on P composition x (Vegard's law). From these calculations, the P composition in grown $GaAs_{1-x}P_x$ can be estimated as below.

$$x = \frac{a_0 - a_{GaAs}}{a_{GaP} - a_{GaAs}} \tag{5.10}$$

5.3.2 GaAsP heteroepitaxy on GaP/Si(1 0 0)

5.3.2.1 GaAsP growth on GaP/Si(1 0 0) at low reactor temperature

Figure 5-51 shows the schematic of process and grown GaAsP/GaP/Si structure by AIX-200/4 reactor.

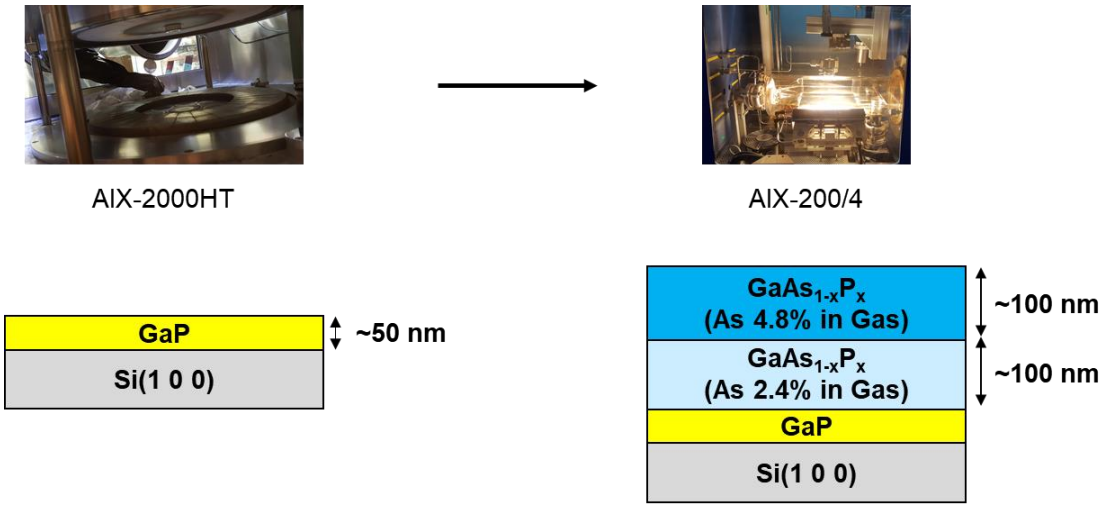

Fig. 5-51 A schematics of process flow and structure of heteroepitaxy: $GaAs_{1-x}P_x$ regrowth in the AIX-200/4 reactor with prepared GaP/Si(1 0 0) sample in the AIX-2000HT reactor.

GaAsP heteroepitaxy is conducted at AIX-200/4 reactor using GaP/Si(1 0 0) template prepared in AIX-2000HT. The experimental details are as below.

- ✓ Bake at 600 °C with TBP during 10 min: remove the surface oxide layer.
- ✓ GaAsP epitaxial layers were grown at 650 °C (reactor temperature), 100 mbar with V (TBP+TBA):III (TMGa) = 10, during 10 min (growth rate: 20 nm / min) for each layer.
  - → 1st GaAsP epitaxial layer: As proportion in total group V (summation of TBA and TBP) gas phase is 2.4 % (TBA/GroupV = 0.024).
  - → 2nd GaAsP epitaxial layer: As proportion in total group V (summation of TBA and TBP) gas phase is 4.8 % (TBA/GroupV = 0.048).

2θ-ω measurement data and RSM image are shown in fig. 5-52 (a) and (b).

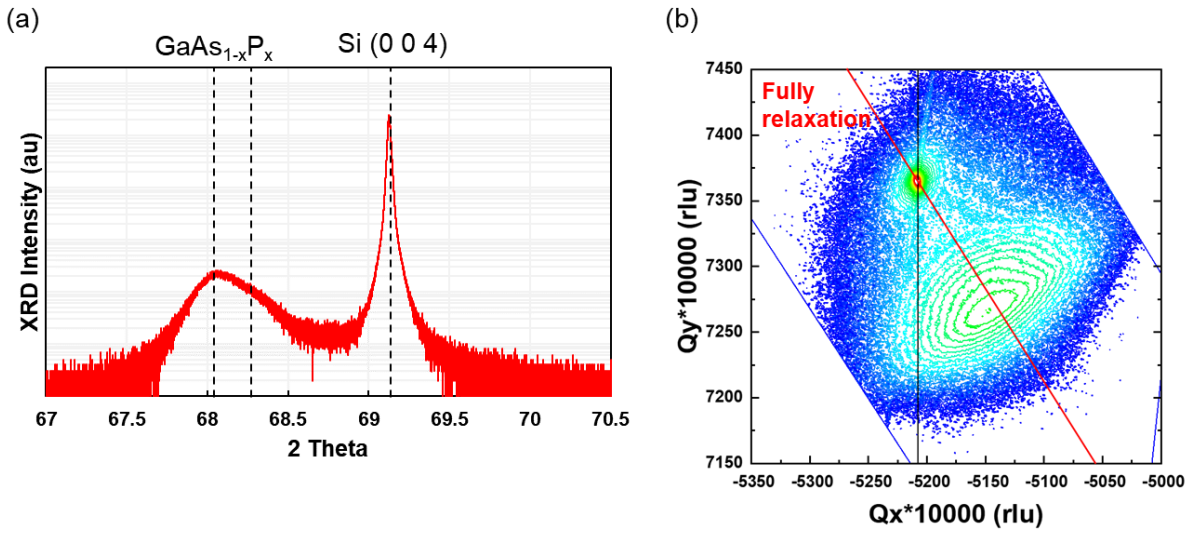

Fig. 5-52 (a) 2θ-ω measurement data for (0 0 4) lattice plane, and (b) RSM image for ($\bar{2}$ $\bar{2}$ 4) plane of $GaAs_{1-x}P_x$ regrowth (in AIX-200/4 reactor) on GaP/Si(1 0 0) template (prepared in AIX-2000HT reactor).

From the XRD measurement data, in the both of 2θ-ω scan and reciprocal space scan, fully relaxed $GaAs_{1-x}P_x$ epitaxial layer is observed. The calculated As component in each layer is described in fig. 5-53.

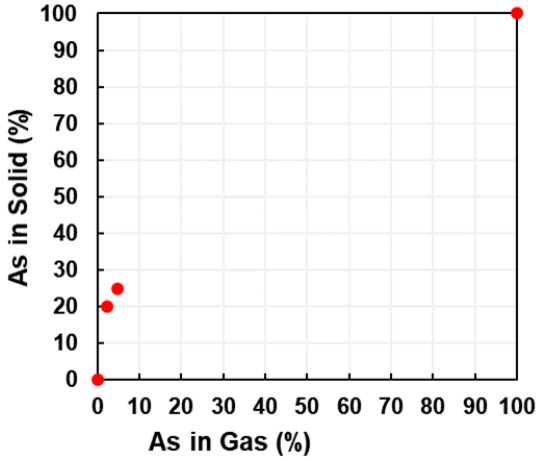

As in Gas	As in Solid
2.4 %	20 %
4.8 %	25 %

Fig. 5-53 The ratio of As in the crystal phase to the ratio of As in the gas.

The As content in the crystal and the As content in the gas are not linear. The As content in solid is very high even by using low proportion in gas phase under growth at 650 °C. Therefore, in the low temperature growth under 650 °C (expected sample surface temperature is 600 °C), it is difficult to design a graded buffer layer because low As content of GaAsP can not be fabricated.

5.3.2.2 Thick GaAsP growth on GaP/Si(1 0 0)

Figure 5-54 shows the schematic of process and grown GaAsP/GaP/Si structure by AIX-2000HT reactor.

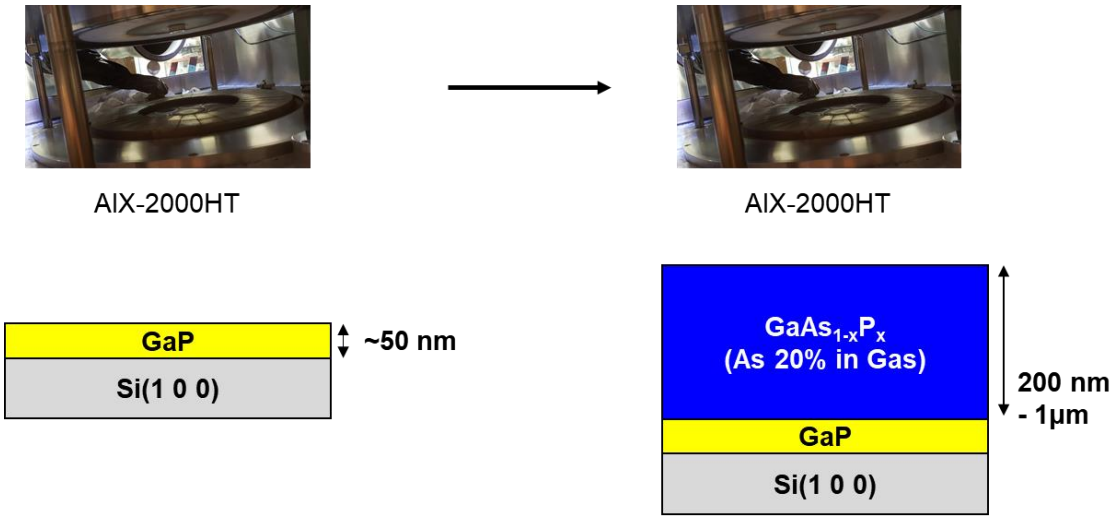

Fig. 5-54 A schematics of process flow and structure of heteroepitaxial layer: $GaAs_{1-x}P_x$ on the GaP/Si(1 0 0) sample prepared in the AIX-2000HT reactor.

Thick GaAsP heteroepitaxy is conducted at AIX-2000HT reactor using GaP/Si(1 0 0) template prepared in AIX-2000HT. The experimental details are as below.

- ✓ Bake at 600 °C with TBP during 10 min: remove the surface oxide layer.
- ✓ GaAsP epitaxial layers were grown at surface temperature of 680 °C with V (TBP+TBA):III (TMGa) = 10, As proportion in total group V (summation of TBA and TBP) gas phase is 20 % (TBA/GroupV = 0.2).
  - → 1st sample for GaAsP/GaP/Si(1 0 0): reactor pressure is 100 mbar. Sample surface temperature is 680 °C (reactor temperature: ~780 °C), and thickness of grown GaAsP layer is 1 μm (growth rate: 20 nm / min).
  - → 2nd sample for GaAsP/GaP/Si(1 0 0): reactor pressure is 750 mbar. Sample surface temperature is 680 °C (reactor temperature: ~750 °C), and thickness of grown GaAsP layer is ~200 nm (growth rate: 17.5 nm / min).

The 2θ-ω measurement data for (0 0 4) lattice plane and RSM images for ($\bar{2}\ \bar{2}$ 4) lattice plane are shown in fig. 5-56, and the in-situ measured reflectance is shown in fig. 5-55. From the XRD measurement data, in the both of 2θ-ω scan and reciprocal space scan, fully relaxed $GaAs_{1-x}P_x$ epitaxial layer is observed. In both of samples, the peak of $GaAs_{1-x}P_x$ epitaxial layer is located in same point, and the calculated As component in grown $GaAs_{1-x}P_x$ is 27 % in both samples. The peak intensity is relying on the thickness of grown GaAsP, so the peak for 100 mbar condition is higher than 750 mbar condition sample.

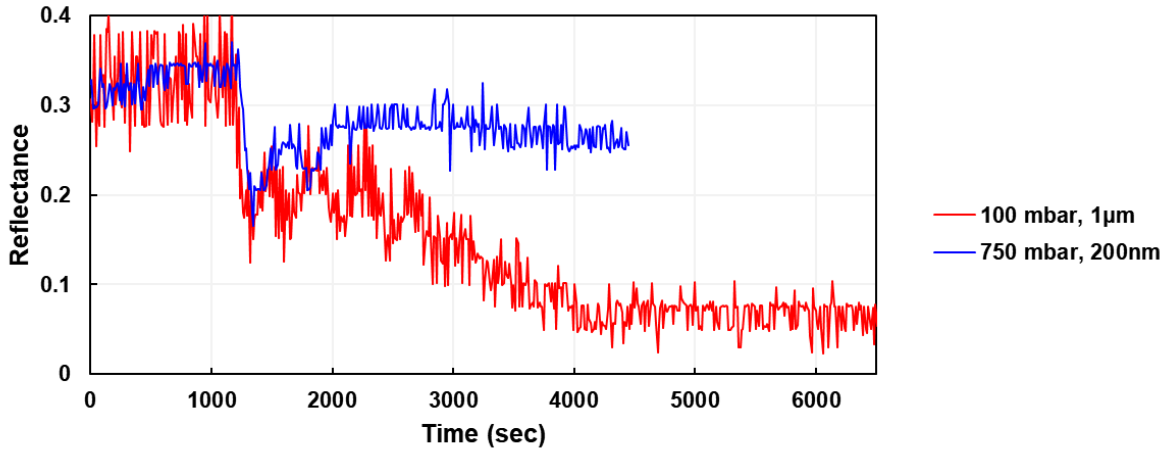

Fig. 5-55 In-situ measured reflectance during the growth.

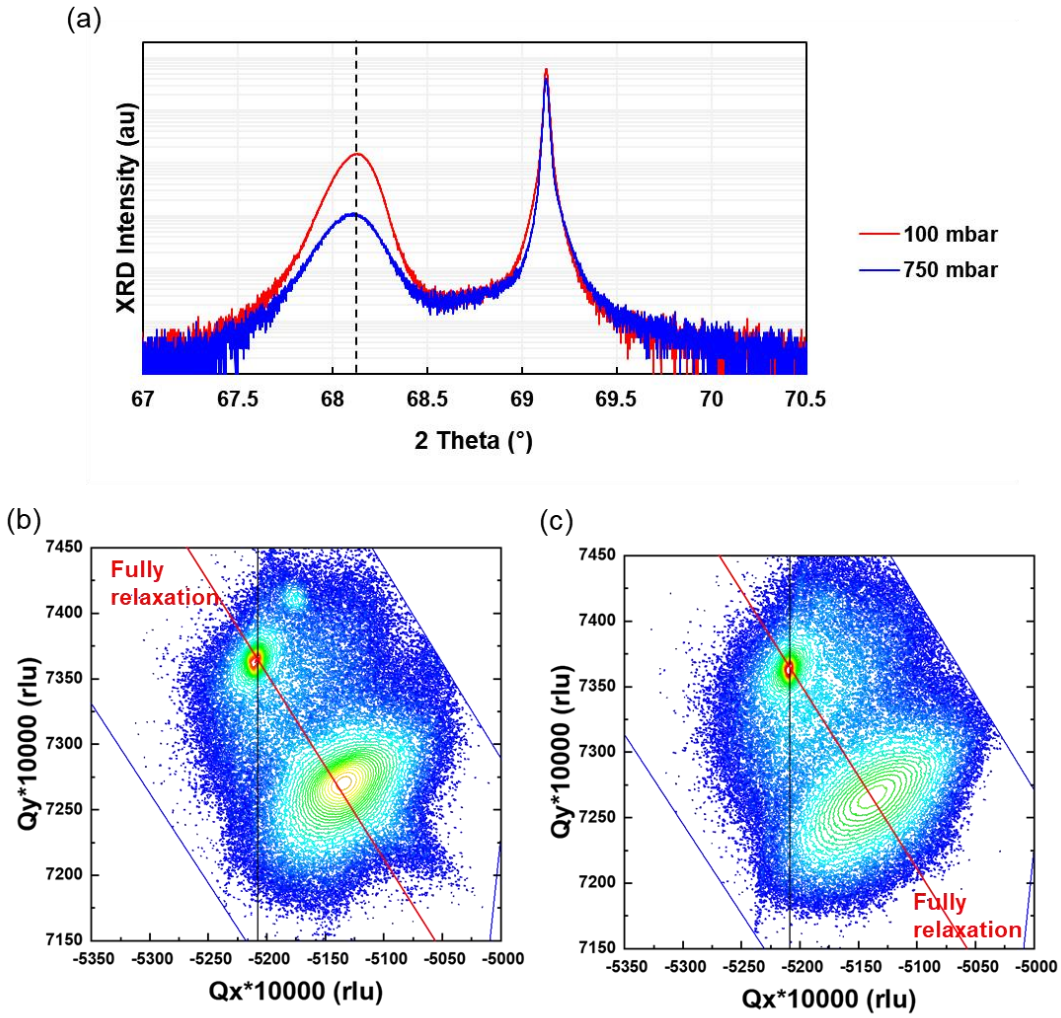

Fig. 5-56 (a) 2θ-ω measurement data for (0 0 4) lattice plane, and RSM image for ($\bar{2}$ $\bar{2}$ 4) plane of $GaAs_{1-x}P_x$ on GaP/Si(1 0 0) template (prepared in AIX-2000HT reactor) grown at the reactor pressure of (b) 100 mbar and (c) 750 mbar.

As the epitaxial layer grew, the in-situ reflectance decreased in both conditions, but there was a difference in the drop rate. Under the growth conditions of 750 mbar, vibration in the reflectance caused by the epitaxial growth was identified, and under the conditions of 2.4 eV the reflectance dropped by 0.15, whereas under the conditions of 100 mbar, reflectance dropped very quickly, and the vibration is not observed.

5.3.2.3 Graded GaAsP layer growth on GaP/Si(1 0 0)

Figure 5-57 shows the schematic of process and grown graded-GaAsP/GaP/Si structure by AIX-2000HT reactor.

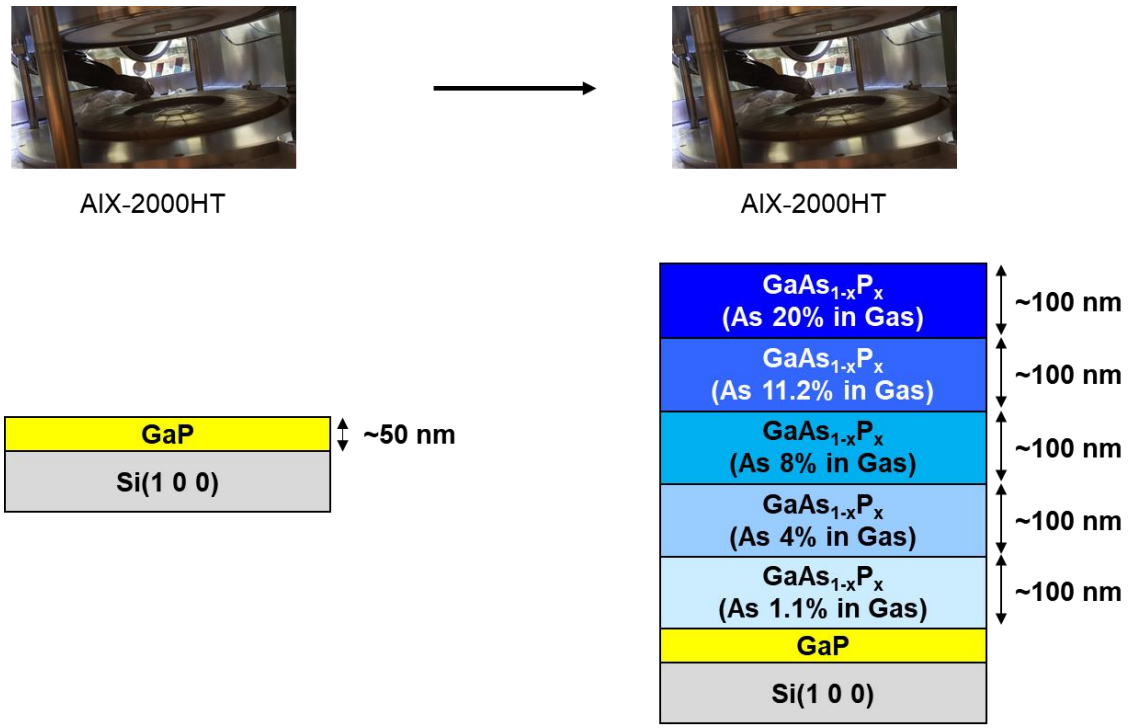

Fig. 5-57 A schematics of process flow and structure of heteroepitaxy: graded-$GaAs_{1-x}P_x$ on the GaP/Si(1 0 0) sample prepared in the AIX-2000HT reactor.

Graded GaAsP heteroepitaxy is conducted at AIX-2000HT reactor using GaP/Si(1 0 0) template prepared in AIX-2000HT. The experimental details are as below.

- ✓ Bake at 600 °C with TBP during 10 min: remove the surface oxide layer.
- ✓ GaAsP epitaxial layers were grown at surface temperature of 680 °C with V (TBP+TBA):III (TMGa) = 10, during 10 min for each layer (growth rate in 100 mbar: 20 nm / min, in 750 mbar: 17.5 nm / min).
  - → 1st GaAsP layer: As proportion in total group V (summation of TBA and TBP) gas phase is 1.1 % (TBA/GroupV = 0.011).
  - → 2nd GaAsP layer: As proportion in total group V (summation of TBA and TBP) gas phase is 2.4 % (TBA/GroupV = 0.024).

→ 3rd GaAsP layer: As proportion in total group V (summation of TBA and TBP) gas phase is 8 % (TBA/GroupV = 0.08).

→ 4th GaAsP layer: As proportion in total group V (summation of TBA and TBP) gas phase is 11.2 % (TBA/GroupV = 0.112).

→ 5th GaAsP layer: As proportion in total group V (summation of TBA and TBP) gas phase is 20 % (TBA/GroupV = 0.2).

✓ Two samples are prepared in different reactor pressure of 100 mbar and 750 mbar.

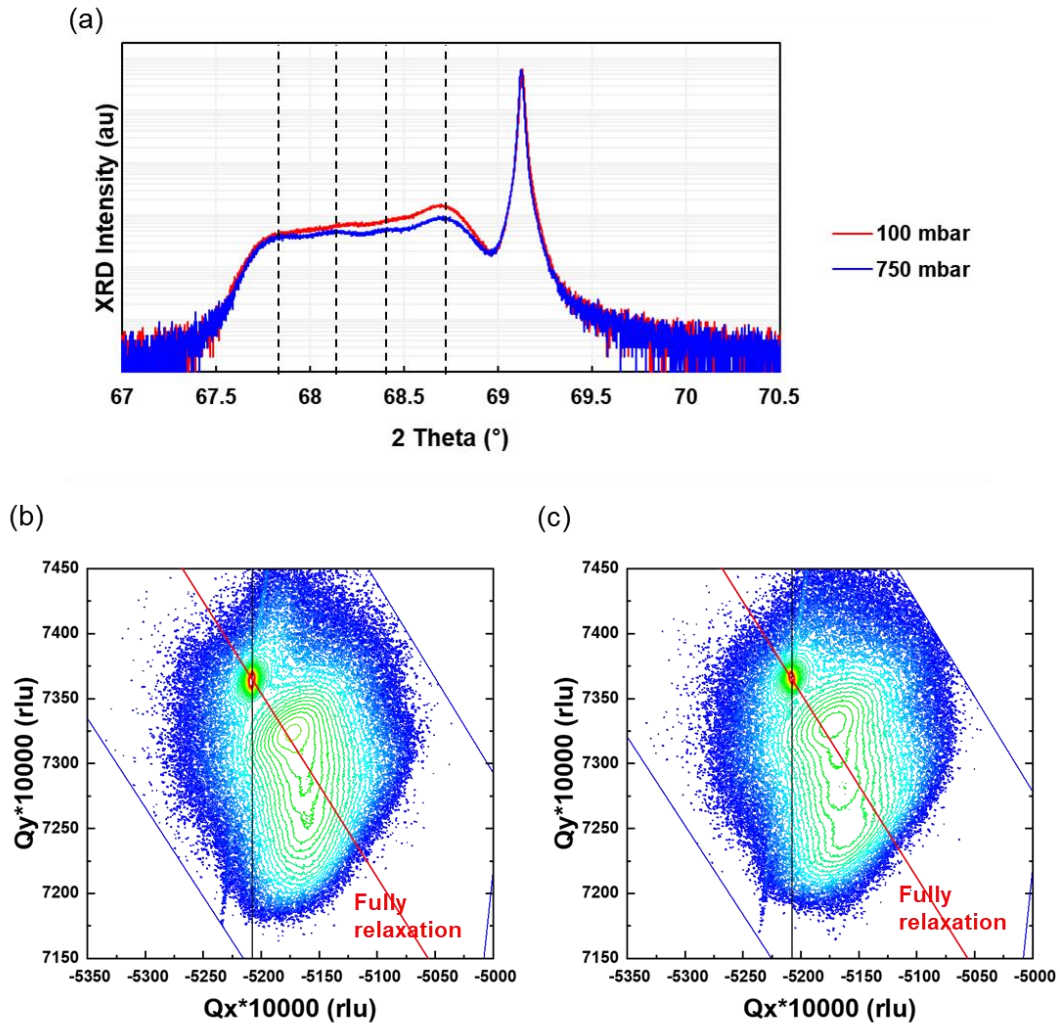

Fig. 5-58 (a) 2θ-ω measurement data for (0 0 4) lattice plane, and RSM image for ($\bar{2}$ $\bar{2}$ 4) plane of graded-$GaAs_{1-x}P_x$ on GaP/Si(1 0 0) template (prepared in AIX-2000HT reactor) grown at the reactor pressure of (b) 100 mbar and (c) 750 mbar.

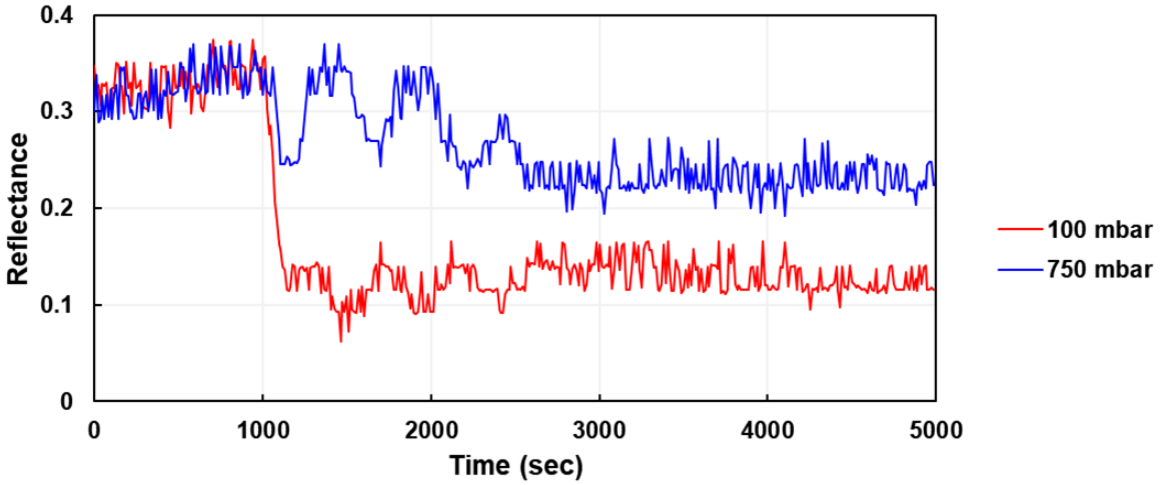

Fig. 5-59 In-situ measured reflectance during the growth.

The 2θ-ω measurement data for (0 0 4) lattice plane and RSM images for ($\bar{2}$ $\bar{2}$ 4) lattice plane are shown in fig. 5-58, and the in-situ measured reflectance is shown in fig. 5-59. From the XRD measurement data, in the both of 2θ-ω scan and reciprocal space scan, partially relaxed graded-$GaAs_{1-x}P_x$ epitaxial layers are observed. In both of samples, the peaks of $GaAs_{1-x}P_x$ epitaxial layers are located in same points, and the calculated As component in grown graded-$GaAs_{1-x}P_x$ layers are shown in fig. 5-60.

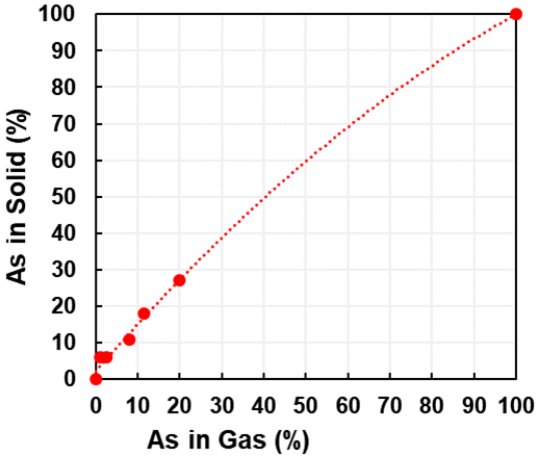

As in Gas	As in Solid
1.2~2.5 %	6 %
8 %	11 %
11.2 %	18 %
20 %	27 %

Fig. 5-60 The ratio of As in the crystal phase to the ratio of As in the gas.

The layer distinction between 1st and 2nd GaAsP is not observed. However, it can be seen that the As content in the crystal and the As partial pressure in the gas phase are close to linear in the growth of the As partial pressure at over 8%.

For the peak for each layer, the peak positions are same in both of reactor pressure conditions. However, the peak sharpness is different in two conditions. This result is same as the result from previous experiment of GaAsP/GaP/Si(1 0 0) heteroepitaxy.

In summary of GaAsP heteroepitaxy on GaP/Si(1 0 0) template,

1) High growth temperature (the sample surface temperature of 680 °C) is required to fabricate low As content GaAsP layer.

2) High reactor pressure (750 mbar) shows better quality of epitaxial layer than low reactor pressure (100 mbar).

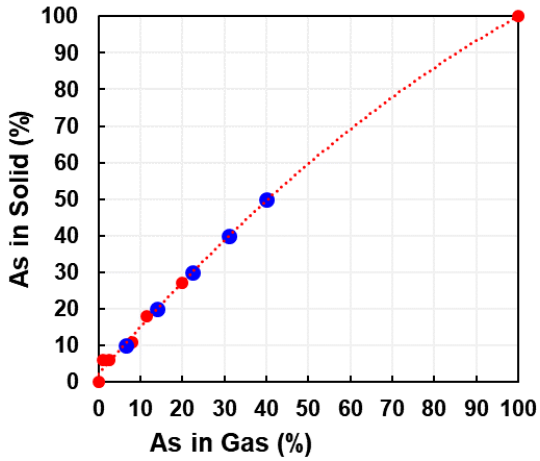

As in Gas	As in Solid
6.5 %	10 %
14 %	20 %
22.5 %	30 %
31 %	40 %
40 %	50 %

Fig. 5-61 The expected ratio of As content in the crystal phase to the As in the gas phase which are represented in blue dots.

Figure 5-61 shows the expected As content to be obtained in solid phase, when GaAsP was grown at a surface temperature of 680 °C. From this estimation, graded buffer layer for $GaAs_{0.5}P_{0.5}$ heteroepitaxy on GaP/Si(1 0 0) surface can be designed.

As can be seen from the above results, As has a high rate of incorporation into grown crystals even at very low partial pressures compare to the P even in the high temperature growth. Therefore, in the fabrication of the proposed structure in chapter 4, gas changing process at the interface between the barrier (GaP) and the well ($GaAs_{0.8}P_{0.2}$) should be done carefully to form a abrupt GaP barrier. Several possible strategies are suggested as below, from the results of this study.

1) Adopting high growth temperature.

2) Stabilizing the surface with TBP a long time before opening the Ga source to minimize the influence of As remaining in the reactor at the gas changing stage.

3) It is conceivable to increase the partial pressure of P during barrier layer, GaP growth and to lower the partial pressure of As remaining in the reactor to a negligible level.

5.4 References

[1] W. I. Wang, "Molecular beam epitaxial growth and material properties of GaAs and AlGaAs on Si(100)", *Appl. Phys. Lett.* **44** (12), p.1149-1151, 1984.

[2] K. Kugimiya, Y. Hirofuji and N. Matsuo, "Si-Beam Radiation Cleanign in Molcular-Beam Epitaxy", *Jpn. J. Appl. Phys.* **24** (5), p.564-567, 1985.

[3] A. Ishizaka and Y. Shiraki, "Low Temperature Surface Cleaning of Silicon and Its Application to Silicon MBE", *J. Electrochem. Soc.* **133** (4), p.666-671, 1986.

[4] T. Sakamoto and G. Hashiguchi, "Si(001)-2×1 Single-Domain Structure Obtained by High Temperature Annealing", *Jpn. J. Appl. Phys.* **25** (1), p.78-80, 1986.

[5] K. Sakamoto, T. Sakamoto, S. Nagao, G. Hashiguchi, K. Kuniyoshi and Y. Bando, "Reflection High-Energy Electron Diffraction Intensity Oscillation during GexSi1-x MBE Growth on Si(001) Substrates", *Jpn. J. Appl. Phys.* **26** (5), p.666-670, 1987.

[6] A. J. Hoeven, E. J. Van Loenen, D. Dijkkamp, J. M. Lenssnck, AND J. Dieleman, "Refelction high energy electron diffraction and scanning tunnelling microscopy study of singledomain growth during silicon molecular beam epitaxy on Si(001)", *Thin Solid Films* **183**, p.263-271, 1989.

[7] N. Jain and M. K. Hudait, “III–V Multijunction Solar Cell Integration with Silicon: Present Status, Challenges and Future Outlook”, *Energy Harvesting and Systems* **1** (3-4), p.121-145, 2014.

[8] S. A. Ringel, J. A. Carlin, T. J. Grassman, B. Galiana, A. M. Carlin, C. Ratcliff, D. Chmielewski, L. Yang, M. J. Mills, A. Mansouri, S. P. Bremner, A. Ho-Baillie, X. Hao, H. Mehrvarz, G. Conibeer, and M. A. Green, “Ideal GaP/Si Heterostructures Grown by MOCVD: III-V/Active-Si Subcells, Multijuntions, and MBE-to-MOCVD III-V/Si Interface Science”, *IEEE 39th Photovoltaic Specialists Conference (PVSC)*, 2013.

[9] T. J. Grassman, M. R. Brenner, A. M. Carlin, S. Rajagopalan, R. Unocic, R. Dehoff, M. Mills, H. Fraser, S. A. Ringe, “Toward Metamorphic Multijunction GaAsP/Si Photovoltaics Grown on

Optimized GaP/Si Virtual Substrates Using Anion-Graded GaAsyP1-y Buffers", *IEEE 34th Photovoltaic Specialists Conference (PVSC)*, 2009.

[10] W. A. Harrison, E. A. Kraut, J. R. Waldrop, and R. W. Grant, "Polar heterojunction interfaces", *Phys. Rev. B* **18**, 4402, 1978.

[11] H. Kroemer, "Polar-on-nonpolar epitaxy", *J. Cryst. Growth* **81**, 193, 1987.

[12] M. Yamaguchi, A. Yamamoto, and Y. Itoh, "Effect of dislocations on the efficiency of thin-film GaAs solar cells on Si substrates", *J. Appl. Phys.* **59**, 1751, 1986.

[13] M. Yamaguchi, "Dislocation density reduction in heteroepitaxial III-V compound films on Si substrates for optical devices", *J. Mater. Res.* **6**, 2, 1991

[14] T. Hannappel, W.E. McMahon, J.M. Olson, "An RDS, LEED, and STM Study of MOCVD-Prepared Si(1 0 0) surfaces", *J. Cryst. Growth* **272**, p.24-29, 2004.

[15] T. Bork, W.E. McMahon, J.M. Olson, T. Hannappel, "Surface science studies including low-temperature RDS on MOCVD-prepared, As-terminated Si(1 0 0) surfaces", *J. Cryst. Growth* **298**, p.54-58 ,2007.

[16] W. E. McMahon, Iskander G. Batyrev, T. Hannappel, J. M. Olson, and S. B. Zhang, "5-7-5 line defects on As/Si(100): A general stress-relief mechanism for V/IV surfaces", *Phys. Rev. B* **74**, 033304, 2006.

[17] O. Supplie, M. M. May, P. Kleinschmidt, A. Nagelein, A. Paszuk, S. Bruckner, and T. Hannappel, "In situ controlled heteroepitaxy of single-domain GaP on As-modified Si(100)", *APL Materials* **3**, 126110, 2015.

[18] A. Navarroa, E. Garcia-Tabares, B. Galiana, P. Cano, I. Rey-Stolle, C. Ballesteros, "MOVPE growth of GaP on Si with As initial coverage", *J. Cryst. Growth* **464**, p.8-13, 2017.

[19] H. Doscher, P. Kleinschmidt, T. Hannappel, "Atomic surface structure of Si(1 0 0) substrates prepared in a chemical vapor environment", *Appl. Surf. Sci.* **257** (2), p.574-580, 2010.

[20] H. Doscher and T. Hannappel, "In situ reflection anisotropy spectroscopy analysis of heteroepitaxial GaP films grown on Si(100)", *J. Appl. Phys.* **107** (12), 123523, 2010.

[21] A. Dobrich, P. Kleinschmidt, H. Doscher, and T. Hannappel, "Quantitative investigation of hydrogen bonds on Si(100) surfaces prepared by vapor phase epitaxy", *J. Vac. Sci. Technol. B* **29** (4), 04D114, 2011.

[22] W. E. McMahon, E. L. Warren, A. E. Kibbler, R. M. France, A. G. Norman, R. C. Reedy, J. M. Olson, A. C. Tamboli, P. Stradins, "Surfaces and interfaces governing the OMVPE growth of APD-free GaP on AsH3-cleaned vicinal Si(100)", *J. Cryst. Growth* **452**, p.235–239, 2016.

[23] A. Navarro, E. Garcia-Tabares, B. Galiana, P. Cano, I. Rey-Stolle, C. Ballesteros, "MOVPE growth of GaP on Si with As initial coverage", *J. Cryst. Growth* **464**, p.8-13, 2017.

[24] E. Garcia-Tabares, D. Martin, I. Garcia, I. Rey-Stolle, "Understanding phosphorus diffusionin to silicon in a MOVPE environment for III–V on silicon solar cells", *SOLMAT* **116**, p.61-67, 2013.

[25] E. Garcia-Tabares, I. Rey-Stolle, "Impact of metal-organic vapor phase epitaxy environment on silicon bulk lifetime for III–V-on-Si multi junction solar cells", *SOLMAT* **124**, p.17-23, 2014.

[26] E. Garcia-Tabares, T. J. Grassman, D. Martin, J. Carlin, L. Rey-Stolle, and S. A. Ringel, "Evolution of the Silicon Bottom Cell Photovoltaic Behavior during III-V on Si Multi-junction Solar Cell Production", *IEEE 42nd Photovoltaic Specialist Conference (PVSC)*, 2015.

[27] J. Ohlmann, M. Feifel, T. Rachow, J. Benick, S. Janz, F. Dimroth, and D. Lackner, "Influence of Metal-Organic Vapor Phase Epitaxy Reactor Environment on the Silicon Bulk Lifetime", *IEEE J-PV* **6** (6), p.1668 - 1672, 2016.

[28] A. Beyer, J. Ohlmann, S. Liebich, H. Heim, G. Witte, W. Stolz, and K. Volz, "GaP heteroepitaxy on Si(001): Correlation of Si-surface structure, GaP growth conditions, and Si-III/V interface structure", *J. Appl. Phys.* **111** (8), p.083534, 2012.

[29] T. Bork, W. E. McMahon, J. M. Olson, T. Hannappel," Surface science studies including low-temperature RDS on MOCVD-prepared, As-terminated Si(1 0 0) surfaces", *J. Cryst. Growth* **298**, p.54-58, 2007.

[30] T. Hannappel, W. E. McMahon, J. M. Olson, "An RDS, LEED, and STM Study of MOCVD-Prepared Si(1 0 0) surfaces", *J. Cryst. Growth* **272**, p.24-29, 2004.

[31] T. Hannappel, S. Visbeck, L. Toben, and F. Willig, "Apparatus for investigating metalorganic chemical vapor deposition-grown semiconductors with ultrahigh-vacuum based techniques", *Rev. Sci. Instrum.* **75** (5), p.1297-1304, 2004.

[32] P. Kaul, A. Schutze, D. Kohl, "Surface chemistry of new As precursors for MOVPE and MOMBE: phenylarsine and tertiarybutylarsine on GaAs(100)", *J. Cryst. Growth* **123**, p.411-422, 1992.

[33] C. H. Patterson, and D. Herrendorfer, "Reflectance anisotropy of the Si(100)1×2-As surface: Discrete dipole calculation", *J. Vac. Sci. Technol. A* **15** (6), p.3036-3043, 1997.

[34] T. Miura, M. Niwano, D. Shoji, and N. Miyamoto, "Kinetics of oxidation on hydrogen-terminated Si(100) and (111) surfaces stored in air", *J. Appl. Phys.* **79** (8), p.4373-4380,1996,

[35] W. Weiss, D. Schmeisser, and W. Gopel, "Kinetics and reconstruction of steps at the Si(001) surface", *Phys. Rev. Lett.* **60**, 1326, 1988.

[36] T. Hannappel, W.E. McMahon, J.M. Olson, "An RDS, LEED, and STM study of MOCVD-prepared Si(100) surfaces", *J. Cryst. Growth.* **272**, p.24-29, 2004.

[37] L. Toben, T. Hannappel, K. Moller, H, Crawack, C. Pettenkofer, F. Willig, "RDS, LEED and STM of the P-rich and Ga-rich surfaces of GaP(100)", *Surface Science* **494**, 755, 2001.

[38] S. Zollner, M. Garriga, J. Kircher, J. Humlicek, M. Cardona, G. Neuhold, "Temperature dependence of the dielectric function and the interband criticalpoint parameters of GaP". *Phys. Rev. B* **48**, 7915, 1993.

[39] P. H. Hahn, W. G. Schmidt, F. Bechstedt, O. Pulci, R. Del Sole, "P-rich GaP(001) (2x1)/(2x2) surface: A hydrogen-adsorbate structure determined from first-principles calculations", *Phys. Rev. B* **68** (3), 033311,2003.

[40] S. Visbeck, T. Hannappel, M. Zorn, J. T. Zettler, F. Willig, "Temperature dependence and origin of InP(100) reflectance anisotropy down to 20 K", *Phys. Rev. B* **63**, 245303, 2001.

[41] V. K. Dixit, T. Ganguli, T. K. Sharma, S. D. Singh, R. Kumar, S. Porwal, P. Tiwari, A. Ingale, S. M. Oak, "Effect of two-step growth process on structural, optical and electrical properties of MOVPE-grown GaP/Si", *J. Cryst. Growth* **310**, p.3428-3435, 2008.

[42] K. Volz, A. Beyer, W. Witte, J. Ohlmann, I. Nemeth, B. Kunert, W. Stolz, "GaP-nucleation on exact Si (0 0 1) substrates for III/V device integration", *J. Cryst. Growth* **315**, p.37–47, 2011.

[43] D. E. Aspnes and A. A. Studna, "Dielectric functions and optical parameters of Si, Ge, GaP, GaAs, GaSb, InP, InAs, and InSb from 1.5 to 6.0 eV", *Phys. Rev. B* **27**, 985, 1983.

[44] P. Lautenschlager, M. Garriga, L. Vina, and M. Cardona, "Temperature dependence of the dielectric function and interband critical points in silicon", *Phys. Rev. B* **36**, 9, 1987.

[45] S. Zollner, M. Garriga, J. Kircher, J. Humlicek, and M. Cardona, "Temperature dependence of the dielectric function and the interband critical-point parameters of GaP", *Phys. Rev. B* **48**, 11, 1993.

Chapter 6 Conclusion

Cell design with MQWs

A new GaAsP/Si tandem cell structure including multi-quantum wells (MQWs) layer is proposed.

✓ Concept for the MQWs-GaAsP/Si tandem solar cell

1) Current matching with active Si substrate: effective band gap of top absorber with MQWs is in the range of 1.65 eV ~ 1.8 eV.

2) Reduce the lattice mismatch between top absorber and Si: the bulk matrix of the top subcell is fixed $GaAs_{0.5}P_{0.5}$.

With the above concept, it is possible to obtain a current-matched top absorber with Si even by reducing the arsenic contents in the bulk matrix by extending the photon absorption region by introducing the MQWs. The most important advantage of this concept of structure is to reduce costs and burden of crystal growth. By reducing the As contents in the bulk matrix while maintaining high energy conversion efficiency, it is possible to reduce the lattice mismatch and thermal mismatch with Si, thereby reducing the thickness of the metamorphic buffer layer.

In theoretical calculation for efficiency of MQWs-GaAsP/Si tandem solar cell, the carrier dynamics (effective mobility and carrier collection efficiency (CCE)) in low-dimensional quantum well are considered, therefore more realistic prediction is possible.

According to the calculation, either very thin (below 4nm) or very thick (over 30 nm) barriers are suitable for enhancing CCE, the optimum stacking periods exists because increasing periods results in both the enhancement in light absorption and the degradation of CCE, and the conversion efficiency can reach 42.6% if we implement 60-periods MQWs composed of $GaAs_{0.8}P_{0.2}$ wells (5 nm) and GaP barriers (3 nm).

Generalization of manufacturing process conditions

In this study, we focused on generalization of the fabrication process condition for GaAsP heteroepitaxy on Si(1 0 0) by MOVPE. Therefore, in order to find the conditions applicable to any MOVPE reactor, a series of experiments were designed focusing on clarifying the relationship between process parameters and surface conditions.

1) Surface preparation

In chapter 5, the relationship between the Si(1 0 0) surface preparation for forming double-layer step on the surface is verified.

✓ Annealing temperature and time

There is strong relationship between annealing temperature and annealing time. For annealing temperature, it should be discussed with the surface temperature, not with the reactor temperature because the difference between temperature on the wafer surface and the reactor temperature is different from reactor to reactor. In this study, IR-heater heating system was applied for the reactor, therefore the following discussed temperatures are the estimated surface temperature.

→ Lower temperature requires longer time to form double-layer step on Si(1 0 0).

→ There is lower limit on annealing temperature: ~790°C

→ Optimized condition: ~820°C for 2~5 min / ~790°C for 10~15 min.

✓ Partial pressure of arsenic

Partial pressure of As and exposure temperature are important parameters for deoxidation on Si surface. It is obvious that, high partial pressure of As can reliably remove the oxide film on Si. However, too high partial pressure or exposure temperature can undesirably roughen the surface and increase material consumption. Therefore, the following conditions are proposed in this study.

→ Partial pressure of As: 0.8 mbar

→ TBA exposure temperature: 420°C~annealing temperature (Open the TBA source line at 420°C, and close it when it reaches the annealing temperature point.)

✓ Partial pressure of hydrogen

Surface reconstruction by atomic scale desorption and adsorption in the MOVPE highly depends on the chemical potential of hydrogen which is flowing as a carrier gas during the process. In this study, the impact of the partial pressure of the hydrogen is verified. The surface anisotropy of the Si(1 0 0) substrate is very well correlated with the hydrogen pressure, and it was clear that higher anisotropic signal can be obtained in the higher hydrogen pressure. Thus, it is suggested that the surface reconstruction process be performed under the highest possible pressure in each reactor.

2) Ga(As)P re-growth on GaP/Si(1 0 0) template

Ga(As)P re-growth conditions were also introduced in chapter 5. Si surface preparation process is very sensitive to the remaining group-III material residuals in the reactor from previous growth. Therefore, after every growth, the reactor quartz tube and susceptor should be cleaned. This kind of cleaning process causes the productivity of the cell to be lowered. In this research, re-growth of Ga(As)P on GaP/Si(1 0 0) template by planetary reactor, which can be cleaned by introducing HCl to the reactor and can fabricate 7-samples of 2-inch wafers in one growth, was investigated.

As a result, the characteristics of regrown Ga(As)P did not show difference depending on the kind of the reactor, but it was different depending on the wafer surface temperature and reactor pressure during crystal growth.

Overview of this research

This research has been carried out from the design of the III-V / Si tandem solar cell to achieve high efficiency at the same time as cost reduction. As for the design of the cell, GaAsP top absorber incorporating multi-quantum well structure was proposed, and the structure was optimized by calculating the realistic expected efficiency of this structure. Regarding the actual fabrication of the cell, experiments were conducted focusing on the generalization of manufacturing process conditions, and proposed process conditions applicable to any reactor.

Appendix A: Calculation parameters

Table. A-1 Calculation parameters

Parameters			Value
Lattice constant [Å]	GaAs		5.6533
	GaP		5.4508
Effective mass ($\boldsymbol{m^*_{3D}}$,$\boldsymbol{m^*_{per}}$)	GaAs	Electron	0.067 m_0
		Heavy hole	0.5 m_0
		Light hole	0.082 m_0
	GaP	Electron	0.17 m_0
		Heavy hole	0.86 m_0
		Light hole	0.14 m_0
Elastic stiffness	GaAs		1.223 [(a)]
	GaP		1.439 [(a)]
Deformation potential for valence band	GaAs		1.16 [(a)]
	GaP		1.7 [(a)]
Deformation potential	GaAs		-1.7 [(a)]
	GaP		-1.5 [(a)]
Deformation potential for conduction band	GaAs		-7.17 [(a)]
	GaP		-7.14 [(a)]
Spin-orbit splitting	GaAs		0.34
	GaP		0.08
Shockley-Read-Hall life time [μsec]			100

[(a)] The values in [1].

In-plane effective mass of GaAs and GaP is used as approximate value as below [2]-[6].

$$m^*_{in,e} = 1.2 \times m^*_{3D,e} \quad (A.1)$$

$$m^*_{in,hh} = 0.4 \times m^*_{3D,hh} \quad (A.2)$$

$$m^*_{in,lh} = 2.4 \times m^*_{3D,lh} \quad (A.3)$$

Where, $m^*_{in,e}$, $m^*_{in,hh}$, and $m^*_{in,lh}$ are in-plane effective mass for electron, heavy hole and light hole respectively.

References

[1] C.G. Van de Walle, "Band lineups and deformation potentials in the model-solid theory", *Phys. Rev. B* **39** (3), 1871, 1989.

[2] B. K. Ridley, "The in-plane effective mass in strained-layer quantum wells", *J. Appl. Phys.* **68**, 4667, 1990.

[3] H. Celik, M. Cankurtran, A. Bayrakli, E. Tiras, and N. Balkan, "Well-width dependence of the in-plane effective mass and quantum lifetime of electrons in GaAs/Ga1-xAlxAs multiple quantum wells", *Semicond. Sci. Technol.* **12**, p.389-395, 1997.

[4] E. D. Jones, H. Ackermann, J. E. Schirber, T. J. Drummond, L. R. Dawson, and I. J. Fritz, "Magneto-optic determination of the light-hole effective masses in InGaAs/GaAs strained-layer superlattices", *Solid State Commun.* **55**, p.525, 1985.

[5] G. Hendorfer, M. seto, H. Ruckser, W. Jantsch, M. Helm, G. Brunthaler, W. Jost, H. Obloh, K. Kohler, and D. J. As, "Enhancement of the in-plane effective mass of electrons in modulation-doped InxGa1-xAs quantum wells due to confinement effects", *Phys. Rev. B* **48**, 2328, 1993.

[6] M. Jaffe, J. E. Oh, J. Pamulapati, J. Singh, and P. Bhattacharya, "In-plane hole effective masses in InxGa1-xAs/Al0.15Ga0.85As modulation-doped heterostructures", *Appl. Phys. Lett.* **54**, 2345, 1989.

Appendix B: Substrate surface morphology and surface reconstruction

Although not covered in the papers, natural Si(1 0 0) surface morphology before the arsenic treatment is a one of the most important factor to reconstruct the surface as a double-layer step. In this study, Si substrates made by three different companies (unknown and EnM from Japan, SiMat from Germany) were used, and except manufacturer all the specs are the same in all wafer. The company of the wafers used in early stage of this research is not clear, and it is called “unknown” here.

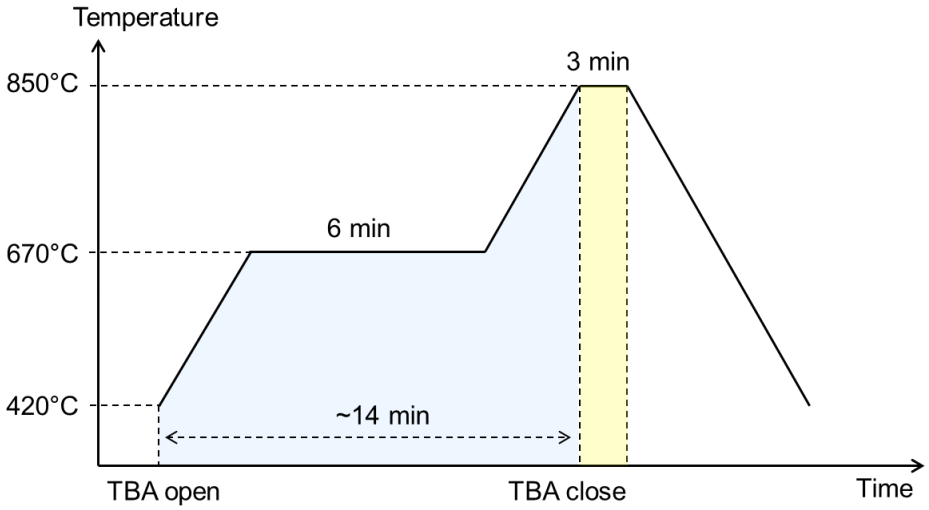

Fig. A-1 A schematic of process flow.

The RA spectra for the three samples of different companies is compared in fig. A-2, which are conducted by same surface treatment condition as described in fig. A-1.

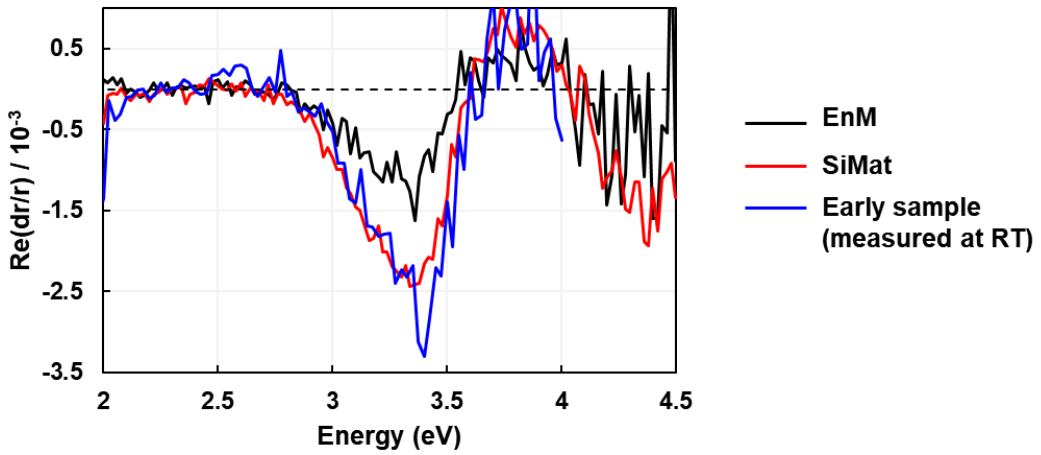

Fig. A-2 RA spectrum measured at 150 °C (only RA for early sample is measured at RT).

As shown in fig. A-2, there is a difference in RA peak intensity due to the manufacturer of the Si substrate. The anisotropy intensity of the sample made by EnM's wafer shows lower intensity than the other wafers even in totally same process conditions are applied for surface reconstruction.

The differences in surface properties according to substrate manufacturers are also confirmed by AFM (measured after the Si surface preparation) images as shown in fig. A-3. The surface roughness by RMS values are not so different from each sample. The RMS value of all the samples are around 1~2Å level. However, the surface morphology is quite different. In the case of EnM's wafer, it seems that it is hard to make flat terrace area due to bumps on the surface.

Even with the same surface reconstruction process conditions, the RA peak intensity varies depending on the substrate manufacturer. Therefore, when providers of Si substrates are changed, it is advisable to conduct the experiment after confirming the surface morphology first.

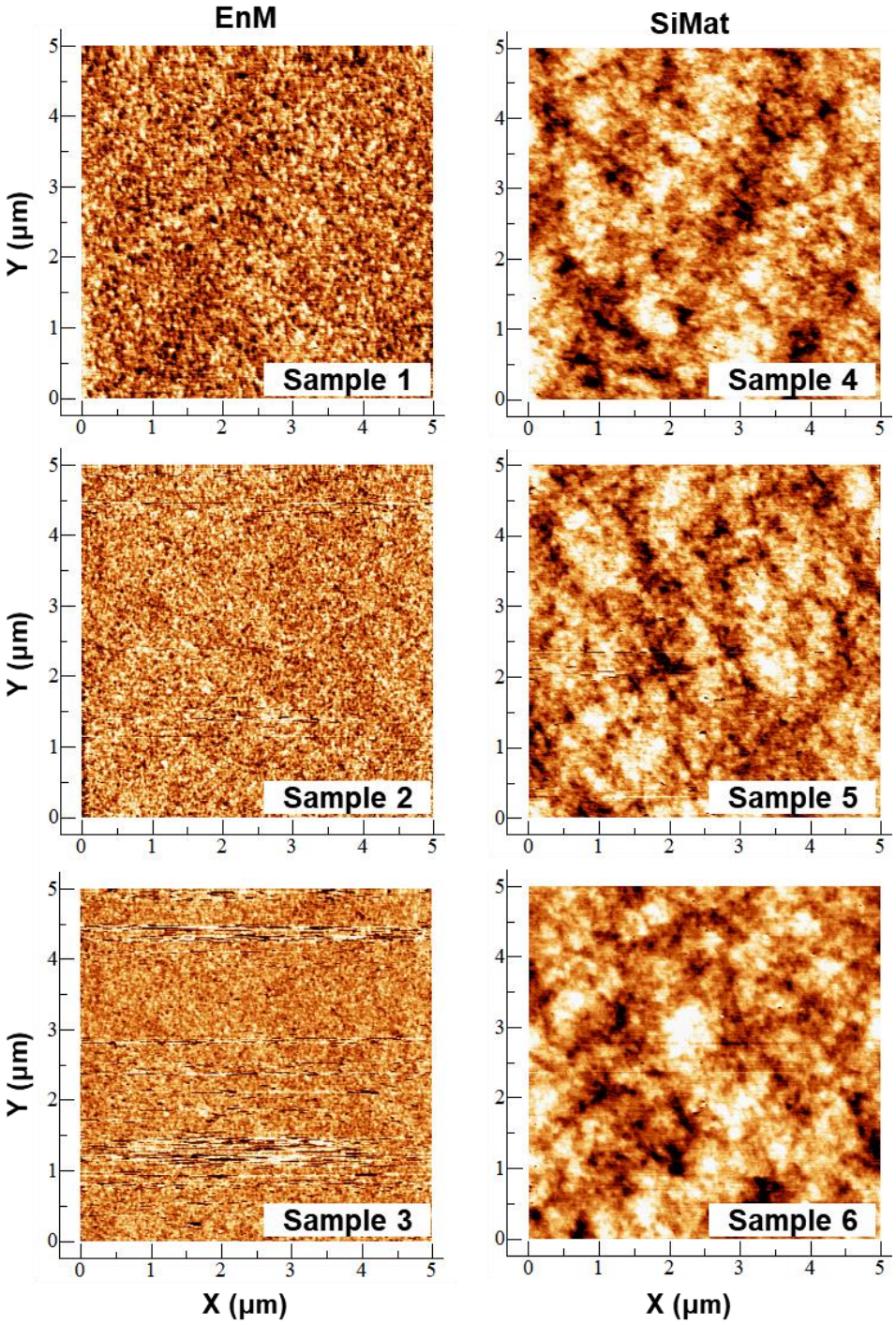

Fig. A-3 AFM images for As-modified Si(1 0 0) surface: sample 1-3 are EnM wafers and sample 4-6 are SiMat wafer.

Appendix C: B-type double-layer step formation on Si(1 0 0) surface

Not only the A-type but also the B-type double-layer step surfaces can be formed in the MOVPE reactor [1]-[2]. Here, process for the A-type and B-type double-layer step surface formation in the As ambience is introduced. The experimental details are as below.

- ✓ Thermal deoxidation: oxide layer removal at 1000 °C with background As ambience.
  - → The reactor was coated at 670 °C with As before raising the temperature to 1000 °C.
- ✓ Surface annealing at 1000 °C for ~10 min.
- ✓ A-type surface formation at 830 °C with cyclic TBA treatment.
  - → TBA supply time was controlled by in-situ RA signal: TBA started to supply when the RA of 3.1 eV has maximum value, and TBA supply stopped when the RA of 3.6 eV has maximum and RA of 3.1 eV disappeared (not at 0 but at the lowest possible level).

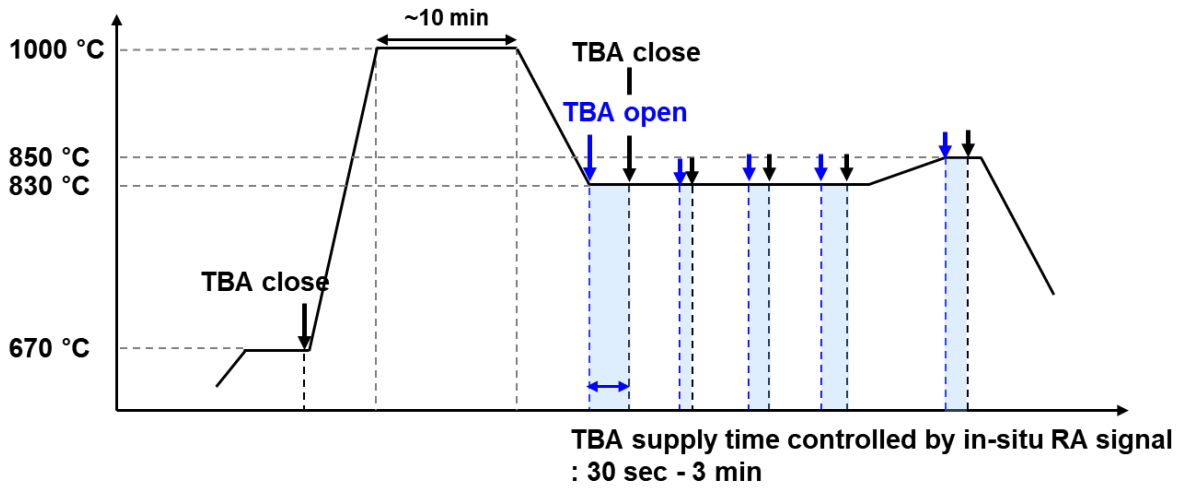

Fig. A-4 A schematic of process flow: thermal deoxidation and double-layer step formation.

Figure A-5(a) show the color plot of time transient RA during the surface preparation process.

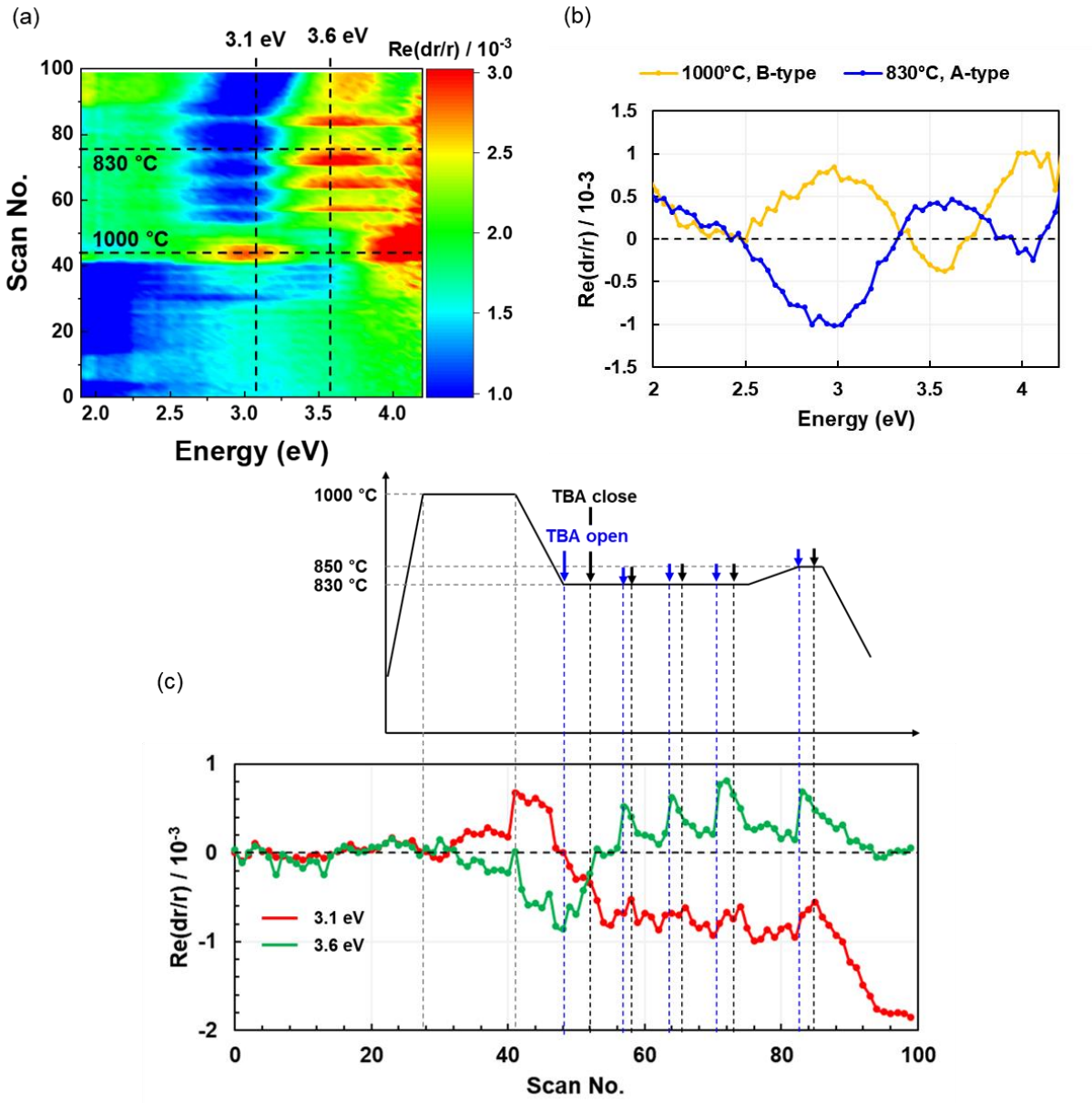

Fig. A-5 (a) Time transient RA (base line is not subtracted). (b) B-type double-layer step at 1000 °C and A-type double-layer step at 830 °C. (c) Process flow and correspondence time transient RA of 3.1 eV (for Si dimer) and 3.6 eV (As modified Si surface).

As shown in fig. A-5(c), the peaks at 3.1 eV and 3.6 eV is changing with TBA supply caused by As absorption and desorption on the Si surface.

It is clear that high temperature of 1000 °C can make B-type double-layer step on Si(1 0 0). The majority surface domain type (A-type or B-type) is also decided by cooling speed [1], but B-type surface domain can not be made with low temperature process at 830 °C.

References

[1] S. Bruckner, P. Kleinschmidt, O. Supplie, H. Doscher and T. Hannappel, "Domain-sensitive in situ observation of layer-by-layer removal at Si(100) in H2 ambient", *New Journal of Physics* **15**, 113049, 2013.

[2] A. Paszuk, O. Supplie, M. Nandy, S. Bruckner, A. Dobrich, P. Kleinschmidt, B. Kim, Y. Nakano, M. Sugiyama, T. Hannappel, "Double-layer stepped Si(1 0 0) surfaces prepared in As-rich CVD ambience", *Appl. Surf. Sci.* **462**, p.1002-1007, 2018.

Appendix D: Correspondence with the publications

A portion of the following chapters is taken from the corresponding publications. See List of Publications for the full publication details.

Chapter 4.

Boram Kim, Kasidit Toprasertpong, Agnieszka Paszuk, Oliver Supplie, Yoshiaki Nakano, Thomas Hannappel, Masakazu Sugiyama, "GaAsP/Si tandem solar cells: Realistic prediction of efficiency gain by applying strain-balanced multi-quantum wells", *Solar Energy Materials and Solar Cells* **180**, p.303-310, 2018.

Publication list

1. Journal paper

First author

[1] Boram Kim, Kasidit Toprasertpong, Agnieszka Paszuk, Oliver Supplie, Yoshiaki Nakano, Thomas Hannappel, Masakazu Sugiyama, “GaAsP/Si tandem solar cells: Realistic prediction of efficiency gain by applying strain-balanced multi-quantum wells”, *Solar Energy Materials and Solar Cells* **180**, p.303-310, 2018.

Co-author

[1] Kenaroh Watanabe, Boram Kim, Tomoyuki Inoue, Hassanet Sodabanlu, Masakazu Sugiyama, Masanao Goto, Shinya Hayashi, Kenjiro Miyano, and Yoshiaki Nakano, “Thin Film InGaAs/GaAsP MQWs Solar Cell with Backside Nano-Imprinted Pattern for Light-Trapping”, *IEEE J. Photovoltaics* **4** (4), p1086-1090, 2014.

[2] Agnieszka Paszuk, Oliver Supplie, Boram Kim, Sebastian Brückner, Alexander Heinisch, Peter Kleinschmidt, Yoshiaki Nakano, Masakazu Sugiyama and Thomas Hannappel, "GaAsP/Si tandem solar cells: In situ study on GaP/Si:As virtual substrate preparation”, *Solar Energy Materials and Solar Cells* **180**, p.343-349, 2018.

[3] Agnieszka Paszuk, Oliver Supplie, Manali Nandy, Sebastian Bruckner, Anja Dobrich, Peter Kleinschmidt, Boram Kim, Yoshiaki Nakano, Masakazu Sugiyama, Thomas Hannappel, "Double-layer stepped Si(1 0 0) surfaces prepared in As-rich CVD ambience", *Applied Surface Science* **462**, p.1002-1007, 2018.

1. Conference

1.1 International conference

First author

[1] B. Kim, K. Watanabe, H. Sodabanlu, M. Sugiyama, and Y. Nakano, “Drastic QE enhancement by light-trapping structure in InGaAs/GaAsP multiple quantum-well solar cells”, *PVSEC-22*, Hangzhou, China, Nov. 2012.

[2] B. Kim, O. Supplie, T. Watanabe, A. Paszuk, T. Hannappel, Y. Nakano and M. Sugiyama,“Double-layer step formation on Si (100) surfaces by moderate-temperature annealing coupled with TBA exposure”, *CSW2017*, Berlin, Germany, May 2017.

[3] Boram Kim, Kasidit Toprasertpong, Oliver Supplie, Agnieszka Paszuk, Thomas Hannappel, Yoshiaki Nakano and Masakazu Sugiyama, “Efficiency of GaAs P/Si Two-junction Solar Cells with

Multi-Quantum Wells: a Realistic Modeling with Carrier Collection Efficiency", *PVSC-44*, Washington D.C., United States of America, June 2017

[4] Boram Kim, Oliver Supplie, Agnieszuka Pasazuk, Thomas Hannappel, Yoshiaki Nakano and Masakazu Sugiyama, "The In-situ observation of reflectance anisotropic signal during GaP growth on Si(100) surface by MOVPE", *PVSEC-27*, Shiga, Japan, Nov. 2017.

[5] Boram Kim, Tetsuaki Okada, Oliver Supplie, Agnieszka Paszuk, Thomas Hannappel, Yoshiaki Nakano and Masakazu Sugiyama, "Impact of process parameters on double-layer step formation of Si (100) surface using TBA for III-V integration on Si by MOVPE", *ICMOVPE-XIX*, Nara, Japan, 2018.

Co-author

[1] Kasidit Toprasertpong, Boram Kim, Yoshiaki Nakano, and Masakazu Sugiyama, "Carrier Collection Model and Design Rule for Quantum Well Solar Cells", *PVSC-44*, Washington D.C., United States of America, June 2017.

[2] A. Paszuk, O. Supplie, S. Brückner, M. M. May, A. Nägelein, B. Kim, T. Watanabe, Y. Nakano, M. Sugiyama, P. Kleinschmid1, T. Hannappel, "In-situ control over dimer orientation on Si(100) surfaces in arsenic ambience and its impact on the sublattice orientation of subsequently grown GaP", *CSW2017*, Berlin, Germany, May 2017.

[3] Agnieszka Paszuk, Oliver Supplie, Sebastian Brückner, Matthias M. May, Anja Dobrich, Andreas Nägelein, Boram Kim, Tohma Watanabe, Yoshiaki Nakano, Masakazu Sugiyama, Peter Kleinschmidt, and Thomas Hannappel, "In situ control over the sublattice orientation of heteroepitaxially grown single-domain GaP/Si:As virtual substrates for tandem absorbers", *PVSC-44*, Washington D.C., United States of America, June 2017.

[4] Agnieszka Paszuk, Oliver Supplie, Sebastian Brückner, Matthias M. May, Anja Dobrich, Andreas Nägelein, Boram Kim, Yoshiaki Nakano, Masakazu Sugiyama, Peter Kleinschmidt and Thomas Hannappel, "Optical in-situ control over dimer orientation on Si(100) surfaces in arsenic ambience", *17th European Workshop on Metalorganic Vapour Phase Epitaxy*, Grenoble, France, June 2017.

[5] Agnieszka Paszuk, Oliver Supplie, Manali Nandy, Sebastian Brueckner, Anja Dobrich, Peter Kleinschmidt, Boram Kim, Yoshiaki Nakano, Masakazu Sugiyama, Thomas Hannappel, "Arsenic-modified Si(100) Surfaces for III-V-on-Si Tandem Solar Cells", *7th World Conference on Photovoltaic Energy Conversion*, Hawaii, United States of America, June 2018.

1.2 Domestic conference

First author

[1] B. Kim, K. Watanabe, H. Sodabanlu, M. Sugiyama, and Y. Nakano, "光閉じ込め構造を用いた高効率量子井戸太陽電池の作製", 2012 年秋季第73回応用物理学会学術講演会, September 2012, 愛媛大学・松山大学, Matsuyama, Japan

[2] Boram Kim, Oliver Supplie, Agnieszka Pasuzuk, Thomas Hannappel, Yoshiaki Nakano and

Masakazu Sugiyama, "MOVPEによるSi(100)基板上のGaP成長: 反射率異方性分光法による in-situ 表面観測", March 2018, Waseda University, Tokyo, Japan

Co-author

[1] Tetsuaki Okada, Boram Kim, Oliver Supplie, Agnieszka Pasuzuk, Thomas Hannappel, Yoshiaki Nakano and Masakazu Sugiyama, "MOVPEによるSi(100)基板上のGaP成長: Si表面再構成プロセス条件の検討", March 2018, Waseda University, Tokyo, Japan

Acknowledgements

I would like to express my gratitude to all people who supported my doctoral research.

First, I am very grateful to Prof. Yoshiaki Nakano for the opportunity to work in NSTL, and for his support in my research. I would like to offer my sincere appreciation to my adviser Prof. Masakazu Sugiyama for his incalculable supports including supervising the research plan and strategy, data analysis, preparation of academic conferences and correction of my papers, and the opportunity for having collaborative research with Ilmenau University of Technology for his kindness. Thanks to Prof. Sugiyama's full support, I could complete this dissertation. I would also like to give my thanks to Assoc. Prof. Takuo Tanemura for his support in this research.

My sincere appreciation also goes to Prof. Thomas Hannappel, Dr. Oliver Supplie, Dr. Agnieszka Paszuk, Mr. Manali Nandy for their insightful discussion and suggestion for completing my thesis.

Special thanks to all solar group members (Dr. Kentaroh Watanabe, Dr. Hassanet Sodabanlu, Dr. Amaury Delramarre, Dr. Kasidit Toprasertpong, Dr. Warakorn Yanwachirakul, Mr. Hsiang-Hung Huang, Mr. Hao Xu, Tetsuaki Okada, Meita Asami) and MOVPE group members (Dr. Masahiro Saito, Dr. Tohma Watanabe, Hiroaki Maruyama, Takahiro Suganuma, and Eisaku Kato).

I would like to gratefully acknowledge Atsumi Foundation for providing me a scholarship and encouraging my researches.

Finally, I would like to express appreciation to my family and friends for their support.

감사의 말씀

박사학위 논문을 퇴고하며 제 연구생활을 지지해준 모든 분들께 감사의 말씀을 전합니다.

먼저, 저를 이곳에 있게 해 주시고 저의 모든 활동을 믿고 지지해 주신 부모님께 감사의 말씀을 드립니다. 두 분의 무한한 사랑으로 오늘의 제가 있을 수 있었습니다. 모든 영광을 두 분께 드리고 싶습니다. 그리고 일본 생활의 동반자, 고운이 용선이에게 고맙다는 말을 전하고 싶습니다. 또 한국에서 항상 이 친구의 안부를 걱정하고 연구를 지지해 준 모든 친구들에게 감사의 말을 전하고 싶습니다. 마지막으로 박사 논문 퇴고까지 3년간의 생활에서 멘탈케어에 가장 큰 힘이 되어준 엑소, 백현에게 진심으로 감사의 말을 전하고 싶습니다.

마지막으로 저를 이곳에 있게 해 주신 모든 분들께 감사의 말씀을 드립니다

2018. 11. 30
Boram Kim
金 ボラム